Synthesis, characterization and novel properties of nanocomposites comprising covalently linked MOFs, graphene, BN and CNTs

A Thesis Submitted for the Degree of

Doctor of Philosophy

by

Ram Kumar

Chemistry and Physics of Materials Unit
Jawaharlal Nehru Centre for Advanced Scientific Research
(A Deemed University)
Bangalore, India

September 2016

Dedicated to my late grandfather

Declaration

I hereby declare that the thesis entitled **"Synthesis, characterization and novel properties of nanocomposites comprising covalently linked MOFs, graphene, BN and CNTs"** is an authentic record of research work carried out by me under the supervision of Prof. C. N. R. Rao, FRS, at the Chemistry and Physics of Materials Unit, Jawaharlal Nehru Centre for Advanced Scientific Research, Bangalore, India and it has not been submitted elsewhere for the award of any degree or diploma.

In keeping with the general practice of reporting scientific observations, due acknowledgement has been made whenever the work described is based on the findings of other investigators. Any oversight due to error of judgments is regretted.

Ram Kumar

Certificate

I hereby certify that the matter embodied in this thesis entitled **"Synthesis, characterization and novel properties of nanocomposites comprising covalently linked MOFs, graphene, BN and CNTs"** has been carried out by Mr. Ram Kumar at the Chemistry and Physics of Materials Unit, Jawaharlal Nehru Centre for Advanced Scientific Research, Bangalore, India under my supervision and it has not been submitted elsewhere for the award of any degree or diploma.

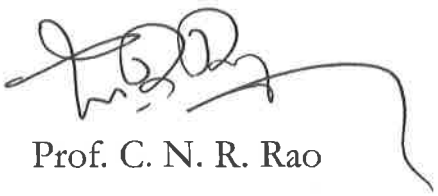

Prof. C. N. R. Rao

Acknowledgements

This thesis is the result of my work in the Jawaharlal Nehru Centre for Advanced Scientific Research, at Bangalore, India. During my stay, I have been accompanied and supported by many people. It is a pleasant duty to express my gratitude to all of them.

First and foremost, I would like to take this opportunity to express deepest gratitude to my teacher and research supervisor, a great scientist and leader, visionary and inspiration for many young minds Professor C. N. R. Rao. I thank him for suggesting interesting research problems, giving me the opportunity and freedom to work in various fields, for teaching me the art of research and for many things that I have learned just by being with him. A lesson which I have learned from him is to stay focused on work and achieve the aim under any circumstances. He will always remain a source of courage and inspiration in the most important moments of making right decisions. It is an honour to have had the privilege of being his student. I hope I will be able to stand up to his expectations and continue to do science till the end of my life.

It is a special pleasure to thank Prof. T. K. Maji and Prof. U. Ramamurty for their constant guidance, fruitful discussions and suggestions in various collaborative projects.

I am thankful to Prof. H. Ila, Prof. G. U. Kulkarni, Prof. S. Balasubramanian and Prof. Chandrabhas Narayan for their constant encouragement and support on various occasions.

A lot is owed to faculty members of JNCASR for their extremely useful courses. In particular, I would like to thank Prof. H. Ila, Prof. Aloknath Chakarborty, Prof. S. Balasubramanian, Prof. A. Sundaresan, Prof. M. Eswarmoorthy, Prof. Sridhar Rajaram, Prof. S. M. Shivaprasad, Prof. Shobhana Narsimhan, Prof. K. S. Narayan and Prof. U. V. Wagmare. The knowledge and exposure which I have received from these courses have helped me a lot.

It is a delight to work in the pleasant atmosphere and experimental facilities of CPMU, NCU and ICMS of JNCASR and Materials Engineering, IISC Bangalore. I would like to thank all the people associated in managing the department and experimental facilities. In particular, enthusiasm of Mr. S. Sashidhara while working long hours in mechanical testing lab, IISC was very inspiring.

I would like to thank all of my present and past labmates and seniors for their constant cheerful company and help in various occasions. I express my gratitude to all of my Int. Ph.D batchmates and friends for their help and support on various occasions. Rajsekhar, Sisir, Somnath, Ramanna, Chandan De, Sunita, Nitesh, Ritesh and Urmi were always a helping hand whenever I asked. I wish all of them good luck.

I thank Mrs. Indumati Rao and Sanjay Rao for the concern and care they have shown on various occasions.

I am thankful to Prof. S. K. Dash, NCERT, Bhubaneswar, for his encouragement to pursue a carrier in science at very right moment of my life. His encouragements in B.Sc. inspired me and many others to pursue a carrier in Science. I wish to express my gratitude to my family members, for without their support and encouragement, this study would not have been possible. Heartful thanks to Nivi for her support and love.

Preface

This thesis discusses composites of metal-organic frameworks (MOFs) with 2-D materials such as graphene and BN as well as composites of BN and graphene synthesized by covalent-cross linking. New porous solids based on covalent cross-linking of graphene and single-walled carbon nanotubes (SWNTs) with different length organic linkers are also the part of the thesis. This work demonstrates synergy as well as new properties in the composites. The thesis contains nine chapters. **Chapter 1** gives a brief introduction to porous solids. It also introduces the contribution of this thesis in the area of porous solids.

C**hapter 2** describes hybrid nanocomposites of the metal-organic framework ZIF-8 with graphene. These nanocomposites exhibit new and enhanced properties compared to the constituents. In continuation with this theme, **Chapter 3** presents the synthesis, characterization and functional properties of a 2D MOF with graphene. The layers of the composite can be easily exfoliated in a polar solvent such as methanol giving rise to a stable colloidal dispersion of the MOF layer supported on graphene. The composites show adsorption properties different from their parent MOF. **Chapter 4** describes the optical properties of the composites of a lanthanide-based MOF with graphene. Quenching of lanthanide emission in the composite due to charge or energy transfer process is observed as found by lifetime and quantum yield measurements.

Chapter 5 discusses a novel class of all-carbon porous solid synthesized by the pillaring of graphene with uniform length organic linkers. The pillared graphene frameworks (PGFs) were synthesized using Pd(0) catalyzed Sonogashira cross-coupling reaction. The PGFs show promising adsorption properties comparable to some of the high surface area MOFs with open metal centers, along with the advantage of high thermal, chemical and mechanical stability and superhydrophobicity.

Nano-composites of BN and graphene covalently linked by the amide bond form the subject matter of **Chapter 6**. Along with characterization of its porosity, the use of the nanocomposites in supercapacitors and as an electrocatalyst in oxygen reduction reaction has been investigated. By varying the composition (BN content) various functional properties can be tuned and exploited for various applications.

Chapter 7 tries to address the low mechanical properties of MOFs which hinders its widespread practical applications. Composites of ZIF-8 nanoparticles supported on BN shows significant improvement in the elastic modulus, hardness and thermal stability, retaining the porosity and adsorption properties. In continuation of our effort to improve

mechanical properties of MOFs, MOF graphene composites wherein graphene uniformly reinforces the MOF matrix by chemical bond formation have been investigated (**Chapter 8**). M/DOBDC (M = Mg^{2+}, Ni^{2+} and Co^{2+}, DOBDC = 2,5-dioxide-1,4-benzenedicarboxylate) shows remarkable improvement in the elastic modulus and hardness after bonding to graphene. A significant increase in surface area, CO_2 uptake, and CO_2/N_2 selectivity is also observed whereas the microporous feature of framework remains intact.

Chapter 9 investigates covalently cross-linked single-walled carbon nanotubes (SWNTs) assemblies with uniform length organic linkers. Raman spectroscopy has been explored for characterization besides other techniques. The SWNT assemblies exhibit ordered porous architecture and high surface area as well as thermal and chemical stabilities. They are superhydrophobic with good gas storage properties.

Chapter 10 correlates the findings in chapters 2-9 and gives overall conclusions of the thesis along with future directions of present investigations.

Contents

Declaration i

Certificate ii

Acknowledgements iii

Preface v

Contents vii

Chapter 1: A brief introduction to porous solids

1.1 Zeolites 2

1.2 Other important ordered and disordered porous solids 6

1.3 Metal-organic frameworks (MOFs) 9

1.3.1 Classification of MOFs 11

1.3.2 Zeolitic imidazolate frameworks 12

1.3.3 Luminescent MOFs 13

1.3.4 Nano-MOFs and coordination modulation 15

1.3.5 Gas storage/Separation 16

1.3.6 Catalysis 17

1.3.7 Mechanical properties of the MOFs 18

1.3.8 MOFs and zeolites: a brief comparison 19

1.3.9 Composites of MOFs with 2D materials graphene and BN 20

1.4 New porous solids based on covalent cross-linking and pillaring of nanomaterials (Covalent assemblies) 22

1.5 Characterization of porous solids 23

1.5.1 Adsorption isotherms 24

1.5.2 Determination of the adsorbate accessible surface area, pore size, and pore volume of porous solids 26

1.6 Conclusions 27

Chapter 2: Hybrid nanocomposites of ZIF-8 with graphene oxide exhibiting tunable morphology, significant CO_2 uptake, and other novel properties

Summary 32

2.1 Introduction 33

2.2 Scope of the present investigations 34

2.3 Experimental section 35

2.4 Results and discussion 37
2.5 Conclusions 43

Chapter 3: Growth of 2D sheets of a MOF on graphene surfaces to yield composites with novel gas adsorption characteristics

Summary 46
3.1 Introduction 47
3.2 Scope of the present investigations 48
3.3 Experimental section 48
3.4 Results and discussion 50
3.5 Conclusions 59

Chapter 4: Quenching of lanthanide emission in the composite of graphene with a Bi-based MOF

Summary 61
4.1 Introduction 62
4.2 Scope of the present investigations 62
4.3 Experimental section 63
4.4 Results and discussion 65
4.5 Conclusions 77

Chapter 5: Porous graphene frameworks pillared by organic linkers with tunable surface area and gas storage properties

Summary 79
5.1 Introduction 80
5.2 Scope of the present investigations 82
5.3 Experimental section 83
5.4 Results and discussion 86
5.5 Theoretical studies of pillared graphene frameworks 95
5.6 Conclusions 98

Chapter 6: BN-graphene composites generated by covalent cross-linking with organic linkers

Summary 101
6.1 Introduction 102
6.2 Scope of the present investigations 103

6.3 Experimental section 105
6.4 Results and discussion 107
6.5 Conclusions 119

Chapter 7: Functionality preservation with enhanced mechanical integrity in the nanocomposites of the metal-organic framework, ZIF-8, with BN nanosheets

Summary 122
7.1 Introduction 123
7.2 Scope of the present investigations 123
7.3 Experimental section 124
7.4 Results and discussion 126
7.5 Conclusions 134

Chapter 8: Remarkable improvement in the mechanical properties and CO_2 uptake of MOFs brought about by covalent linking to graphene

Summary 137
8.1 Introduction 138
8.2 Scope of the present investigations 139
8.3 Experimental section 140
8.4 Results and discussion 141
8.5 Conclusions 159

Chapter 9: Assemblies of single-walled carbon nanotubes generated by covalent cross-linking with organic linkers

Summary 163
9.1 Introduction 164
9.2 Scope of the present investigations 165
9.3 Experimental section 166
9.4 Results and discussion 169
9.5 Theoretical studies of pillared graphene frameworks 178
9.6 Conclusions 181

Chapter 10: Conclusions of the thesis and future directions 184

Chapter 1: A brief introduction to porous solids

Porous solids can be defined as solids having adsorbate accessible pores, channels, cavities and empty spaces available for physisorption. Due to the presence of porous architecture in the bulk of solid, porous solids exhibit high adsorbate accessible surface area in comparison to non-porous solids which only show surface adsorption and hence low adsorbate accessible surface area. Various gas molecules and adsorbates depending on the dimension of the pores and channels available can easily permeate and pass through the bulk of these solids. The porous architecture of solids can be uniform and well-ordered as in the case of zeolites, metal-organic frameworks (MOFs), and ordered mesoporous silica such as MCM-41 or SBA-15 or random with a non-uniform distribution of cavities pores and channels as in activated charcoal.[1] Porous solids, although having well-ordered porous architecture, may or may not be crystalline. For example, MOFs, zeolites, MCM-41 and SBA-15 have uniform well-ordered porous architecture but MOFs and zeolites are crystalline with well-defined atomic positions, but the walls of MCM-41 and SBA-15 are amorphous. Voids in these porous solids are generally occupied by guest or template molecules and can be easily removed by heating or evacuation. Based on the International Union of Pure and Applied Chemistry (IUPAC) classification of pores, porous solids can be classified into three categories. Porous solids with a width not exceeding about 2 nm are called microporous, solids having pore width between 2 nm and 50 nm are mesoporous solids, whereas solids with pore width more than 50 nm can be defined as macroporous solids.[2] The ordered porous solids have very well defined pore size distribution. Non–ordered porous solids have a range of pore size distribution due to the random distribution of pores and channels of different size, shape, and dimension. Ordered porous solids, in addition to the main well-defined pores, often show minor contribution in the mesoporous or macroporous region of pore width due to the particle agglomeration and should not be confused with the main pores of the material. All these porous solids have characteristic adsorption isotherms due to the porous architecture present in them as discussed in detail in the section on characterization of porous solids. Porous solids have immense practical and commercial importance. There has been intense research in the development, characterization and applications of porous solids. Several decades of research in the area of porous solids have resulted in the development of wide range of crystalline, amorphous, ordered and non-ordered porous solids. Chemical compositions of porous solids vary from completely inorganic to porous organic polymers

and inorganic–organic hybrids such as MOFs. Till 1990s, zeolites and activated carbons were the most explored porous solids. In the 1990s, mesoporous silica-based porous solids (MCM-41 and SBA-15) were developed.[3] Followed by the initial work of Robson *et al.* in 1990 there has been significant development in high surface area MOFs since 1995.[4] Along with conventional porous materials, nanocarbons such as carbon nanotubes and carbon fibers were also studied for gas storage applications.[5] Recently, graphene-based carbon materials have been studied for gas storage and catalyst support.[6] Some of the new materials with high surface area and remarkable CO_2 and CH_4 adsorption capability that have been developed recently are graphene-like borocarbonitrides, $B_xC_yN_z$.[7] Other important developments in last decade are covalent organic frameworks (COFs) and conjugated microporous polymers. Owing to the well-known industrial requirement for porous solids in storage/separation, catalysis, ion exchange, sensors etc.[8] Significant development is expected in the area of porous solids, depending on the required applications. CO_2 sequestration is another area where porous solids can have a significant advantage over amine-based solvents.[9] Graphene-based porous solids are promising for CO_2 sequestration applications. Porous solids are used in wide range of applications such as catalysis, gas adsorption, purification, and separation, as electrodes in energy storage devices, as desiccants/adsorbents, for ion exchange and transport and other industrial processes.

1.1 Zeolites

The word "zeolite" has been derived from Greek words '*zein*' (to boil) and '*lithos*' (rock) meaning boiling rock and was given in 1756 by Swedish chemist and mineralogist Alex Fredrik Cronstedt also known for the discovery of nickel reported in 1751.[10] It was Cronstedt who observed that on heating a natural zeolite material, the solid material appeared to bubble and the particles to dance, as water was lost as steam from the pores of the mineral. Cronstedt's zeolite was most likely predominantly stellerite mixed with a minor amount of stilbite (Figure 1).[11] Among other contributions of Cronstedt, he was the first to advocate the use of chemical composition instead of physical properties for the classification of minerals.

Zeolites were largely ignored by chemists for almost 200 years although some investigations for synthesis and applications in ion exchange for water softening and molecular sieving properties were explored. The breakthrough came in 1948 when R. M. Barrer synthesized an analogue ZK-5 of naturally occurring zeolite Chabazite (Figure 2).[12] Although naturally–occurring zeolites had previously been synthesised in the laboratory, Barrer's was the first material with no known natural counterpart. This lead to significant

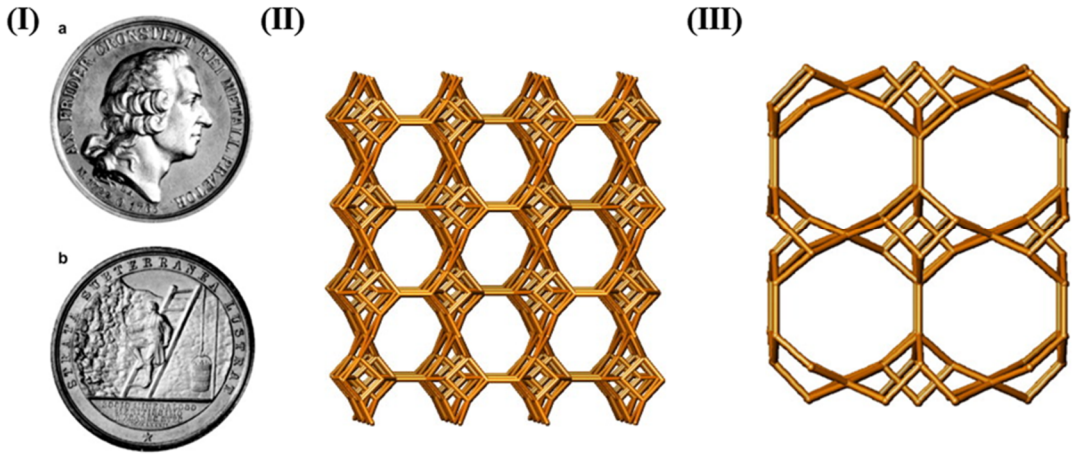

Figure 1. (I) The two sides of the silver medal in the honour of Alex Fredrik Cronstedt designed by the Royal Swedish Academy of Sciences. (II) Naturally occurring zeolite stilbite structure showing only T–T atom vectors. Oxygen atoms are at the midpoints of the T–T vectors. (III) The stellerite structure. (Adapted with permission from ref. 10).

research in the area of zeolites in both academia and industry and as of 2015, 229 unique zeolite frameworks have been identified, and over 40 naturally occurring zeolite frameworks are known. The importance of these porous solids can be recognized form the fact that millions of tons of synthetic zeolites are produced and used worldwide.

Zeolites can be defined as crystalline porous aluminosilicates built up of TO_4 tetrahedra having a Si^{4+} or Al^{3+} cation (T-atoms) at the center and four oxygen atoms at the corners. Each corner is shared by two TO_4 units resulting in a three–dimensional framework with channels, cavities and empty spaces denoted as "micropores". The basic molecular formula for zeolites is $M_{2/n}O.Al_2O_3.xSiO_2.yH_2O$, where M is a cation of n valence. Although the initial

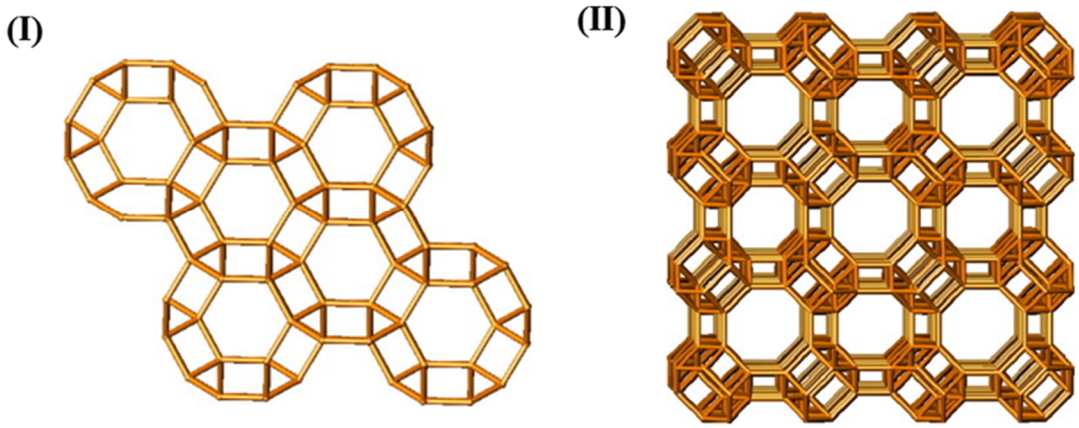

Figure 2. (I) Structure of naturally occurring zeolite chabazite showing the only T–T atom vectors. (II) The nSi/nAl framework of zeolite ZK-5 first synthetic zeolite synthesized by Barrer. (Adapted with permission from ref. 10)

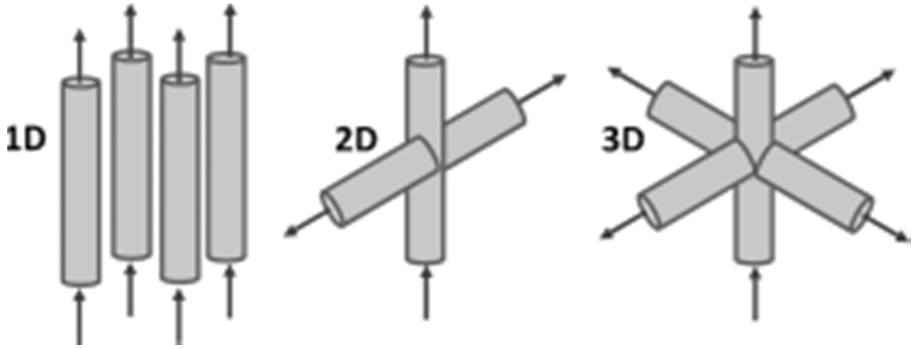

Figure 3. Classification of zeolites based on the dimensions through which a molecule can diffuse within the zeolitic crystal. (Adapted with permission from ref. 14)

compositions were limited to aluminosilicates, many heteroatoms such as B, P, Sn,Ti, Fe,Ge, Ta, and V, have been introduced in the framework in addition to Si and Al.[13] This large chemical versatility has allowed in controlling the physical and chemical functionalities such as acidity, redox properties, or hydrophilic–hydrophobic nature resulting in a large number of applications.

Zeolites are classified depending on the size of the opening that defines the pores or the number of dimensions through which a molecule can diffuse within the crystal (Figure 3). The Zeolites with pore opening limited by 8 atoms in tetrahedral coordination are defined as "small pore zeolite" (8–rings), by 10 atoms as "medium pore zeolites" (10–rings), by 12 atoms are "large pore zeolites" and with more than 12 atoms as "extra-large pore zeolites" (12–rings).[13b,14]

Zeolites are porous solids of choice in catalysis, gas adsorption, purification and separation, desiccant/adsorbent and ion-exchange.[10,13b,15] It is important to understand the

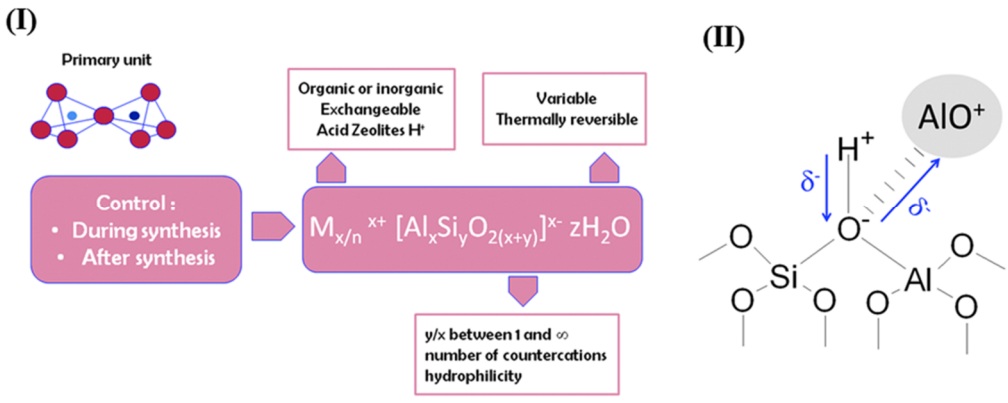

Figure 4. (I) The chemical composition of zeolites and possibilities for its control. The key parameters controlling functional properties are nature of charge-balancing cations and Si/Al ratio. (II) The acidity observed in zeolites due to the synergy between Lewis acid sites (AlO^+) and Brönsted OH site. (Adapted with permission from ref. 15)

properties of zeolites which make it useful as it helps in designing other porous solids. Zeolites are microporous with pores in the molecular dimension of 0.3–1.5 nm making it useful in molecular sieving and trafficking. The Si/Al ratio in the frameworks determines many properties (Figure 4). Low Si/Al ratio zeolites are susceptible to attack by acid, water, and steam and are highly hydrophilic. The silica enriched zeolites are hydrophobic and organophilic adsorbents. The counter-ion present in the cavity for charge electroneutrality of the AlO_4 ion can be easily exchanged making it useful as an additive in detergents for water softening and for nuclear waste treatment. The protonic forms of zeolites are Brönsted acids whereas the Al-enriched zeolites are Lewis acidic due to the formation of octahedrally coordinated extra framework aluminium (EFAL)(Figure 4).[15] This makes zeolites good heterogeneous solid acid catalysts for a host of acid–catalyzed reactions, such as isomerization, alkylation, and cracking. Zeolites confine molecules in a small space, which causes changes in their structure and reactivity. Most zeolitic catalysts used in petrochemical applications involve Lewis acidic reaction sites.

Zeolites have a reasonable Brunauer–Emmet–Teller (BET) surface area in the range of 200–500 m^2/g and pore volume around 0.1–0.5 cm^3.[16] The other properties making it remarkably useful are high thermal and chemical stabilities and mechanical properties. The zeolites have an elastic modulus in the range of 40–100 GPa and a hardness of 2.5–10 GPa.[17] The zeolites frameworks are rugged and sturdy to various mechanical deformations. The industrial process involves the formation of densely packed adsorption bed and porous membranes through which adsorbates are passed and adsorption bed or porous membranes are regenerated for another cycle. In fact, external hydrostatic pressure of several GPa

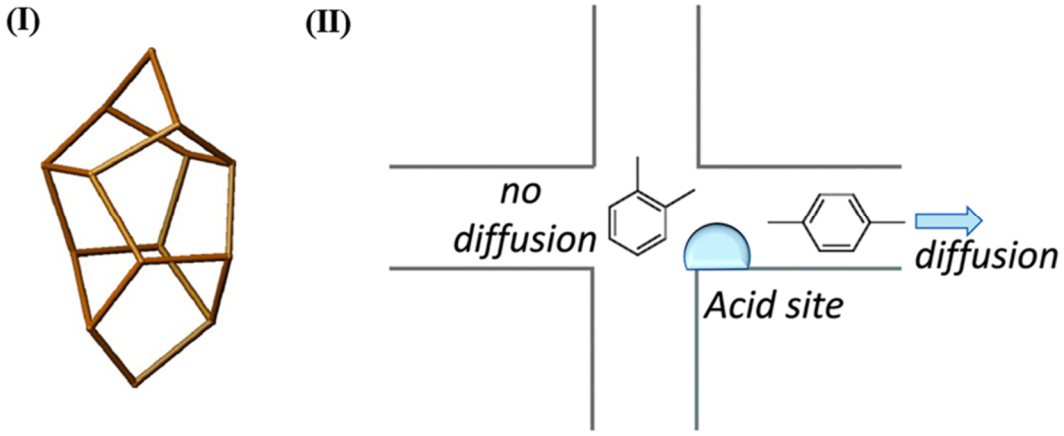

Figure 5. (I) The fundamental penatsil repeating unit of ZSM-5. (II) Schematic representation of shape selectivity in ZSM-5 for the formation of p-xylene in toluene disproportionation. (Adapted with permission from ref. 10 and 15)

is common under practical situations. The collapse of framework structure will result in is loss of porosity and catalytic center. High framework stability under various mechanical deformations and high performance for several cycles is an important requisite before considering any practical applications. The high mechanical strength of zeolite crystals increases the performance lifetime and efficiency of the process and in turn, decreases the overall cost making it a reliable porous solid. The vast amount of research in the area of zeolites has inspired the search for analogues porous solids and resulted in the discovery of ordered porous metal phosphates such as aluminium phosphate and reduced molybdenum phosphates.[1a,18]

1.2 Other important ordered and disordered porous solids

In addition to zeolites, other high surface area porous solids are porous carbons, pillared layer solids synthesized from clay, mesoporous silica such as MCM-41 and SBA-15, covalent organic frameworks, microporous organic polymers, few-layer borocarbonitrides, nanocarbons single and multi-walled carbon nanotubes and graphene and ceramic material few-layer BN.[1c,5,7,19] The breakthrough in ordered mesoporous solids came in the 1990s when MCM-41 was reported, although such ordered mesoporous solids have been patented and synthesized previously.[3a,20] Mesoporous silica has a very well-ordered hexagonal array of pores and is generally synthesized from the organic-inorganic assembly of the silicate produced by the hydrolysis of silane precursors (tetraalkoxysilane) with soft matter like organic molecules or supramolecules (e.g. amphiphilic surfactants and bio-macromolecules) which act as structure directing agents. Surfactants are most commonly used as templates. The cooperative self-assembly between the surfactants and silicate species is driven by weak, non-covalent interactions such as hydrogen bonds, van der Waals forces and electrostatic interactions. Mesoporous silica is obtained by the removal of surfactant templates (Figure 6(III)).[21] The porous pillared layer solids include mostly pillaring of smectite clays, phosphates, and phosphonates of tetravalent metals, and layered double hydroxides with cations and different intercalating species. Uniform pillaring between the layers creates addition adsorbate accessible space in the interstices (Figure 6(I)).[19a]

Along with zeolites, disordered porous carbon synthesized using various techniques is another porous solid of choice due to various factors. It has been reported in the literature over 100 years and companies produce porous carbon commercially with a ultrahigh surface area of ~ 3000 m^2/g.[22] The covalent organic frameworks are made entirely of light elements

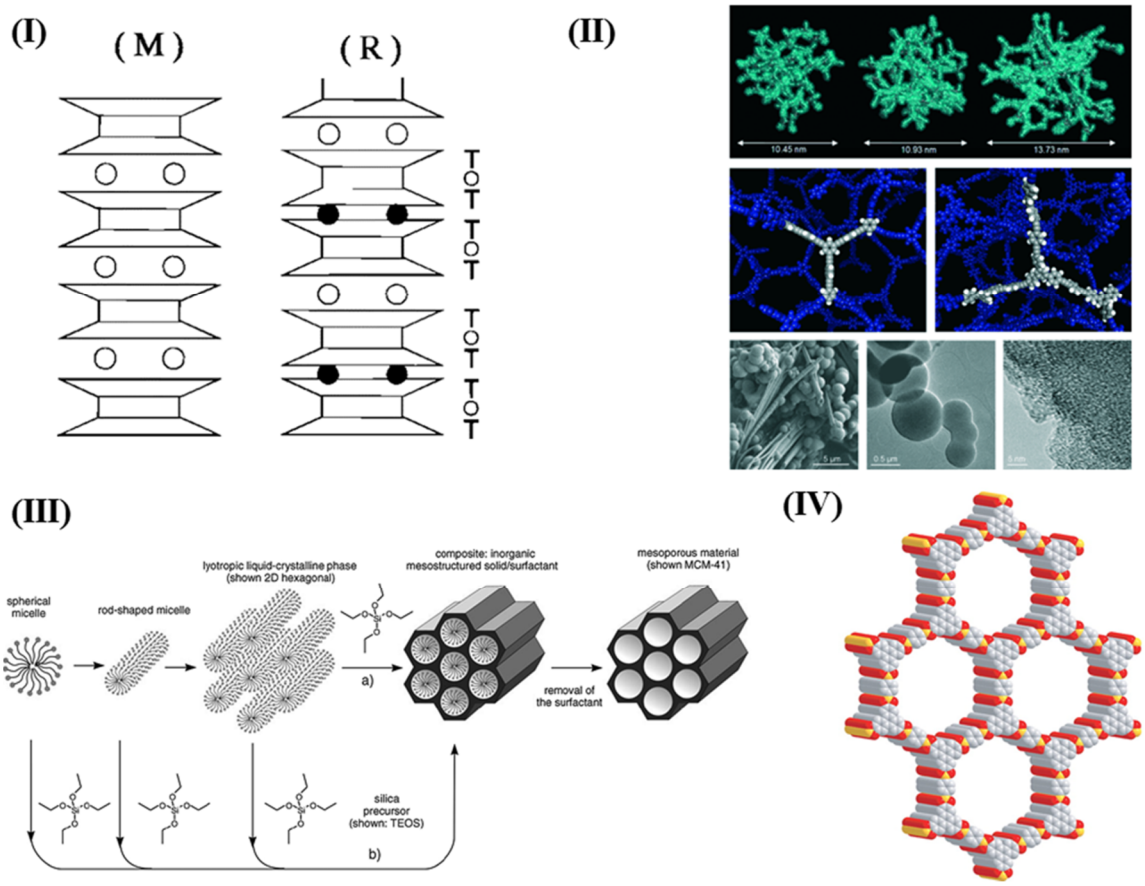

Figure 6. (I) Schematic structure of pillared layer clay montmorillonite (M) and rectorite (R). The T-O-T layer structure (T = tetrahedral, O = octahedral) is represented by trapezoids and rectangles. The exchangeable and nonexchangeable charge compensating cations are represented by open and solid circles respectively. (II) Simulated and microscopic porous architecture of a prototypical conjugated microporous polymer. (III) Schematic representation of surfactant template-assisted synthesis of mesoporous silica MCM-41. (IV) The porous architecture of COF-5. (Adapted with permission from ref. 19 (a), 22, 21 and 19b)

(H, B, C, N and O) by a covalent bond. They have high surface area, ordered and crystalline porous architecture although hydrothermal stability is a concern for boronic acid based COFs (Figure 6(IV)).[19b] Amorphous porous organic polymers are microporous solids with the ultrahigh surface area and diverse chemical functionality can be introduced with relative ease (Figure 6(II)).[23] The B, N and C atoms are adjacent elements in the periodic table with similar radius and can be substituted in the lattice to form a ternary alloy. Substituting the sp^2 hybridised C atoms on the graphene basal plane results in the formation of borcarbonitrides ($B_xC_yN_z$) (Figure 7(II)).[19c,24] The composition of BCN can be varied in a uniform fashion to control the substitution level and functional properties. The 2D layers of borocarbonitrides have a high surface area but they have nonuniform pore size distribution.[7] The nanocarbon such as graphene and single-walled carbon nanotubes (SWNTs) exhibits a reasonably high

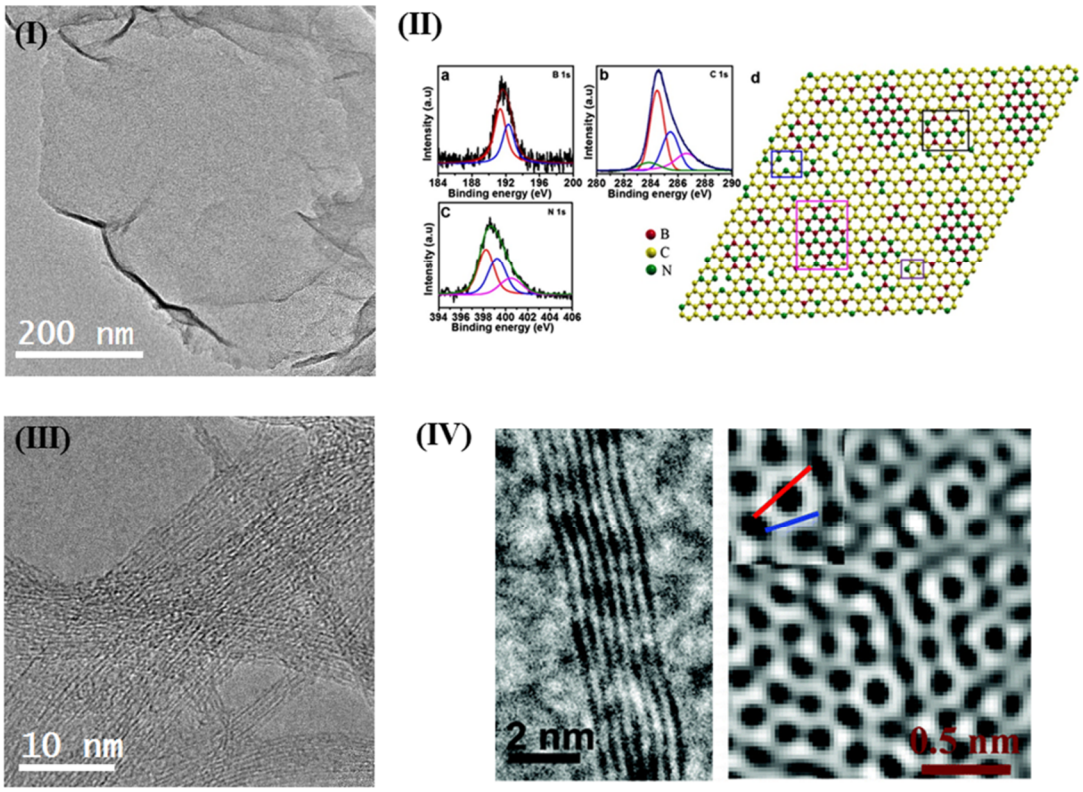

Figure 7. Tem image of high surface area few-layer graphene produced by thermal exfoliation of graphene oxide (typical BET surface area ~900-1000 m^2/g). (II) Schematic representation of BCN synthesized by substituting C atoms with B and N atoms in the graphene lattice. (III) Single-walled carbon nanotube bundles showing ~ 1 nm nanotubes aggregated due to van der Waals interaction (typical BET surface area ~ 200-400 m^2/g). (IV) High surface area Few-layer BN synthesized by urea route (Typical BET surface area ~ 700-1000 m^2). The observed surface area depends on the number of layers present. (Adapted with permission from ref. 24 and 19d)

surface area and different porous solids have been developed from them as an electrode material in supercapacitors, catalysis, gas storage and separation applications (Figure 7(I and III)).[6a,7,25] In particular, single-walled carbon nanotubes (SWNTs) and graphene were widely investigated for hydrogen storage applications.[5-6,26] SWNTs have a uniform diameter of ~0.9–1.2 nm and uniform porous architecture for molecular trafficking from inside the tube can be prepared (Figure 7(III)). The carbon chemistry is very versatile and porous solids derived from graphene and BN can be functionalized with different functional groups depending on the requirement. BN is a ceramic material with high surface area, very high thermal and chemical stabilities. Recently few-layer BN and BN microbelts have been synthesized with good adsorption properties for various gases and organic compounds (Figure 7(IV)).[19d,19f] The advantage of using BN is that it can be easily regenerated and used several times by heating in an oxygen atmosphere at high temperature.

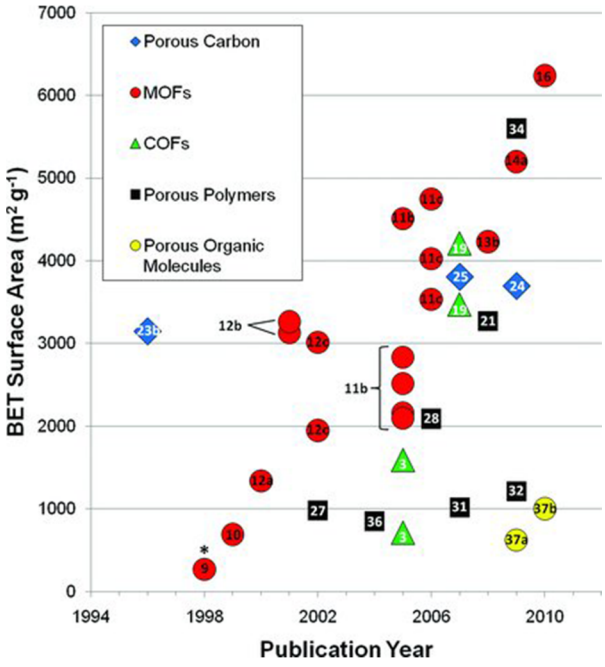

Figure 8. The plot of BET surface area versus publication year for examples of materials with exceptional surface areas in their class. The asterisk represents a Langmuir surface area measurement. (Adapted with permission from ref. 1c)

When considering the practical applications of porous solids, the surface area is only one of a number of properties which is important in porous solids. Physical and chemical properties of porous solids are important aspects which need consideration. Metal-organic frameworks (MOFs) have ultrahigh surface areas but suffer from low framework stability, when subjected to mechanical deformations (Figure 8). The low framework stability is a major concern before considering practical applications. There is a need to understand in detail the nature of the interaction between adsorbents and adsorbates. Commercially available materials such as porous carbons exhibit high surface areas and are chemically stable, scalable, and comparatively inexpensive. The incorporation of useful properties and functions within robust and scalable porous solids with high surface areas is the subject of this thesis.

1.3 Metal-organic frameworks (MOFs)

Metal-organic frameworks (MOFs) or porous coordination polymers (PCPs) are an important class of well-ordered crystalline porous solids consisting of inorganic vertices and organic struts, connected by coordination bonds of moderate strength (Figure 9).[27] MOFs have attracted widespread attention because of the well-ordered crystalline microporous architecture analogues to the zeolites along with the potential of exploiting both inorganic and organic components within the same framework structure.[28] In addition to the porous

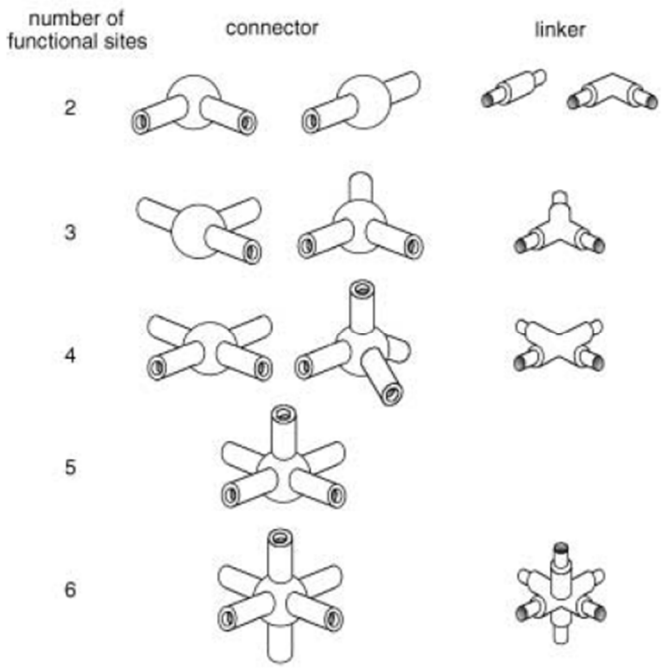

Figure 9. Components of metal-organic frameworks (MOFs). (Adapted with permission from ref. 27)

architecture, they also have interesting optical and magnetic properties.[29] Organic ligands offer tunable properties based on shape, size, and functionality. By changing the length of ligand, the binding site of the ligands and introducing different functional group in linker important functional properties, flexibility, and pore size can be tuned. The advantage of having a library of metal ions from the periodic table gives the privilege of designing magnetic, optical and multifunctional materials. Large numbers of organic ligands are commercially available or can be designed according to pore size and functionality requirements. Most MOFs are microporous although a few mesoporous frameworks have also been reported. The design of MOFs with an ordered array of the basic building units has been extensively studied for the development of new solid state functional materials. A large number of dense, as well as porous structure based on the carboxylate group, has been synthesized with interesting properties.[30] Generally, framework structures based on metal carboxylates are rigid and have been used to design high surface area materials for gas storage applications.[31] Other interesting classes of MOFs are flexible which responds reversibly to external stimuli. In addition to the coordinate bond other weak interactions such as hydrogen bonding, π-π interactions and van der Waals interactions are generally utilized for designing flexible MOFs. Crystalline structures are generally rigid and flexibility of framework structures is an important property of MOFs.[32] The topology of MOFs is intimately related to the coordination environment of metal ion and the geometry of the organic ligand, which

together form overall framework structure and dictate the property. Hybrid organic–inorganic analogues of zeolites synthesized using imidazole based ligands and Zn (II) metal ion with very good chemical and thermal stability are other important class of MOFs.[4b]

Typically, MOFs are synthesized under solvothermal conditions by taking an appropriate concentration of the metal ion, organic ligand, and a suitable solvent. The reaction temperature, choice of the solvent, reaction time and pH plays an important role in designing the framework structure. Other important parameters controlling the formation of framework structure are kinetic and thermodynamic control. Slow diffusion technique has also been used to grow MOF crystals under ambient condition. In this technique metal, ion and ligand are dissolved in two different solvent and slow diffusion forms the MOF crystals at liquid- liquid interface. Other techniques such as sonochemical, microwave and mechanochemical synthesis etc. have also been developed for the synthesis of MOFs.

Highly porous structure with well-defined and tailorable pores and specific functionality make MOFs promising materials for gas storage/separation, catalysis and sensing applications.[33] In addition to gas storage applications, lanthanide/lanthanide doped frameworks and lanthanide and transition metal based heterometallic frameworks show interesting optical and magnetic properties.[31,34] Using a proper choice of the metal ion and the ligand, multifunctional materials with luminescence, magnetism and porosity can be designed. These materials will have promising optical, optoelectronic, sensing and biomedical applications. Recently, many nano-MOFs and hybrid composites have been synthesized.[35] Brief accounts of some of the promising applications of these hybrid organic-inorganic framework materials relevant to the thesis are given in separate sections.

1.3.1 Classification of MOFs

Table1 shows the complete range of possibilities in terms of M–ligand–M connectivity and extended inorganic dimensionalities.[31,34] In table1, *m* represents the dimensionality of ligand bridging (O^m) and *n* represents the dimensionality of inorganic connectivity (I^n). Overall the structure is represented by the notation I^nO^m and the sum of exponents gives the overall dimensionality of the structure. Interestingly the entire family of organometallic chemistry and much of classical coordination chemistry is represented within a single box (I^0O^0) in table1 (i.e. both the ligand connectivity M–L–M *(m)* and inorganic connectivity *(n)* = 0). The remaining three boxes in the first column represent the coordination polymers with extended ligand connectivity in a different dimension and overall dimensionality 1–3. The three boxes in the second column represent hybrid compounds with extended inorganic connectivity in

Table 1. Classification of hybrid inorganic-organic framework solids.[31]

Metal-organic-metal connectivity, O^n (n = 0-3) \ Dimensionality of inorganic connectivity, I^n (n = 0-3)	**0**	**1**	**2**	**3**
0	Molecular complexes I^0O^0	Hybrid inorg chains I^1O^0	Hybrid inorg. layers I^2O^0	3-D Inorg. hybrids I^3O^0
1	Chain coordination polymers I^0O^1	Mixed inorg.-organic layers I^1O^1	Mixed inorg.-organic3-D framework I^2O^1	___
2	Layered coordination polymers I^0O^2	Mixed inorg.-organic 3-D framework I^1O^2	___	___
3	3-D coordination polymers I^0O^3	___	___	___

one dimension (I^1) with an overall dimensionality between 1 and 3. The two boxes in the third column represent hybrid compounds with extended inorganic connectivity in two dimensions with the overall dimensionality of structure between 2 and 3. The first box in the fourth column represents a rare class of hybrid compound (I^3O^0) with the extended inorganic connectivity in all the three dimensions (I^3) and overall dimensionality of 3. Hybrid compounds with zero inorganic connectivity and ligand connectivity M-L-M in different dimensions are coordination polymers, which can be represented as ${}_xI^0O^m$ where *x* represents the nuclearity of the metal site. For coordination polymers with isolated metal sites, $x = 1$ and for cluster metal sites, $x > 1$.[31]

1.3.2 Zeolitic imidazolate frameworks

Zeolitic imidazolate frameworks are an important class of MOFs with a structure analogous to zeolites. These framework structures are designed by carefully selecting metal ion and imidazole based linkers. These imidazole-based ligands make M-Im-M angle close to 145 °, which is coincident with the Si-O-Si angle commonly found in many zeolite structures. ZIFs have been shown to have high thermal and chemical stability and surface area.[4b] ZIFs

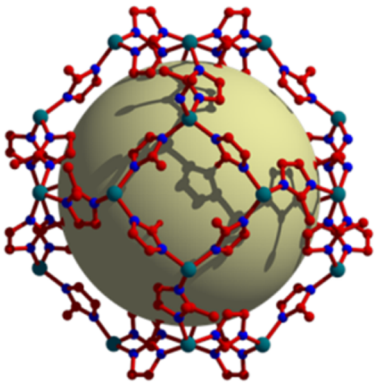

ZIF-8

Figure 10. Pore of ZIF-8**.**

have an advantage in comparison to conventional zeolites; many ZIF structure has been reported to have a remarkably high surface area in comparison to inorganic zeolites. In addition to a higher surface area, the different functional group can be attached to imidazole linkers for specific applications. ZIF-8 is one of the widely studied zeolitic imidazolate frameworks with a sodalite zeolite structure, containing large cavities (~11.7 Å of diameter) interconnected by narrow windows (~3.40 Å) (Figure 10). ZIF-8 nanoparticles can be synthesized by mixing 2-methylaimidazole and Zn (II) ions in water or methanol. The high surface area with good thermal and chemical stability has made ZIF-8 promising in catalysis, gas storage, polymer membranes for gas separation etc. Hybrid nanocomposites of ZIF-8 with metal, semiconductor and transition metal oxide nanoparticles with interesting optical and magnetic property have been studied.[36] The thesis explains a simple method for the growth of ZIF-8 nanoparticles on the graphene surface. ZIF-8 nanoparticles are chemically bonded with the functional groups present on the graphene basal plane. The functionalized graphene basal plane controls the nucleation and growth of ZIF-8 nanoparticles by coordination modulation. The resulting composites can be used for gas storage, membranes for gas separation and catalyst design.

1.3.3 Luminescent MOFs

Luminescence in MOFs arises from ligand excitation of highly conjugated ligands, charge transfer processes such as metal to ligand charge transfer (MLCT) and ligand to metal charge transfer (LMCT) and metal-centered emission in case of lanthanide ions. The 4f orbital in lanthanide ions (Ln^{3+}) are shielded by filled $5s^2$ and $5p^6$ orbitals.[37] Due to the shielding of 4f orbital lanthanide ions are less sensitive to the chemical environment around the metal ion

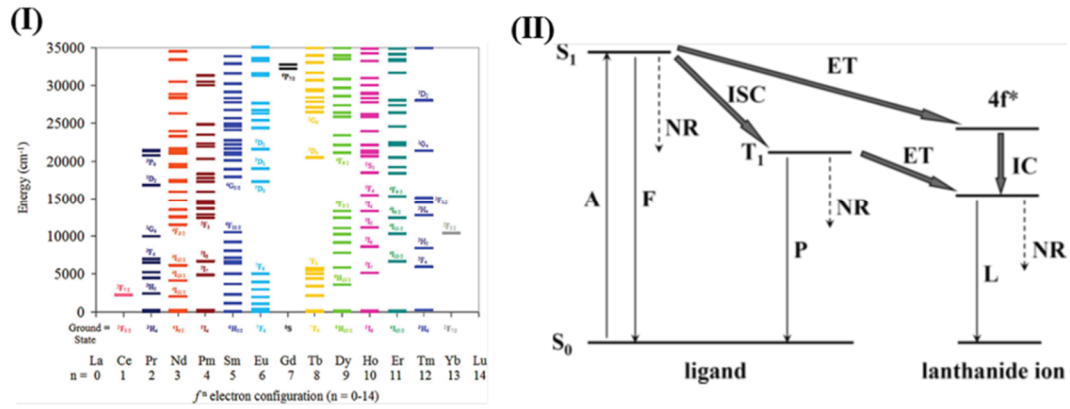

Figure 11. (I) Electronic excited-state energy levels for Ln^{3+} ions. (II) Schematic representation of energy transfer process involved in lanthanide MOFs. Energy transfer process is sometimes referred as antenna effect. (Adapted with permission from ref. 37)

and have well-defined energy levels. Owing to the well-defined energy levels each lanthanide ion exhibits narrow and characteristic 4f-4f transitions. Figure 11 shows the electronic energy levels of lanthanide ions. Due to the forbidden f-f transitions, lanthanide ions suffer from weak light absorption, which makes the direct excitation of metal ions very inefficient. However, in the case of MOFs, this is not a problem due to energy transfer from the photoexcited organic ligand to the lanthanide centers. Figure 10 shows the process of energy transfer from ligand to lanthanide ions. The main energy transfer process involves ligand centered absorption followed by intersystem crossing $S_1 \rightarrow T_1$, $T_1 \rightarrow Ln^{3+}$ transfer, and metal-centered emission. Another possible energy transfer process involves direct energy transfer

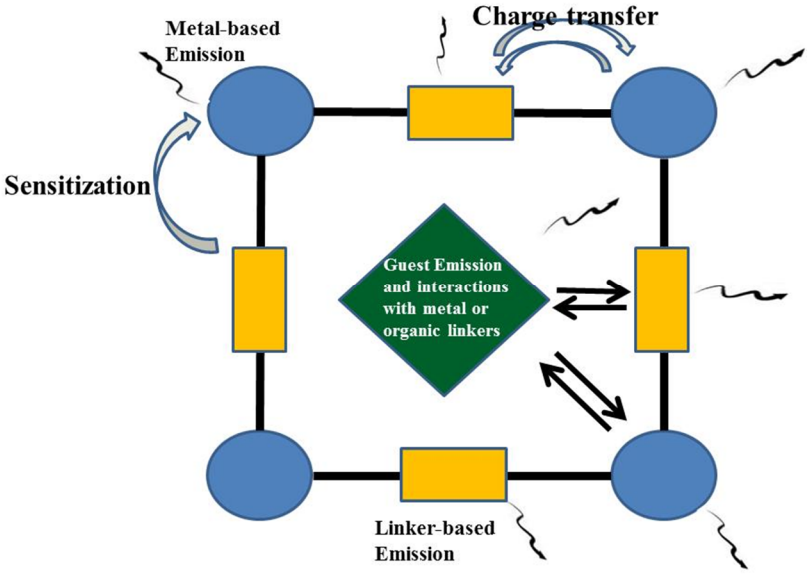

Figure 12. Various possibilities of luminescence in MOFs

from excited singlet state S_1 of ligand to the energy levels of lanthanide ion. This mechanism of direct energy transfer is known for Eu^{3+} and Tb^{3+}. If the process of energy transfer is not very efficient, both remaining ligand fluorescence and the lanthanide centered emission are observed. Efficient energy transfer is achieved by a proper choice of ligands. The lowest triplet state of the organic linker should be located at an energy level nearly equal to or above the resonance level of the lanthanide ions.[38]

Lanthanide ion based MOFs have promising optical, optoelectronic and biomedical applications. Several heterometallic lanthanide frameworks have also been designed. Recently bismuth-based frameworks which have not been studied in detail have been shown as an efficient host for lanthanide ions with efficient energy transfer and high quantum yield.[39] The possibility of having optical, magnetic and porosity properties in the same hybrid material is interesting. The thesis discusses the quenching of lanthanide emission in a lanthanide-based graphene–MOF composite.

In addition to lanthanide ion based luminescent MOFs several other luminescent MOFs due to flourishing highly conjugated ligands or fluorescent guest have been studied. The Charge transfer luminescence in d^{10} metal ions has been explored. Ligand-based luminescence is generally stronger in MOFs in comparison to solution due to the rigid arrangement of linkers around the metal ions. In addition to the enhancement in lifetime and quantum yield of ligand-based luminescence in the framework structure, a shift in the absorption maxima is generally observed due to enhanced molecular interactions. Loss of fine structure and broadening of the emission spectrum is also observed.[40]

1.3.4 Nano-MOFs and coordination modulation

Nanoscale MOFs have higher gas permeability resulting in higher gas uptake along with highly porous architecture. They are considered a porous solid of importance in drug delivery, gas separation membranes and a material with enhanced gas uptake capacity, separation, and catalytic performance. One of the strategies used to control the crystal growth process is coordination modulation. Various coordination modulating agents having same functional groups as the linker are used to control the particle size and morphology. It has been observed that functionalized graphene used in the synthesis of MOF-graphene nanocomposites in this thesis is a good coordination modulating agent. The particle size and morphology of MOF-graphene and MOF-BN nanocomposites changes significantly. The functionalized graphene and BN basal plane control the nucleation and growth of MOFs. A

significant decrease in particle size and change in morphology are observed in the nanocomposites.

1.3.5 Gas storage / Separation

One of the most important properties of MOFs which has been studied in detail for clean energy applications is the high surface area with well-defined pore structure.[41] Some of the remarkably high surface area MOFs reported in the literature are MOF-177 (5640 m^2g^{-1}), MIL-101 (5900 m^2g^{-1}), UMCM-2 (6000 m^2g^{-1}) and MOF-210 (6240 m^2g^{-1}).[42] The exceptionally high surface area along with well-defined nanospace inside their framework structure allows them to efficiently trap various gas molecules. Because of their high crystallinity, porosity, and controllable structural characteristics, MOFs have been studied for

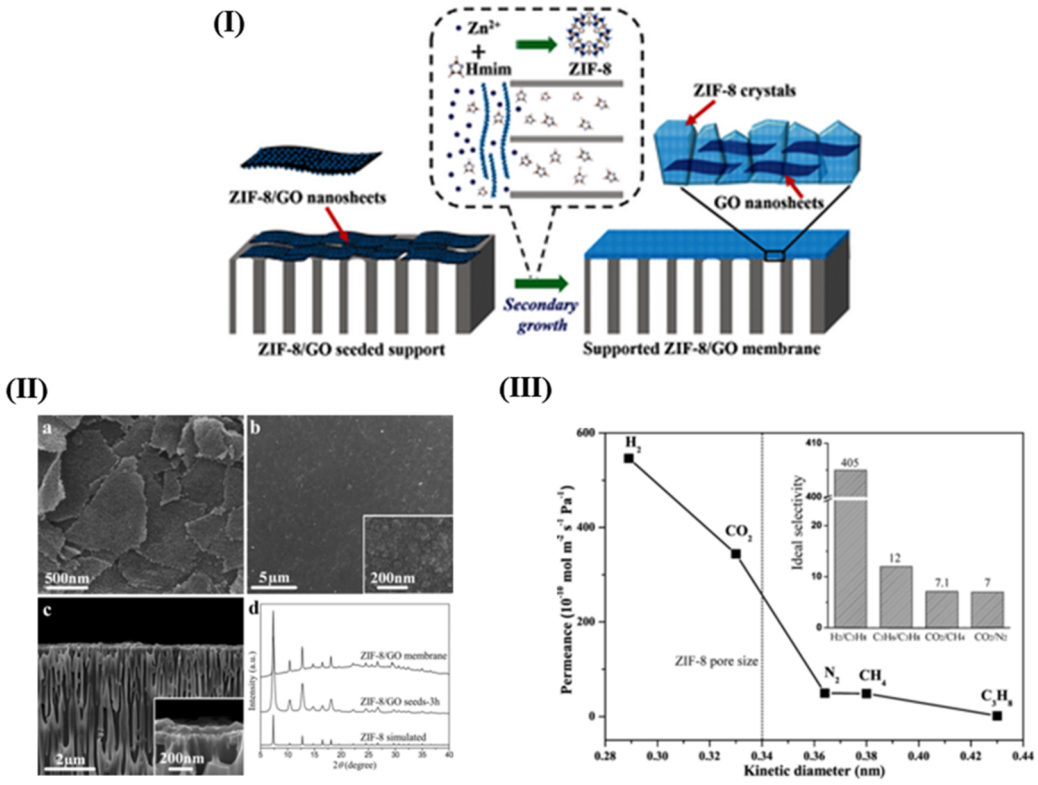

Figure 13. Schematic representation of the synthesis of ultrathin ZIF-8/GO membrane: coating of flexible ZIF-8/GO composites on anodic aluminium oxide (AAO), and subsequent secondary growth by the contra-diffusion method. (II) SEM images of the seeds-3h (a) the surface morphology (b) and cross-section (c) of ZIF-8/GO membrane (M-3h-3h) on the AAO substrate. d) PXRD patterns of simulated ZIF-8 structure, seeds-3h and ZIF-8/GO membrane (M-3h-3h). The inset in b is a high-magnification surface view, and c is a high-magnification cross-sectional view. (III) Single gas permeances of different gases through ZIF-8/GO membrane (M-3h-3h) at 25 °C and 1 bar as a function of the kinetic diameter. The inset shows the ideal gas selectivity for H_2/C_3H_8, C_3H_6/C_3H_8, CO_2/CH_4, and CO_2/N_2. ZIF-8 pore size (dashed line) estimated from crystal structure data. (Adapted with permission from ref. 44b)

H_2, CH_4 storage, and CO_2 sequestration. Hydrogen storage in MOFs has been studied extensively but methane storage in MOFs has not been explored in as much detail. Compared to petroleum oil, methane can provide much more energy because of its higher hydrogen-to-carbon ratio. Another area where MOFs have promising application is CO_2 sequestration. MOFs provide a significant advantage over amine based solvents presently used for CO_2 sequestration in thermal power plants. Amine-based solvents suffer from solvent degradation, toxicity, corrosive nature, and high energy demand for the solvent regeneration.[9]

Adsorptive separation is an important industrial process. Industrial separation processes use porous solid materials such as zeolites, silica gel, and activated carbon as adsorbents. The basic principle of separation is a different affinity between different adsorbates and the surface of adsorbents. Adsorption capacity and selectivity of an adsorbent are requisites for adsorptive gas separation. Adsorption capacity depends on the equilibrium pressure and temperature, the nature of the adsorbate, and the nature of the micropores in the adsorbent. Selectivity is significantly more complicated, though it is related to the operational temperature and pressure and the nature of the adsorbate- adsorbent interaction.[27,41] Many MOFs and MOF-polymer membrane composites have been studied for gas separation applications. ZIF-8 polymer membranes have been studied for gas separation with interesting results.[43] Based on the study reported in the thesis, MOF nanoparticles grown on graphene sheets appear to be highly promising for gas separation applications (Figure 13).[44] In particular, ZIF-8 nanoparticles supported on BN nanosheets investigated in the thesis may be further promising as BN is a ceramic material with very high thermal and chemical stabilities whereas graphene oxide (GO) based gas separation membrane have low thermal stability. This thesis also investigates the epitaxially grown 2D-MOFs on graphene which can be used to make gas separation membranes.

1.3.6 Catalysis:

One of the important applications of MOFs is in catalysis. Metals or metal clusters, used as connecting nodes can be used to catalyze organic reactions. Shape and selectivity are important parameters in industrial catalytic processes and MOFs with tunable pore size and functionality attached to ligands have been utilized.[31,34] The catalyst must have uniform pores with molecular dimensions, in order to provide shape/sizes selective behavior. Uniform porosity in the case of MOFs is an outcome of the highly ordered structure. Due to the open architecture, self-diffusion coefficients of molecules in the pore system are only slightly lower than in the bulk solvent. Mass transport in the pore system is not hindered. The ordered

structure offers the opportunity to spatially separate active centers. Due to their high surface areas, MOF- based catalysts contain a high density of fully exposed active site per unit volume. This feature results in enhanced activity, and hence a more effective catalytic system. In addition to the non-coordinated catalytically active metal site, catalytically active centers can also be generated from the functional groups attached to the ligand. Unlike traditional immobilized catalysts, the active catalytic sites generated are predictable and tunable due to the known chemical property of the linker.[27]

1.3.7 Mechanical properties of the MOFs

One of the key challenges in the practical applications of MOFs is low mechanical robustness and stability as they contain significant structural porosity and are typically fragile in nature (Figure 14).[45] The moderate strength coordinate bond is fragile and collapses when subjected to mechanical deformation and attacked by electron donating adsorbents such as H_2O, NH_3, and H_2S. The application of MOFs in gas adsorption/separation and catalysis involves the formation of densely packed adsorption bed and porous membranes. These porous beds and membranes are subjected to various modes of mechanical stress and strain. In fact external hydrostatic pressure of several GPa is common in practical situations. Most of the low density (density < 1 g/cm^3) MOFs are not mechanically robust and have a low elastic modulus in the range of 3 – 4 GPa and hardness of 200 – 500 MPa.[45b,46] Inorganic zeolites, although having a significantly lower surface area in comparison to MOFs (BET surface area generally in the range of 200–500 m^2/g), have an elastic modulus of 40 – 100 GPa and hardness of 2.5 – 10 GPa. The above-mentioned applications of MOFs cannot be realized if the porous framework architecture is perturbed. The loss of crystallinity results in loss of pores and catalytically active adsorption sites. In addition, the MOFs have to undergo several such cycles of mechanical stress and strain without the loss of crystallinity and porous architecture. Thus a strategy which can enhance the mechanical properties of highly porous frameworks without compromising with intrinsic porosity and gas storage properties is required. One possible way of overcoming this drawback is by making composites with two-dimensional nanomaterial such as graphene and BN which has very high mechanical strength. This thesis investigates the possibility of enhancing the mechanical properties MOFs by growing the MOF nanoparticles on BN nanosheets or by reinforcing the MOF matrix with graphene. Uniform reinforcement of the MOF matrix with graphene sheets results in significant improvement of the mechanical properties. The enhancement in the mechanical properties is attributed to the synergistic interaction between the MOFs and 2D layered

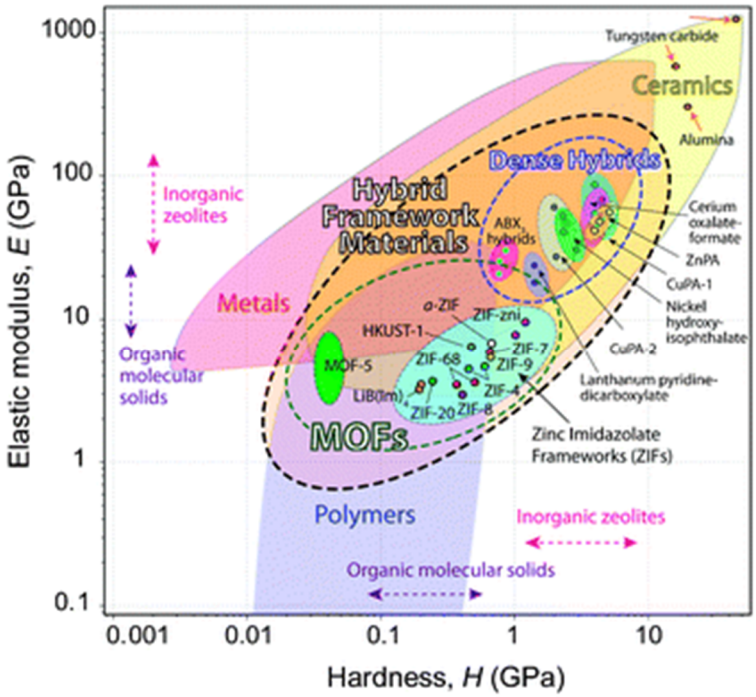

Figure 14. Elastic modulus *versus* hardness map for different materials. A comparison of both dense as well as porous metal organic frameworks (MOFs) elastic modulus and hardness with inorganic counterpart zeolites and other materials. (Adapted with permission from ref. 46)

materials. The composites retain the intrinsic microporous feature with an increase in surface area and gas adsorption properties. The strategy of reinforcing MOF matrix with few weight % high mechanical strength graphene, BN and single–walled carbon nanotube to bestow it with significantly enhanced mechanical properties and gas storage properties is of significant practical importance.

1.3.8 MOFs and zeolites: a brief comparison

Most of the MOFs and zeolites are microporous and have a uniform porous architecture and crystallinity. Zeolites have high thermal and chemical stabilities; they are stable above 450 °C and to various solvents, acids and various oxidizing and reducing agents. They have reasonable BET surface areas in 200–500 m^2/g range.[16] Zeolites have an elastic modulus in the range of 40–100 GPa and a hardness of 2.5–10 GPa. Zeolite frameworks are rugged and stable to various mechanical deformations. They can be recycled and regenerated and are excellent vapour phase catalyst. They are the porous material of choice in the petrochemical industry which involves high-temperature processes, hydrostatic pressure and several cycles of regeneration and use. The advantages of MOFs over zeolites are that they have large porosity; the zeolites have a pore volume in the range of 0.1–0.5 cm^3 whereas MOFs have

pore volume over 1 cm^3. They have a large BET surface area of up to 5000 – 6000 m^2/g.[1c] The MOFs have a high percentage of metal frameworks that could act as Lewis acid or redox sites whereas the zeolites have typically an unstable low percentage of metal frameworks. The pore size, surface area and functionalities of MOFs can be designed by crystal engineering.[47] Even though having all these properties which can enhance the performance of porous solid significantly, MOFs cannot be used for many practical applications because of low mechanical, thermal and chemical stabilities. MOF catalysts cannot be regenerated by thermal activation in the petrochemical industry.

This thesis explains a strategy to enhance the mechanical strength of MOFs by making composite with graphene and BN. Recent investigation has shown significant improvement in the hydrothermal stability of MOFs which is another important requirement for many applications. Chiral MOFs can be designed by selecting chiral linkers which can be used as a chiral catalyst for enantioselective reactions. The higher pore size of MOFs allows diffusion of much larger organic molecules which is not possible in case of zeolites due to the limitation of pore size.

The present discussion brings us to the conclusion that although very high surface area have been achieved in the area of porous solids which can significantly enhance their potential use in industrial processes, mechanical, thermal and chemical stabilities are other important parameters of importance. The present thesis tries to address the low mechanical properties of MOFs.

1.3.9 Composites of MOFs with 2D materials graphene and BN

There has been a significant progress in the area of 2D layered materials such as graphene, BN, and transition metal chalcogenides.[48] These 2D materials exhibit many interesting properties.[48a,49] In particular graphene and BN have been used for the synthesis of various composites with a variety of properties.[48b,50] Graphene is a conductor whereas BN is an insulating ceramic.[19d] Composites of these 2D materials with MOFs, exhibit interesting properties and synergistic interaction between the individual components. This thesis discusses composites of MOFs with graphene and BN and their properties. Graphene can be chemically modified in various ways. Graphene oxide itself has a large concentration of epoxides, hydroxyls, and carboxylates. Oxygen-containing functional groups provide coordination centers for metal ions and can be utilized for the synthesis of graphene-MOF hybrid composites. Oxygen functionalities present on the graphene basal plane modulate the growth mechanism of MOF crystals, graphene also acts as a nucleation center for the growth

of MOF crystals. Large area functionalized graphene sheets can be used to grow MOF nanocrystals with many interesting properties due to the synergistic effect of the MOF and graphene. Such hybrid composites may have different adsorption properties in comparison to the parent MOF. Lanthanide-based MOFs show interesting optical properties. Study of optical properties of such hybrid composites will be interesting. This thesis explores the role of graphene in the emission properties of lanthanide-based MOFs. BN another layered 2D material with high thermal stability can be used as a support for the growth of MOFs. This thesis also addresses the mechanical strength of frameworks by compositing with BN and graphene.

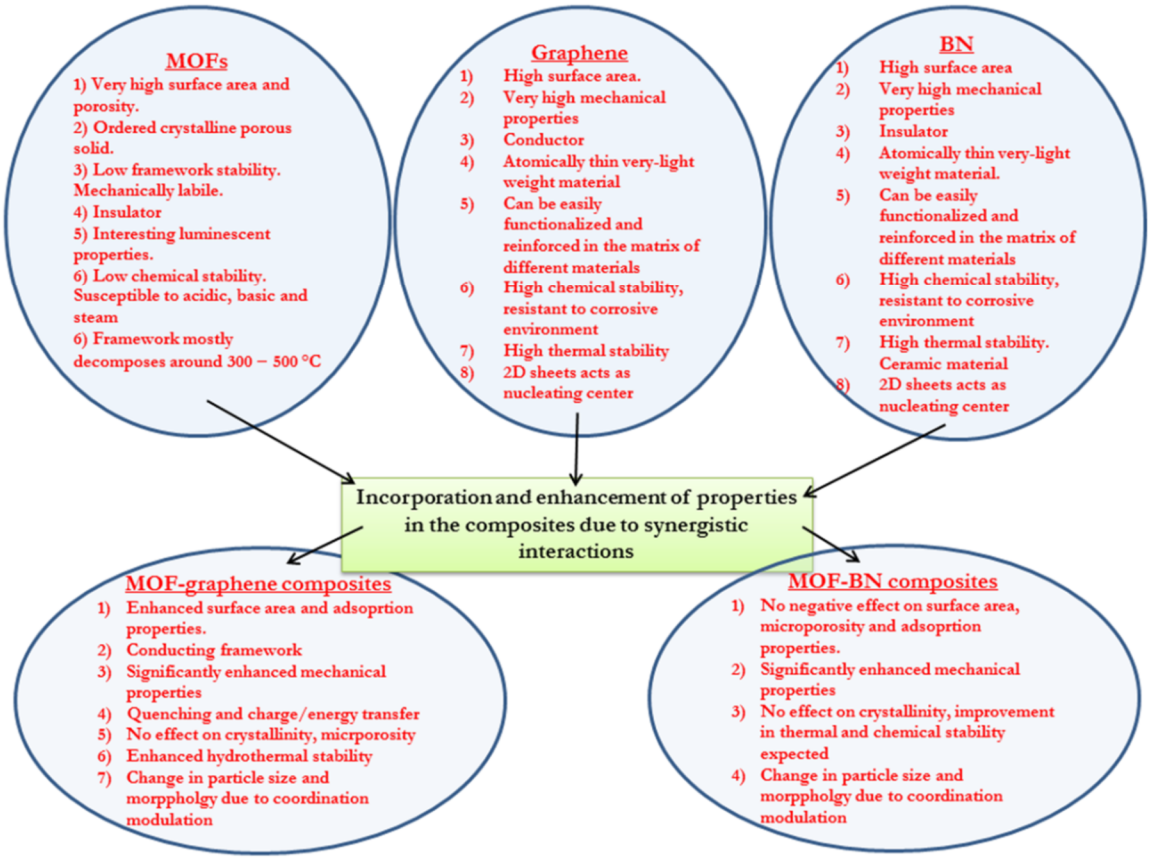

Figure 15. Scheme showing the incorporation of functional properties of both MOFs and graphene/BN in the composite. Enhancement in the functional properties due to the synergistic interactions is also observed in the composites.

1.4 New porous solids based on covalent cross–linking and pillaring of nanomaterials (Covalent assemblies)

Graphene has been theoretically predicted to have an ultra high surface area of 2600 m^2/g.[51] Few-layer BN a sp^2 hybridised network of B and N atoms and single–walled carbon nanotubes (SWNTs) are expected to have reasonably high surface areas.[19d,25] These materials have high thermal and chemical stabilities and high mechanical strength.[50b,52] These solids are however highly agglomerated due to van der Waals interaction and have low adsorbate accessible surface area.[53] Agglomeration and random arrangement of sheets and bundles result in a non-uniform pore size distribution. Removal of van der Waals interaction by pillaring with uniform length organic linkers results in significant improvement in the adsorbate accessible surface area as new adsorption sites are generated in the interstices.[54] In this thesis, a new class of highly robust porous assemblies generated by covalently cross-linking with organic linkers have been investigated. Graphene and single-walled carbon nanotubes have been covalently cross-linked via C–C bond with different length organic linkers using efficient Pd(0) catalysed Sonogashira coupling reaction. Combining these graphene and BN using uniform length organic linkers can result in porous solids with high surface area and tunable properties. For example, conductivity can be tuned by varying the individual components and hence the resulting properties and applications. Graphene sheets have been functionalized using carboxylate groups and amine functionalized few-layer BN was prepared using the urea route. BN-graphene composites have been assembled layer-by-layer by amide bond formation between them. The amide formation between BN and graphene is performed using EDC coupling strategy. These porous solids have high surface areas and uniform pore size distribution. Since the starting precursors have high thermal and chemical stabilities, the resulting porous assembly has high thermal and chemical stability. Graphene-SWNT based porous solids are also superhydrophobic.

One of the applications of porous carbon-based materials is as electrodes in supercapacitors. A good electrode material is expected to have (i) a porous architecture with high surface area as well as a hierarchical, well–balanced pore-size distribution for efficient charge storage and high specific capacitance; (ii) high electrical conductivity for high power density and rate capability; (iii) a superior compatibility with the electrolyte to facilitate ion diffusion and to maximize the ion accessible–surface area and (iv) high chemical stability to avoid corrosion and material degradation from the electrolyte. Covalently cross-linked carbon and BN-based porous solids possess desired properties and are good supercapacitor electrode

materials. The amide bond cross-linked BN-graphene assemblies are also good electrocatalysts for the oxygen reduction reaction (ORR) in fuel cell applications. The covalently cross-linked SWNT assemblies have a very uniform mesh like assembly connecting individual ~ 0.9–1.2 nm SWNTs to ~ 2 nm length organic linkers. These materials may have molecular sieving applications due to the ordered porous architecture and hydrophobic pores.

1.5 Characterization of porous solids

Porous solids are generally characterized using X-ray diffraction, various spectroscopic techniques, thermogravimetric and microscopic techniques to determine the chemical composition, phase purity, crystallinity, atomic coordinates, thermal stability and porous architecture. Porosity and adsorption properties of the porous solids are determined by gas and solvent adsorption experiments. The surface area, pore size distribution and pore volume of porous solids are determined using nitrogen adsorption–desorption isotherm at cryogenic temperature of 77 K. Depending on the pores present in the porous solid and adsorbate–adsorbent interaction they have a characteristic nitrogen adsorption–desorption isotherm and gives important information about the porosity of solids. The hydrophilic and hydrophobic nature of porous solids can be investigated by water, methanol, benzene, toluene and other hydrocarbon adsorption. If the porous solids have good water uptake they are hydrophilic and if the porous solids have good benzene uptake considering that the pore size is large enough to allow the adsorption of benzene, they are hydrophobic.

MOF-graphene, MOF-BN composites, and porous solids prepared by covalent cross-linking of graphene, graphene–BN and single–walled carbon nanotubes (SWNTs) with organic linkers have been characterized and properties investigated by a combination of above-mentioned techniques and few additional techniques. In particular, Raman spectroscopy plays an important role in the characterization of graphene, SWNTs, BN and various other 2D nanomaterials such as transition metal chalcogenides MoS_2, $MoSe_2$ etc. Raman spectroscopy has been extensively used for the characterization of homogeneity and quality of MOF–graphene and MOF–BN composites. In addition various phonon modes, metal–oxygen bonding and crystallinity of MOF–graphene composites can also be explored using Raman spectroscopy. Further, Raman spectroscopy has been also used in the characterization of covalently cross–linked porous assemblies. The textural parameters, reinforcement of graphene in the MOF matrix and porous architecture of the porous solids investigated have been studied using transmission and electron microscopy with a care taken to avoid beam induced damages of the sample. The ordering obtained in covalently cross–

linked assemblies and phase purity of MOF composites have been determined using powder X-ray diffraction (PXRD). X-ray photoelectron spectroscopy (XPS) a surface sensitive technique have been used to access the extent of reaction and covalent bond formation on the solid surface along–with the determination of various functional group present on the surface and chemical composition. Thermal stabilities of all the materials investigated have been determined using thermogravimetric analysis. The luminescent properties of rare earth (Eu/Tb) based MOF–graphene composites have been studied using photoluminescence spectroscopy. The mechanical properties of graphene–reinforced MOF composites have been also investigated using the nanoindentation technique and elastic modulus and hardness were extracted using the Oliver–Pharr method. In addition solid state NMR, infrared and electron energy loss spectroscopy have been also used for accessing the local bonding and chemical environment and characterization of the material. The most important properties of the porous solids, adsorption and porosity needs a wider attention. The methods used to investigate these properties in the thesis are briefly discussed below.

1.5.1 Adsorption isotherms

IUPAC has classified physisorption isotherms obtained in porous solids into six types (Figure 16).[2] In most of the porous solids at sufficiently low surface coverage the isotherm reduces to a linear form ($n^a \propto p$) referred as the Henry's Law region.

Where, n^a is the amount of gas adsorbed.

The reversible Type I isotherm is concave to the $p/p°$ axis with n^a approaching a limiting value as $p/p° \rightarrow 1$ and given by microporous solids (e.g. metal–organic frameworks and zeolites).

The reversible Type II isotherm is obtained with a non-porous or macroporous adsorbent and represents unrestricted monolayer-multilayer adsorption. Point B, the onset of the almost linear middle section of the isotherm, is considered the stage at which monolayer coverage is complete and multilayer is about to start.

The reversible Type III isotherm is convex to the $p/p°$ axis over its entire range and does not exhibit a Point B. Isotherms of this type are not common in porous solids, but there are systems (e .g. nitrogen on polyethylene) which give isotherms with gradual curvature and an indistinct Point B.

The Type IV isotherm has characteristic hysteresis loop associated with the capillary condensation in the mesopores of solid, resulting in limiting uptake over a range of high $p/p°$. The initial part of the isotherm is due to monolayer-multilayer adsorption since it follows the

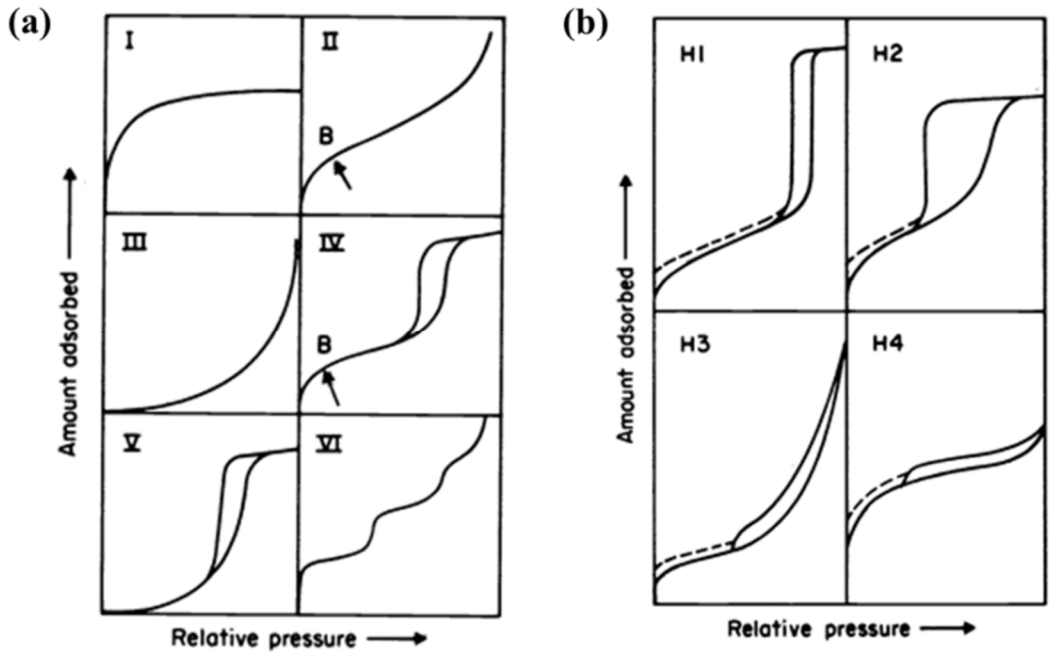

Figure 16. (a) IUPAC classification of types of physisorption isotherm. (b) IUPAC classification of the different types of hysteresis loops observed in porous solids due to the capillary condensation.

same path as the corresponding part of a Type II isotherm obtained with the given adsorptive on the same surface area of the adsorbent in a non-porous form. The Type IV isotherms are observed in many mesoporous industrial adsorbents.

The Type V isotherm is not common and related to the Type III isotherm in that the adsorbent-adsorbate interaction is weak.

The Type VI isotherm, in which the sharpness of the steps depends on the system and the temperature, represents stepwise multilayer adsorption on a uniform non-porous surface. The step-height now represents the monolayer capacity for each adsorbed layer and, in the simplest case, remains nearly constant for two or three adsorbed layers. Amongst the best examples of Type VI isotherms are those obtained with argon or krypton on graphitised carbon blacks at liquid nitrogen temperature.

Hysteresis in mesoporous solid isotherms

Mesoporous solids show hysteresis in the adsorption profile due to capillary condensation. There is a relationship between the shape of the hysteresis loop and the texture such as pore size distribution, pore geometry, and connectivity of mesoporous solids. According to the IUPAC classification, Type H1 is associated with porous materials consisting of well-defined cylindrical-like pore channels or agglomerates of compacts of approximately uniform spheres. The Type H2 hysteresis is due to disordered pores, the

distribution of pore size and shape is not well defined. The Type H3 hysteresis do not exhibit any limiting adsorption at high p/p_0, this isotherm is generally observed with non-rigid aggregates of plate-like particles and formation of slit-shaped pores. The desorption branch for Type H3 hysteresis has a steep region associated with a forced closure of the hysteresis loop, due to the tensile strength effect. This phenomenon occurs in the relative pressure region of 0.4 – 0.45 in case of nitrogen at 77 K. The Type H4 loops are associated with narrow slit pores, but also include pores in the micropore region.

1.5.2 Determination of the adsorbate accessible surface area, pore size, and pore volume of porous solids

Brunauer-Emmett-Teller (BET) theory of multilayer adsorption is used to determine the surface area of porous solids investigated in the thesis. The BET method is the most widely used procedure for the determination of the surface area and also helps in comparison with other porous solids reported in the literature.[2] BET equation can be given by:

$$\frac{1}{w((p/p_0)-1)} = \frac{1}{w_m c} + \frac{c-1}{w_m c}\left(\frac{p}{p_0}\right) \quad \ldots\ldots\ldots\ldots\ldots\ldots\ldots\ldots\ldots\ldots (1)$$

Where, w is the weight of gas adsorbed at a relative pressure, p/p_0, and w_m is the weight of adsorbate constituting a monolayer of surface coverage. The BET c constant is related to the energy of adsorption in the first adsorbed layer and consequently, its value is an indication of the magnitude of the adsorbent/adsorbate interactions. The surface area is obtained by fitting the $0.05<p/p_0 0.35$ region to BET equation.

Pore size distribution of porous solids investigated in the thesis has been calculated using non-local density functional theory (NLDFT). Density Functional Theory (DFT) gives a more realistic sorption and phase behavior of fluids in narrow pores on a molecular level and is considered a reliable method for pore size analysis.[55] The non-local density functional theory (NLDFT) correctly explains the local fluid structure near curved solid walls. The adsorption isotherms in model pores are obtained by using the intermolecular potentials of the fluid-fluid and solid-fluid interactions. The relation between isotherms determined by NLDFT and the experimental isotherm on a porous solid is given by generalized adsorption isotherm (GAI) equation:

$$N\left(\frac{P}{P_0}\right) = \int_{w_{min}}^{w_{max}} N\left(\frac{P}{P_0}, w\right) f(w)\, dw \quad \ldots\ldots\ldots\ldots\ldots\ldots (2)$$

Where,

$N(P/P_0)$ = experimental adsorption isotherm

w = pore width

$N(P/P_0, w)$ = isotherm on a single pore of width w

$F(w)$ = pore size distribution function

In GAI equation it is assumed that the total isotherm consists of a number of individual "single pore" isotherms multiplied by their relative distribution, $f(W)$, over a range of pore sizes. The set of $N(P/P_0, w)$ isotherms for a given system (adsorbate/adsorbent) is obtained by density functional theory and is available as kernel files with the software. The pore size distribution is obtained by solving the GAI equation numerically via a fast non-negative least square algorithm.

The total pore volume is derived from the amount of vapor adsorbed at p/p_0 close to unity, by assuming that the pores are then filled with liquid adsorbate. The volume of nitrogen adsorbed (v_{ads}) is converted to the volume of liquid nitrogen (v_{liq}) contained in the pores using the equation:

$$v_{liq} = \frac{p_a v_{ads} v_m}{RT} \quad \ldots\ldots\ldots\ldots\ldots\ldots\ldots\ldots\ldots\ldots \quad (3)$$

Where, p_a and T are ambient pressure and temperature, respectively, and v_m is the molar volume of the liquid adsorbate (34.7 cm^3mol^{-1} for nitrogen).

1.6 Conclusions

The preceding sections were intended to provide a brief overview of porous solids and their properties. Research in the area has resulted in the development of several ultra-high surface areas crystalline, amorphous, ordered and disordered porous solids. The high surface area is one of the requirements for practical applications. However, several other physical and chemical properties determine the suitability of a porous solid for specific purposes. Metal-organic frameworks have several important properties for numerous applications, but suffer from low mechanical stability. This thesis tries to address this aspect by making composites with mechanically strong graphene and BN. In addition, gas adsorption and coordination action modulation properties of MOF-graphene and MOF-BN composites have also been studied. The composites show enhanced adsorption and gas separation performance. Another class of porous can be generated by covalently cross-linking nanomaterials such as graphene,

BN, and single-walled carbon nanotube. These porous solids are robust and stable. They have high surface areas and ordered porous architecture with potential applications in gas storage/separation, energy storage device, and catalysis.

References

[1] a) M. E. Davis, *Nature* **2002**, *417*, 813; b) A. Stein, *Adv. Mater.* **2003**, *15*, 763; c) J. R. Holst and A. I. Cooper, *Adv. Mater.* **2010**, *22*, 5212.

[2] K. S. W. Sing, D. H. Everett, R. A. W. Haul, L. Moscou, R. A. Pierotti, J. Rouquerol and T. Siemieniewska in *Reporting Physisorption Data for Gas/Solid Systems*, Wiley-VCH Verlag GmbH & Co. KGaA, **2008**.

[3] a) C. T. Kresge, M. E. Leonowicz, W. J. Roth, J. C. Vartuli and J. S. Beck, *Nature* **1992**, *359*, 710; b) M. Kruk, M. Jaroniec, C. H. Ko and R. Ryoo, *Chem. Mater.* **2000**, *12*, 1961.

[4] a) B. F. Hoskins and R. Robson, *J. Am. Chem. Soc.* **1990**, *112*, 1546; b) K. S. Park, Z. Ni, A. P. Côté, J. Y. Choi, R. Huang, F. J. Uribe-Romo, H. K. Chae, M. O'Keeffe and O. M. Yaghi, *Proc. Natl. Acad. Sci. USA* **2006**, *103*, 10186.

[5] G. Gundiah, A. Govindaraj, N. Rajalakshmi, K. S. Dhathathreyan and C. N. R. Rao, *J. Mater. Chem.* **2003**, *13*, 209.

[6] a) A. Ghosh, K. S. Subrahmanyam, K. S. Krishna, S. Datta, A. Govindaraj, S. K. Pati and C. N. R. Rao, *J. Phys. Chem. C* **2008**, *112*, 15704; b) K. S. Subrahmanyam, P. Kumar, U. Maitra, A. Govindaraj, K. P. S. S. Hembram, U. V. Waghmare and C. N. R. Rao, *Proc. Natl. Acad. Sci. USA* **2011**; c) S. Moussa, A. R. Siamaki, B. F. Gupton and M. S. El-Shall, *ACS Catalysis* **2011**, *2*, 145.

[7] N. Kumar, K. S. Subrahmanyam, P. Chaturbedy, K. Raidongia, A. Govindaraj, K. P. S. S. Hembram, A. K. Mishra, U. V. Waghmare and C. N. R. Rao, *ChemSusChem* **2011**, *4*, 1662.

[8] A. Thomas, *Angew. Chem. Int. Ed.* **2010**, *49*, 8328.

[9] P. Markewitz, W. Kuckshinrichs, W. Leitner, J. Linssen, P. Zapp, R. Bongartz, A. Schreiber and T. E. Muller, *Energy. Environ. Sci.* **2012**, *5*, 7281.

[10] A. F. Masters and T. Maschmeyer, *Microporous Mesoporous Mater.* **2011**, *142*, 423.

[11] C. Colella and A. F. Gualtieri, *Microporous Mesoporous Mater.* **2007**, *105*, 213.

[12] R. M. Barrer, *J. Chem. Soc. (Resumed)* **1948**, 127.

[13] a) A. Corma and M. E. Davis, *ChemPhysChem* **2004**, *5*, 304; b) M. Moliner, C. Martínez and A. Corma, *Chem. Mater.* **2014**, *26*, 246.

[14] M. Moliner, C. Martínez and A. Corma *Angew. Chem. Int. Ed.* **2015**, *54*, 3560.

[15] A. Primo and H. Garcia, *Chem. Soc. Rev.* **2014**, *43*, 7548.

[16] A. Dhakshinamoorthy, M. Alvaro, A. Corma and H. Garcia, *Dalton Trans.* **2011**, *40*, 6344.

[17] a) M. C. Johnson, J. Wang, Z. Li, C. M. Lew and Y. Yan, *Mater. Sci. Eng. A* **2007**, *456*, 58; b) L. Brabec, P. Bohac, M. Stranyanek, R. Ctvrtlik and M. Kocirik, *Microporous Mesoporous Mater.* **2006**, *94*, 226; c) Z. A. D. Lethbridge, R. I. Walton, A. Bosak and M. Krisch, *Chem. Phys. Lett.* **2009**, *471*, 286.

[18] R. C. Haushalter and L. A. Mundi, *Chem. Mater.* **1992**, *4*, 31.

[19] a) A. Corma, *Chem. Rev.* **1997**, *97*, 2373; b) A. P. Côté, A. I. Benin, N. W. Ockwig, M. O'Keeffe, A. J. Matzger and O. M. Yaghi, *Science* **2005**, *310*, 1166; c) N. kumar, K. Moses, K. Pramoda, S. N. Shirodkar, A. K. Mishra, U. V. Waghmare, A. Sundaresan and C. N. R. Rao, *J. Mater. Chem. A* **2013**, *1*, 5806; d) A. Nag, K. Raidongia, K. P. S. S. Hembram, R. Datta, U. V. Waghmare and C. N. R. Rao, *ACS Nano* **2010**, *4*, 1539; e) Q. Weng, X. Wang, C. Zhi, Y. Bando and D. Golberg, *ACS Nano* **2013**, *7*, 1558; f) W. Lei, D. Portehault, D. Liu, S. Qin and Y. Chen, *Nat. Commun.* **2013**, *4*, 1777; g) J. S. Beck, J. C. Vartuli, W. J. Roth, M. E. Leonowicz, C. T. Kresge, K. D. Schmitt, C. T. W. Chu, D. H. Olson, E. W. Sheppard, S. B. McCullen, J. B. Higgins and J. L. Schlenker, *J. Am. Chem. Soc.* **1992**, *114*, 10834.

[20] Y. Tsuneo, S. Toshio, K. Kazuyuki and K. Chuzo, *Bull. Chem. Soc. Jpn.* **1990**, *63*, 988.

[21] L. T. Gibson, *Chem. Soc. Rev.* **2014**, *43*, 5163.

[22] a) T. Otowa, R. Tanibata and M. Itoh, *Gas Separation & Purification* **1993**, *7*, 241; b) S. Sircar, T. C. Golden and M. B. Rao, *Carbon* **1996**, *34*, 1; c) Y. Xia, G. S. Walker, D. M. Grant and R. Mokaya,

J. Am. Chem. Soc. **2009**, *131*, 16493; d) M. Jordá-Beneyto, F. Suárez-García, D. Lozano-Castelló, D. Cazorla-Amorós and A. Linares-Solano, *Carbon* **2007**, *45*, 293.

[23] J.-X. Jiang, F. Su, A. Trewin, C. D. Wood, N. L. Campbell, H. Niu, C. Dickinson, A. Y. Ganin, M. J. Rosseinsky, Y. Z. Khimyak and A. I. Cooper, *Angew. Chem.* **2007**, *119*, 8728.

[24] M. B. Sreedhara, K. Gopalakrishnan, B. Bharath, R. Kumar, G. U. Kulkarni and C. N. R. Rao, *Chem. Phys. Lett.* **2016**, *657*, 124.

[25] M. Eswaramoorthy, R. Sen and C. N. R. Rao, *Chem. Phys. Lett.* **1999**, *304*, 207.

[26] P. Chen, X. Wu, J. Lin and K. L. Tan, *Science* **1999**, *285*, 91.

[27] S. Kitagawa, R. Kitaura and S.-i. Noro, *Angew. Chem. Int. Ed.* **2004**, *43*, 2334.

[28] M. Eddaoudi, D. B. Moler, H. Li, B. Chen, T. M. Reineke, M. O'Keeffe and O. M. Yaghi, *Acc. Chem. Res.* **2001**, *34*, 319.

[29] a) B. V. Harbuzaru, A. Corma, F. Rey, P. Atienzar, J. L. Jordá, H. García, D. Ananias, L. D. Carlos and J. Rocha, *Angew. Chem. Int. Ed.* **2008**, *47*, 1080; b) P. Falcaro and S. Furukawa, *Angew. Chem. Int. Ed.* **2012**, *51*, 8431.

[30] C. N. R. Rao, S. Natarajan and R. Vaidhyanathan, *Angew. Chem. Int. Ed.* **2004**, *43*, 1466.

[31] A. K. Cheetham, C. N. R. Rao and R. K. Feller, *Chem. Commun.* **2006**, 4780.

[32] S. Horike, S. Shimomura and S. Kitagawa, *Nat. Chem.* **2009**, *1*, 695.

[33] H. He, T. Riedl, A. Lerf and J. Klinowski, *J. Phys. Chem.* **1996**, *100*, 19954.

[34] C. N. R. Rao, A. K. Cheetham and A. Thirumurugan, *J. Phys.: Condens. Matter* **2008**, *20*, 083202.

[35] W. J. Rieter, K. M. L. Taylor, H. An, W. Lin and W. Lin, *J. Am. Chem. Soc.* **2006**, *128*, 9024.

[36] G. Lu, S. Li, Z. Guo, O. K. Farha, B. G. Hauser, X. Qi, Y. Wang, X. Wang, S. Han, X. Liu, J. S. DuChene, H. Zhang, Q. Zhang, X. Chen, J. Ma, S. C. J. Loo, W. D. Wei, Y. Yang, J. T. Hupp and F. Huo, *Nat. Chem.* **2012**, *4*, 310.

[37] Y. Cui, Y. Yue, G. Qian and B. Chen, *Chem. Rev.* **2011**, *112*, 1126.

[38] F. S. Richardson, *Chem. Rev.* **1982**, *82*, 541.

[39] A. Thirumurugan and A. K. Cheetham, *Eur. J. Inorg. Chem.* **2010**, *2010*, 3823.

[40] M. D. Allendorf, C. A. Bauer, R. K. Bhakta and R. J. T. Houk, *Chem. Soc. Rev.* **2009**, *38*, 1330.

[41] G. Ferey, *Chem. Soc. Rev.* **2008**, *37*, 191.

[42] a) H. K. Chae, D. Y. Siberio-Perez, J. Kim, Y. Go, M. Eddaoudi, A. J. Matzger, M. O'Keeffe and O. M. Yaghi, *Nature* **2004**, *427*, 523; b) G. Férey, C. Mellot-Draznieks, C. Serre, F. Millange, J. Dutour, S. Surblé and I. Margiolaki, *Science* **2005**, *309*, 2040; c) K. Koh, A. G. Wong-Foy and A. J. Matzger, *J. Am. Chem. Soc.* **2009**, *131*, 4184; d) H. Furukawa, N. Ko, Y. B. Go, N. Aratani, S. B. Choi, E. Choi, A. Ö. Yazaydin, R. Q. Snurr, M. O'Keeffe, J. Kim and O. M. Yaghi, *Science* **2010**, *329*, 424.

[43] Q. Song, S. K. Nataraj, M. V. Roussenova, J. C. Tan, D. J. Hughes, W. Li, P. Bourgoin, M. A. Alam, A. K. Cheetham, S. A. Al-Muhtaseb and E. Sivaniah, *Energy Environ. Sci.* **2012**, *5*, 8359.

[44] a) A. Huang, Q. Liu, N. Wang, Y. Zhu and J. Caro, *J. Am. Chem. Soc.* **2014**, *136*, 14686; b) Y. Hu, J. Wei, Y. Liang, H. Zhang, X. Zhang, W. Shen and H. Wang, *Angew. Chem. Int. Ed.* **2016**, *55*, 2048; c) W. Huang, X. Zhou, Q. Xia, J. Peng, H. Wang and Z. Li, *Ind. Eng. Chem. Res.* **2014**, *53*, 11176; d) X. Zhou, W. Huang, J. Miao, Q. Xia, Z. Zhang, H. Wang and Z. Li, *Chem. Eng. J.* **2015**, *266*, 339.

[45] a) Y. H. Hu and L. Zhang, *Phys. Rev. B, PRB* **2010**, *81*, 174103; b) J. C. Tan, T. D. Bennett and A. K. Cheetham, *Proc. Natl. Acad. Sci. USA* **2010**, *107*, 9938.

[46] J. C. Tan and A. K. Cheetham, *Chem. Soc. Rev.* **2011**, *40*, 1059.

[47] O. M. Yaghi and Q. Li, *MRS Bull.* **2009**, *34*, 682.

[48] a) C. N. R. Rao, A. K. Sood, K. S. Subrahmanyam and A. Govindaraj, *Angew. Chem. Int. Ed.* **2009**, *48*, 7752; b) C. N. R. Rao and A. Nag, *Eur. J. Inorg. Chem.* **2010**, *2010*, 4244; c) C. N. R. Rao, H. S. S. Ramakrishna Matte and U. Maitra, *Angew. Chem. Int. Ed.* **2013**, *52*, 13162.

[49] a) A. K. Geim and K. S. Novoselov, *Nat. Mater.* **2007**, *6*, 183; b) C. N. R. Rao, K. S. Subrahmanyam, H. S. S. R. Matte, B. Abdulhakeem, A. Govindaraj, B. Das, P. Kumar, A. Ghosh and D. J. Late, *Sci. Tech. Adv. Mater.* **2010**, *11*, 054502.

[50] a) K. E. Prasad, B. Das, U. Maitra, U. Ramamurty and C. N. R. Rao, *Proc. Natl. Acad. Sci. USA* **2009**, *106*, 13186; b) M. S. R. N. Kiran, K. Raidongia, U. Ramamurty and C. N. R. Rao, *Scripta Mater.* **2011**, *64*, 592.

[51] A. Peigney, C. Laurent, E. Flahaut, R. R. Bacsa and A. Rousset, *Carbon* **2001**, *39*, 507.

[52] a) C. Lee, X. Wei, J. W. Kysar and J. Hone, *Science* **2008**, *321*, 385; b) S. Park and R. S. Ruoff, *Nat. Nano* **2009**, *4*, 217; c) Y. Zhu, S. Murali, W. Cai, X. Li, J. W. Suk, J. R. Potts and R. S. Ruoff, *Adv. Mater.* **2010**, *22*, 3906.

[53] C. H. A. Wong, Z. Sofer, M. Kubešová, J. Kučera, S. Matějková and M. Pumera, *Proc. Natl. Acad. Sci. USA* **2014**, *111*, 13774.

[54] a) P. F. Weck, E. Kim, N. Balakrishnan, H. Cheng and B. I. Yakobson, *Chem. Phys. Lett.* **2007**, *439*, 354; b) M. M. Biswas and T. Cagin, *J. Phys. Chem. B* **2010**, *114*, 13752; c) G. Garberoglio, N. M. Pugno and S. Taioli, *J. Phys. Chem. C* **2015**, *119*, 1980.

[55] a) P. I. Ravikovitch, A. Vishnyakov, R. Russo and A. V. Neimark, *Langmuir* **2000**, *16*, 2311; b) J. Landers, G. Y. Gor and A. V. Neimark, *Colloids Surf., A* **2013**, *437*, 3.

Chapter 2: Hybrid nanocomposites of ZIF-8 with graphene oxide exhibiting tunable morphology, significant CO_2 uptake, and other novel properties*

Summary

Metal-organic frameworks (MOFs) possess high surface area and uniform porous network whereas 2D graphene can act as a template for the growth of MOFs. Resulting MOF-graphene composites are expected to have interesting properties due to a synergistic interaction between the individual components. Hybrid nanocomposites of graphene oxide (GO) with the metal-organic framework, ZIF-8 exhibit tunable nanoscale morphology, and porosity, both determined by the GO content, coordination modulation being responsible for such properties. These materials also give rise to high CO_2 storage capability and can be used as precursors to prepare GO@ZnS nanocomposites.

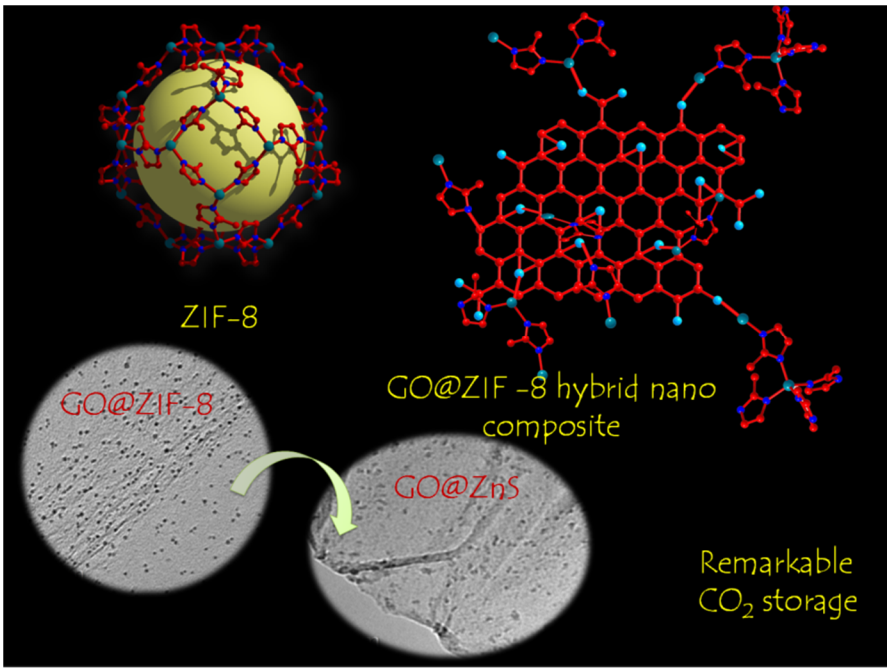

A paper based on these studies has appeared in Chem. Commun. 2013, 49, 4947.

2.1 Introduction

Metal-organic frameworks (MOFs) or porous coordination polymers (PCPs) have attracted great attention in recent years because of their possible use in gas storage, catalysis, and optoelectronic devices.[1] The modifiable pore surface of MOFs props them to the forefront of clean energy and drug delivery research.[2] Scaling down these materials to nanoscale keeping the same periodic structure of the bulk state can give rise to novel applications in bioimaging, biosensing, and other areas.[3] Furthermore, nanoscale MOFs enables solution-based processability and increased gas uptake.[4] Methodologies such as solvent induced precipitation, solvo(hydro)thermal or microwave treatment, coordination modulation techniques and reverse microemulsion have been employed for the synthesis of nanoscale MOFs.[3-4] In the last few years, graphene oxide (GO) has become a material of vital importance because of its unique properties.[5] GO has a functionalized basal plane with anchoring groups like hydroxy, epoxy or carboxyl which are useful for forming graphene-based soft materials and hybrid composites.[6] Hybrid composites based on MOFs and graphene afford integration of the unique properties of these two fascinating materials, thus allowing one to design materials possessing properties not possessed by either component.[7] Bandosz *et al*. have recently reported GO–MOF composites for the adsorption of ammonia and nitric oxide[7b] while Loh *et al.* have described conducting nanowires comprising MOF-5 and benzoic acid functionalized graphene wherein MOF-5 is intercalated between graphene sheets.[7d] The growth of MOF nanocrystals of different morphologies on graphene sheets has not been explored adequately. One can envisage GO as a potential platform and as a structure-directing agent for the growth and stabilization of MOF nanoparticles, where coordination modulation occurs through the different functional groups on the surface.[6b] In this context, making use of zeolitic imidazolate frameworks (ZIFs), a new class of zeolite-like MOFs, possessing a high degree of microporosity and exceptional thermal and chemical stabilities to prepare composites with GO appeared attractive. Prototypical ZIF-8 ($Zn(MeIM)_2$, MeIM = 2-methylimidazolate) with a sodalite zeolite structure, containing large cavities (~11.7 Å of diameter) interconnected by narrow windows (~3.40 Å) was used for the purpose (scheme 1a).[12] It may be noted that ZIF-8 has been exploited for developing thin films, membranes for catalysis and separation of gases.[8]

Since the present investigation, there have been significant developments in the MOF-graphene composites and many new properties and applications have been investigated. This class of MOF-nanocarbon composites (ZIF-8@graphene oxide, ZIF-8@carbon nanotube, and ZIF-8@carbon quantum dot) has been used for gas and chromatographic separation,[9]

increased CO_2 and organic molecule uptake,[10] electrocatalysis in oxygen reduction reaction,[11] photocatalysis, in lithium–ion battery,[12] proton exchange membranes,[13] drug delivery and fluorescence imaging,[14] and as catalysts in cycloaddition reactions.[15] The diverse applications of prototypical ZIF-8@nanocarbon based composites show the importance of combining two materials in the composite form. Synergistic interaction between the two components MOF and graphene plays a key role in determining such properties and applications. In addition to the prototypical composite of ZIF-8 with nanocarbons showing functional properties and applications several other MOF systems and their composites have been investigated. Some of the functional properties which these class of MOF–graphene composites show are enhancement in hydrothermal stability,[16] enhanced gas and organic molecule uptake,[17] application in gas separation such as CO_2/CH_4, H_2/CO_2, H_2/CH_4 etc.,[18] and co-ordination modulation agent for the growth of MOF nanoparticle on graphene basal plane.[19]

2.2 Scope of the present investigations

Metal–organic frameworks have high crystallinity, uniform and tunable porous architecture which can be designed by the proper choice of metal ion and linker, the advantage of both organic (linker) and inorganic (metal) components in the same hybrid structure in contrast to the inorganic zeolites and very high surface area.[20] These porous properties make it suitable for a wide range of applications in gas storage and separation, catalysis, sensing, drug delivery and energy storage devices.[1d,21] Graphene has many fascinating properties such as high surface area, mechanical, electrical and optoelectronic properties.[5a,22] In addition to important physical properties for different applications, the chemical properties are also interesting.[23] Graphene can be easily synthesized and functionalized using different chemical and physical approach.[24] Hybrid composites of two fascinating materials graphene and metal-organic frameworks (MOFs) would afford integration of properties which can't be realized by either individual component. The present study deals with the synthesis and potential of such hybrids for different applications. A simple and facile strategy for the growth of nanoscale ZIF-8 of different morphologies on graphene oxide (GO) nanosheets is discussed. GO acts as a structure directing agent for stabilizing nanoscale ZIF-8 via coordination modulation through various functional groups on the basal plane. Rhombic dodecahedral to a smaller spherical morphology of ZIF-8 nanocrystals in the composites has been modulated based on graphene oxide content. The composites also exhibit tunable surface area. The remarkable increase in CO_2 uptake by

GO@ZIF-8 composites with a decrease in surface area, which can be attributed to strong GO···CO_2 interactions. It has been possible to obtain GO@ZnS nanocomposite from GO@ZIF-8 by reacting with thioacetamide where ZIF-8 acts a self-sacrificing Zn(II) source.

2.3 Experimental section

Materials: All the reagents and solvents were commercially available and used as supplied without further purification. $Zn(NO_3)_2.6H_2O$, 2-methylimidazole were obtained from Aldrich Chemical Co.

Room temperature synthesis of nanoscale ZIF-8 crystals: Nanoscale ZIF-8 with rhombic dodecahedral morphology was prepared according to the literature procedure reported by Wiebcke *et al.*[8d] In a typical synthesis methanolic solution (25 ml) $Zn(NO_3)_2 \cdot 6H_2O$ (16 mmol, 366 mg) was slowly added to a methanolic solution (25 ml) of 2-methylimidazole (8 mmol, 811 mg) with constant stirring. Stirring was stopped after combining the component solutions and a *gel*-like solid was recovered by centrifugation and washed with methanol for three times and then dried under vacuum. Yield: 60%. Anal. Calcd. for $C_8H_{10}N_4Zn$: C, 42.18; H, 4.3; N, 24.6; Found: C, 41.54; H, 4.86; N, 24.39 %.

Synthesis of graphite oxide (GO): GO was prepared using a modified Hummers and Offeman method.[25] In a typical synthesis, 1.5 g of $NaNO_3$ and 1.5 g graphite powder were slowly added to 75 ml conc. H_2SO_4 in an ice bath and allowed to mix properly under constant stirring for 10 min. 10 g $KMnO_4$ was added to this uniform mixture and then it was transferred into an oil bath (40 °C) under the stirring condition for 0.5 h. Oxidation of graphite occurred and very viscous dark brown product formed after 30 min. To this mixture 75, ml deionized water was added and the temperature of oil bath was raised to 75 °C. The reactants were stirred at 75 °C for another 15 min. Then 15 ml H_2O_2 (30%) was mixed with 150 ml warm water (~70 °C) and added to the reaction mixture. Colour of dispersion was changed from brown to yellow. Then the product was centrifuged and washed several times with water. Washed product was dispersed in water and dialysis was performed for 24 h. Dialysed product was centrifuged to remove excess water and the solid product was transferred to the Petri dish. The obtained product was stored under vacuum for drying.

Preparation of GO@ZIF-8 hybrid nanocomposites: First bare X mg of GO was dispersed in methanol and sonicated for 5 hours. For the synthesis of GO@ZIF-8 composites, different wt% of GO solution was added during the preparation of ZIF-8

nanocrystals under constant stirring. The resultant product was centrifuged and washed several times with water-methanol mixture and dried at 60 ^{o}C. The resulting solid composites obtained by variation of GO content were denoted by ZG-X, X indicated wt% (X = 1, 2, 4, 10 and 20 wt %) of GO in comparison to Zn(II) metal. The obtained samples were designated as **ZG** (**ZG-0**, **ZG-1**, **ZG-2**, **ZG-4**, **ZG-10** and **ZG-20**) based on the different amount of GO loading.

Preparation of GO@ZnS hybrid nanocomposites: For the *in situ* stabilization of zinc sulphide (ZnS) nanoparticles on the graphene sheets, as-prepared **ZG-20** (20 wt% of GO) was added into a round bottom flask containing thioacetamide (0.5 M) in 50 ml methanol and 5 ml water at 60 °C. The mixture was refluxed for 6 h under vigorous stirring. The resultant product was collected by centrifugation, washed with anhydrous methanol and dried under vacuum.

Characterization: The synthesized ZIF-8, GO@ZIF-8 composites, and Go@ZnS were characterized through different techniques. Powder X-ray diffraction (PXRD) pattern was recorded on a Bruker D8 Discover instrument using Cu-Kα radiation. The morphology and porous nature of ZG-Xs' were characterized with Transmission electron microscopy (TEM) (JEOL JEM-3010 with an accelerating voltage of 300 KV). Raman spectra of the samples were recorded in backscattering arrangement, using 532 nm laser excitation and 6 mW laser power. Thermogravimetric analyses (TGA) were carried out under nitrogen atmosphere (flow rate of 50 mL/min) with Metler Toledo TGA-850 TG analyzer in the temperature range between 25 - 600°C at a heating rate 3°C / min.

Adsorption measurements: Adsorption studies of N_2 (77 K) and CO_2 (195 K) on ZIF-8 and ZG composites were carried out using *QUANTACHROME AUTOSORB-1C* analyzer. Prior to the measurements, the samples were activated at 433 K under high vacuum. In the sample chamber (~12 mL) maintained at T ± 0.03 K the adsorbent sample (100-150 mg) was placed, which had been prepared at 423 K and 10^{-1} Pa for 18 hours prior to the measurement of isotherms. The adsorbate was charged into the sample tube, and then change in the pressure was monitored and the degree of adsorption was determined by the decrease of pressure in equilibrium state. All operations were computer-controlled and automatic. High-pressure CO_2 sorption measurements were carried out on a fully computer controlled volumetric BELSORP-HP, BEL JAPAN high-pressure instrument. The CO_2 used for high-pressure measurements are scientific/research grade with 99.999% purity. For the measurements, approximately 300 mg sample was taken in a stainless-steel sample holder and

degassed at 493 K for a period of 18 hours under 10^{-1} Pa vacuum. The dead volume of the sample cell was measured with helium gas of 99.999% purity. Non-ideal correction for CO_2 gas was made by applying virial coefficients at the measurement temperature.

2.4 Results and discussion

In this chapter, a simple route for the preparation of hybrid nanocomposites of graphene oxide and ZIF-8, where the growth of the ZIF-8 nanocrystals, as well as their sizes and morphologies, are tuned by the different concentration of GO is discussed. The obtained GO@ZIF-8 (ZG) hybrid nanocomposites show tunable surface areas and pore volumes depending on the proportion of GO. Interestingly the hybrid nanocomposites exhibit characteristics by nature of both GO and ZIF-8. The composites exhibit remarkable CO_2 uptake characteristics with increasing GO concentration. Furthermore, the generation of ZnS nanoparticles on the GO sheets by using external sulphur source is discussed, where GO acts as a template and ZIF-8 as the sacrificial Zn source. Scheme 1b show the method of synthesis of GO@ZIF-8 hybrid nanocomposites with different GO content (ZG-0, ZG-1, ZG-2, ZG-4, ZG-10 and ZG-20 corresponding 0, 1, 2, 4, 10 and 20 wt% GO, respectively. See experimental section 2.3 for details).

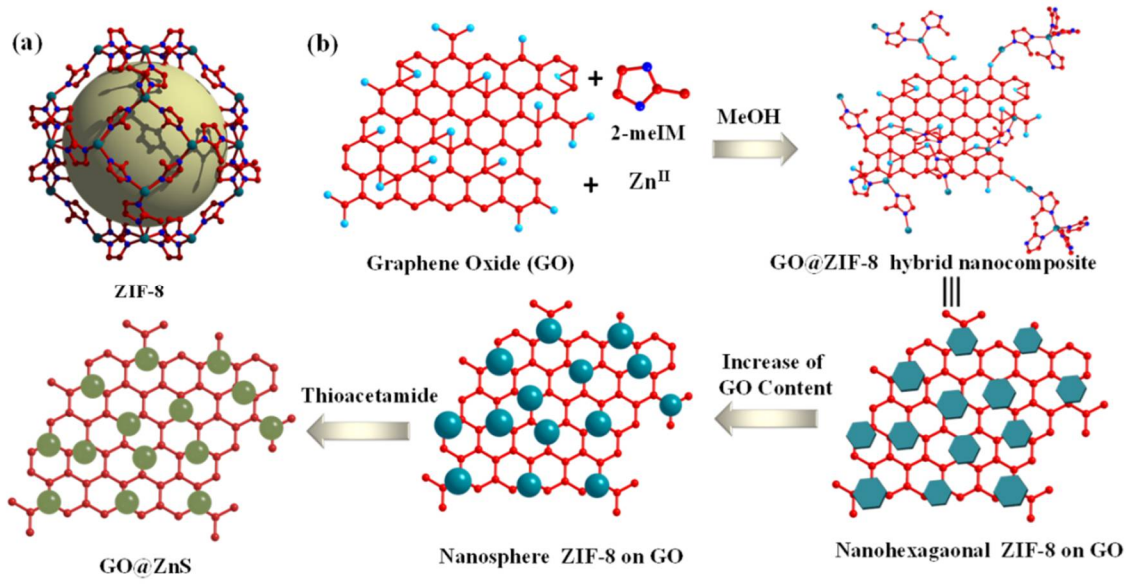

Scheme 1. (a) View of the ZIF-8 framework showing large cavities with narrow windows; (b) Stepwise synthesis of GO@ZIF-8 hybrid nanocomposites with tunable morphology, nanospheres from rhombic dodecahedral ZIF-8 nanocrystals and *in-situ* stabilization of ZnS nanoparticles on the GO sheet.

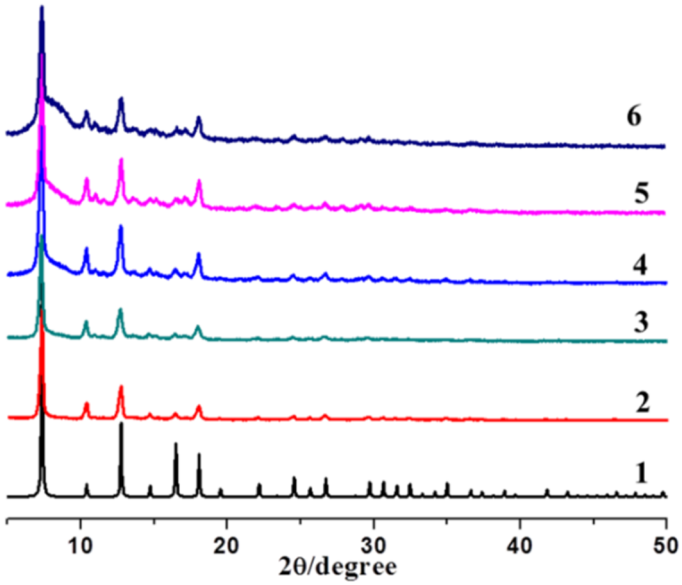

Figure 1. (Left) PXRD patterns of ZIF-8 and GO@ZIF-8 hybrid nanocomposites; (1) ZG-0 (ZIF-8), (2) ZG-1, (3) ZG-2, (4) ZG-4, (5) ZG-10, and (6) ZG- 20.

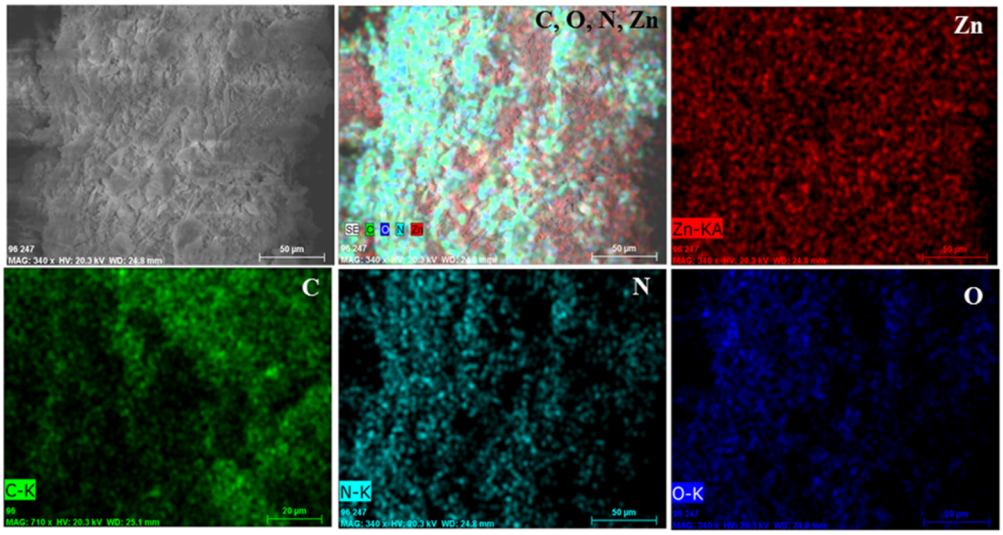

Figure 2. Colour mapping of **ZG-10** sample showing phase purity with homogeneously distributed throughout the sample.

Powder X-ray diffraction patterns of the composites with different GO contents show the reflections of ZIF-8 (cubic space group; figure 1). With the increase of GO content, a new reflection appears at $2\theta = 8.6°$ close to the 110 peak of ZIF-8, which would be attributed to GO. Such low angle shift compared to pristine GO indicating intercalation of ZIF-8 nanocrystals between the GO sheets. The phase purity of the nanocomposite was established through elemental analysis in energy dispersive X-ray spectroscopy (EDAX; Figure 2).

ZIF-8 show bands in the Raman spectrum corresponding to the 2-methylimidazole linker while GO shows bands at 1333 cm^{-1} and 1594 cm^{-1} due to the *D* and *G* bands

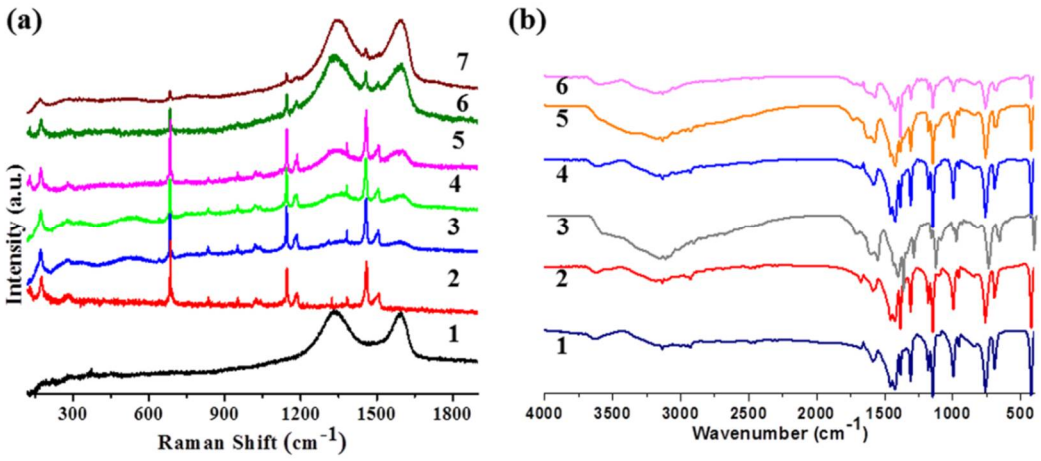

Figure 3. (a) Raman spectra of (1) graphene oxide (GO), (2) ZG-0 (ZIF-8), (3) ZG-1, (4) ZG-2, (5) ZG-4, (6) ZG-10 and (7) ZG-20. Infrared spectra of (1) ZG-0 (ZIF-8), (2) ZG-1, (3) ZG-2, (4) ZG-4, (5) ZG-10 and (6) ZG-20.

respectively. The Raman spectra of composites show bands corresponding to ZIF-8 as well as the *D* and *G* bands (Figure 1a).With increasing GO concentration the intensities of the *D* and *G* bands increase. Furthermore, peaks at 175 cm^{-1} and 390 cm^{-1} corresponding to Zn-O and Zn-O-Zn vibrational bands are also seen due to bonding between -OH, and -COOH functional groups decorated on the GO with Zn(II). Table 1 summarizes the different bands observed in the Raman spectra of the composite. The infrared spectra of the ZG hybrid nanocomposites show bands due to ZIF-8 as well as GO, the frequencies being shifted to slightly lower frequencies (Figure 3b) due to interaction with the functional groups present on graphene oxide basal plane.

The morphologies of ZIF-8 and the ZG composites were characterized by transmission electron microscopy (TEM). We show typical TEM images in Figure 4. The as-synthesized ZIF-8 (without any GO) shows rhombic dodecahedral morphology with a particle size in the range ~100 - 150 nm as shown in Figure 4a. Similar rhombic dodecahedral morphology and particle size are also found in ZG-1 (1 wt% of GO), with the ZIF-8 particles being stabilized within the dense GO sheets (Figure 4b). With increasing GO content, the particle size of ZIF-8 decreases. In the case of ZG-2, distorted rhombic dodecahedral of 50 -100 nm size are seen and covered between the GO sheets (Figure 4c). On increasing the GO content to 4 wt% in (ZG-4), irregular particles transform to a spherical shape, the size being 40 - 50 nm (Figure 4d). In ZG-10 (10 wt% GO) spheres of 20 nm diameter (with a few of the bigger size of 40-50 nm) are formed (Figure 4e). In the case of ZG-20 (20 wt% GO), the size of the nanocrystals gets significantly reduced and we see a homogenous distribution of uniform

Table 1. Raman peak assignment of ZIF-8 (ZG-O) and ZIF-8 graphene oxide composites (ZG).

Raman Shift (cm^{-1})	Assignment
685 (s)	ν (CCH_3) due to C-C stretching of the methyl group attached to an imidazole ring.
1145 (s)	Methyl rocking vibration ρ (CH_3). Bending mode of the CH_3 group attached to an imidazole ring.
1460 (s)	Antisymmetric deformation vibrations of C-H in methyl group
1380 (w)	Symmetric deformation vibrations of C-H in methyl group
834 (w)	γ (CH) modes. Out of plane, C-H bending mode of H attached to the 2-methylimidazole ring.
1508 (m)	ν (R) In-plane imidazole ring stretching mode.
2930 (m)	C-H stretching vibration of a methyl group (sp^3 C-H stretching vibration).
3114, 3135 (m)	C-H stretching vibration of H attached to 2-methylimidazole ring (sp^2 C-H stretching vibration)
1333 (broad)	*D* band of graphite oxide.
1594 (broad)	*G* band of graphite oxide.

[w = weak, s = strong, m = medium intensity]

nanospheres of ~4 nm diameter in Figure 4f. Clearly, the size and morphology of ZIF-8 are controlled by the percentage of GO in the composite. The GO sheets appear to provide a platform for the nucleation and growth of nanocrystals. The shapes and sizes (hexagonal to a sphere) are probably controlled by –OH and –COOH groups through coordination modulation which inhibits the growth of large crystals. The functionalized GO sheets act as both structure-directing and size-controlling agents for ZIF-8 nanocrystals.

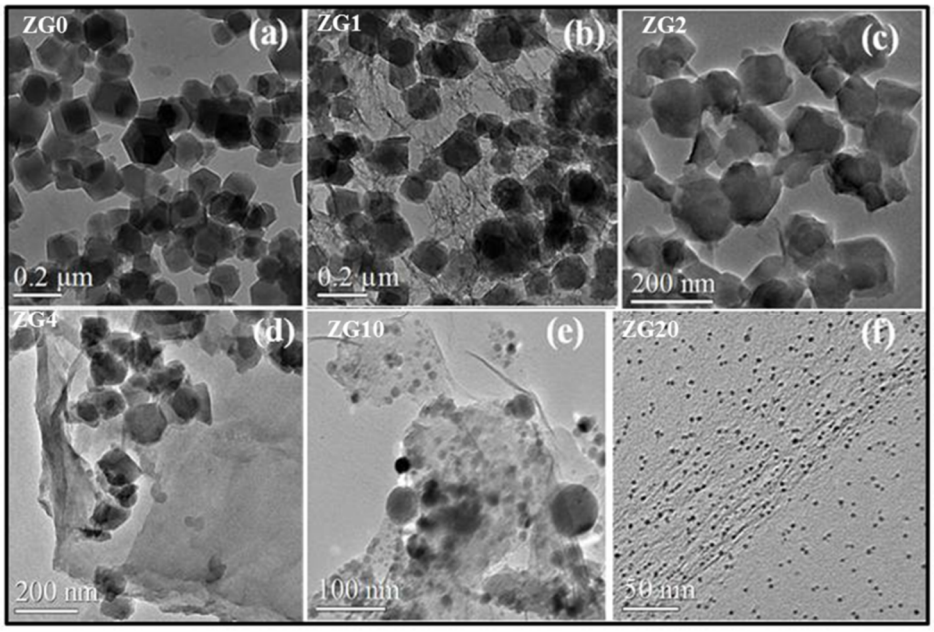

Figure 4. TEM images of ZG samples (a) ZG-0, (b) ZG-1, (c) ZG-2, (d) ZG-4, (e) ZG-10 and (f) ZG-20.

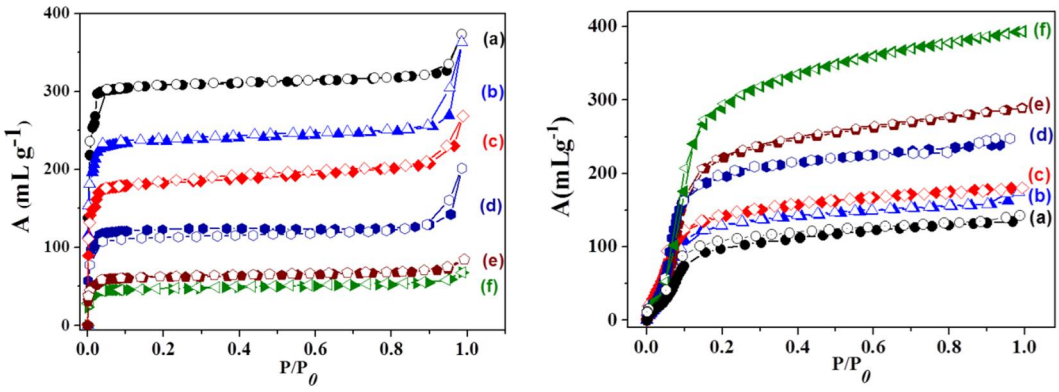

Figure 5. (Left) Nitrogen (at 77 K), (right) Carbon dioxide (at 195 K) adsorption-desorption isotherms of ZG samples (a) ZG-0, (b) ZG-1, (c) ZG-2, (d) ZG-4 (e), ZG-10 and (f) ZG-20. Closed symbol in the isotherm corresponds to adsorption cycle whereas open circle corresponds to desorption cycle in all the adsorption-desorption isotherms of the thesis.

Textural parameters such as surface area, pore volume and pore size of the ZG hybrid nanocomposites were obtained from N_2 adsorption-desorption measurements at 77 K (Figure 5, left). The BET surface area of the GO sample is around ~15 m^2/g (Figure 6). On the other hand, N_2 adsorption of the nanoscale ZIF-8 (ZG-0) shows typical type –I profile with a surface area of about 1120 m^2/g comparable with the literature value.[10] The textural parameters of the ZG composites are given in Table 2. The BET surface area of the composites decreases relative to ZG-0 (ZIF-8) with increasing GO content. Thus, the surface areas of ZG-1, ZG-2, ZG-4, ZG-10 and ZG-20 are 819, 675, 450, 320, 280 m^2/g respectively (Table 2). The decrease in surface area can arise due to an increasing proportion of nonporous GO in the composites. The ZG composites exhibit good CO_2 storage capacity with the CO_2 uptake at 195 K increasing with the increasing GO content (Figure 5 (right) and Table 2). Note that pristine ZIF-8 (ZG-0) and GO show 27.2 wt% and 33 wt% of

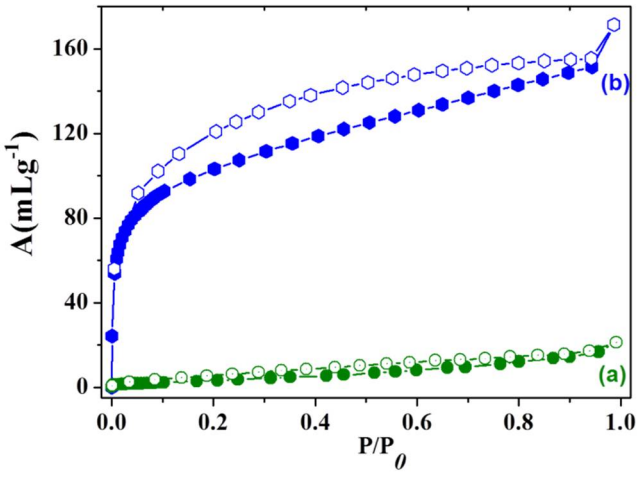

Figure 6. (a) Nitrogen, (b) Carbon dioxide adsorption isotherm of GO at 77 and 195 K respectively.

Table 2. Textural parameters and CO_2 storage capacities of as-synthesized nanocrystals of ZIF-8 and ZG composite.

Sample	S_{BET} (m2/g)	Vp (cm^3/g)	CO_2 (wt%)	Q (KJ/mol)
ZIF-8	1120	0.56	27.2	-
ZG-1	819	0.45	32.4	28.9
ZG-2	675	0.23	35.1	29.4
ZG-4	450	0.19	48.4	30.3
ZG-10	320	0.11	55.3	31.4
ZG-20	289	0.09	72.4	31.9

CO_2 uptake, respectively (Figure 6 and Table 2). ZG-4 exhibits CO_2 uptake of about 49 wt% at 195 K (1 atm) which increases further to 72 wt% in ZG-20. This unusual CO_2 uptake can be attributed the cumulative effect of ZIF8 and GO as later provide specific interaction with CO_2 based functionalities on the sheets. This is supported by the high heat of CO_2 sorption ($q_{st,\phi}$) 31.9 kJ/mol in the case of ZG-20 obtained from Dubinin-Radushkevich (DR) equation.[26] The present study of GO@ZIF-8 hybrid nanocomposites with tunable porosity and significant CO_2 storage capacity may have important applications in gas separation, storage, and catalysis.

Zinc sulphide (ZnS) shows fascinating electrical and optical properties, which would be further modified into nanoscale or in hybridization with other materials like graphene oxide (GO).[27] The GO@ZIF-8 composite, ZG-20 was used for the synthesis of the GO@ZnS composite. On reaction with ZG-20 with thioacetamide, the ZIF-8 in the composite acts as

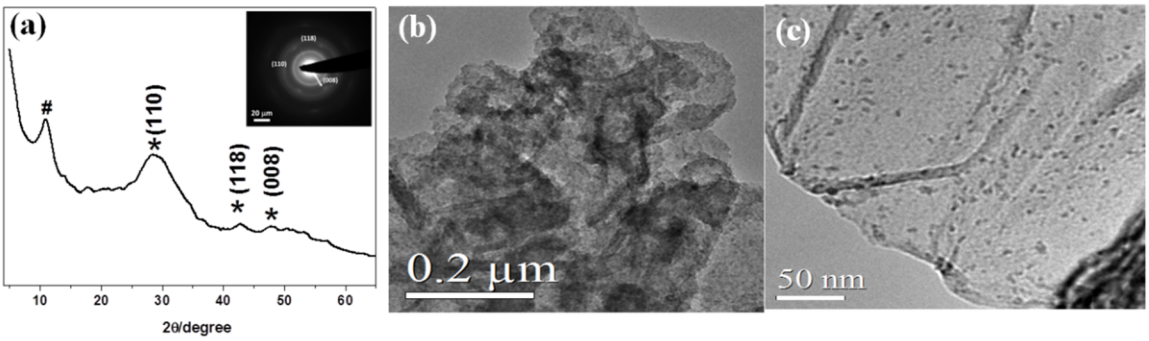

Figure 7. Characterization of GO@ZnS composites: (a) powder XRD pattern (ED pattern inset shows three planes of the ZnS corresponding Wurtzite structure); (b-c) TEM images show ZnS nanoparticles on the GO sheet.

the sacrificial Zn source and reacts with the sulphur produced by thioacetamide. Figure 7a shows the powder X-ray different pattern of the GO@ZnS nanocomposite with broad reflections corresponding to the Wurtzite structure of ZnS (*JCPDS N0 39-1363*). The reflection at 12.21° corresponds to GO and the slight shift to a higher angle corroborates a decrease in the interlayer separation between two successive graphene sheets (Figure 7). Figures 7b-c shows TEM images of the GO@ ZnS, revealing that the ZnS nanoparticles of ~ 3 nm are stabilized on the GO sheet. This particle size is consistent with the XRD data and this hybrid also shows uptake of CO_2 about 9 wt% as shown in Figure 8.

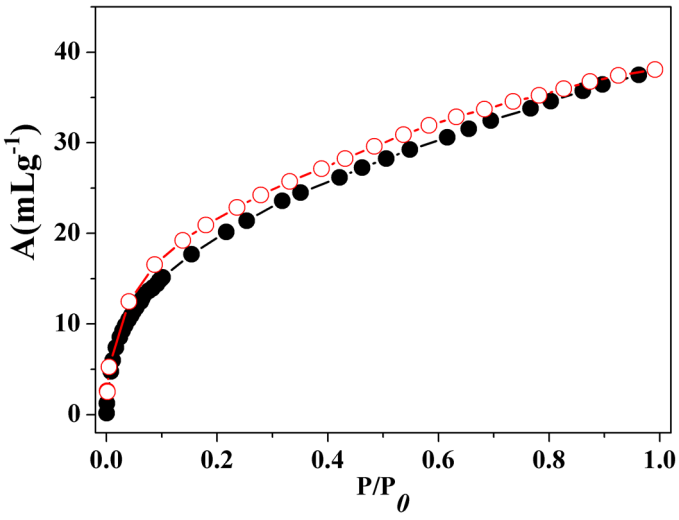

Figure 8. CO_2 adsorption profile of GO@ZnS nanocomposite at 195 K.

2.5 Conclusions

In conclusion, a simple procedure to prepare GO@ZIF-8 hybrid nanocomposites was discussed. ZIF-8 is stabilized on the GO surfaces through functional groups and the nanoscale morphology of the composite (from hexagonal to spherical) can be tuned by the concentration of GO. GO acts as a structure-directing agent for the growth of nanocrystals of ZIF-8 through coordination modulation. The composites show remarkable CO_2 storage capacity compared to the parent ZIF-8. This study also discusses the growth and stabilization of nanoscale MOF on a graphene surface, with tunable morphology and gas storage characteristics which may have important applications. The GO-ZIF composite can be used as a precursor for obtaining the GO@ZnS composite by reaction with thioacetamide, where ZIF-8 acts as the sacrificial source of Zn(II).

References

[1] a) L. J. Murray, M. Dinca and J. R. Long, *Chem. Soc. Rev.* **2009**, *38*, 1294; b) S. Kitagawa, R. Kitaura and S.-i. Noro, *Angew. Chem. Int. Ed.* **2004**, *43*, 2334; c) D. Bradshaw, J. B. Claridge, E. J. Cussen, T. J. Prior and M. J. Rosseinsky, *Acc. Chem. Res.* **2005**, *38*, 273; d) J. Lee, O. K. Farha, J. Roberts, K. A. Scheidt, S. T. Nguyen and J. T. Hupp, *Chem. Soc. Rev.* **2009**, *38*, 1450; e) A. Dhakshinamoorthy, M. Alvaro, A. Corma and H. Garcia, *Dalton Trans.* **2011**, *40*, 6344; f) C. H. Hendon, D. Tiana and A. Walsh, *PCCP* **2012**, *14*, 13120.

[2] a) J.-R. Li, R. J. Kuppler and H.-C. Zhou, *Chem. Soc. Rev.* **2009**, *38*, 1477; b) P. Horcajada, T. Chalati, C. Serre, B. Gillet, C. Sebrie, T. Baati, J. F. Eubank, D. Heurtaux, P. Clayette, C. Kreuz, J.-S. Chang, Y. K. Hwang, V. Marsaud, P.-N. Bories, L. Cynober, S. Gil, G. Ferey, P. Couvreur and R. Gref, *Nat. Mater.* **2010**, *9*, 172.

[3] a) W. Lin, W. J. Rieter and K. M. L. Taylor, *Angew. Chem. Int. Ed.* **2009**, *48*, 650; b) A. M. Spokoyny, D. Kim, A. Sumrein and C. A. Mirkin, *Chem. Soc. Rev.* **2009**, *38*, 1218; c) A. Carne, C. Carbonell, I. Imaz and D. Maspoch, *Chem. Soc. Rev.* **2011**, *40*, 291.

[4] a) H. J. Lee, W. Cho, S. Jung and M. Oh, *Adv. Mater.* **2009**, *21*, 674; b) O. K. Farha, A. M. Spokoyny, K. L. Mulfort, S. Galli, J. T. Hupp and C. A. Mirkin, *Small* **2009**, *5*, 1727.

[5] a) C. N. R. Rao, A. K. Sood, K. S. Subrahmanyam and A. Govindaraj, *Angew. Chem. Int. Ed.* **2009**, *48*, 7752; b) D. Chen, H. Feng and J. Li, *Chem. Rev.* **2012**, *112*, 6027.

[6] a) K. Yang, L. Feng, X. Shi and Z. Liu, *Chem. Soc. Rev.* **2013**, *42*, 530; b) X. Li, W. Qi, D. Mei, M. L. Sushko, I. Aksay and J. Liu, *Adv. Mater.* **2012**, *24*, 5136; c) J. Kim, L. J. Cote and J. Huang, *Acc. Chem. Res.* **2012**, *45*, 1356.

[7] a) Z.-H. Huang, G. Liu and F. Kang, *ACS Appl. Mater. Interfaces* **2012**, *4*, 4942; b) C. Petit and T. J. Bandosz, *Adv. Mater.* **2009**, *21*, 4753; c) Y. Guo, Y. Han, S. Shuang and C. Dong, *J. Mater. Chem.* **2012**, *22*, 13166; d) M. Jahan, Q. Bao, J.-X. Yang and K. P. Loh, *J. Am. Chem. Soc.* **2010**, *132*, 14487; e) D. Li, L. Qiu, K. Wang, Y. Zeng, T. Williams, Y. Huang, M. Tsapatsis and H. Wang, *Chem. Commun.* **2012**, *48*, 2249.

[8] a) K. S. Park, Z. Ni, A. P. Côté, J. Y. Choi, R. Huang, F. J. Uribe-Romo, H. K. Chae, M. O'Keeffe and O. M. Yaghi, *Proc. Natl. Acad. Sci. USA* **2006**, *103*, 10186; b) Y. Pan, Y. Liu, G. Zeng, L. Zhao and Z. Lai, *Chem. Commun.* **2011**, *47*, 2071; c) Z. Jiang, H. Sun, Z. Qin, X. Jiao and D. Chen, *Chem. Commun.* **2012**, *48*, 3620; d) J. Cravillon, S. Münzer, S.-J. Lohmeier, A. Feldhoff, K. Huber and M. Wiebcke, *Chem. Mater.* **2009**, *21*, 1410; e) Q. Song, S. K. Nataraj, M. V. Roussenova, J. C. Tan, D. J. Hughes, W. Li, P. Bourgoin, M. A. Alam, A. K. Cheetham, S. A. Al-Muhtaseb and E. Sivaniah, *Energy Environ. Sci.* **2012**, *5*, 8359; f) G. Lu, O. K. Farha, W. Zhang, F. Huo and J. T. Hupp, *Adv. Mater.* **2012**, *24*, 3970.

[9] a) A. Huang, Q. Liu, N. Wang, Y. Zhu and J. Caro, *J. Am. Chem. Soc.* **2014**, *136*, 14686; b) Y. Hu, J. Wei, Y. Liang, H. Zhang, X. Zhang, W. Shen and H. Wang, *Angew. Chem. Int. Ed.* **2016**, *55*, 2048; c) X. Yang, C. Li, M. Qi and L. Qu, *J. Chromatogr. A* **2016**, *1460*, 173.

[10] a) B. Chen, Y. Zhu and Y. Xia, *RSC Advances* **2015**, *5*, 30464; b) Y. Yang, L. Ge, V. Rudolph and Z. Zhu, *Dalton Trans.* **2014**, *43*, 7028; c) Y. Zhou, L. Zhou, X. Zhang and Y. Chen, *Microporous Mesoporous Mater.* **2016**, *225*, 488; d) D. Kim, D. W. Kim, W. G. Hong and A. Coskun, *J. Mater. Chem. A* **2016**, *4*, 7710.

[11] H.-x. Zhong, J. Wang, Y.-w. Zhang, W.-l. Xu, W. Xing, D. Xu, Y.-f. Zhang and X.-b. Zhang, *Angew. Chem. Int. Ed.* **2014**, *53*, 14235.

[12] X. Cao, B. Zheng, X. Rui, W. Shi, Q. Yan and H. Zhang, *Angew. Chem.* **2014**, *126*, 1428.

[13] L. Yang, B. Tang and P. Wu, *J. Mater. Chem. A* **2015**, *3*, 15838.

[14] L. He, T. Wang, J. An, X. Li, L. Zhang, L. Li, G. Li, X. Wu, Z. Su and C. Wang, *CrystEngComm.* **2014**, *16*, 3259.

[15] Y. Wei, Z. Hao, F. Zhang and H. Li, *J. Mater. Chem. A* **2015**, *3*, 14779.

[16] D.-D. Zu, L. Lu, X.-Q. Liu, D.-Y. Zhang and L.-B. Sun, *J. Phys. Chem. C* **2014**, *118*, 19910.

[17] a) H. Zhou, X. Liu, J. Zhang, X. Yan, Y. Liu and A. Yuan, *Int. J. Hydrogen Energy* **2014**, *39*, 2160; b) X. Sun, Q. Xia, Z. Zhao, Y. Li and Z. Li, *Chem. Eng. J.* **2014**, *239*, 226; c) Z. Kang, M. Xue, D. Zhang, L. Fan, Y. Pan and S. Qiu, *Inorg. Chem. Commun.* **2015**, *58*, 79.

[18] a) W. Huang, X. Zhou, Q. Xia, J. Peng, H. Wang and Z. Li, *Ind. Eng. Chem. Res.* **2014**, *53*, 11176; b) X. Zhou, W. Huang, J. Miao, Q. Xia, Z. Zhang, H. Wang and Z. Li, *Chem. Eng. J.* **2015**, *266*, 339.

[19] X. Qiu, X. Wang and Y. Li, *Chem. Commun.* **2015**, *51*, 3874.

[20] a) H.-C. Zhou, J. R. Long and O. M. Yaghi, *Chem. Rev.* **2012**, *112*, 673; b) S. L. James, *Chem. Soc. Rev.* **2003**, *32*, 276; c) C. N. R. Rao, S. Natarajan and R. Vaidhyanathan, *Angew. Chem. Int. Ed.* **2004**, *43*, 1466; d) J. L. C. Rowsell and O. M. Yaghi, *Microporous Mesoporous Mater.* **2004**, *73*, 3.

[21] a) Y. Cui, Y. Yue, G. Qian and B. Chen, *Chem. Rev.* **2012**, *112*, 1126; b) J. Liu, L. Chen, H. Cui, J. Zhang, L. Zhang and C.-Y. Su, *Chem. Soc. Rev.* **2014**, *43*, 6011; c) R. J. Kuppler, D. J. Timmons, Q.-R. Fang, J.-R. Li, T. A. Makal, M. D. Young, D. Yuan, D. Zhao, W. Zhuang and H.-C. Zhou, *Coord. Chem. Rev.* **2009**, *253*, 3042; d) H. Furukawa, K. E. Cordova, M. O'Keeffe and O. M. Yaghi, *Science* **2013**, *341*.

[22] a) X. Huang, X. Qi, F. Boey and H. Zhang, *Chem. Soc. Rev.* **2012**, *41*, 666; b) Y. Zhu, S. Murali, W. Cai, X. Li, J. W. Suk, J. R. Potts and R. S. Ruoff, *Adv. Mater.* **2010**, *22*, 3906.

[23] a) A. Hirsch, J. M. Englert and F. Hauke, *Acc. Chem. Res.* **2013**, *46*, 87; b) H. Zhang, E. Bekyarova, J.-W. Huang, Z. Zhao, W. Bao, F. Wang, R. C. Haddon and C. N. Lau, *Nano Lett.* **2011**, *11*, 4047; c) L. Dai, *Acc. Chem. Res.* **2013**, *46*, 31.

[24] a) R. Ruoff, *Nat. Nano* **2008**, *3*, 10; b) S. Park and R. S. Ruoff, *Nat. Nano* **2009**, *4*, 217; c) J. M. Englert, C. Dotzer, G. Yang, M. Schmid, C. Papp, J. M. Gottfried, H.-P. Steinrück, E. Spiecker, F. Hauke and A. Hirsch, *Nat. Chem.* **2011**, *3*, 279; d) C. K. Chua and M. Pumera, *Chem. Soc. Rev.* **2013**, *42*, 3222.

[25] W. S. Hummers and R. E. Offeman, *J. Am. Chem. Soc.* **1958**, *80*, 1339.

[26] M. M. Dubinin, *Chem. Rev.* **1960**, *60*, 235.

[27] S. Pan and X. Liu, *J. Solid State Chem.* **2012**, *191*, 51.

Chapter 3: Growth of 2D sheets of a MOF on graphene surfaces to yield composites with novel gas adsorption characteristics*

Summary

Homogeneous graphene-MOF composites based on a 2D pillared-bilayer MOF (Cd-PBM), $\{[Cd_4(azpy)_2(pyrdc)_4(H_2O)_2].9H_2O\}_n$ (azpy = 4,4′-azopyridine, pyrdc = pyridine-2,3-dicarboxylate), have been synthesized, using both graphene oxide (GO) and benzoic acid functionalized graphene (BFG). The composites GO@Cd-PBM and BFG@Cd-PBM demonstrate the growth of the 2D nanosheets of MOF on the graphene surface. While the pristine MOF, Cd-PBM, shows selective CO_2 uptake with a single-step type-I adsorption profile, the composites show stepwise CO_2 uptake with large hysteresis. With H_2O and MeOH, on the other hand, the composites show a single-step adsorption, unlike the parent MOF. The epitaxial growth of 2D MOF on 2D graphene surface suggests a new possibility of MOF-based multifunctional composites with combined properties of both the constituents and new properties due to a synergistic interaction between the constituents as observed in the present investigation.

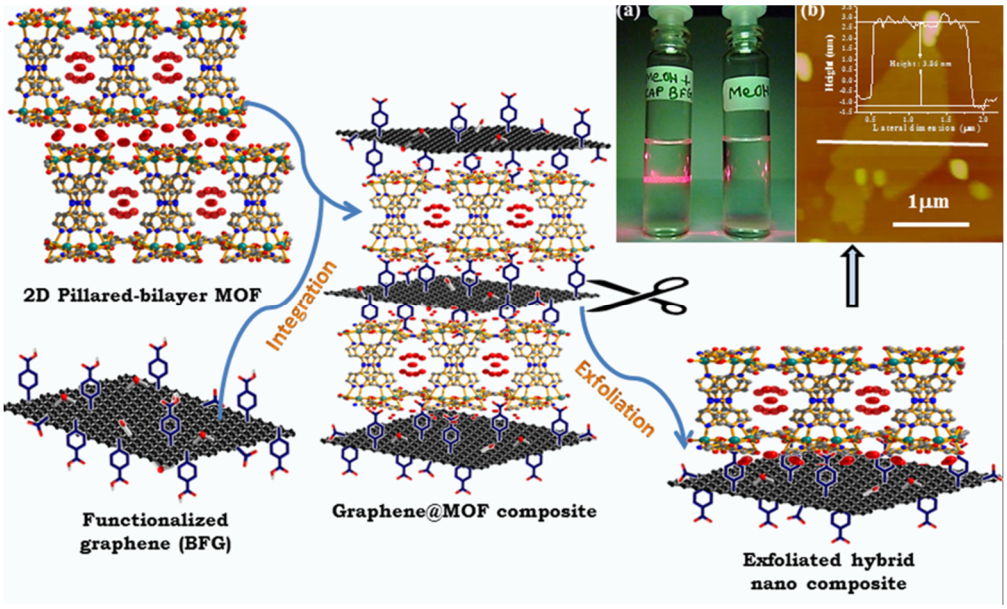

A paper based on these studies has appeared in Dalton Trans. 2014, 43, 7383.

3.1 Introduction

As mentioned earlier in the thesis, graphene is a promising material for applications in electronics, energy storage, sensors and gas storage.[1] Graphene oxide (GO) containing hydroxyl, epoxy and carboxylic acid groups on the basal plane and edges,[2] enables further chemical functionalization but also provides a nanoscale building block for generating novel hybrid materials.[3] Metal-organic frameworks (MOFs), on the other hand, are porous inorganic-organic hybrid materials with a variety of potential applications.[4] MOFs have the tunable surface area, pore size, and modular pore environment, properties which have pushed these materials to the forefront of clean energy research, in particular, H_2 and CO_2 storage.[5] One can envision using graphene as a novel building block and structure-directing agent for generating interesting materials incorporating the MOF nanostructure.[3a,6] Integration of MOFs and graphene would also allow one to create properties which would otherwise not be present in either component. Chapter 2 demonstrated the growth of ZIF-8 nanocrystals of different sizes and morphologies on GO surfaces and showed that CO_2 uptake increases with increase in GO content in the composite compared to pristine ZIF-8.[3a] Bandosz *et al.* and Loh *et al.* have reported MOF-graphene composites and their applications in NH_3 uptake and NO_2 storage. [6-7] In this chapter, epitaxial growth of a 2D MOF on 2D graphene surface is discussed. The oxygen containing functionalities present on the graphene basal plane form strong chemical bonds with the metal ion and stabilize the epitaxial growth of MOF layers.

The present investigation reports a simple and facile strategy for the growth of 2D– MOF nano-sheet on functionalized graphene surface based on the face-to-face assembly. Such growth will give rise to a unique 2D composite of graphene and MOF. The hybrid composite shows interesting adsorption behavior in contrast to pristine MOFs. The hybrids GO@Cd-PBM and BFG@Cd-PBM show stepwise uptake of CO_2 with large hysteresis rather than a single-step uptake as found in pristine MOF itself. On the other hand, H_2O and MeOH exhibit single-step sorption profiles in these composites unlike the double-step uptake in pristine MOF. The 2D hybrid nanocomposite BFG@Cd-PBM was further exfoliated in methanol to obtain a stable colloidal dispersion. Individual or few–layer MOF sheets supported on graphene basal plane can be used for making MOF films using Langmuir–Blodgett technique from the colloidal suspension of dispersed nanosheets. Several important synthesis methods and applications of MOF thin films are reported in the literature and present strategy may be useful for various practical applications.[8]

3.2 Scope of the present investigations

Hybrid composites of two interesting materials metal-organic frameworks (MOFs) and graphene will have interesting properties due to synergistic effects, which can-not be realized by the individual components. A study of these hybrid materials unique properties is the subject of present investigation. The 2D functionalized graphene sheets can act as a template for the nucleation and growth of MOF units. Graphene oxide and benzoic acid−functionalized graphene have various oxygen-containing functional groups such as carboxylates, epoxides, and hydroxyls. These oxygen functionalities can easily coordinate and stabilize various metal ions on the graphene basal plane. Several two–dimensional metal organic frameworks with interesting magnetic, optical and gas adsorption properties are reported in the literature.[9] Epitaxial growth of these 2D-MOF on 2D graphene surface assisted by chemical bond formation between the oxygen functionalities on graphene basal plane with the MOF units gives rise to new hybrid composites. The coordinate bond between oxygen functionalities on graphene basal plane and 2D–MOF layers can result in uniform composites with synergistic interactions.

3.3 Experimental section

Graphite powder, Cadmium perchlorate hydrate, and 2,3-Pyridinedicarboxylic acid were obtained from Sigma-Aldrich. 4,4'-Azopyridine was synthesized using the procedure reported in the literature.[10] Methanol, $KMnO_4$, $NaNO_3$ and other chemicals were obtained from Merck chemicals.

Synthesis of GO and BFG: Graphite oxide was prepared using a modified Hummers and Offeman method.[11] In a typical synthesis 1.5 g, graphite powder and 1.5 g of $NaNO_3$ were slowly added to 75 ml conc.H_2SO_4 and allowed to mix properly under constant stirring for 10 min. In the uniform mixture, 10 g $KMnO_4$ was added and transferred to an oil bath maintained at 40 °C. The mixture was allowed to stir for next 30 min. The viscous dark brown product was formed due to the oxidation of graphite. In the uniform viscous product, 75 ml deionized water was added and the temperature of oil bath was raised to 75 °C. The stirring was performed for another 15 min with an oil bath maintained at 75 °C. In 150 ml warm water (~ 70 °C) 15 ml H_2O_2 (30%) was mixed and added to the reaction mixture. The Colour of dispersion changed from dark brown to yellow. Obtained product was centrifuged and washed several times with water to remove excess acid. Washed product was again

dispersed in water and dialysis was performed till dialysate became neutral. Dialysed product was centrifuged to remove excess water. Obtained solid product was transferred to a petri dish and stored under vacuum for drying. Reduction of GO with Sodium borohydride and Benzoic acid functionalization was performed using the procedure given in the literature.[6] A detailed synthesis procedure along with characterization is given in pages 64, 65 and 66 of chapter 4.

Synthesis of Cd-PBM, GO@Cd-PBM and BFG@Cd-PBM: In 50 ml water, 22 mg GO was dispersed by sonication for 2 hrs. The wt% was calculated based on the obtained solid product of pristine MOF. In the uniform colloidal dispersion, Cd (II) ion (~ 0.5 mmol, $Cd(ClO_4)_2 \cdot xH_2O$) was added and allowed to stir for next 15 min. After 15 min Na_2pyrdc (0.5 mmol) and methanolic solution (25 ml) of azpy (0.5 mmol) was slowly added and allowed to stir overnight. The product was centrifuged and washed with water. Obtained product was dried under vacuum at room temperature. BFG@Cd-PBM was obtained by the same procedure except the initial dispersion of BFG was obtained by sonication in water maintained at pH 10. Cd-PBM was obtained by simple mixing and overnight stirring of ligand solution with metal ion solution.[12] Phase purity of obtained product was checked by matching powder X-ray diffraction pattern with simulated pattern.

Liquid-phase exfoliation of BFG@Cd-PBM: BFG@Cd-PBM was exfoliated in methanol by ultrasonication. The composite was dispersed with a concentration of 1 mg/ml in methanol and sonicated in a bath sonicator (Branson-3510) for 90 minutes. The dispersion was centrifuged at 3000 rpm for 30 minutes. The middle portion of the supernatant was collected and drop cast on Si/SiO_2 substrate for AFM analysis. A colloidal dispersion was drop cast on NaCl window and IR spectrum of exfoliated nanocomposite was collected. The obtained colloidal dispersion of exfoliated sheet was stable when observed for a month.

Characterization: Powder X-ray diffraction (PXRD) pattern of obtained composites was recorded on a Bruker D8 Discover instrument using Cu-Kα radiation. Morphology of BFG@Cd-PBM, GO@Cd-PBM and Cd-PBM were characterized with Transmission electron microscopy (TEM) (JEOL JEM-3010 with an accelerating voltage of 300 KV). SEM images were obtained from Nova Nano SEM 600, FEI Company. AFM was carried out using Innova scanning probe microscope. Raman spectra of the samples were recorded in backscattering arrangement, using 514.53 nm Ar^+ laser using LabRam HR 800 spectrometer. Thermogravimetric analysis (TGA) was carried out under nitrogen (flow rate of 50 mL/min) with Metler Toledo TGA-850 TG analyzer in the temperature range between 30 °C – 600 °C at a heating rate of 5 °C / min. Infrared spectra of the compounds were recorded on a Bruker IFS 66v/S spectrophotometer using the KBr pellets in the region 4000-400 cm^{-1}. IR spectrum

of exfoliated BFG@Cd-PBM was recorded by drop casting MeOH colloidal dispersion on NaCl crystal and drying in 100 °C oven to remove the solvent.

Gas adsorption measurement: The adsorption isotherms for N_2, (at 77K), and CO_2 (at 195 K) gases were carried out using *QUANTACHROME AUTOSORB-1C* analyzer. The solvent adsorption isotherms MeOH (at 293 K) and H_2O (at 298 K) were measured using BELSORP aqua-3 volumetric adsorption instrument from BEL, Japan. Known weights (100-125 mg) of the as-synthesized samples were placed in the sample cell. Prior to measurements, the samples were dried under high vacuum at 373 K for 12 h to remove the adsorbed water molecules. The adsorbate was charged into the sample tube, and change of the pressure was monitored. The degree of adsorption was determined by the decrease in pressure at the equilibrium state. All operations for measurement were computer-controlled and automatic.

3.4 Results and discussion

Epitaxial growth of a 2D MOF on 2D graphene surface has not been achieved so far. In this chapter an investigation is carried out based on a 2D pillared bi-layer MOF, $\{[Cd_4(azpy)_2(pyrdc)_4(H_2O)_2].9H_2O\}_n$ (azpy = 4,4′-azopyridine, pyrdc = pyridine-2,3-dicarboxylate), expecting the growth of a 2D nanosheet on the graphene surface based on the face-to-face assembly (see experimental section 3.3 and scheme 1 for details). Such growth will give rise to a unique 2D composite of graphene and MOF. Graphene oxide (GO) which is very rich in oxygen-containing functional groups such as epoxide and hydroxyl, as well as benzoic acid, functionalized graphene (BFG) synthesized from reduced graphene oxide using diazonium salt grafting was used for the epitaxial growth of 2D MOF on the graphene surface.[6,11] These oxygen-containing functional groups coordinate with the metal ion and stabilize the nucleation and growth of 2D MOF layers on the graphene basal plane. The successful growth of 2D MOF sheets on both these graphene surfaces (GO and BFG) and their adsorption properties are investigated. The hybrids GO@Cd-PBM and BFG@Cd-PBM show stepwise uptake of CO_2 with large hysteresis rather than a single-step uptake as found in pristine MOF itself. On the other hand H_2O and methanol (MeOH) exhibit single-step sorption profiles in these composites unlike the double-step uptake in pristine MOF.

The structure of $\{[Cd_4(azpy)_2(pyrdc)_4(H_2O)_2].9H_2O\}_n$ (Cd-PBM) is reported to consist of a 2D corrugated sheet of $[Cd_4(pyrdc)_4]_n$ formed by linking of pyrdc ligands with Cd^{II} centre in crystallographic *bc* plane.[13] The 2D corrugated sheets are connected by the azpy pillars along the crystallographic *a* direction to form a 2D pillared bilayer network (Scheme 1 and Figure1).

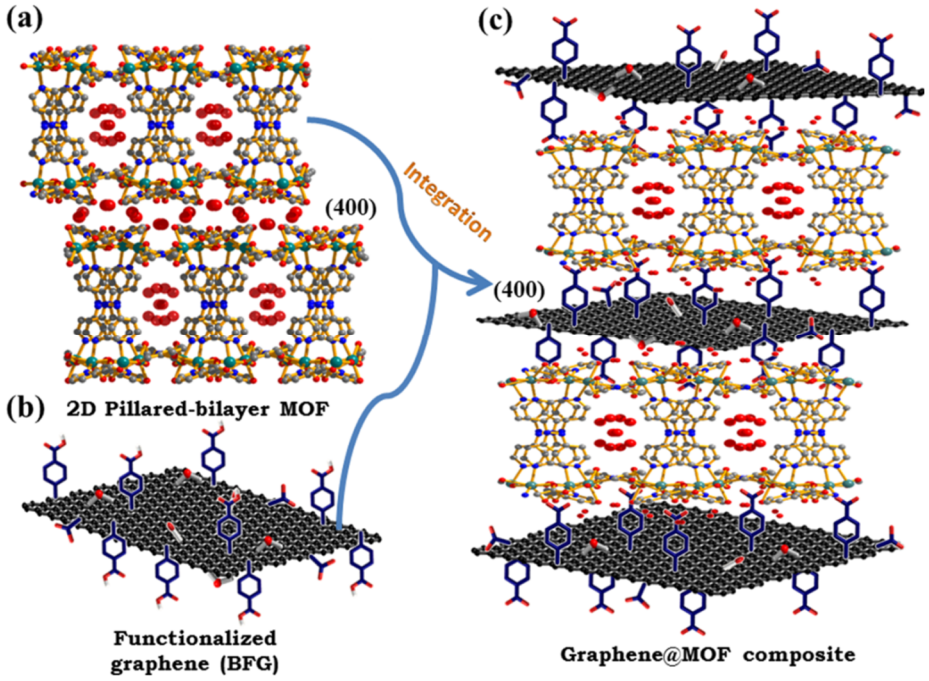

Scheme 1. Schematic representation of intercalation of 2D Cd-PBM between functionalized graphene sheets.

Convex type 1-D water filled channels with a window of ~ 3.5 × 8.8 $Å^2$ dimension are formed along the crystallographic *c* axis due to the azpy pillars arranged in a cris-cross and canted fashion due to π-π interaction. The 2D coordination spaces between two consecutive pillared-bilayer networks are occupied by the guest water molecules. The framework structure thus consists of two different adsorbate accessible spaces, 1D channel and 2D space in the interlayer region. The MOF-graphene composites, GO@Cd-PBM and BFG@Cd-PBM were prepared by mixing the solutions containing the metal ion and ligands with dispersions containing 10 wt. % of GO or BFG (See experimental section 3.3 for details).

Powder X-ray diffraction (PXRD) patterns of the composites BFG/GO@Cd-PBM show all the Bragg's reflections (monoclinic space group) of Cd-PBM (Figure 1) and also a shift in the (400) reflection corresponding to the 2D interlayer spacing to a higher angle compared to the pristine MOF. The shift can be related to the distortion of the lattice of Cd-MOF, probably due to the intercalation of the 2D bilayer network between the GO or BFG sheets. Furthermore, the functional groups present on the graphene surface can participate in hydrogen bonding with the MOF through the water molecules and carboxylate oxygen providing extra stability to the composite (see figure 2 for the IR spectra of functionalized graphene (GO and BFG)). BFG shows a stronger band in the IR spectrum at 1715 cm^{-1} (C=O) than GO indicating a high density of carboxyl groups on the surface after benzoic acid immobilization (Figure 2). Figure 3(I) show the infrared spectra of Cd-PBM, GO@Cd-PBM,

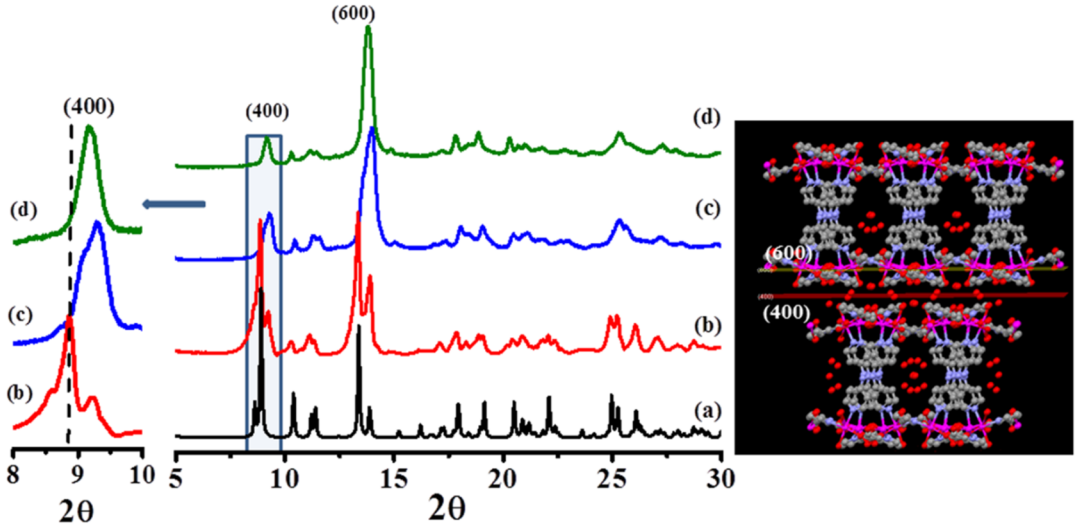

Figure 1. PXRD pattern of (a) simulated Cd-PBM, (b) As-synthesized Cd-PBM, (c) BFG@Cd-PBM and (d) GO@Cd-PBM.

and BFG@Cd-PBM. The bands at 1580 cm^{-1} and 1400 cm^{-1} can be attributed to the asymmetric and symmetric stretches of the carboxylate group respectively. The composites GO@Cd-PBM and BFG@Cd-PBM show similar ν_s(COO) and ν_{as}(COO) stretching frequencies. Raman spectroscopy provides a useful measure of the homogeneity and authenticity of the nanocarbon composites.[14] The Raman spectrum of pristine Cd-PBM shows bands associated with the various vibration modes of the pyrdc and azpy ligands (Figure 3(II)). The composites GO@Cd-PBM and BFG@Cd-PBM show bands associated

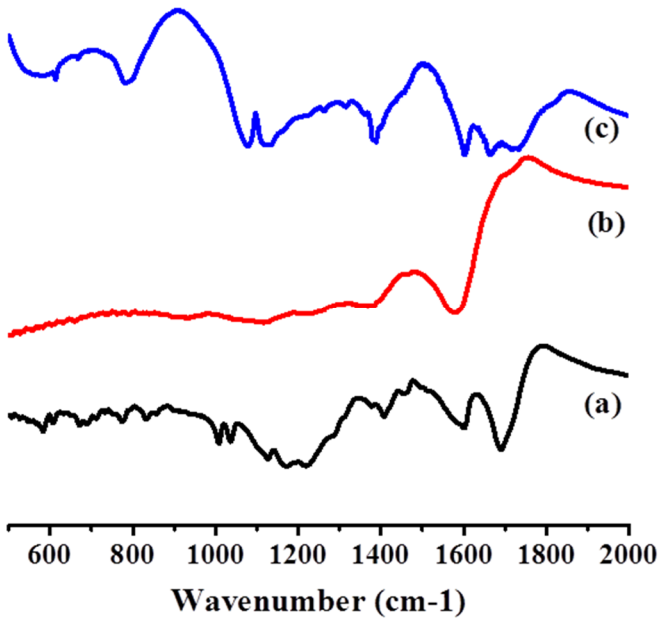

Figure 2. Infrared spectra of (a) BFG (black), (b) RGO (red) and (c) GO (blue).

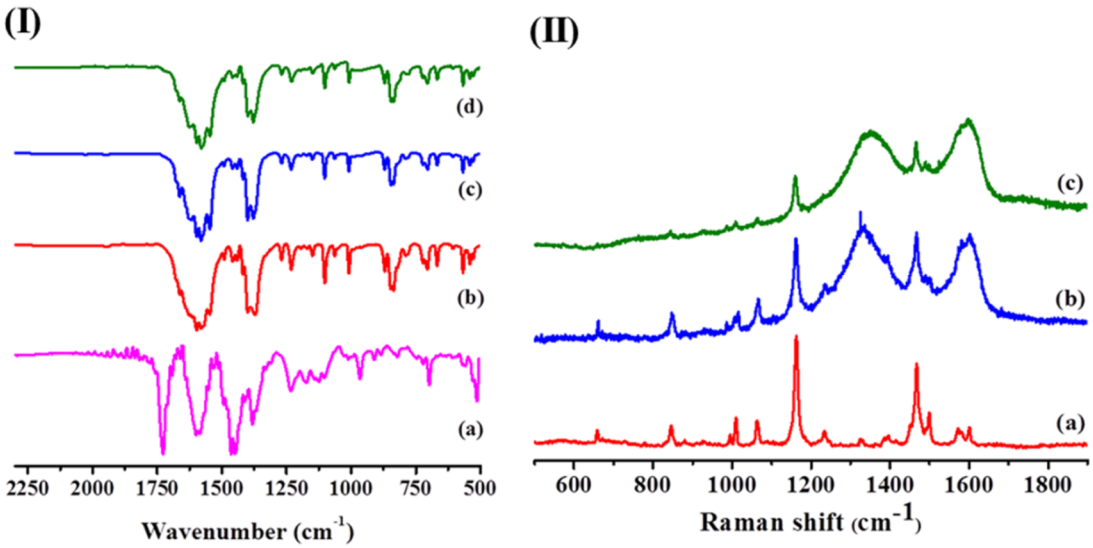

Figure 3. (I) Infrared spectra of (a) Exfoliated BFG@Cd-PBM (magenta) (b) Cd-PBM (red), (c) BFG@Cd-PBM (blue) and (d) GO@Cd-PBM (olive). (II) Raman spectra of (a) Cd-PBM (red), (b) BFG@Cd-PBM (blue) and (c) GO@Cd-PBM (olive).

with the MOF, in addition to bands at 1340 cm^{-1} and 1595 cm^{-1} due to the *D* and *G* bands of graphene, the *G* band slightly overlapping with the 1600 cm^{-1} band of the MOF. Thermogravimetric analysis of Cd-PBM, GO@Cd-PBM, and BFG@Cd-PBM (Figure 4) reveals first weight loss around 115 °C due to the loss of water molecules, the composites show stability up to 280 °C, without further weight loss.

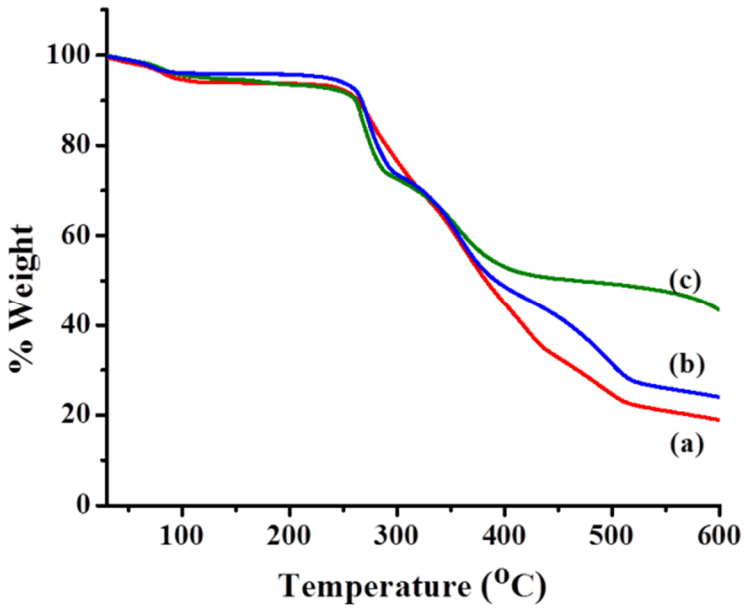

Figure 4. Thermogravimetric analysis of (a) Cd-PBM (red), (b) BFG@Cd-PBM (blue) and (c) GO@Cd-PBM (olive) at a heating rate 5 °C min^{-1} under N_2 atmosphere.

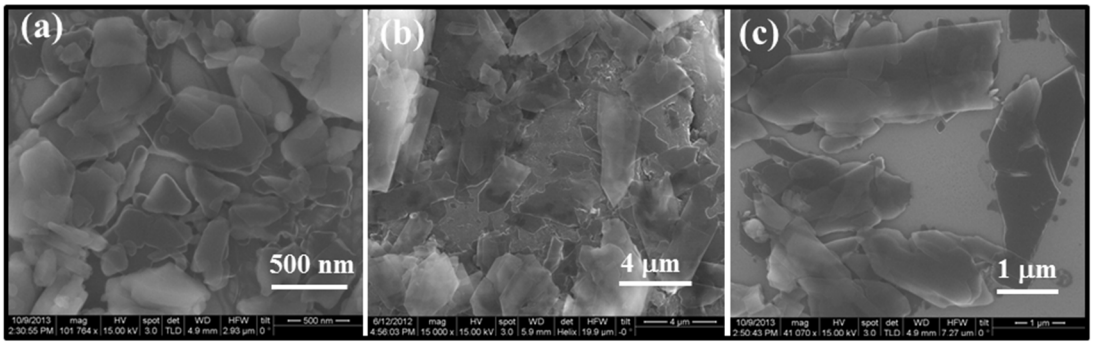

Figure 5. SEM images of (a) Cd-PBM, (b) BFG@Cd-PBM and (c) GO@Cd-PBM showing an increase in the lateral dimension of crystals in composites in comparison to pristine MOF.

The morphology and homogeneity of the composites were examined by scanning and transmission electron microscopy (SEM and TEM respectively) and atomic force microscopy (AFM). The SEM images of Cd-PBM show well-separated crystals with an average size between 300 nm – 700 nm. The composites unveil plate-like morphology (1 μm – 3 μm) with larger lateral dimension compared to pristine Cd-PBM. The bigger crystal size in composites can be attributed to the growth of 2D MOF on graphene sheets with larger lateral dimension (Figure 5). TEM images of BFG exhibit wrinkles and folding on the edges while those of

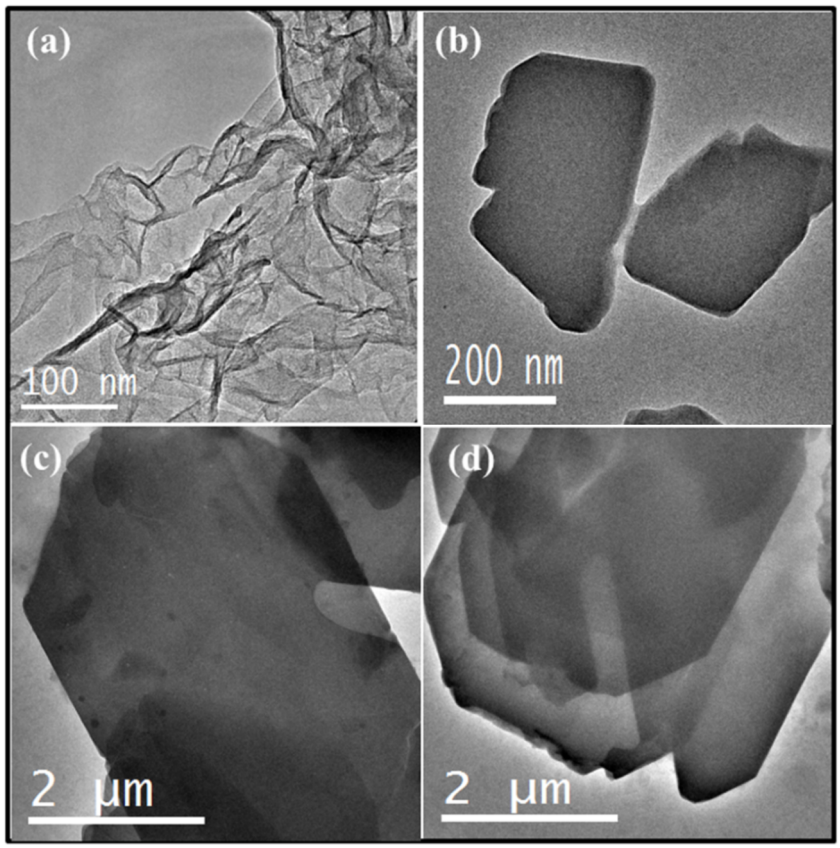

Figure 6. TEM images of (a) BFG, (b) Cd-PBM, (c) BFG@Cd-PBM, (d) GO@Cd-PBM.

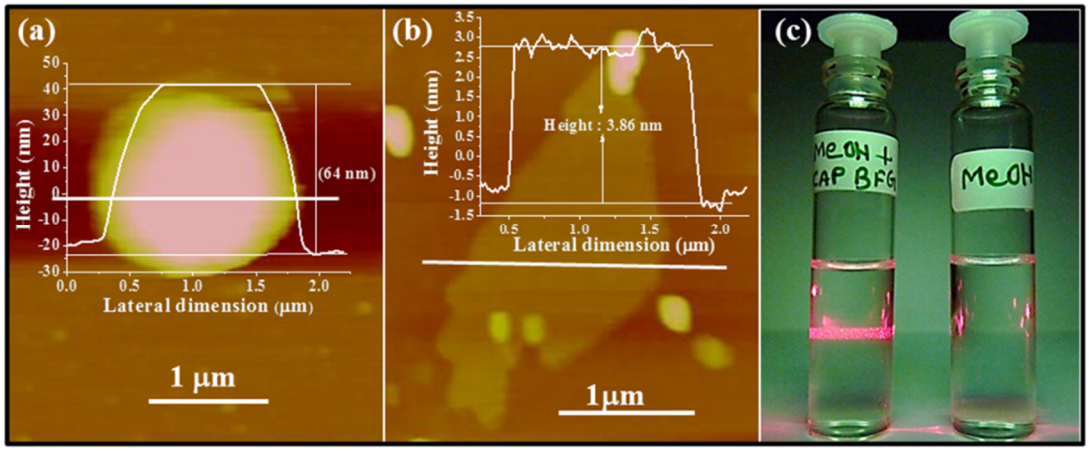

Figure 7. AFM height profile of (a) BFG@Cd-PBM (Height = 64 nm). (b) BFG@Cd-PBM after exfoliation (Height = 3.86 nm). (c) (Left) The colloidal dispersion of BFG@Cd-PBM showing Tyndall effect; (Right) Methanol.

GO@Cd-PBM and BFG@Cd-PBM consist of the uniform plate-like morphology arranged in layers (Figure 6). The detailed microscopic investigation showed no unreacted graphene sheets or MOF particles in the composites confirming the composites to be uniform and homogeneous. The functionalized 2D graphene sheets are very good support for the growth of 2D MOF layers. The epitaxial growth of 2D MOF layers is facilitated by the chemical bond formation of the metal ion with the oxygen functionalities present on the graphene basal plane.

Atomic force microscope images of the composites have been used to determine the number of layers. The images of BFG@Cd-PBM and GO@Cd-PBM show average height between 50 nm - 80 nm (see figure 7a). Considering that the average thickness of pillared bilayer galleries is ~ 1.5 nm and the thickness of few layer functionalized graphene (GO and BFG) is between 1 nm to 1.5 nm, a single layer of the 2D pillared bilayers on the graphene

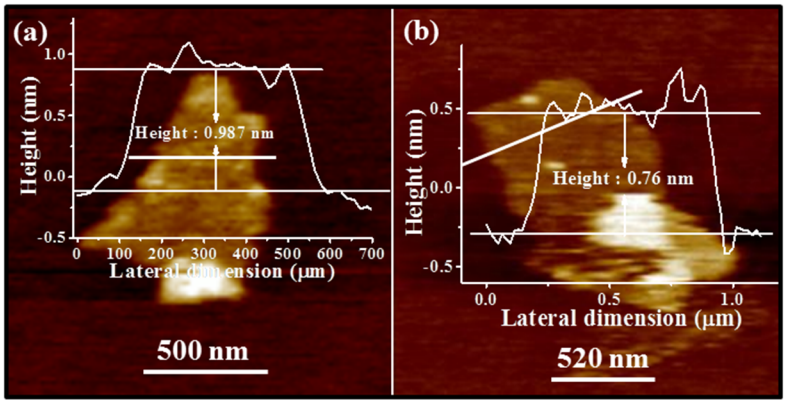

Figure 8. AFM height profile of (a) GO (average height = 0.987 nm) and (b) BFG (average height = 0.76 nm).

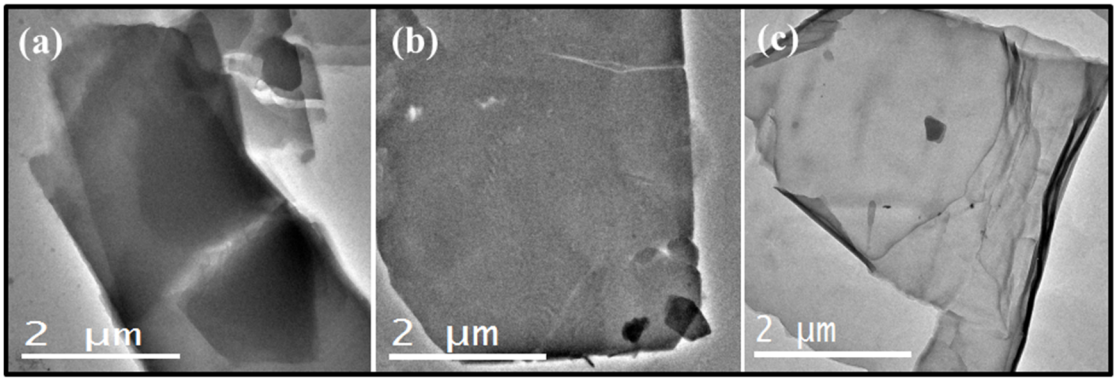

Figure 9. TEM images of (a) BFG@Cd-PBM, (b) GO@Cd-PBM and (c) Partially exfoliated BFG@Cd-PBM after 30 min sonication in MeOH.

sheets will have an average thickness of 2.5 nm to 3 nm. This thickness corresponds to 20 to 30 stacked layers of MOF and GO/BFG. The BFG@Cd-PBM on exfoliation by ultrasonication in methanol yields layers with an average thickness between 3.4 nm to 4.6 nm (Figure 7b). The infrared spectrum of exfoliated BFG@Cd-PBM (Figure 3) shows a band at 1725 cm^{-1} due to C=O stretching of non-coordinated carboxylate on BFG basal plane. The colloidal dispersion of exfoliated sheets was stable for a month and showed Tyndall effect due to the scattering of light (Figure 7c).

The parent MOF Cd-PBM exhibits typical type-I adsorption profile for CO_2 (at 195 K, 1 atm) suggesting the microporous nature of the framework (Figure 10). The amount of CO_2 uptake is 43 ml at $P/P_0 \sim 1$. It shows high selectivity for CO_2 at 195 K among (N_2, O_2, H_2, Ar, and CH_4).[9] The CO_2 adsorption isotherms of BFG@Cd-PBM and GO@Cd-PBM show two-step uptake with large hysteresis which is remarkably different from Cd-PBM. In the first step, up to $P/P_0 \sim 0.5$ GO@Cd-PBM and BFG@Cd-PBM show an uptake of ~ 12 ml and ~ 14 ml of CO_2 respectively, followed by the second step, with a final uptake of 30 ml and 34 ml respectively at $P/P_0 \sim 1$(Figure 10). As synthesized Cd-PBM contains 1D nanochannels (~ 3.5 × 8.8 $Å^2$) and kinetic diameter of CO_2 (3.3 Å) is very close to the 1D channel dimension, therefore CO_2 diffuse into the 1D pore resulting in CO_2 selectivity. The diffusion barrier is overcome by the interaction of CO_2 molecules with the –N=N– and –COO functional groups present on the wall of 1D channel. The stepwise gradual uptake and large hysteresis in the composites GO@Cd-PBM and BFG@Cd-PBM compared to the Cd-PBM are attributed to distortion in the MOF structure resulting in contraction of the 1D channel. Contracted channel will increase the diffusion barrier, therefore smaller amount and gradual CO_2 uptake are observed in the composite. Similarly, there will be diffusion barrier in the release of CO_2, which results in hysteresis in the adsorption profile. Similar to Cd-PBM, both the composites,

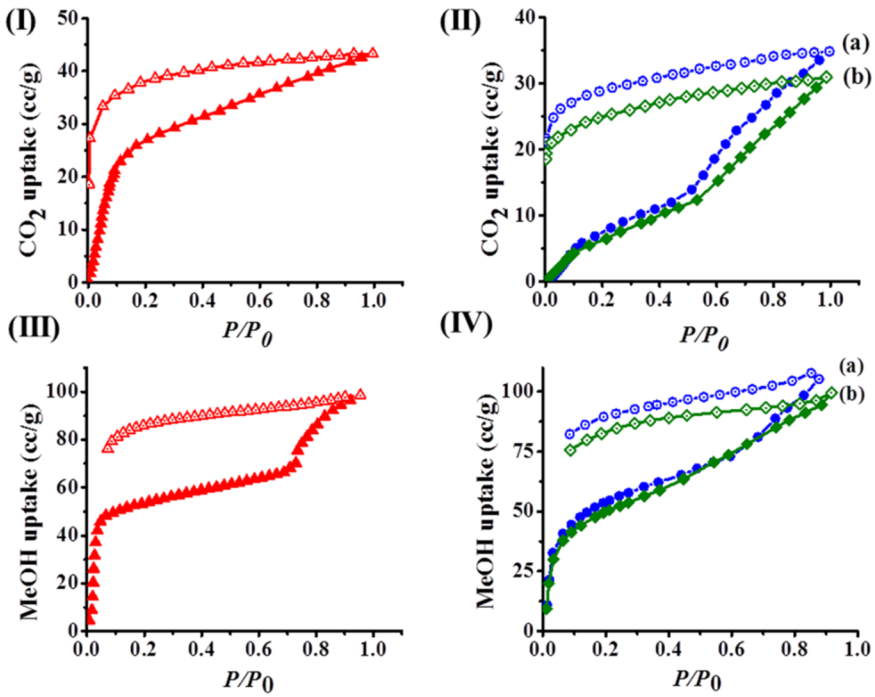

Figure 10. CO_2 sorption isotherm of (I) Cd-PBM (red triangles), (II a) BFG@Cd-PBM (blue circles) and (II b) GO@Cd-PBM (olive diamond). Methanol sorption isotherm of (III) Cd-PBM (red triangles), (IV-a) BFG@Cd-PBM (blue circles), (IV b) GO@Cd-PBM (olive diamond).

BFG@Cd-PBM and GO@Cd-PBM, show negligible N_2 uptake (Figure 11). This selectivity for CO_2 over N_2 has implications for the separation of CO_2 from post-combustion flue gas.[12,15] To support the hypothesis of contracted channels due to intercalation, the H_2O (at 298 K) and methanol (MeOH; at 293 K) adsorption profiles were measured (Figure 10 and 12). Cd-PBM shows two-step adsorption profiles for H_2O and MeOH which can be related to adsorption in two different nano space. The first step correlates to the accommodation of

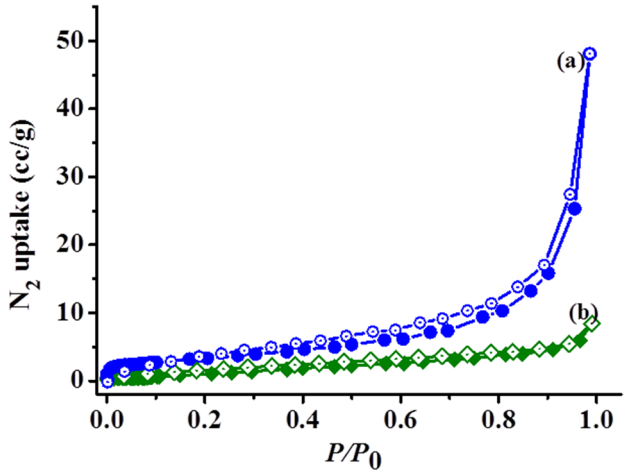

Figure 11. N_2 adsorption isotherm of (a) BFG@Cd-PBM (blue circles) and (b) GO@Cd-PBM (olive diamond) at 77 K and 1 atm.

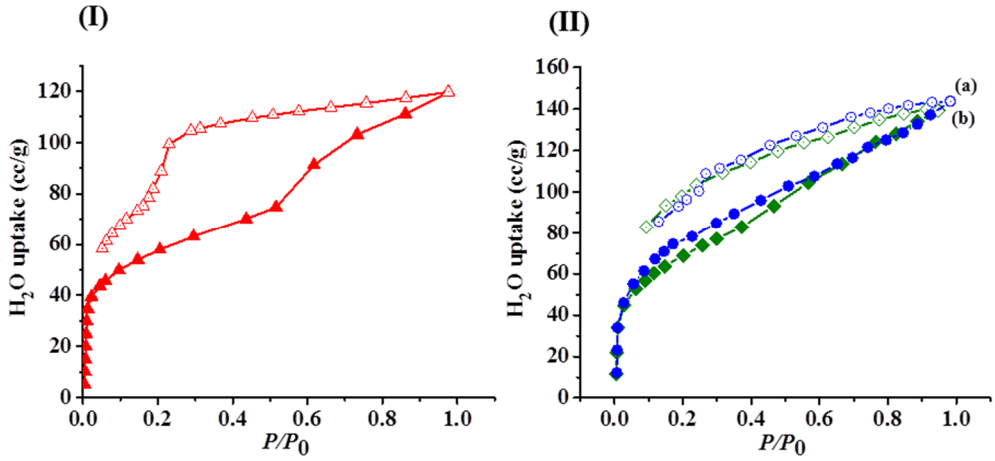

Figure 12. (I) Water sorption isotherm of Cd-PBM (II a) BFG@Cd-PBM (blue circles) and (II b) GO@Cd-PBM (olive diamond) at 298 K.

molecules in the 1D channels and the second step to the encapsulation in the 2D interlayer space. The MOF@graphene composites reveal only one-step type-I profiles for MeOH and H_2O suggesting that the 2D interlayer space no longer exists, being occupied by the 2D graphene sheets. The higher uptake can arise from the presence of polar groups on the graphene. Further, the adsorption profile of same weight ratio physical mixture containing functionalized graphene and Cd-PBM was also carried out as a control sample. The adsorption profile had the same feature as pristine Cd-PBM confirming that adsorption property is dominated by pristine MOF. The observed changes in the adsorption profile and PXRD patterns of BFG@Cd-PBM and GO@Cd-PBM are due to face by face assembly of 2D graphene and MOF layers facilitated by the chemical bond formation at MOF-graphene interface.

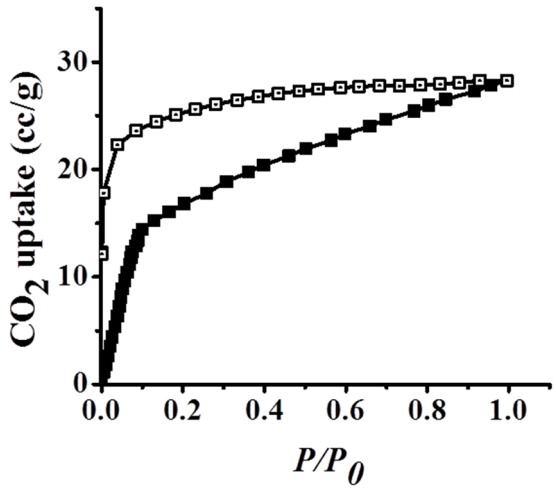

Figure 13. CO_2 sorption isotherm of a physical mixture containing 10 wt% BFG (benzoic acid functionalized graphene) and Cd-PBM at 195 K.

3.5 Conclusions

In conclusion, the present study has enabled the epitaxial growth of 2D MOF nano-sheets on two different functionalized graphene. The functional groups on GO and BFG help to stabilize the 2D-MOF nanocrystals on the graphene surface. The resulting composites BFG@Cd-PBM and GO@Cd-PBM have been characterized by spectroscopic and microscopic techniques and exhibit unique two-step CO_2 uptake profile with large hysteresis. The uptake in the two composites is comparable to that of the pristine MOF. Present study suggests that it is possible to fabricate a variety of composites of MOFs on graphene surfaces possessing novel applications.

References

[1] a) A. K. Geim and K. S. Novoselov, *Nat. Mater.* **2007**, *6*, 183; b) C. N. R. Rao, A. K. Sood, K. S. Subrahmanyam and A. Govindaraj, *Angew. Chem. Int. Ed.* **2009**, *48*, 7752; c) C. N. R. Rao and A. K. Sood in *Graphene*, *Vol.* Wiley-VCH, Weinheim, **2012**; d) L. Dai, *Acc. Chem. Res.* **2012**, *46*, 31.

[2] a) H. He, T. Riedl, A. Lerf and J. Klinowski, *J. Phys. Chem.* **1996**, *100*, 19954; b) A. Lerf, H. He, M. Forster and J. Klinowski, *J. Phys. Chem. B* **1998**, *102*, 4477; c) W. Cai, R. D. Piner, F. J. Stadermann, S. Park, M. A. Shaibat, Y. Ishii, D. Yang, A. Velamakanni, S. J. An, M. Stoller, J. An, D. Chen and R. S. Ruoff, *Science* **2008**, *321*, 1815.

[3] a) R. Kumar, K. Jayaramulu, T. K. Maji and C. N. R. Rao, *Chem. Commun.* **2013**, *49*, 4947; b) P. V. Kamat, *J. Phys. Chem. Lett.* **2009**, *1*, 520; c) M. Jahan, Q. Bao and K. P. Loh, *J. Am. Chem. Soc.* **2012**, *134*, 6707; d) D. Li, L. Qiu, K. Wang, Y. Zeng, T. Williams, Y. Huang, M. Tsapatsis and H. Wang, *Chem. Commun.* **2012**, *48*, 2249.

[4] a) H. Li, M. Eddaoudi, M. O'Keeffe and O. M. Yaghi, *Nature* **1999**, *402*, 276; b) A. K. Cheetham and C. N. R. Rao, *Science* **2007**, *318*, 58; c) D. Britt, D. Tranchemontagne and O. M. Yaghi, *Proc. Natl. Acad. Sci. USA* **2008**, *105*, 11623; d) J. Della Rocca, D. Liu and W. Lin, *Acc. Chem. Res.* **2011**, *44*, 957; e) A. Dhakshinamoorthy, M. Alvaro and H. Garcia, *Chem. Commun.* **2012**, *48*, 11275; f) A. K. Cheetham, C. N. R. Rao and R. K. Feller, *Chem. Commun.* **2006**, 4780.

[5] a) S. Kitagawa, R. Kitaura and S.-i. Noro, *Angew. Chem. Int. Ed.* **2004**, *43*, 2334; b) J.-R. Li, R. J. Kuppler and H.-C. Zhou, *Chem. Soc. Rev.* **2009**, *38*, 1477; c) N. L. Rosi, J. Eckert, M. Eddaoudi, D. T. Vodak, J. Kim, M. O'Keeffe and O. M. Yaghi, *Science* **2003**, *300*, 1127; d) J. L. C. Rowsell and O. M. Yaghi, *Angew. Chem. Int. Ed.* **2005**, *44*, 4670; e) R. Sathre and E. Masanet, *RSC Advances* **2013**, *3*, 4964.

[6] M. Jahan, Q. Bao, J.-X. Yang and K. P. Loh, *J. Am. Chem. Soc.* **2010**, *132*, 14487.

[7] a) C. Petit and T. J. Bandosz, *Adv. Funct. Mater.* **2010**, *20*, 111; b) B. Levasseur, C. Petit and T. J. Bandosz, *ACS Appl. Mater. Interfaces* **2010**, *2*, 3606; c) C. Petit and T. J. Bandosz, *Adv. Funct. Mater.* **2011**, *21*, 2108.

[8] a) A. Bétard and R. A. Fischer, *Chem. Rev.* **2012**, *112*, 1055; b) L. E. Kreno, K. Leong, O. K. Farha, M. Allendorf, R. P. Van Duyne and J. T. Hupp, *Chem. Rev.* **2012**, *112*, 1105.

[9] a) M. Zhang, G. Feng, Z. Song, Y.-P. Zhou, H.-Y. Chao, D. Yuan, T. T. Y. Tan, Z. Guo, Z. Hu, B. Z. Tang, B. Liu and D. Zhao, *J. Am. Chem. Soc.* **2014**, *136*, 7241; b) H. Walch, J. Dienstmaier, G. Eder, R. Gutzler, S. Schlögl, T. Sirtl, K. Das, M. Schmittel and M. Lackinger, *J. Am. Chem. Soc.* **2011**, *133*, 7909; c) L. Wang, M. Yang, Z. Shi, Y. Chen and S. Feng, *J. Solid State Chem.* **2005**, *178*, 3359; d) B. Mandal and P. Sarkar, *PCCP* **2015**, *17*, 17437; e) S. Huh, S. Jung, Y. Kim, S.-J. Kim and S. Park, *Dalton Trans.* **2010**, *39*, 1261; f) Y. Wang, B. Bredenkotter, B. Rieger and D. Volkmer, *Dalton Trans.* **2007**, 689; g) C. N. R. Rao, S. Natarajan and R. Vaidhyanathan, *Angew. Chem. Int. Ed.* **2004**, *43*, 1466.

[10] a) E. V. Brown and G. R. Granneman, *J. Am. Chem. Soc.* **1975**, *97*, 621; b) O. Theilmann, W. Saak, D. Haase and R. d. Beckhaus, *Organometallics* **2009**, *28*, 2799.

[11] W. S. Hummers and R. E. Offeman, *J. Am. Chem. Soc.* **1958**, *80*, 1339.

[12] P. Kanoo, R. Sambhu and T. K. Maji, *Inorg. Chem.* **2010**, *50*, 400.

[13] P. Kanoo, G. Mostafa, R. Matsuda, S. Kitagawa and T. Kumar Maji, *Chem. Commun.* **2011**, *47*, 8106.

[14] a) M. S. Dresselhaus, *Phys. Scr.* **2012**, *2012*, 014002; b) M. S. Dresselhaus, A. Jorio and R. Saito, *Annu. Rev. Condens. Matter Phys.* **2010**, *1*, 89.

[15] a) S. Horike, D. Tanaka, K. Nakagawa and S. Kitagawa, *Chem. Commun.* **2007**, 3395; b) D. Bradshaw, J. B. Claridge, E. J. Cussen, T. J. Prior and M. J. Rosseinsky, *Acc. Chem. Res.* **2005**, *38*, 273.

Chapter 4: Quenching of lanthanide emission in the composite of graphene with a Bi-based MOF

Summary

Effect of graphene on the optical properties of lanthanide-based graphene-MOF hybrid composites has been investigated. Graphene is found to be a very efficient quencher of lanthanide emission. For this purpose, hybrid composites of a bismuth-based MOF [Bi(1,4-bdc)$_2$].(dma) (where 1,4-bdc = Benzene-1,4-dicarboxylate anion, dma = dimethyl ammonium cation) doped with lanthanide ions were prepared with different proportions of benzoic acid functionalized graphene (BFG). A large decrease in the luminescence intensity is observed even with a very small concentration (2 wt%) of benzoic acid functionalized graphene (BFG). The quantum yield decreased from 50 % to 1.4 % in case of Tb-doped samples. A similar effect of huge quenching in the photoluminescence (PL) emission was observed in Eu-doped and Eu/Tb codoped samples. On subsequent addition of higher concentration of functionalized graphene, a small decrease in luminescence intensity and hence fluorescence quenching was observed. The observed fluorescence quenching is further supported by the decrease in PL emission lifetime. The observed quenching of lanthanide emission is attributed to excited state energy/charge transfer from bdc ligand to graphene which perturbs the energy transfer from ligand to lanthanide metal ion. Even very small concentration of graphene is sufficient to quench lanthanide emission very effectively.

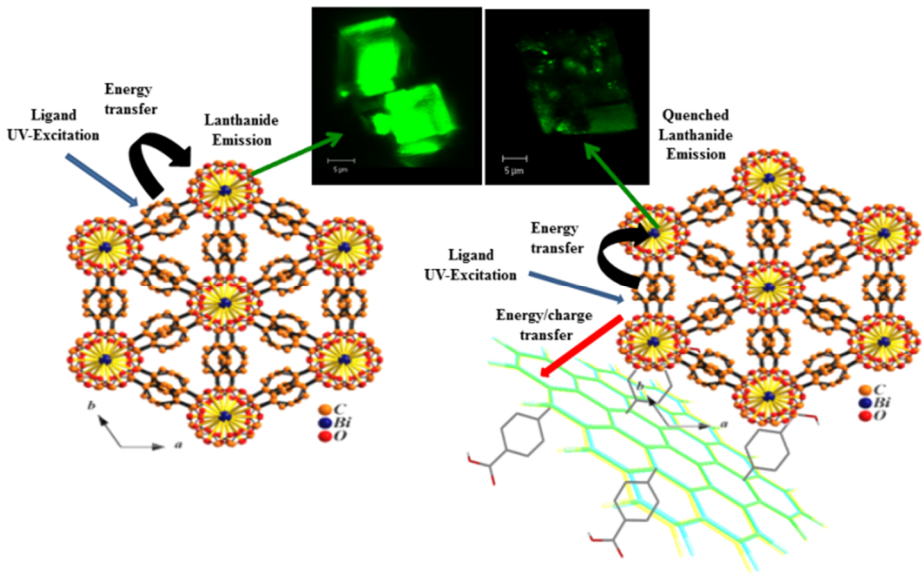

4.1 Introduction

Graphene possesses interesting electronic, optical, mechanical, chemical and other properties as mentioned earlier in the thesis.[1] Fluorescence quenching is one of the important properties of graphene and has been utilized in sensing biomolecules and visualization of graphene sheets on various substrates.[2] Interaction of graphene and various chemically modified forms of graphene with semiconductor nanoparticles and dye molecules has been studied to understand the mechanism of fluorescence quenching.[3] Lanthanide-based metal-organic frameworks (MOFs) have been studied for their optical, magnetic and catalytic property.[4] Bi^{3+} based frameworks have been recently investigated as hosts for lanthanide ions with interesting optical properties.[5] Lanthanide-based phosphors and metal organic frameworks have promising optoelectronic applications. Since graphene and various modified forms of graphene have been utilized for various optical and optoelectronic applications, [6] lanthanide-based hybrid graphene composites with metal organic framework was synthesized. Interaction of graphene with lanthanide-based frameworks and its effect on quenching lanthanide emission is largely unexplored. A detailed study of the optical properties of graphene and lanthanide-based MOF composites has been undertaken. For this purpose, the bismuth-based framework $[Bi(1,4\text{-bdc})_2]\cdot(dma)$ (BDC) [1,4-bdc = Benzene-1,4-dicarboxylate anion, dma = dimethyl ammonium cation] with lanthanide ion doping was utilized.[5b] The lanthanide doped framework shows strong luminescence corresponding to rare earth emission due to the very efficient ligand to rare earth ion energy transfer. In order to make uniform composites and provide coordination center to the metal ions, graphene basal plane was functionalized with benzoic acid (BFG).[7] Optical properties of BFG-Ln doped BDC composites are investigated in this chapter using photoluminesce spectroscopy, emission lifetime and quantum yield measurements.

4.2 Scope of the present investigations

Due to the shielding of 4f orbitals lanthanide-based metal–organic frameworks have narrow emission and high color purity.[4a,8] The shielded 4f orbital ensures narrow and characteristic 4f–4f transitions and are less sensitive to the chemical environment around the lanthanide ion. The antenna effect of organic linkers enhances the lanthanide emission making it a promising material for sensing, optical and optoelectronic applications.[4a,b,9] Doping a framework structure with few mol% of lanthanides removes the chance of self–quenching of lanthanide emission and decrease the need of costly lanthanide precursors,

making it promising for large-scale synthesis and bulk commercial optical and optoelectronic applications.[5b,10] Graphene with its electrical and optical properties is considered a material of importance for optoelectronic applications.[6a,11] Forming a uniform composite of lanthanide-based MOFs with graphene will ensure electrical conductivity[7] and new optical properties are expected as the graphene sheets are known to quench the emission by charge or energy transfer process.[3b,12] The present chapter investigates graphene−MOF composites of Eu/Tb doped Bi-based MOF $[Bi(1,4\text{-bdc})_2]\cdot(dma)$ (BDC) [1,4-bdc = Benzene-1,4-dicarboxylate anion, dma = dimethyl ammonium cation]. The present study focuses mainly on the effect of graphene on lanthanide emission. Graphene was observed to be very efficient quencher of lanthanide emission due to the energy or charge transfer from the aromatic linker to graphene which perturbs the energy transfer process to the emitting lanthanide centers. The long range resonance energy transfer in graphene has d^{-4} dependence which ensures the fluorescence quenching by graphene to significant distances that can't be reached with normal molecular donor–acceptor pairs, for which energy transfer decreases d^{-6}.[12b] This has a significant effect when graphene is incorporated in the framework structure with very efficient quenching of lanthanide emission. The present study of quenching of lanthanide emission by graphene may find applications in designing lanthanide-based graphene composite materials for optoelectronic applications.

4.3 Experimental section

Chemicals used in the synthesis were of high purity and obtained from commercial sources.

Synthesis of graphite oxide: Graphite oxide was prepared using a modified Hummers and Offeman method. In an ice bath 75 ml conc. H_2SO_4, 1.5 g graphite powder, and 1.5 g $NaNO_3$ were added and stirred for10 min to make a uniform mixture. To this mixture, 10 g $KMnO_4$ was slowly added. The reactants were allowed to mix properly then transferred to an oil bath maintained at 40 °C and stirred for 45 min. Oxidation of graphite powder occurred and dark brown colored viscous product formed. In the reaction mixture 75 ml distilled water was slowly added followed by stirring for another 15 min at 70 °C. Brown color suspension formed. The temperature was then raised to 80 °C followed by the addition of 15 ml H_2O_2 in 150 ml warm water (~70 °C). Colour of suspension changed from dark brown to yellow. Obtained product was centrifuged then washed repeatedly with distilled water to remove excess acid. The product was again dispersed in water and dialyzed for 24 hours to remove

any residual acid. GO suspension was then centrifuged to remove excess water. Obtained solid product was transferred to a petri dish and kept under vacuum at room temperature for drying.

Reduction of graphite oxide: Obtained graphite oxide was dispersed in water and reduced using $NaBH_4$ according to the procedure reported in the literature.[7] In a round bottom flask, 400 mg of GO was dispersed in 320 ml water by sonication. The pH was adjusted to10 by adding 5% Na_2CO_3 solution. Then, the dispersion was stirred at 90 °C for 9 hours. The pH was again checked using a pH meter and adjusted to 10. Then, 3.2g $NaBH_4$ in 80 ml H_2O was added to dispersion under constant stirring, with the temperature maintained at 80 °C. The dispersion was stirred for next 3 hours. The color of dispersion changed from dark brown to black accompanied by outgassing. The final product was filtered and washed several times with water and ethanol and dried under vacuum.

Benzoic acid functionalization of graphene (BFG): Benzoic acid functionalization of graphene was obtained by reacting the RGO dispersion with 4-carboxybenzenediazonium chloride. The diazonium salt was synthesized *in situ* from 4-aminobenzoic acid. In 80 ml water 960 mg, 4-aminobenzoic acid and 280 mg NaOH (7 mmol) were added. In the solution, 526 mg $NaNO_2$ and 6 ml 20% HCl (6.4 M, 19.2 mmol) were added with the temperature maintained at 0 °C and stirred for 45 min. The color of the solution changed to pale yellow due to the formation of the diazonium salt. RGO (300 mg) was dispersed in water by sonication in 1 wt% sodium dodecylbenzenesulfonate (SDBS) solution. RGO dispersion was added to the diazonium salt solution and stirred at 0°C for 4 hours. Then, the ice bath was removed and stirred for another 4 hours at room temperature. The resulting dispersion was filtered and washed with the ethanol-water mixture, ethanol, and acetone to remove the surfactant properly. TEM images of RGO and characterization of RGO and BFG are given in Figure 2.1.

BDC {Bi(1,4-bdc)$_2$.dma} and BDCG graphene composites: Benzoic acid functionalized graphene was dispersed in 5 ml *N, N*-dimethylformamide (DMF) by sonication for 45 mins. Benzoic acid functional group present of graphene helps in dispersing graphene sheets in DMF. A stable colloidal dispersion of BFG was obtained. To the colloidal dispersion of BFG, $Bi(NO_3)_3.5H_2O$ (0.3 mmol), 1,4-H_2bdc (1.5 mmol, Benzene-1,4-dicarboxylic acid), Him (1.2 mmol, Imidazole) and DMF were added and allowed to stir for 30 min to form a homogeneous mixture. The homogeneous mixture was sealed in a 23 ml stainless steel reactor

with a PTFE liner and heated at 100 °C for 72 hours, then cooled to room temperature. 10 mol% Eu^{3+}, Tb^{3+}, and 5 mol% each Eu^{3+}/Tb^{3+}doped BDC/BFG composites were obtained by replacing stoichiometric amounts of Eu/Bi and Tb/Bi nitrates. BDC and rare earth doped BDC were obtained by the same procedure without adding functionalized graphene. The product was filtered, washed with DMF and acetone and dried at room temperature under vacuum.

Physical measurements: Powder X-ray diffraction (PXRD) pattern of all samples was recorded in Bruker D8 X-ray diffractometer with Cu Kα radiation. Raman spectra were recorded using Jobin Yvon LabRam HR spectrometer with 632.8 nm HeNe laser in backscattering geometry. Infrared spectra were recorded on a Bruker IFS 66v/S using KBr pellets. Thermogravimetric analysis (TGA) was carried out on Mettler Toledo TGA850 instrument with a heating rate of 10 °C/min in air. Scanning electron microscope (SEM) images were obtained from Nova Nano SEM 600, FEI Company. Transmission electron microscope images of samples were obtained with a JEOL JEM 3010 microscope operating at an accelerating voltage of 300 kV. Photoluminescence measurements of solid samples were carried out using Flurolog-3 spectrophotometer from Horiba Jobin Yvon. PL measurements of solid samples were done by taking approximately equal amount of sample and placing between quartz plates. Illumination area of the sample was kept constant during measurement. Lifetime measurements were carried out on Edinburgh PL spectrometer using pulsed Xenon lamp.

4.4 Results and discussion

Reduced graphene oxide (RGO) obtained by sodium borohydride reduction of graphene oxide (see experimental section 4.3 for details) show a strong peak at 1577 cm^{-1} due to C=C bond vibration (Figure 1 (I)). In benzoic acid functionalized graphene (BFG) strong peak at 1691 cm^{-1} is due to COOH groups of benzoic acid attached to graphene basal plane. The peak at 1600 cm^{-1} in BFG is due to C=C stretching vibration (Figure 1(I)). UV-Visible absorption spectra of GO, RGO and BFG were collected by dispersing in water. GO showed absorption maxima at 227 due to $\pi \rightarrow \pi*$ transition (Figure 1(II)). In RGO $\pi \rightarrow \pi*$ transition absorption maxima peak was red shifted to 250 nm due to partial recovery of conjugation after reduction. Red shift in $\pi \rightarrow \pi*$ was also observed in BFG with the absorption maximum at 247nm (Figure 1(II)). TEM image of reduced graphene oxide (RGO) used for the benzoic

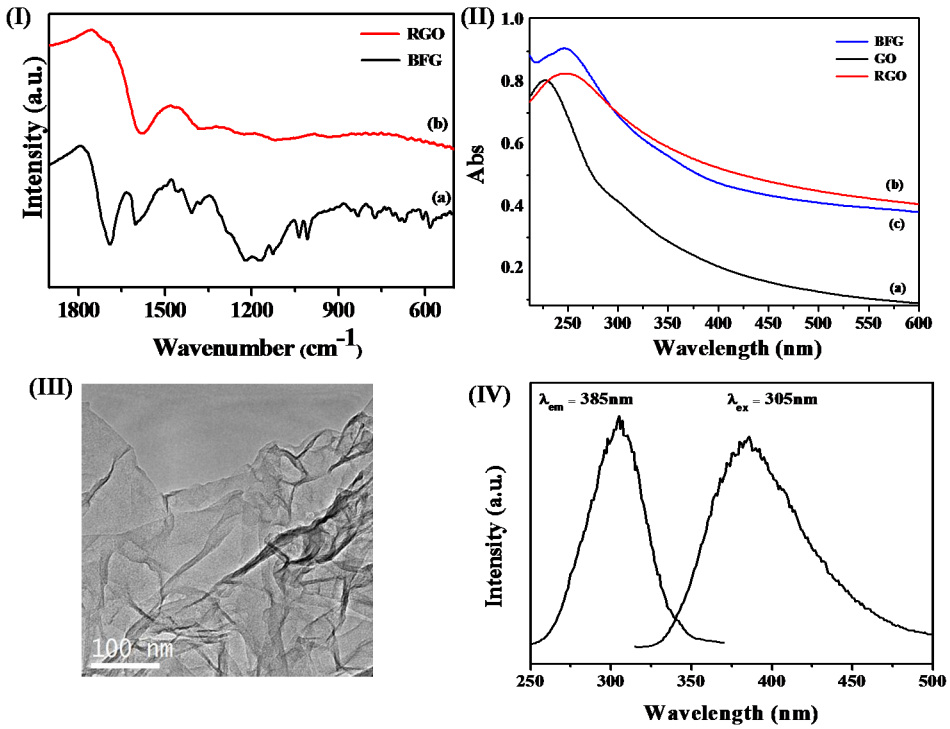

Figure 1. (I) Infrared spectra of (a) RGO (red) and (b) BFG (Black). **(II)** UV- Visible absorption spectra of (a) GO (black), (b) RGO (red) and (c) BFG (blue). **(III)** TEM image of RGO. **(IV)** PL excitation and emission spectra of BFG.

acid functionalization of graphene is given in figure 1(III). RGO synthesized using sodium borohydride as reducing agent were agglomerated due to strong π-π interaction between graphene sheets. PL excitation and emission spectrum of BFG is given in figure 1(IV).

The $[Bi(1,4\text{-}bdc)_2]\cdot(dma)$ (BDC) [1,4-bdc = Benzene-1,4-dicarboxylate anion, dma = dimethyl ammonium cation] and BDC graphene composites BDCG with different concentration of graphene and Eu/TB doping was synthesized using solvothermal route. The samples were prepared with three different benzoic acid functionalized graphene (BFG) concentration 3 wt% (BDC3G), 6 wt% (BDC6G) and 9 wt% (BDC9G). BDC host framework and corresponding composites were doped with 10 mol % Eu, 10 mol % Tb and 5 mol % Eu/ 5 mol % Tb respectively. Obtained BDC and BDCG were characterized with powder X-ray diffraction (Figure 2) to check phase purity and were consistent with the simulated pattern. No change was observed in PXRD pattern between BDC and BDCG. BDC crystallizes in rhombohedral *R-3c* space group with two crystallographically different Bi^{3+} cation. Two different Bi^{3+} sites B1 and B2 correspond to twelve and nine coordination with a stereochemically inactive lone pair of electrons. The dma cation occupies space between the

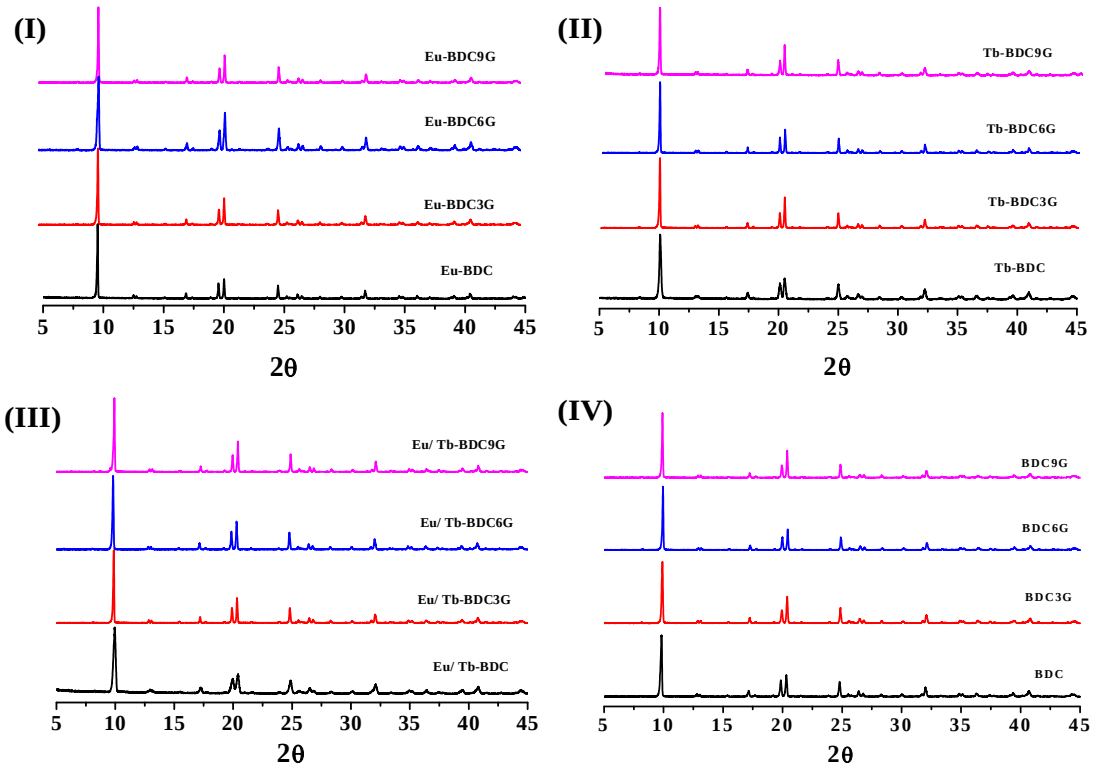

Figure 2. PXRD pattern of lanthanide doped BDC and BDCG. **(I)** Eu-doped BDC and BDCG. **(II)** Tb doped BDC and BDCG. **(III)** Eu/Tb doped BDC and BDCG. **(IV)** undoped BDC. 3G, 6G, and 9G correspond to 3 wt%, 6 wt% and 9 wt% of functionalized graphene respectively. BDC 3G, 6G, and 9G composites are represented in black, red, blue and magenta respectively.

bdc anion by hydrogen bonding interaction with the oxygen atom of the carboxylate group. Overall the framework forms a dense structure without any void space.

Raman spectroscopy gives an important insight on the homogeneity and quality of nanocarbon composites.[13] Figure 3 show the Raman spectra of BFG, BDC, and BDCG. Raman spectra were collected in backscattering geometry using 632.8 nm He-Ne laser by focusing on an individual cube-shaped crystals. BFG shows characteristic *D* and *G* band at 1330 cm^{-1} and 1593 cm^{-1} respectively. Peaks at 631 cm^{-1}, 836 cm^{-1} and 874 cm^{-1} in BDC and BDCG can be assigned to out of plane deformation modes of the C-H bond in benzene ring of 1,4-bdc ligand. Peaks at 1425 cm^{-1} and 1607 cm^{-1} are due to the stretching modes of carboxylate groups and symmetric benzene ring stretching vibration.[14] In addition to the Raman modes corresponding to BDC, characteristic *D* and *G* bands of graphene at 1330 cm^{-1} and 1593 cm^{-1} were observed in BDCG. The *G* band at 1593 cm^{-1} merged with 1607 cm^{-1} peak. The intensity of the *D* and *G* bands increased from BDC3G to BDC6G and BDC9G which is consistent with increasing graphene concentration.

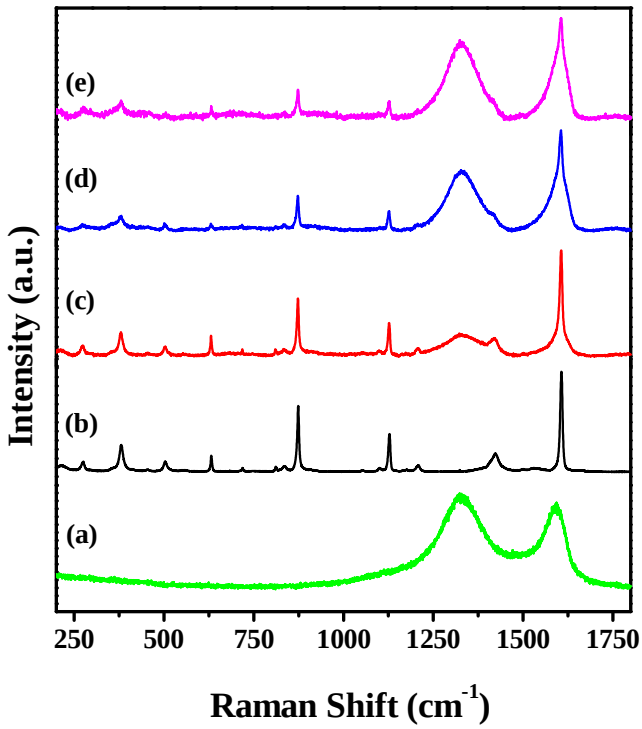

Figure 3. Raman spectra of (a) Benzoic acid functionalized graphene (BFG) (b) Eu-doped BDC (c) Eu-BDC3G (d) Eu-BDC6G and (e) Eu-BDC9G. Eu-doped BDC 3G, 6G, and 9G correspond to 3 wt%, 6 wt% and 9 wt% of functionalized graphene respectively.

Scanning electron microscope (SEM) images of BDC and BDCG (Figure 4) showed cube-shaped morphology for both BDC and BDCG. No significant change in morphology was observed for graphene composites in comparison to pure MOF. The BDC and BDCG crystals were very uniform with cubic morphology and average size variation between 5 μm to 10 μm. An important role of pH was observed in the morphology of BDC crystals. In an acidic environment, BDC1 crystallized in thin approximately 1μm plate-shaped crystals with a

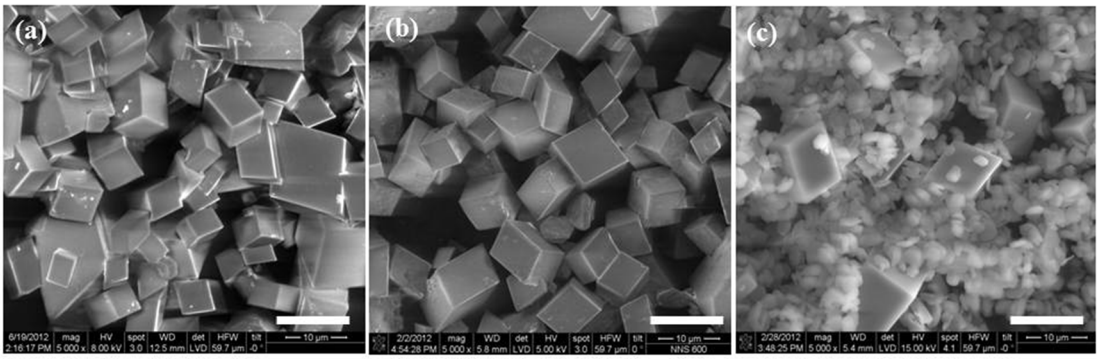

Figure 4. SEM images of (a) Eu-BDC (b) Eu-BDC9G (c) Eu-BDC in acidic condition. Scale bar corresponds to 10 μm.

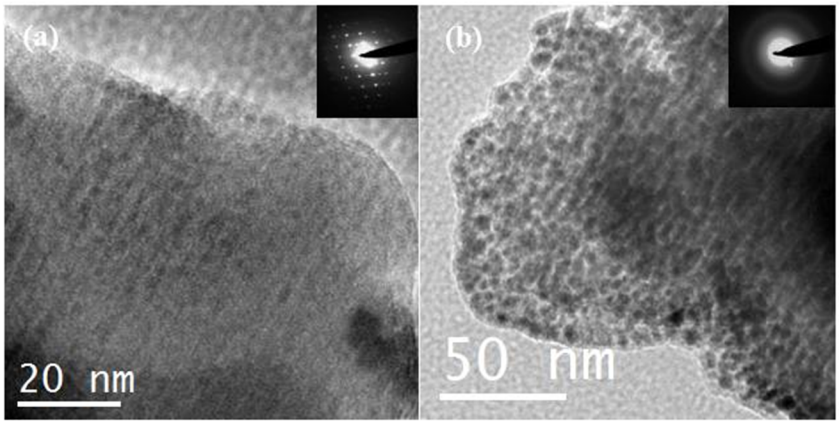

Figure 5. TEM images of (a) Eu-BDC9G and (b) Eu-BDC9G after grinding and 45 min sonication.

small concentration of cubic morphology crystals. In the presence of functionalized graphene even in acidic environment always cube-shaped crystals formed which may be due to functionalized graphene sheets acting as nucleation center for the growth of MOF crystals Transmission electron microscope (TEM) images of composites are given in figure 5. BDCG composites were highly crystalline and electron diffraction pattern was observed. When the crystals were ground and sonicated for 45 min uniform cubic structure collapsed and approximately 10 nm MOF particles strongly agglomerated and supported by graphene sheet was observed.

Thermogravimetric analysis of BDC and different concentration graphene composites BDCG showed two-step weight loss (Figure 6). First weight loss near 300 °C is due to the

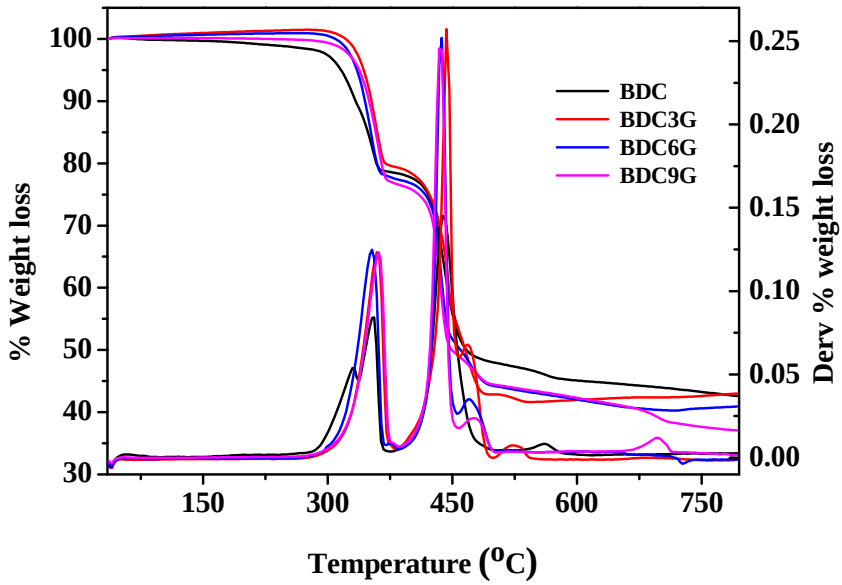

Figure 6. Thermogravimetric analysis of BDC and BDCG. TGA was carried out at a heating rate of 10 °C in air.

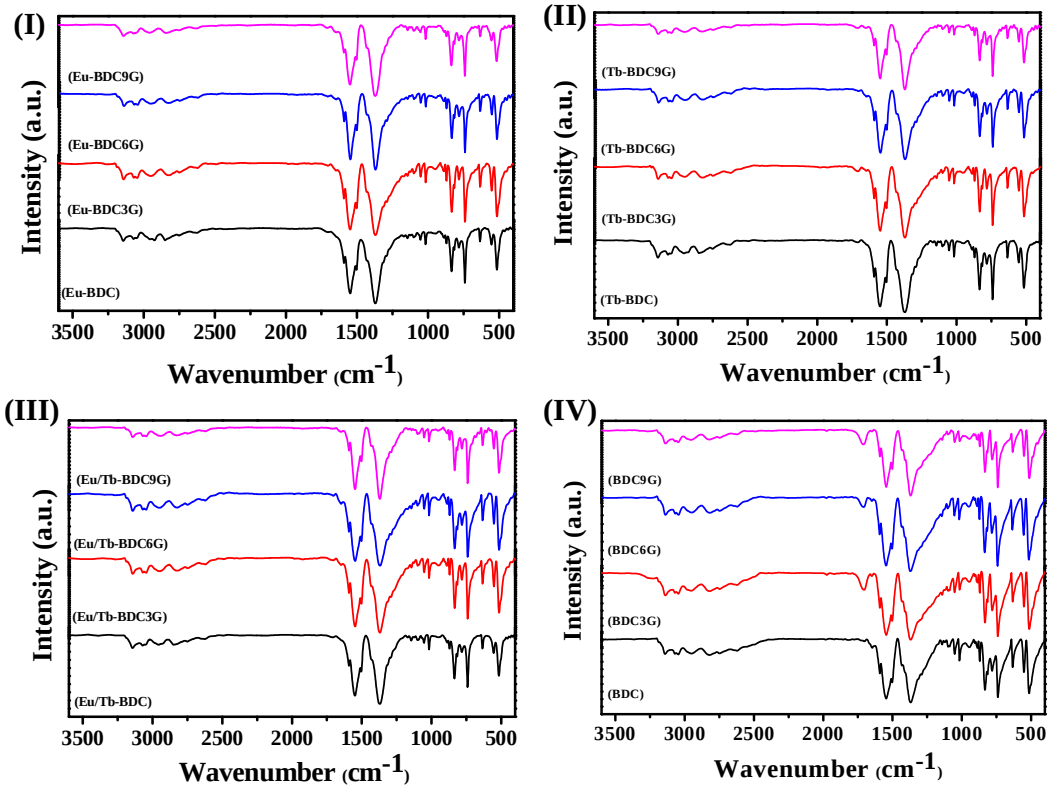

Figure 7. Infrared spectra of lanthanide doped BDC and BDCG. **(I)** Eu-doped BDC and BDCG. **(II)** Tb doped BDC and BDCG. **(III)** Eu/Tb doped BDC and BDCG. **(IV)** undoped BDC. 3G, 6G, and 9G correspond to 3 wt%, 6 wt%, and 9 wt% of functionalized graphene respectively. BDC 3 G, 6 G, and 9 G composites are represented in black, red, blue and magenta respectively.

loss of DMF molecules and second weight loss at 400 °C is due to the decomposition of framework structure. TGA showed similar thermal stability for BDCG and BDC. Thermal stability of graphene MOF composites (BDCG) shows that composites are homogeneous with high thermal stability. Infrared spectra of all the compounds are given in figure 7.

Figure 8 show the photoluminescence spectrum of BDC, BDCG, and rare earth doped BDCG. Very efficient fluorescence quenching of lanthanide emission was observed. BDC showed broad emission with a maximum at approximately 490 nm on excitation at 345 nm. This broad emission spectrum is due to Intra ligand luminescence or charge-transfer transitions. On addition of first 3 wt% of BFG large decrease in emission intensity was observed followed by a small decrease in intensity on subsequent addition of 6 wt% and 9 wt% functionalized graphene. Eu-doped BDC showed a very strong characteristic peak at 615 nm corresponding to $^5D_0 \rightarrow {}^7F_2$ transition at 335 nm excitation wavelength. Low-intensity peaks at 583 nm, 592 nm, and 695 nm can be attributed to $^5D_0 \rightarrow {}^7F_J$ (J = 0, 1, 4) transitions. The low-intensity peak at 583 nm due to $^5D_0 \rightarrow {}^7F_0$ suggests that Eu^{3+} occupy a low symmetry

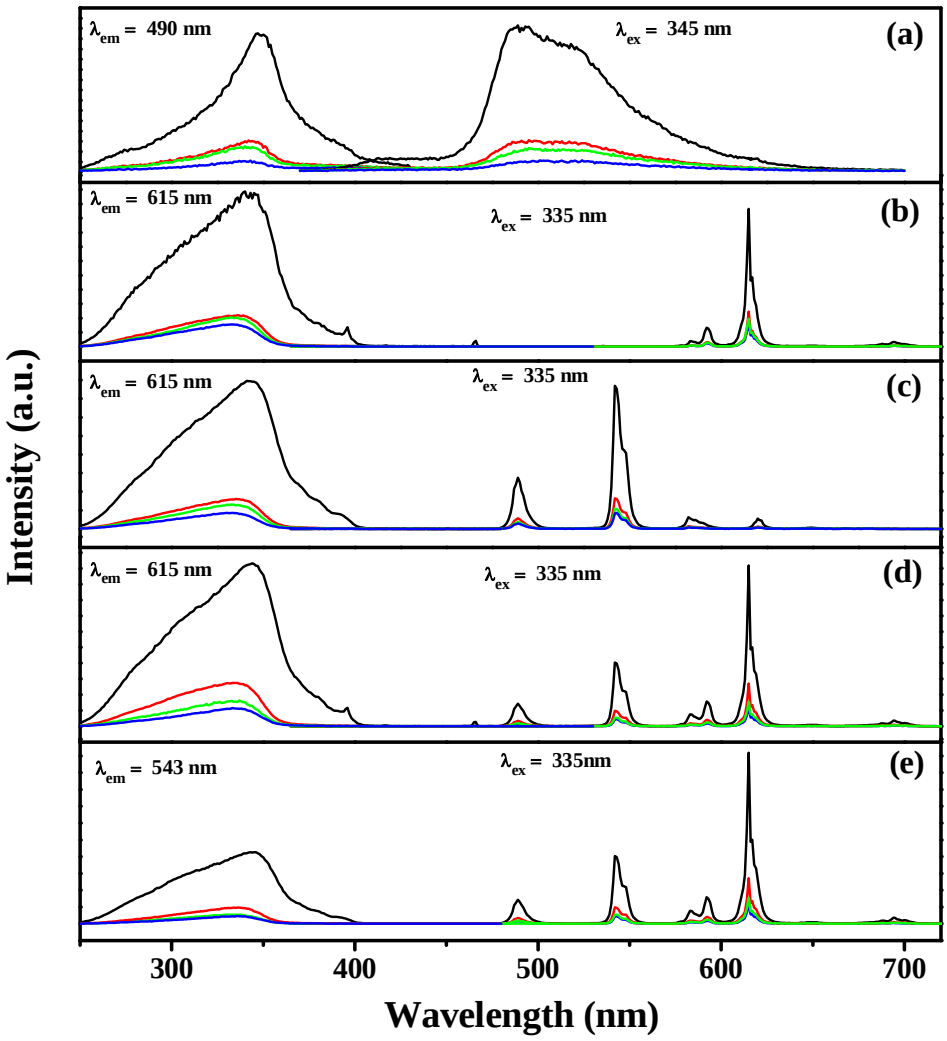

Figure 8. PL excitation and emission spectra of **(a)** BDC (black), BDC3G (red), BDC6G (green) and BDC9G (blue) **(b)** Eu-BDC (black), Eu-BDC3G (red), Eu-BDC6G (green) and Eu-BDC9G (blue) **(c)** Tb-BDC (black), Tb-BDC3G (red) and Tb-BDC6G (green) and Tb-BDC9G (blue) **(d,e)** Eu/Tb-BDC (black), Eu/Tb-BDC3G (red), Eu/Tb-BDC6G (green) and Eu/Tb-BDC9G (blue) with excitation spectra monitored at 615 nm and 543 nm corresponding to Eu^{3+} and Tb^{3+} respectively.

site without an inversion center.[15] The asymmetric ratio of $^5D_0 \rightarrow {}^7F_2/{}^5D_0 \rightarrow {}^7F_1$ transition was 6.2, which indicates that Eu^{3+} ion occupies the highly asymmetric site.[16] With the addition of first 3 wt% functionalized graphene strong quenching of Eu^{3+} emission was observed followed by a small decrease in emission intensity on subsequent addition of 6 wt% and 9 wt% functionalized graphene. Tb doped BDC showed sharp emission peaks at 489 nm, 543 nm, 582 nm and 620 nm due to $^5D_4 \rightarrow {}^7F_J$ (J = 6, 5, 4, 3) transitions at 335 nm excitation wavelength. The peak at 543 nm due to $^5D_4 \rightarrow {}^7F_5$ is the most intense peak. Similar to Eu-doped BDC very strong quenching of Tb emission was observed on the addition of first 3 wt% functionalized graphene followed by a slight decrease in emission intensity for samples

containing 6 wt% and 9 wt% functionalized graphene. Eu and Tb co-doped samples showed emission peaks corresponding to Tb^{3+} at 489 nm and 543 nm due to $^5D_4 \rightarrow {}^7F_J$ (J = 6, 5) transitions. Peaks at 583 nm, 592 nm, 615 nm and 695 nm are due to $^5D_0 \rightarrow {}^7F_J$ (J = 0, 1, 2, 4) transitions of Eu^{3+} at 335 nm excitation. In addition to the observed peaks very weak intensity peak at 649 nm due to $^5D_0 \rightarrow {}^7F_3$ transition is also present in Eu-doped and Eu/Tb codoped samples but is not observable due to very high intensity of 615 nm electric-dipole transition. Observed lanthanide emission quenching in Eu/Tb co-doped samples due to excited state interactions with graphene were similar to Eu and Tb-doped samples. The emission band of the Intra ligand luminescence was not observed in the emission spectra of all the rare earth doped compounds suggesting very efficient energy transfer from ligand to rare earth ions. Lanthanide ion emission was strong and red, green and orange emission can be observed with the naked eye for Eu, Tb, and Eu/Tb doped BDC respectively.

Figure 9 show the images of lanthanide doped BDC and BDC3G samples corresponding to 3 wt% of functionalized graphene under UV light. Quenching of rare earth emission can be easily observed. Strong luminescence of lanthanide doped BDC shows that bismuth-based framework is an efficient host for lanthanide ions in designing high quantum efficiency phosphors.

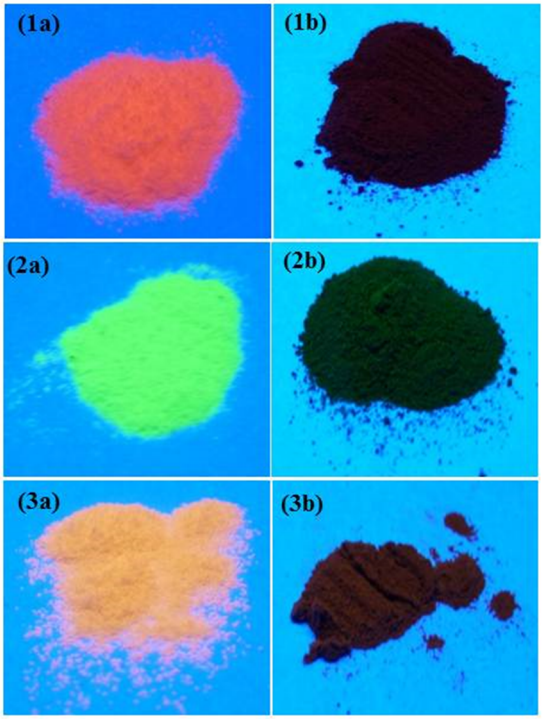

Figure 9. Figure (1a, b) Eu-BDC and Eu-BDC3G; (2a, b) Tb-BDC and Tb-BDC3G; **(**3a, b) Eu/Tb-BDC and Eu/Tb-BDC3G on UV light excitation. 3G corresponds to 3 wt% of benzoic acid functionalized graphene.

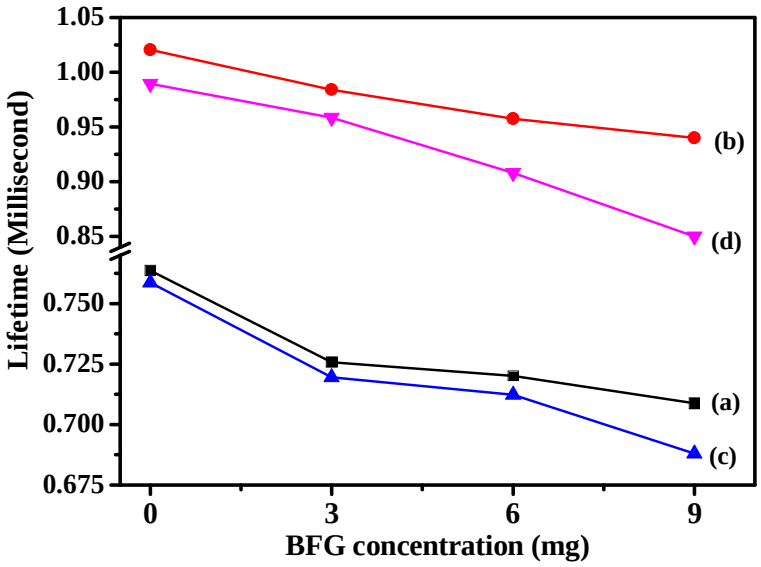

Figure 10. Lifetime value with increasing functionalized graphene concentration (a) Eu-doped (black) (b) Tb doped (red) (c, d) Eu/Tb codoped samples corresponding to Eu (615 nm, blue) and Tb (543 nm, magenta) emission respectively.

Table 1 Lifetime value of lanthanide doped BDC and BDC graphene composites with increasing graphene concentration.

Sample name	Eu doped (λ_{em} = 615 nm) Lifetime (ms)	Tb doped (λ_{em} = 543 nm) Lifetime (ms)	Eu/Tb doped (λ_{em} = 615 nm) Lifetime (ms)	Eu/Tb doped (λ_{em} = 543 nm) Lifetime (ms)
BDC	0.763	1	0.76	0.98
BDC3G	0.725	0.98	0.72	0.95
BDC6G	0.72	0.95	0.71	0.9
BDC9G	0.7	0.93	0.68	0.85

Consistent with observed quenching of rare earth emission, fluorescence decay measurement showed a decrease in the lifetime of emission in rare earth doped graphene-MOF composites. Figure 10 show the lifetime trend of rare earth doped BDC and BDCG samples. The $^5D_0$ decay time of Eu-doped samples were monitored using the strongest $^7F_2$ component at 615 nm using excitation wavelength of 335 nm. The lifetime of Eu-BDCG decreases with increasing BFG concentration which is consistent with observed quenching of Eu emission. The $^5D_4$ decay time of Tb-doped samples was monitored using $^7F_5$ component at 543 nm. Both $^5D_0$ and $^5D_4$ decay time corresponding to Eu^{3+} and Tb^{3+} were monitored for Eu/Tb codoped samples. The $^5D_0$ and $^5D_4$ decay time corresponding to Eu^{3+} and Tb^{3+} co-doping were monitored using $^7F_2$ and $^7F_5$ transitions respectively. Similar to Eu-doped samples

lifetime decreased in Tb-doped and Eu/Tb co-doped BDCG with increasing BFG concentration. The decrease in lifetime is consistent with observed quenching in Eu and Tb emission. Lifetime value of lanthanide doped BDC and BDCG are given in table 1.

Composites of semiconductor nanoparticle with graphene oxide and carbon nanotube show quenching of semiconductor nanoparticle emission.[3a,17] Similar behavior of graphene as a very efficient quencher for aromatic molecule fluorescence has been observed.[3b,18] Graphene and its various functionalized forms act as an electron acceptor and provide an additional non-radiative decay pathway.[3] Although charge transfer has been explained as one of the mechanism, fluorescence quenching of dye molecules has been observed at 4 nm distance which cannot be explained by charge transfer mechanism.[12a] Both energy transfer and charge transfer plays a role in fluorescence quenching property of graphene.[3,12] The high intensity of lanthanide (Eu, Tb) emission in BDC is due to efficient energy transfer from bdc anion to lanthanide ions on UV excitation. Energy transfer from photoexcited bdc anion to graphene may be responsible for observed quenching of rare earth emission. Charge transfer from photoexcited bdc anion to graphene cannot be ruled out due to the close proximity of bdc anion and graphene in the MOF crystal. Excited state charge transfer interaction between graphene and aromatic molecules has been observed in the earlier study. The observed quenching of rare earth emission can be explained by energy transfer and/or charge transfer from photoexcited bdc anion to graphene. Such excited state interactions perturb the

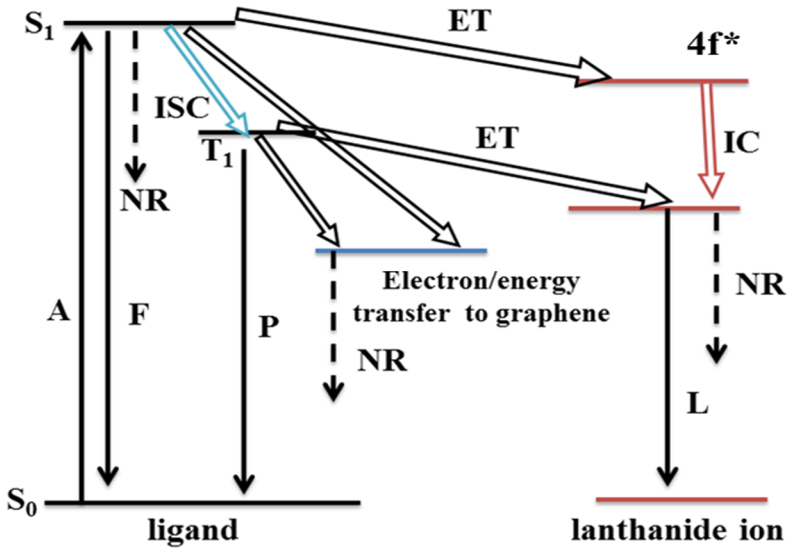

Figure 11. Energy level diagram of lanthanide doped BDC- graphene composite. Graphene provides an additional non-radiative decay pathway via electron/energy transfer. ET = energy transfer, ISC = Intersystem crossing, IC = internal conversion, F = fluorescence, P = phosphorescence, L = lanthanide emission, NR = non-radiative decay.

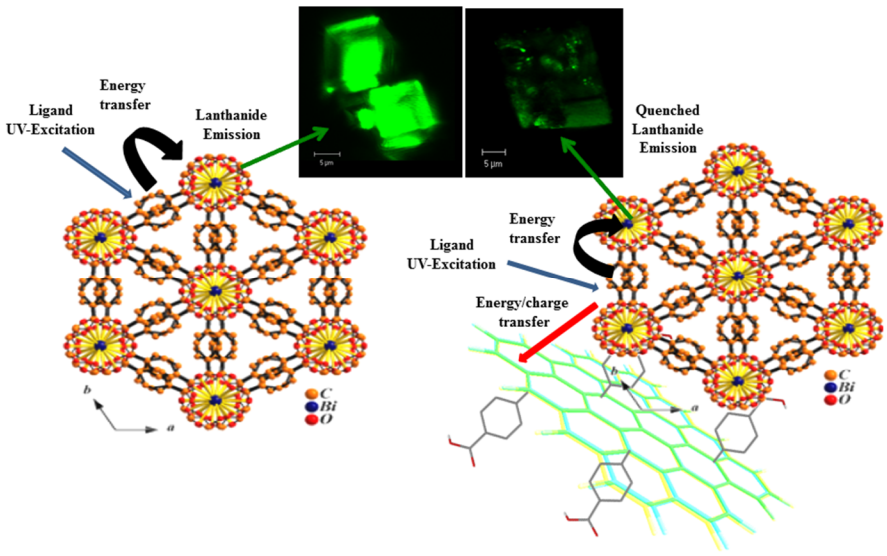

Scheme 1: Schematic representation of a mechanism for quenching of lanthanide emission in BDC graphene composites. The inset shows confocal images of Tb-BDC and Tb-BDC3G crystals on UV light excitation. Scale bar of inset figure 5 μm.

photoexcited energy transfer from bdc anion to lanthanide ion. Scheme 1 shows the schematic mechanism of energy/charge transfer responsible for quenching of lanthanide emission.

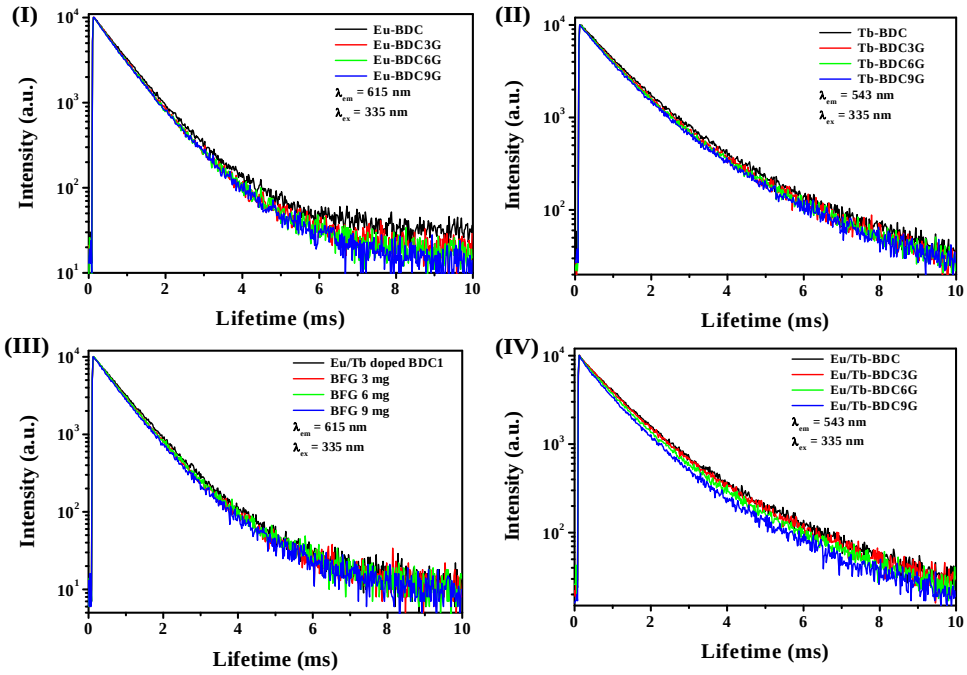

Figure 12. Decay curve of lanthanide doped BDC and BDCG. **(I)** Eu-doped BDC and BDCG **(II)** Tb doped BDC and BDCG **(III, IV)** Eu/Tb doped BDC monitored at 615 nm Eu emission and 543 nm Tb emission respectively. The excitation wavelength is 335 nm in all samples. Black, red, green and blue corresponds to BDC, BD3G, BDC6G and BDC9G composites respectively.

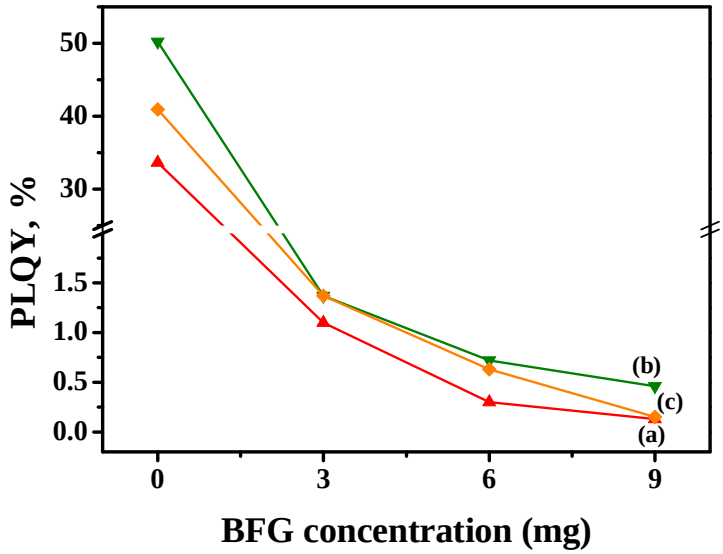

Figure 13. Quantum yield with increasing functionalized graphene concentration (a) Eu-doped BDC (b) Tb doped BDC and (c) Eu/Tb co-doped BDC samples.

Figure 13 show the quantum yield of lanthanide (Eu, Tb) doped BDC and BDCG. Lanthanide-doped BDC has a very high quantum yield of 50.23 %, 33.64% and 40.94 % for Tb-BDC, Eu-BDC, and Eu/Tb-BDC respectively. On the addition of first 3 wt% of BFG large decrease in quantum yield was observed. The quantum yield value decreased to 1.37 %, 1.1 %, and 1.37 % for Tb-BDC3G, Eu-BDC3G, and Eu/Tb-BDC3G respectively. On further addition of 6 wt% and 9 wt% BFG slight decrease in quantum yield was observed for lanthanide doped BDCG. Quantum yield value of lanthanide doped BDC and BDCG are given in table 2. Quantum yield data further confirms the very high efficiency of graphene in quenching rare earth emission.

Table 2. Quantum yield of lanthanide doped BDC and BDC graphene composites with increasing graphene concentration. Large decrease in quantum yield was observed with the first 3 wt% of functionalized graphene.

Sample name	Eu doped	Tb doped	Eu/Tb doped
BDC	33.6	50	41
BDC3G	1.1	1.4	1.4
BDC6G	0.3	0.7	0.6
BDC9G	0.13	0.5	0.2

4.5 Conclusions

Homogeneous graphene-MOF composites of $[Bi(1,4\text{-}bdc)_2]\cdot(dma)$ **(BDC)** doped with Eu and Tb with varying proportions of benzoic acid functionalized graphene (BDCG) were synthesized using a solvothermal route. Very strong quenching of the lanthanide emission is observed even for the very small concentration of the functionalized graphene. Lifetime measurements of lanthanide doped BDC and BDCG showed a decrease in a lifetime with increasing concentration of functionalized graphene consistent with the observed quenching of lanthanide emission. Lanthanide-doped BDC exhibits high quantum yields due to efficient energy transfer from the photoexcited bdc anion to the lanthanide ion. Even a small concentration of functionalized graphene decreased the quantum yield of lanthanide doped BDCG drastically. Photoluminescence, lifetime and quantum yield measurements establish that graphene is highly efficient in quenching lanthanide emission. Utilization of Bi^{3+} based frameworks in designing high quantum efficiency phosphors needs to be explored in detail. Our results on quenching of lanthanide emission will have applications in designing hybrid graphene and lanthanide-based composites for various optical and optoelectronic applications.

References

[1] a) C. N. R. Rao, A. K. Sood, K. S. Subrahmanyam and A. Govindaraj, *Angew. Chem. Int. Ed.* **2009**, *48*, 7752; b) K. E. Prasad, B. Das, U. Maitra, U. Ramamurty and C. N. R. Rao, *Proc. Natl. Acad. Sci. USA* **2009**, *106*, 13186; c) G. Eda and M. Chhowalla, *Adv. Mater.* **2010**, *22*, 2392.

[2] a) C.-H. Lu, H.-H. Yang, C.-L. Zhu, X. Chen and G.-N. Chen, *Angew. Chem. Int. Ed.* **2009**, *48*, 4785; b) E. Treossi, M. Melucci, A. Liscio, M. Gazzano, P. Samorì and V. Palermo, *J. Am. Chem. Soc.* **2009**, *131*, 15576; c) J. Kim, L. J. Cote, F. Kim and J. Huang, *J. Am. Chem. Soc.* **2009**, *132*, 260.

[3] a) G. Williams and P. V. Kamat, *Langmuir* **2009**, *25*, 13869; b) H. S. S. Ramakrishna Matte, K. S. Subrahmanyam, K. Venkata Rao, S. J. George and C. N. R. Rao, *Chem. Phys. Lett.* **2011**, *506*, 260.

[4] a) Y. Cui, Y. Yue, G. Qian and B. Chen, *Chem. Rev.* **2011**, *112*, 1126; b) B. V. Harbuzaru, A. Corma, F. Rey, P. Atienzar, J. L. Jordá, H. García, D. Ananias, L. D. Carlos and J. Rocha, *Angew. Chem. Int. Ed.* **2008**, *47*, 1080; c) A. K. Cheetham and C. N. R. Rao, *Science* **2007**, *318*, 58; d) J. W. Han and C. L. Hill, *J. Am. Chem. Soc.* **2007**, *129*, 15094; e) A. Thirumurugan, S. K. Pati, M. A. Green and S. Natarajan, *J. Mater. Chem.* **2003**, *13*, 2937.

[5] a) A. Thirumurugan, J.-C. Tan and A. K. Cheetham, *Cryst. Growth Des.* **2009**, *10*, 1736; b) A. Thirumurugan and A. K. Cheetham, *Eur. J. Inorg. Chem.* **2010**, *2010*, 3823.

[6] a) H. Chang and H. Wu, *Adv. Funct. Mater.* **2012**, n/a; b) X. Wan, Y. Huang and Y. Chen, *Acc. Chem. Res.* **2012**, *45*, 598.

[7] M. Jahan, Q. Bao, J.-X. Yang and K. P. Loh, *J. Am. Chem. Soc.* **2010**, *132*, 14487.

[8] a) A. K. Cheetham, C. N. R. Rao and R. K. Feller, *Chem. Commun.* **2006**, 4780; b) C. N. R. Rao, A. K. Cheetham and A. Thirumurugan, *J. Phys.: Condens. Matter* **2008**, *20*, 083202; c) M. D. Allendorf, C. A. Bauer, R. K. Bhakta and R. J. T. Houk, *Chem. Soc. Rev.* **2009**, *38*, 1330.

[9] a) E. G. Moore, A. P. S. Samuel and K. N. Raymond, *Acc. Chem. Res.* **2009**, *42*, 542; b) L. D. Carlos, R. A. S. Ferreira, V. de Zea Bermudez, B. Julian-Lopez and P. Escribano, *Chem. Soc. Rev.* **2011**, *40*, 536.

[10] a) P. Falcaro and S. Furukawa, *Angew. Chem. Int. Ed.* **2012**, *51*, 8431; b) A. Thirumurugan, J.-C. Tan and A. K. Cheetham, *Cryst. Growth Des.* **2010**, *10*, 1736.

[11] a) Y. Xu, Z. Liu, X. Zhang, Y. Wang, J. Tian, Y. Huang, Y. Ma, X. Zhang and Y. Chen, *Adv. Mater.* **2009**, *21*, 1275; b) W. Wei, T. He, X. Teng, S. Wu, L. Ma, H. Zhang, J. Ma, Y. Yang, H. Chen, Y. Han, H. Sun and L. Huang, *Small* **2012**, *8*, 2271.

[12] a) A. Kasry, A. A. Ardakani, G. S. Tulevski, B. Menges, M. Copel and L. Vyklicky, *J. Phys. Chem. C* **2012**, *116*, 2858; b) Z. Chen, S. Berciaud, C. Nuckolls, T. F. Heinz and L. E. Brus, *ACS Nano* **2010**, *4*, 2964.

[13] M. S. Dresselhaus, A. Jorio and R. Saito, *Annu. Rev. Condens. Matter Phys.* **2010**, *1*, 89.

[14] S. Bordiga, C. Lamberti, G. Ricchiardi, L. Regli, F. Bonino, A. Damin, K. P. Lillerud, M. Bjorgen and A. Zecchina, *Chem. Commun.* **2004**, *0*, 2300.

[15] F. S. Richardson, *Chem. Rev.* **1982**, *82*, 541.

[16] a) A. F. Kirby and F. S. Richardson, *J. Phys. Chem.* **1983**, *87*, 2544; b) M. G. van der Horst, G. A. van Albada, R.-M. Ion, I. Mutikainen, U. Turpeinen, S. Tanase and J. Reedijk, *Eur. J. Inorg. Chem.* **2008**, *2008*, 2170.

[17] a) V. Biju, T. Itoh, Y. Baba and M. Ishikawa, *J. Phys. Chem. B* **2006**, *110*, 26068; b) J. Cao, J. Z. Sun, J. Hong, H. Y. Li, H. Z. Chen and M. Wang, *Adv. Mater.* **2004**, *16*, 84.

[18] A. Ghosh, K. V. Rao, S. J. George and C. N. R. Rao, *Chem. Eur. J.* **2010**, *16*, 2700.

Chapter 5: Porous graphene frameworks pillared by organic linkers with tunable surface area and gas storage properties*

Summary

In this chapter, a new strategy for the synthesis of graphene frameworks with high surface area, thermal and chemical stability is discussed. Graphene frameworks were synthesized using different length organic linkers with uniform pore size. Two porous graphene frameworks (PGFs) were prepared *via* covalent functionalization of reduced graphene oxide (RGO) with iodobenzene followed by a Pd(0) catalyzed Sonogashira C–C coupling reaction with two different length organic linkers 1,4-diethynylbenzene (PGF-1) and 4,4´-diethynylbiphenyl (PGF-2). The iodobenzene groups on graphene basal plane react with 1,4-diethynylbenzene (PGF-1) and 4,4´-diethynylbiphenyl (PGF-2) resulting in 3–D assembly. In contrast to RGO, these 3D frameworks show high surface area (BET, 825 m^2/g) and pore volumes due to the effect of pillaring. Interestingly, both the frameworks show high CO_2 uptake (112 wt% for PGF-1 and 60 wt% for PGF-2 at 195 K up to 1 atm). The PGFs show nearly 1.2 wt% of H_2 storage capacities at 77 K and 1 atm, increasing to ~1.9 wt% at high pressure. These all carbon-based porous solids resulting from pillaring of graphene with uniform length linkers suggests the possibility of designing related several such novel porous materials with attractive properties.

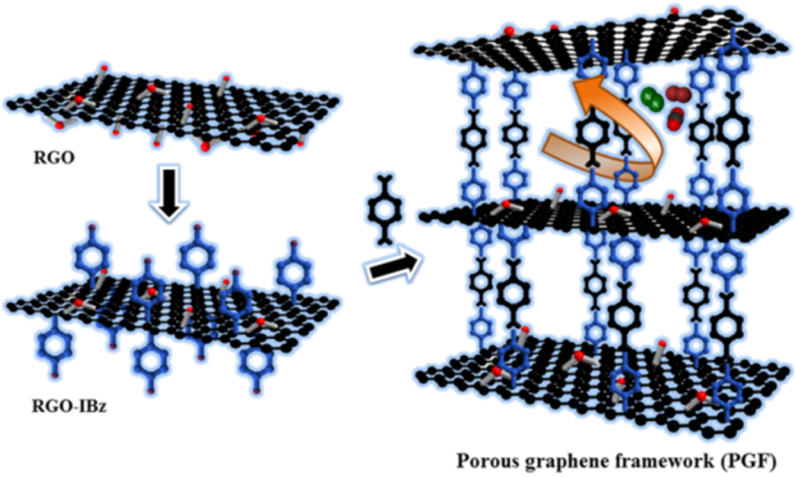

A paper based on these studies has appeared in Chem. Commun. 2014, 50, 2015.

5.1 Introduction

Graphene, the two-dimensional material has many unique properties.[1] Besides its unusual electronic properties, it is associated with high-surface-area, the predicted value being close to 2600 m^2/g.[2] Graphene samples using different synthesis routes and its analogues borocarbonitrides, $B_xC_yN_z$ with a high surface area approaching 1800 m^2/g have been prepared.[3] Atomically thin sp^2 hybridized graphene sheets due to very high chemical, thermal, mechanical stability and light weight can be an important precursor for the synthesis of high-performance porous materials for gas storage, separation, and catalysis. Although predicted surface area of the single layer graphene sheet is very high, most of the graphene synthesized in bulk using chemical route are highly agglomerated due to van der Waals interaction. The maximum accessible surface area for practical applications is hardly few hundred m^2/g. The interlayer spacing in few-layer graphene can be uniformly increased by pillaring with uniform length organic linkers to generate novel porous graphene-based materials. These classes of all carbon-based materials can be considered analogues to the metal-organic frameworks and zeolites with high surface area and tunable pore size, which depends on the length and functionality of the linker used to covalently cross-link the individual graphene sheets. Modification of graphene oxide (GO) layers through intercalation or covalent linking with amines, surfactants, and such species has been attempted.[4] Theoretically constructed graphene networks pillared by carbon nanotubes are predicted to exhibit high H_2 storage capacity.[5] Pillared GO frameworks making use of boronate ester as the linker have been reported, but this linker is moisture sensitive and the framework does not exhibit increased surface area.[6] Linking graphene or GO layers by rigid organic pillars covalently would clearly be a more attractive strategy. Such a graphene framework comprising stable organic linkers of different length and functionality would permit tunability of the surface area and pore size distribution. In this chapter, an efficient strategy to design such pillared graphene frameworks by linking reduced graphene oxide layers with different length organic linkers is discussed. Because of the C-C coupling between the graphene layers and the linkers, these materials have good stability and more importantly, tunable specific surface area in the region of 800 m^2/g, uniform pore size as well as good CO_2 and H_2 storage capacities.

The present experimental design of pillared graphene frameworks has resulted in a theoretical investigation of such structures in gas storage and separation applications. Theoretical investigations by Garberogolio *et al.* show promising performance of these all carbon-based porous materials with performance comparable to well-investigated metal–organic frameworks (MOFs) with open metal centres.[7]

Covalent cross-linking strategy has been used to design porous solids for different applications. Scherf *et al.* have used the present strategy to design PGF using Yamamoto aryl–aryl coupling reaction for high-performance supercapacitors.[8] Scherf *et al.* have also used the present Pd(0) catalyzed coupling chemistry to design graphene–based conjugated microporous polymer sheets.[9] These composite sheets were converted into 2D porous carbon nanosheets by pyrolysis with hierarchical pore system for high ion–accessible surface area. The designed porous architecture with the presence of graphene–based conduction paths allowed accelerated electron and ion diffusion/transport leading to high specific capacitance as well as good rate capability and cycling stability. Surungot *et al.* have synthesized 3D porous composite of graphene and polyaniline with high supercapacitor performance.[10] Shi *et al.* have designed porphyrin pillared graphene frameworks with ultra-large d-spacing as an electrocatalyst in oxygen reduction reaction.[11] In addition to the electrochemical applications of pillared graphene structures recent investigation have shown the promising application in dispersing metal nanoparticle in the pores for catalytic application. Wang *et al.* have used Pd-rGOF for Tsuji–Trost reaction with high catalytic efficiency and recyclability.[12] The PGFs prepared using different routes have shown promising application as a CO_2 adsorbent.[13] The present strategy has been used to design covalently cross–linked assemblies of MoS_2 and MoS_2–graphene composites with high performance in photocatalytic hydrogen evolution due to high surface area, uniform pore size and catalytically available sites for hydrogen evolution.[14] Transition metal chalcogenides and graphene are agglomerated due to van der Waals interaction and catalytically active centres are blocked. Covalently cross-linked layers with uniform length linkers generate a uniform porous architecture with new catalytic centres to improve the catalytic performance. Further, two different layered materials such as MoS_2 and graphene were cross-linked by a covalent bond with a linker to form homogeneous composites. These assemblies with varying ratio of MoS_2 and graphene were observed to be very good photocatalyst for hydrogen evolution. The enhanced photocatalytic activity in such assemblies can be attributed to the synergistic interaction between two components, new catalytic centres due to the removal of van der Waals interaction and more homogeneity of composites due to the uniform covalent bond between the individual components. The efficient Pd(0) catalyzed chemistry has been further extended to the chemistry of transition metal chalcogenides. This strategy of covalent cross-linking has been used to combine two different carbon allotropes graphene and single–walled carbon nanotube using covalent bond.[15] Single-walled carbon nanotube and graphene were covalently cross-linked using 1,4-diethynylbenzene linker employing Sonogashira coupling.

The obtained covalently cross-linked assemblies were superhydrophobic with high surface area and adsorption properties. Further, the assemblies showed synergistic interaction with enhanced surface area in comparison to the individual component. This brief overview gives an insight into the application of this new class of all carbon-based porous materials for different applications with many more interesting results to come.

5.2 Scope of the present investigations

Properties of graphene make it suitable in numerous applications.[1c,16] Several important physical and chemical routes have been explored to synthesize graphene in bulk quantity and the synthesis protocol varies depending on the application.[1c,16b,17] The various applications of graphene exploit the porous architecture and high surface area.[5c,18] Although theoretically predicted surface area of graphene is very high the observed surface area of various graphene samples prepared using chemical route is low due to van der Waals interaction between the individual layers.[19] In the present investigation uniform length organic linkers 1,4-diethynylbenzene (PGF-1) and 4,4´-diethynylbiphenyl (PGF-2) were used to uniformly pillar the individual graphene sheets and overcome the strong π-π interaction. The resulting graphene frameworks have a high surface area of ~ 800 m^2/g and a uniform porous architecture, investigated in detail using microscopic and adsorption studies. Further, these all carbon-based porous architectures have high thermal and chemical stabilities and are expected to have high mechanical properties due to the high mechanical strength of graphene.[20] These properties are important for above mentioned practical applications. The present study has resulted in several such porous pillared graphene structures for different applications and they are widely named in literature as pillared graphene framework (PGFs), reduced graphene oxide framework (rGOF), graphene oxide framework (GOF) and pillared graphene oxide framework (PGOF).

In addition to the aim of obtaining a uniform porous architecture for practical applications, the application of efficient Pd(0) catalyzed coupling reaction in nanocarbon chemistry is also explored. Pd(0) catalysed coupling reaction are some of the most efficient protocol in synthetic organic chemistry.[21] Pd(0) catalyzed coupling reactions are not well explored in nanocarbon chemistry. The present investigation explores one such application in designing a novel porous material by using the Sonogashira coupling.

5.3 Experimental section

Materials: Chemicals used in the synthesis were of high purity and obtained from commercial sources. All the solvents used for synthesis were pre-dried before the synthesis.

Synthesis of graphite oxide (GO): Graphite oxide was synthesized using a modified hummers method.[22] In an ice bath 75 ml conc. H_2SO_4 was mixed with 1.5 g graphite powder and 1.5 g $NaNO_3$ and allowed to stir for 10 min. In the uniform mixture, 10 g of $KMnO_4$ was added slowly and allowed to mix properly. The reactants were transferred to an oil bath maintained at 40 °C and stirred for 45 min. To this mixture 75 ml distilled water was added followed by stirring for 15 min at 70 °C. Uniform brown color suspension was formed. The temperature was then raised to 80 °C and 15 ml H_2O_2 in 150 ml warm water (~70 °C) was added. The color of suspension changed from brown to yellow. Obtained product was centrifuged and washed repeatedly with deionized water. Graphite oxide was again dispersed in water and dialyzed till dialysate became neutral. Excess water was removed by centrifugation and obtained solid product was freeze dried.

Preparation of reduced graphene oxide (RGO): In a typical batch 500 mg graphite oxide was dispersed in 500 ml water by sonication, sodium carbonate solution was added to adjust the pH to 10 and stirred at 90 °C for 12 h. Subsequently, 5 g $NaBH_4$ dissolved in 100 ml water was added to the GO dispersion, with pH adjusted to 10. The mixture was maintained at 80 °C for next 6 h. The reduction was accompanied by outgassing with solution changing from brown to black and precipitation of reduced graphene oxide from the solution. Obtained product was filtered (0.45 μm, PTFE membrane) and washed with copious amount of water and ethanol. Obtained product has a small concentration of residual epoxide, hydroxyl and carboxylic acid functional groups on basal plane and edges.

Preparation of RGO-IBz: Diazonium salt used for iodobenzene functionalization of graphene was prepared *in situ* using 4-iodoaniline.[23] 960 mg (4.3 mmol) 4-iodoaniline was dissolved in 80 ml water by adding the minimum amount of conc. HCl dropwise. The 4-iodoaniline solution was then transferred to a round bottom flask maintained at 0 °C in an ice bath. To this solution, 483 mg $NaNO_2$ (7 mmol) and 4 ml 20% HCl (6.4 M) was added and allowed to stir for 45 min. The color of the solution changed from transparent to yellow due to the formation of 4-iodobenzene diazonium chloride. Reduced graphene oxide obtained after sodium borohydride reduction was agglomerated with poor dispersion in water. RGO (125 mg) was dispersed in 125 ml 1 wt% sodium dodecylbenzene sulfonate (SDBS) surfactant

solution. RGO dispersion was then added to the diazonium salt solution. Reactant mixture was maintained at 0 °C for next 2 hours followed by stirring at room temperature for next 4 hours. Obtained product was filtered and washed with copious amount of water, (1:1) water-ethanol solution, ethanol, and THF to remove the surfactant properly. The final product was dried in a vacuum desiccator at room temperature.

Synthesis of 1,4-diethynylbenzene (linker 1): The reaction was performed under nitrogen. In the mixture of 1,4-diiodobenzene (2 g, 6 mmol), $Pd(PPh_3)_4$ (100 mg), CuI (50 mg) and toluene (30 ml) at 80 °C trimethylsilylacetylene (2 ml, 14 mmol) dissolved in 10 ml triethylamine was added dropwise and allowed to stir for 1 h. The product was diluted with ethyl acetate, passed through celite bed, washed with 1% $NaHCO_3$ aqueous solution, dried over anhydrous sodium sulphate, evaporated in a rotary evaporator and purified by column chromatography (silica, hexane) to give 1,4-bis[(trimethylsilyl)ethynyl]benzene as an intermediate. (1.34 g, 82 %). The deprotection was carried out by stirring intermediate (1.25 g, 1equivalent) with K_2CO_3 (5g, ~ 8 equivalents) in 35 ml methanol for 5 h. Excess methanol was evaporated in a rotary evaporator, diluted with ethyl acetate, washed with water and dried over anhydrous sodium sulphate. The organic layer was dried in a rotary evaporator to give 1,4-diethynylbenzene as the final product. (562 mg, 96%) 1H NMR ($CDCl_3$, 400 MHz): (ppm) 7.44 (s, 4 H; Ar*H*), 3.16 (s, 2H; C≡CH).

Synthesis of 4,4′-diethynylbiphenyl (linker 2): 4,4′-Diethynylbiphenyl was prepared using the same procedure used for 1,4-diethynylbenzene. 4,4′-diiodobiphenyl (6 mmol) remaining reagents and condition same. (930 mg, 76.7 %) 1H NMR ($CDCl_3$, 400 MHz): δ (ppm) 7.55–7.56 (m, 8 H; Ar*H*), 3.14 (s, 2H; C≡CH).

Synthesis of PGF-1: In a typical procedure, a mixture of RGO-IBz (40 mg), 1,4-diethynylbenzene (177 mg), $Pd(PPh_3)_4$ (3 mol%), CuI (6 mol%) were degassed by four freeze-thaw pump cycles and purged with N_2. To this 4 ml, dry DMF, and 1 mL anhydrous triethylamine were added under continuous N_2 flow. The reaction mixture was stirred at 140 °C for 48 h and cooled to room temperature. Precipitates were collected by filtration and washed several times with water, ethanol and THF. Further purification was carried out using Soxhlet extraction technique with methanol and THF for 24 hrs each. Compounds were dried under vacuum at room temperature for 24 hrs. The obtained PGF samples were observed to be superhydrophobic. Yield: 83%. FTIR in KBr (cm^{-1}): 3428(br), 3293(br), 3027(w), 2919(w),

2184(w), 1907 (w), 1664(br), 1600(s), 1502(m), 1384(m), 1261(w), 1178(w), 1099(s), 1016(m), 898(sh), 833(s), 543(w).

S**ynthesis of PGF-2:** Similar procedure as of PGF-1 was adopted for the synthesis of PGF-2, except 4, 4′-diethynylbiphenyl was used as the linker. Yield: 78%. FTIR in KBr (cm^{-1}): 3438(br), 3299(br), 3029(w), 2919(w), 2184(w), 1909 (w), 1664(br), 1604(s), 1492(m), 138(m), 1261(w), 1178(w), 1099(s), 1004(m), 898(sh), 833(s), 543(w).

Instrumentation

Infrared (IR) spectra were recorded using KBr pellets on a Bruker FT-IR spectrometer. Solid state ^{13}C magic angle spinning (MAS) NMR spectrum was measured on a Varian infinity plus 300 WB spectrometer at a MAS rate of 5 kHz and 11 kHz. Morphological studies have been carried out using Nova Nano SEM 600, FEI Company. Transmission Electron Microscopy (TEM) analysis has been performed using FEI TITAN3TM with an accelerating voltage of 80 kV to avoid beam induced damages. Thermogravimetric analysis (TGA) was done using Mettler Toledo TGA 850 instrument in a nitrogen atmosphere in the range of 30-900 °C with a heating rate of 3 °C/min. X-ray photoelectron spectra (XPS) were recorded in an Omicron Nanotechnology Spectrometer with Mg Kα as the X-ray source. Powder X-ray diffraction patterns (PXRD) of PGF-1 and PGF-2 were recorded in PANanlytical Empyrean using Cu K-α radiation. PXRD pattern of GO and RGO were recorded on Bruker D8 Discover using Cu K-α radiation.

Adsorption measurements

The adsorption isotherm of N_2 (77 K), H_2 (77 K) and CO_2 (195 K, 273 K and 298 K) up to 1 atm for the sample of PGF-1 and PGF-2 were measured by using QUANTACHROME QUADRASORB-*SI* analyzer. In the sample tube, the adsorbent sample (~100-150 mg) was placed which had been prepared at 433 K under a 1×10^{-1} Pa vacuum for about 6 h prior to the measurement of isotherms. Helium gas (99.999% purity) at a certain pressure was introduced into the gas chamber and allowed to diffuse into the sample chamber by opening the valve. The amount of gas adsorbed was calculated readily from pressure difference (P_{cal} - P_e), where P_{cal} is the calculated pressure with no gas adsorption and P_e is the observed equilibrium pressure. All operations were computer-controlled and automatic.

High-pressure H_2 (77 K) and CO_2 (273 K) sorption isotherm measurements were carried out on a fully computer controlled volumetric BELSORP-HP, BEL JAPAN high-pressure instrument. The hydrogen and CO_2 used for the high-pressure measurements are

scientific/research grade with 99.999% purity. For the measurements, approximately 200 mg sample was taken in a stainless-steel sample holder and degassed at 433 K for a period of 18 hours under 0.1 Pa vacuum. Dead volume of the sample cell was measured with helium gas of 99.999% purity. Non-ideal correction for hydrogen and carbon dioxide gas were made by applying virial coefficients at the respective measurement temperature.

The P_0 value used for adsorption measurements are 640 Torr for CO_2 at 195 K and 690 Torr for N_2 at 77 K. For H_2 uptake P_0 value used was 760 Torr. For all low-pressure CO_2 uptake measurements done at 273 K and 298 K, P_0 value used was 760 Torr.

5.4 Results and discussion

Scheme 1 show steps involved in the synthesis of pillared graphene frameworks (PGF-1 and PGF-2). In synthesizing the pillared graphene frameworks, reduced graphene oxide (RGO) was used as the starting material rather than graphene oxide to avoid excessive surface oxygen functionalities which do not favour gas adsorption. RGO was prepared by $NaBH_4$ reduction of graphene oxide.[23] The RGO sheets were functionalized with iodobenzene using *in situ* generated 4-iodobenzene diazonium chloride leaving free iodobenzene functional groups on both sides of RGO denoted by RGO-IBz (see experimental section 4.3 for details). The formation of RGO-IBz was confirmed by X-ray photoelectron spectroscopy (XPS), Raman, and Fourier transform infrared spectroscopies. Strong band in the IR spectrum at 466 cm^{-1} was observed due to C-I bond stretching (Figure 2b). The presence of iodobenzene is further confirmed by I 3d signals in the XPS spectrum of RGO-IBz (Figure 2a). The

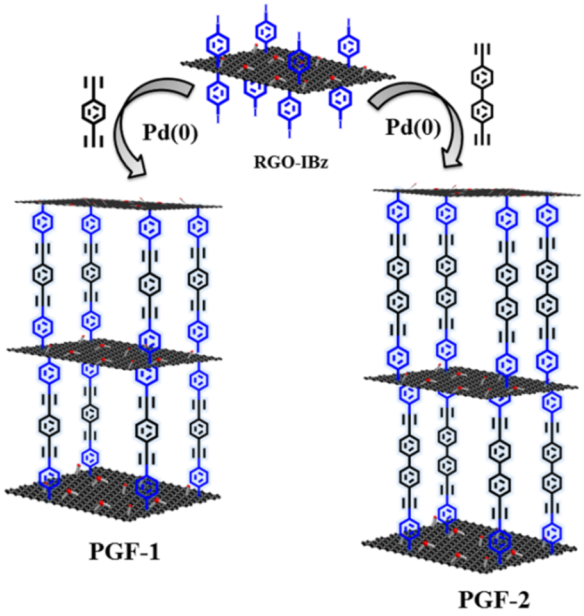

Scheme 1. Synthesis strategy for pillared graphene frameworks (PGFs) using Sonogashira coupling.

characteristic *D* and *G* bands of RGO and RGO-IBz in the Raman spectra were found at1342 cm^{-1} and 1592 cm^{-1} respectively (Figure 3a).

RGO-IBz was reacted with the required quantities of the 1,4-diethynylbenzene linker or 4,4´-diethynylbiphenyl in *N, N´*-dimethylformamide (DMF) following the Sonogashira coupling strategy, to obtain the 3D frameworks, PGF-1 and PGF-2 respectively (Scheme 1, see experimental section 4.3 for details)). Initially, Pd(0) undergoes oxidative addition with the free iodobenzene present on RGO and forms a Pd(II) intermediate which undergoes transmetallation with copper acetylide and subsequent reductive elimination forming a C-C bond, resulting in a pillared graphene framework (see figure 1 for reaction mechanism).

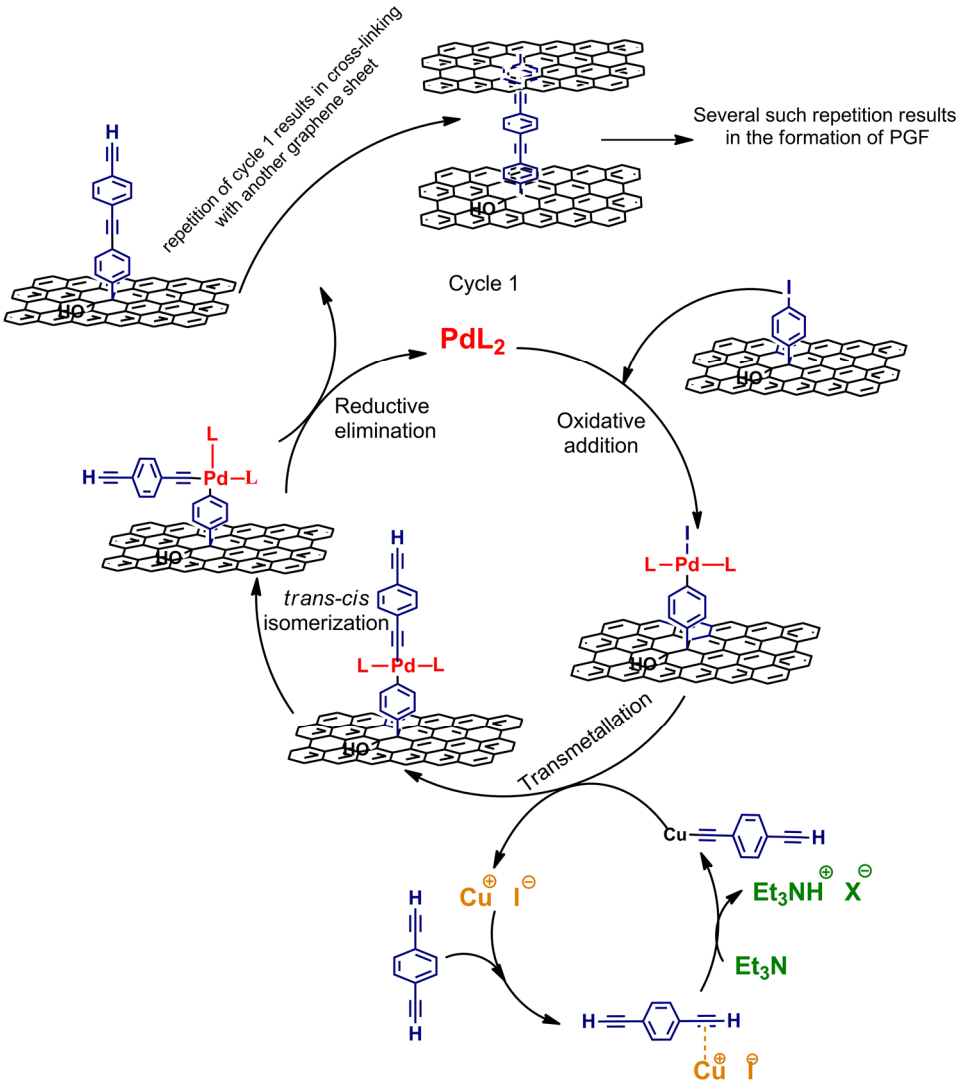

Figure 1. Reaction mechanism of the Sonogashira coupling in iodobenzene functionalized graphene. Cycle 1 shows the C–C bond formation with 1,4-diethynylbenzene in iodobenzene functionalized graphene. Subsequent cycle 1 with another graphene sheet results in the cross-linking of another graphene sheet. Several catalytic cycles 1 result in PGF formation. Present mechanism shows only one such cycle.

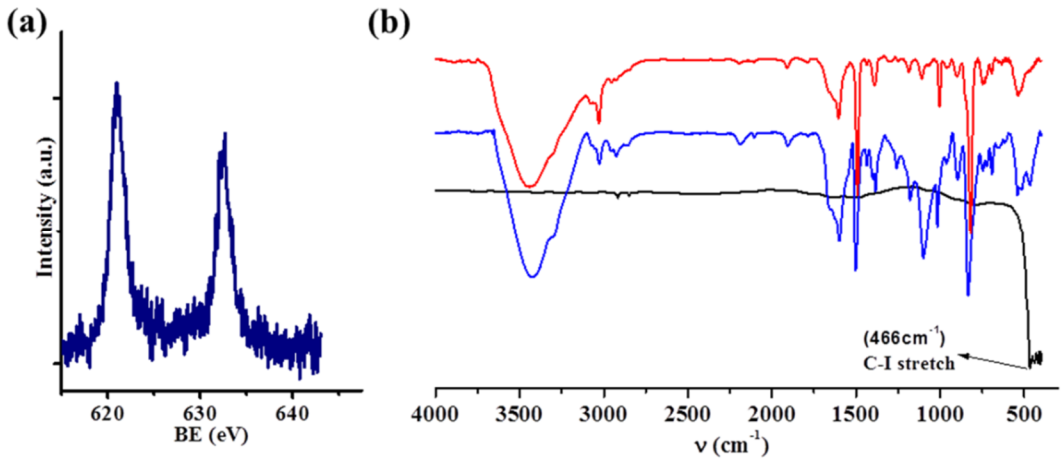

Figure 2. (a) High resolution I 3d XPS spectrum of RGO-IBz. (b) FTIR spectra for RGO-IBz (black), PGF-1 (blue) and PGF-2 (red).

FTIR spectra of these materials show a band at 2184 cm^{-1} due to the C≡C stretching vibration, thereby confirming the incorporation of 1,4-diethynylbenzene and 4,4´-diethynylbiphenyl linkers between the RGO-IBz sheets (Figure 2b). In the Raman spectrum, bands at 1342 cm^{-1} (D-band) and 1592 cm^{-1} (G-band) of the graphene are observed (Figure 3a). Solid state ^{13}C-MAS NMR spectra of PGFs (Figure 3b) show signals at 90.1 and 91.33 ppm due to the C≡C bond of the linkers, besides features in the 120-150 ppm region due to sp^2 and aromatic carbons of pillars which are consistent with the reported values.[23]

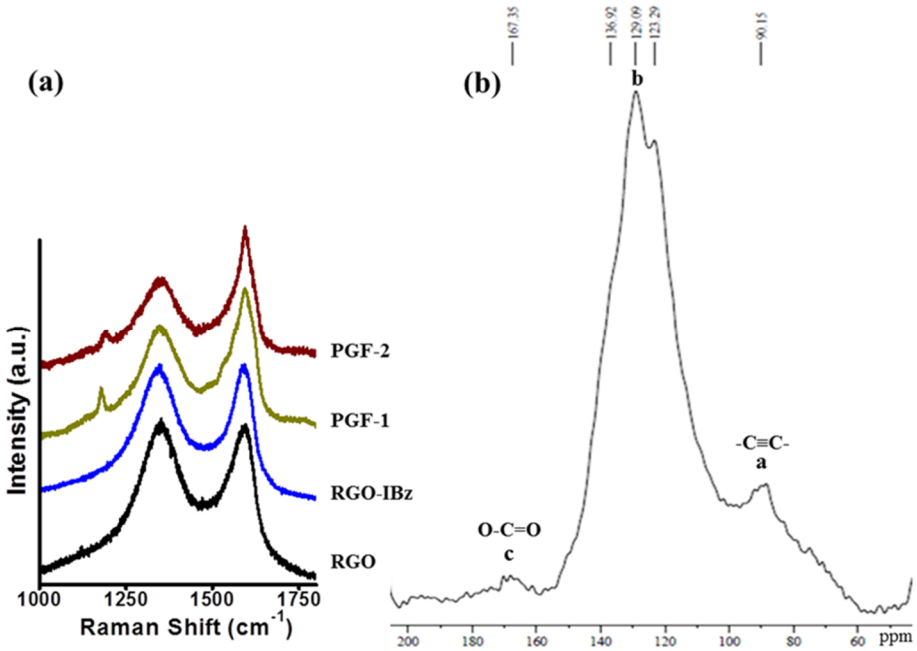

Figure 3. (a) Raman spectra of RGO, RGO-IBz and pillared graphene frameworks PGF-1 and PGF-2. (b) Solid state ^{13}C NMR spectrum of PGF-1 at 11 kHz MAS.

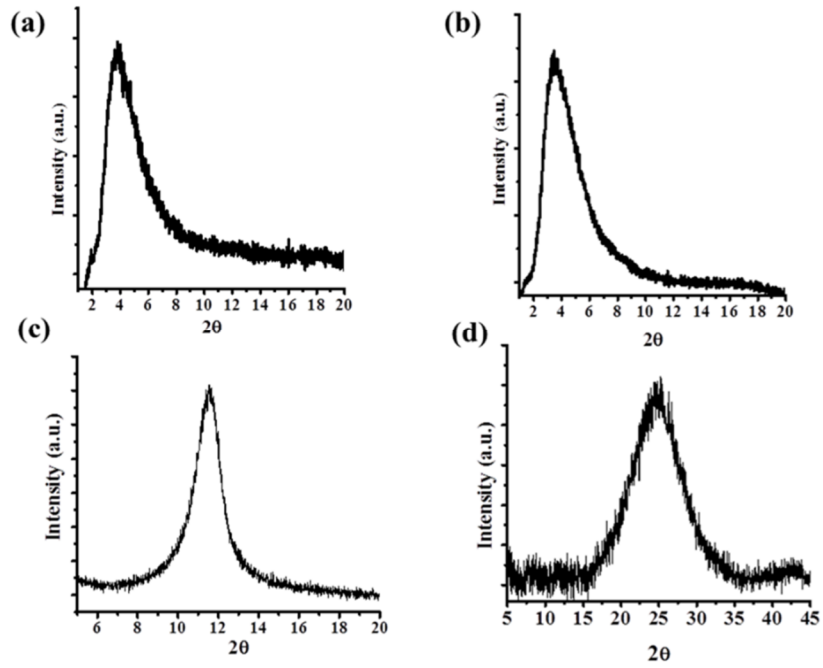

Figure 4. PXRD patterns of (a) PGF-1 (b) PGF-2 (c) GO (graphite oxide) and (d) RGO (reduced graphene oxide).

Powder X-ray diffraction patterns (PXRD) of PGF-1 and PGF-2 show peaks at 2θ values 4° and 3.6° with the corresponding *d*-spacing values of 2.1 and 2.4 nm respectively, which closely match the pillar lengths (Figure 4). The PXRD patterns unequivocally suggest pillaring of the graphene layers by the organic linkers. It is worth mentioning that the interlayer spacing between the graphene layers in RGO is about 0.34 nm.

Scanning electron microscope (SEM) images of PGF-1 and PGF-2 show the formation of micrometer-sized particles ranging from 2 to 6 μm (Figure 5c, d). The linking of several

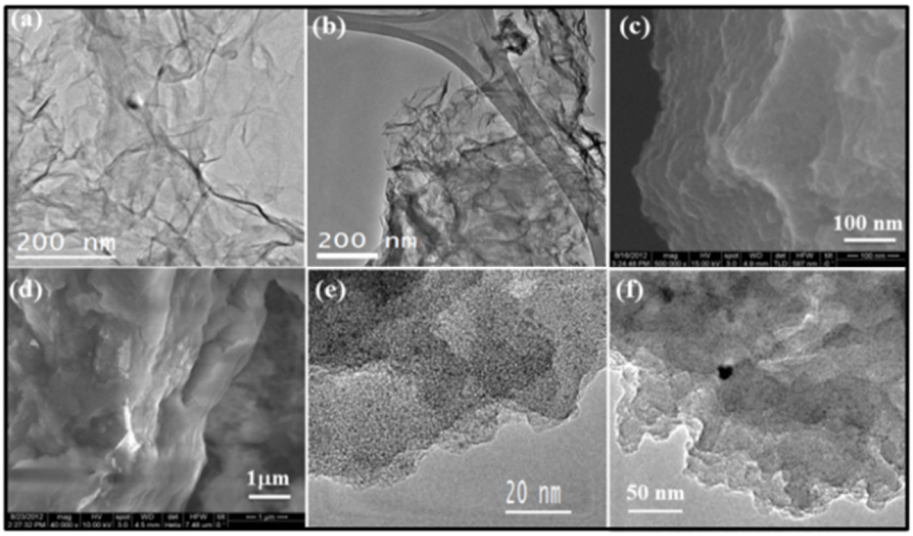

Figure 5. (a, b) TEM images of RGO. SEM images of (c) PGF-1 and (d) PGF-2. TEM images of (e) PGF-1 and (f) PGF-2.

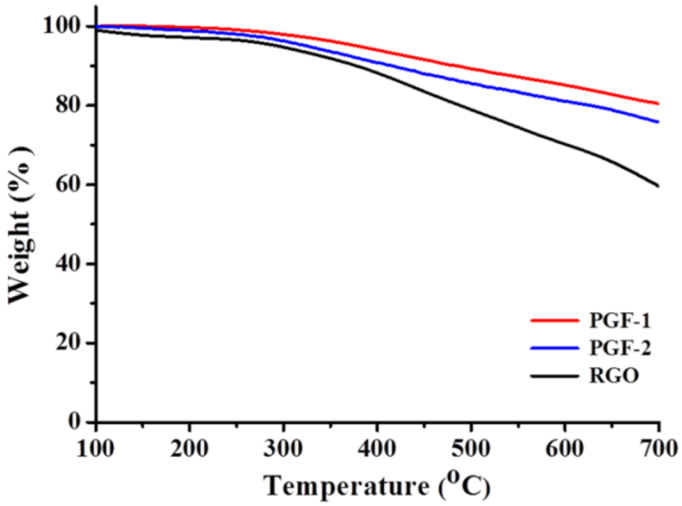

Figure 6. TGA profiles of (a) RGO (black), (b) PGF-1(red) and (c) PGF-2 (blue) in a nitrogen atmosphere.

RGO-IBz sheets through pillars can be visualized in the images revealing the stacking of RGO sheets. Transmission electron microscope (TEM) images indicate packing of graphene sheets into several nanometers (Figure 5e, f) unlike those of RGO which only show transparent sheets with folded boundaries (Figure 5a, b). Thermogravimetric analysis (TGA) of PGF-1 and PGF-2 reveals no weight loss up to 300 °C, further, heating causes a steady decrease in weight of 10-15% up to 700 °C suggesting high thermal stability of PGFs (Figure 6).

The porosity of the PGF frameworks was characterized by N_2 adsorption measurements at 77 K carried out after heating the samples at 160 °C for 12 h to remove any moisture and solvent molecules present in the pores. The N_2 adsorption isotherm of PGF-1 shows combined characteristics of type-I and type-IV profiles (Figure 7a) with a steep uptake in the low-pressure region up to $P/P_0 \sim 0.1$ and hysteresis in the higher pressure region, suggesting the mesoporous nature of the pillared framework. The final N_2 uptake was 477 mL, the application of Brunauer-Emmet-Teller (BET) model giving a surface area of 825 m^2/g. The Langmuir surface area is 1850 m^2/g. A non-local density functional theory (NL-DFT) model fitted to the N_2 adsorption isotherm reveals the presence of a wide distribution of pores from micro to mesopores ranges (pore width of 1 nm to 3 nm, Figure 8a) estimated pore volume being 0.74 cm^3/g. The PGF-2 show combined characteristics of type-I and type-II profiles (Figure 7a) with pore sizes varying from micro to mesopores (1.5 – 4.0 nm, Figure 8b). BET and Langmuir surface area for PGF-2 are 770 m^2/g and 1799 m^2/g respectively. The final uptake was found to be 571 mL, a value higher than that of PGF-1 indicating the effect of increasing the pillar length from 1, 4-diethynylbenzene to 4, 4´-diethynylbiphenyl. The pore

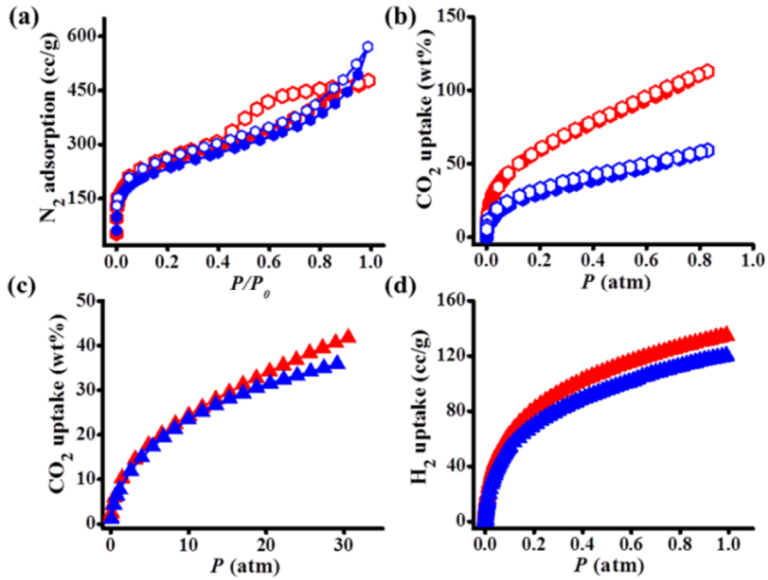

Figure 7. Adsorption isotherms of PGF-1 (red) and PGF-2 (blue); (a) N_2 at 77 K, (b) CO_2 at 195 K, (c) CO_2 at 273 K and (d) H_2 at 77K.

size distribution (Figure 8b) reveals a major micropore contribution in PGF-2 compared to PGF-1. RGO used for the synthesis of PGFs are non-porous and have type-II adsorption profile with BET surface area of only 42 m^2/g (Figure 9).

High thermal stability and surface area of the PGF frameworks prompted us to study their potential for clean energy applications such as storage of CO_2 and H_2. The CO_2 adsorption data of PGF-1 and PGF-2 show typical type-I profiles with adsorbed quantities of 572 mL and 301 mL corresponding to 112 wt% and 60 wt% respectively at 195 K (~ 0.85 atm, Figure 7b). The values of the heat of adsorption calculated using the Dubinin-Raduskevich (DR) equation[24] are 27.4 and 27.7 kJ/mol for PGF-1 and PGF-2 respectively. At high pressure and 273 K, adsorbed quantities of CO_2 in the two frameworks are 42 wt%

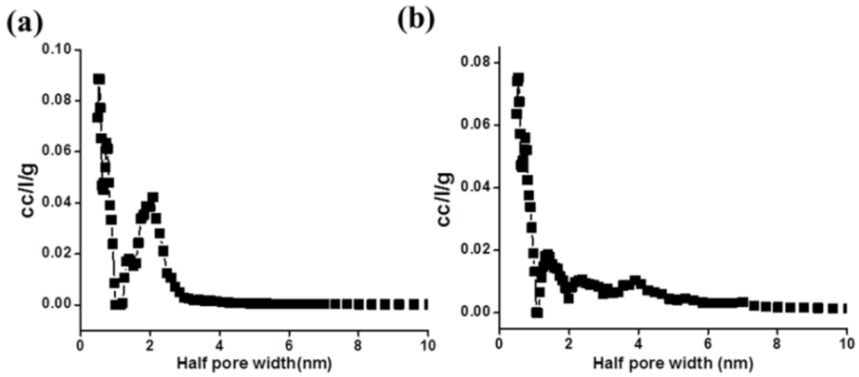

Figure 8. Pore-size distribution for (a) PGF-1 and (b) PGF-2 calculated using non-local density functional theory (NLDFT) from N_2 adsorption isotherm at 77 K.

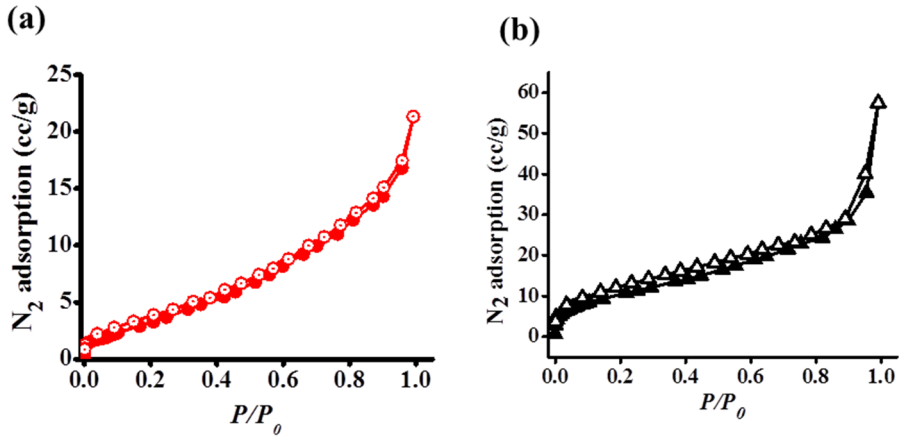

Figure 9. N_2 adsorption profile of (a) GO (graphite oxide, red), (b) RGO (reduced graphene oxide, black) at 77 K. GO and RGO have BET surface area of 14 m^2/g and 42 m^2/g respectively.

and 36 wt% (~ 30 atm, Figure 7c) which are higher than those of any graphene-based framework[6b,25] and comparable to those of high surface area MOFs.[26] The PGF frameworks were also examined for the CO_2 uptake under ambient conditions (273 K, 293 K, and 1 atm), PGF-1 shows nearly 7.2 wt% at 273 K and 5.5 wt%, at 293 K (Figure 10a). The corresponding CO_2 uptake values for PGF-2 are 7.7 wt% and 6.3 wt%, which is comparable to MOFs (Figure 10b).[27]

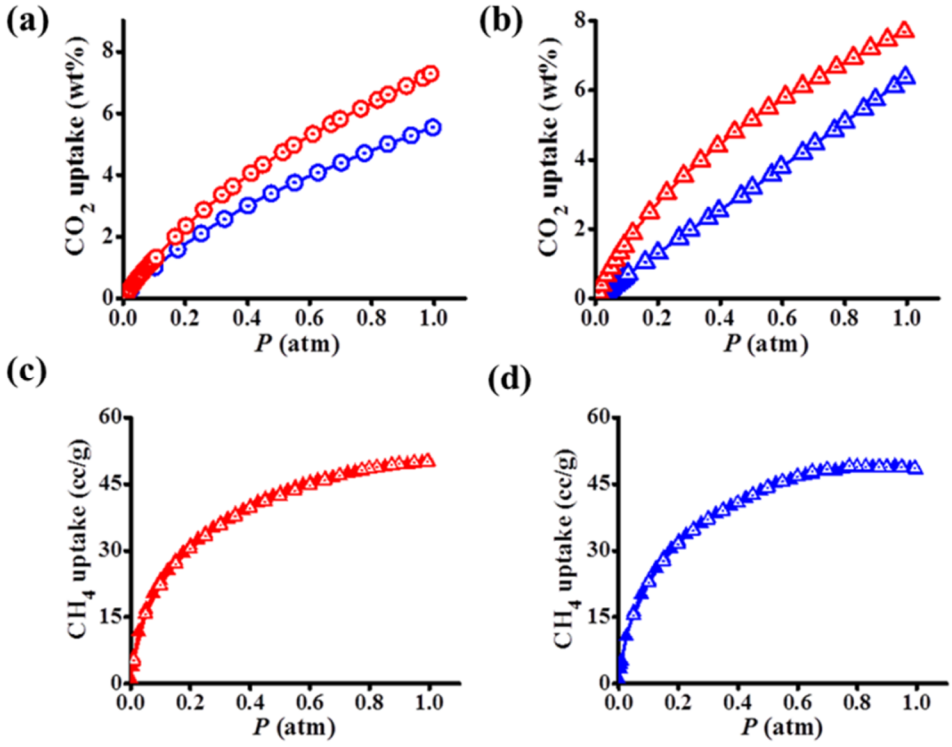

Figure 10. CO_2 adsorption isotherms at 273 K (red) and 293 K (blue) of (a) PGF-1 and (b) PGF-2. Methane uptake of (a) PGF-1 (red) and (b) PGF-2 (blue) at 195 K and 1atm.

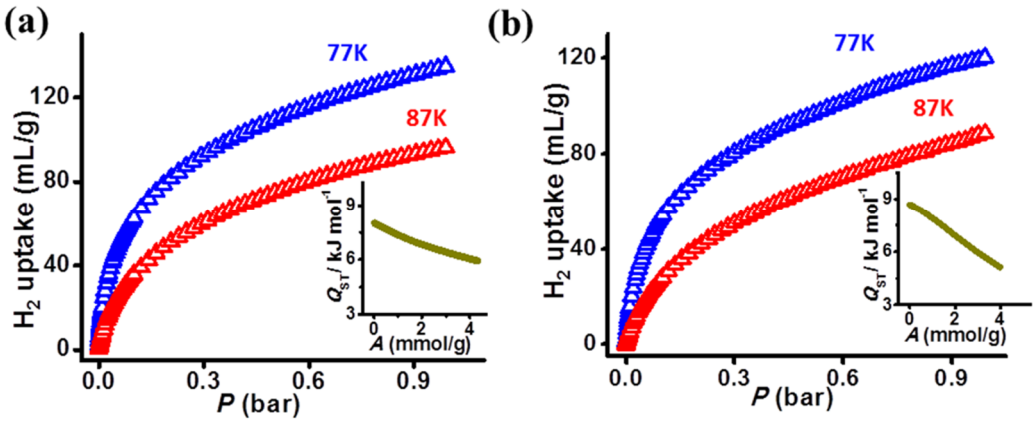

Figure 11. H_2 adsorption isotherms of (a) PGF-1 and (b) PGF-2 at 77 K (blue) and 87 K (red), inset change in the isosteric heat of adsorption versus uptake for PGF-1. Fitting parameter obtained from the Virial fitting given in table 1.

The capacity of the PGF frameworks for H_2 storage is also investigated. PGF-1 and PGF-2 adsorb 1.2 and 1.0 wt% of H_2 respectively at 1 atm and 77 K (Figure 7d). These values are similar to those of graphene-based frameworks and to the values shown by high-surface-area MOFs.[28] The initial isosteric heat of hydrogen adsorption (Q_{ST}) is found to be 7.9 kJ/mol for PGF-1 (Figure 11a) and 8.7 kJ/mol for PGF-2 (Figure 11b). The Q_{ST} decreases gradually with loading due to the heterogeneity of the surface. Once all the sites with higher Q_{ST} get filled up, then only low Q_{ST} sites are available for further loading, showing a falling Q_{ST} trend.[29] This observed feature of isosteric heat of adsorption is due to the presence of residual oxygen functionalities on the graphene basal plane in PGFs. These oxygen functionalities provide higher van der Waals interaction energy and when these high Q_{ST} sites get filled the H_2 molecules adsorb on sp^2 bonded carbon network with a gradual decrease in

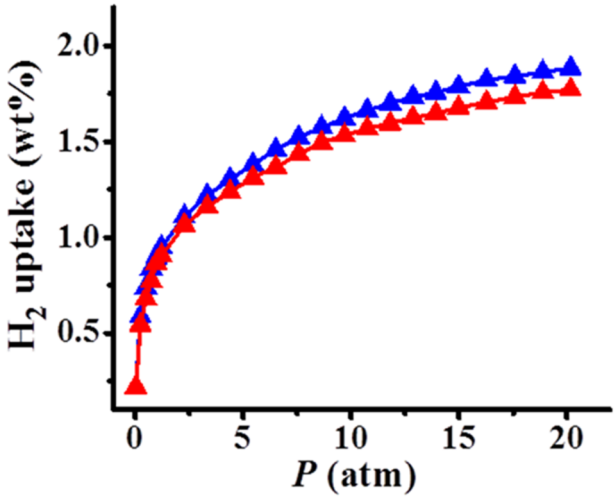

Figure 12. High-pressure H_2 uptake of PGF-1 (blue) and PGF-2 (red) at 77 K.

Table 1: Fitting parameters obtained from the Virial fitting of two H_2 isotherms measured at 77 and 87 K for PGF-1 and PGF-2.

Model		Virial (User)	
Equation (PGF-1)		$y = \ln(x) + ((1/T)*(a_0 + (a_1*x) + (a_2*x^{\wedge}2) + (a_3*x^{\wedge}3) + (a_4*x^{\wedge}4) + (a_5*x^{\wedge}5) + (a_6*x^{\wedge}6))) + (b_0 + (b_1*x) + (b_2*x^{\wedge}2) + (b_3*x^{\wedge}3))$	
Reduced Chi-Sqr			6.76431E-5
Adj. R-Square			0.99998
		Value	Standard Error
ln(P)/torr	a_0	-963.47162	3.99308
	a_1	84.73803	8.22954
	a_2	-0.62746	4.6993
	a_3	-6.53631	1.61601
	a_4	2.34401	0.48837
	a_5	-0.34227	0.07122
	a_6	0.01847	0.00395
	b_0	13.969	0.04659
	b_1	-0.35635	0.09489
	b_2	0.07548	0.04936
	b_3	-0.00584	0.0072
	T	77	0
	T	87	0

Model		Virial (User)	
Equation (PGF-2)		$y = \ln(x) + ((1/T)*(a_0 + (a_1*x) + (a_2*x^{\wedge}2) + (a_3*x^{\wedge}3) + (a_4*x^{\wedge}4) + (a_5*x^{\wedge}5) + (a_6*x^{\wedge}6))) + (b_0 + (b_1*x) + (b_2*x^{\wedge}2) + (b_3*x^{\wedge}3) + (b_4*x^{\wedge}4))$	
Reduced Chi-Sqr			0.03183
Adj. R-Square			0.99332
		Value	Standard Error
ln(P)/torr	a_1	-1046.34355	38.30645
	a_2	33.7413	9.81092
	a_3	-9.04943	2.8599
	a_4	0.75196	0.26867
	b_0	15.73052	0.45882
	b_1	-0.85578	0.18815
	T	77	0
	T	87	0

Q_{ST} profile. Interestingly, at high pressure, the PGF frameworks show nearly 1.9 wt% and 1.8 wt% of H_2 uptake (~ 20 atm, Figure 12). Another feature which can be generalized from high-pressure adsorption profile is that the hydrogen uptake increases at relatively low pressure and saturates by ~ 20 bar. The interaction energy of H_2 with carbon-based materials are dominated by van der Waals interactions and is less than 1 kcal/mol. The observed pressure dependence of H_2 uptake profile can be attributed to the higher interaction between pore surfaces and H_2 molecule.[30] The residual 10 to 15% oxygen functionalities increases the interaction of H_2 molecules with the pore surface further, confirmed by the isosteric heat of hydrogen adsorption (Q_{ST}) between ~ 8 to 9 kJ/mol for PGFs. The present strategy of having slight oxygen functionalities on pore surface to enhance the interaction energy of gases can be an alternative to lithium doping widely reported in theoretical investigations.[5a,30-31] Higher CO_2 and H_2 uptake capacities compared to related porous materials can be related to the increased surface area due to the pillaring of the graphene sheets with organic linkers. The high Q_{ST} values for CO_2 and H_2 are attributed to the strong adsorbate-adsorbent interactions where the pore surfaces are decorated with the hydroxy, epoxy and carboxyl functional groups from RGO and the aromatic π-cloud of the pillar modules. Such interactions of CO_2 and H_2 with the pore surface are well documented experimentally and theoretically in the case of MOFs consisting of functional organic linkers.[28a,32] PGF-1 and PGF-2 show CH_4 uptakes of 50 ml (3.57%) and 48 ml (3.40%) respectively at 195 K and 1 atm (Figure 10c, d).

5.5 Theoretical studies of pillared graphene frameworks

The pillared graphene framework structures synthesised experimentally in this chapter have been investigated theoretically in detail by Garberogolio *et al.* independently.[7] Garberogolio *et al.* have used first, atomistic simulations based on the density functional theory to generate the structures whereas Grand Canonical Monte Carlo was used to predict the adsorption properties of the PGFs in the case of two different gases notably CO_2 and H_2. The theoretical investigation considers the realistic structure where even on the reduction of graphene oxide using various routes oxygen functionalities remains on the graphene basal plane along with defects generated on the basal plane due to the harsh oxidation conditions. The subsequent pillaring results in corrugation which significantly affects the adsorption properties and selectivity in a gas separation process (Figure 13). The theoretically modelled structures have 10 and 15 % oxygen concentration and corrugated graphene sheets pillared by the linker. The theoretical study shows that gas adsorption and separation performance are comparable to the metal organic frameworks (MOFs). Theoretically predicted hydrogen

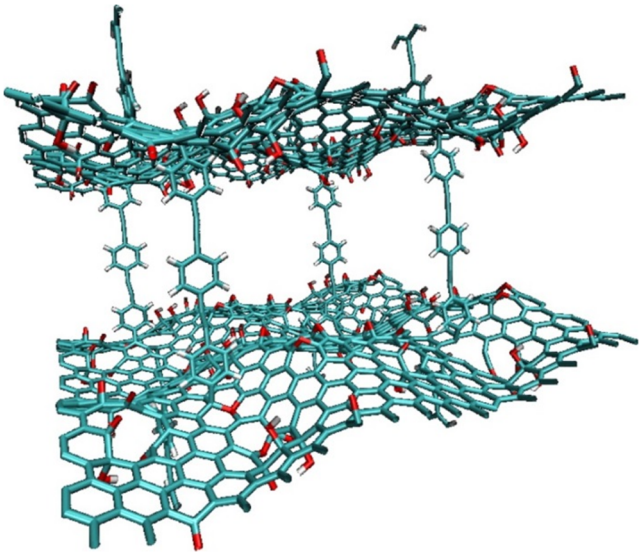

Figure 13. Realistic PGOF structure considered in the theoretical investigation which takes into account the residual oxygen functionalities along with corrugation of graphene basal plane due to pillaring. Carbon, oxygen, and hydrogen atoms are colored in green, red, and white, respectively. Reproduced with permission from ref [13].

uptake values are less than experimentally obtained values but the decrease is attributed to the pillar density with a prediction of improvement on optimizing the density (Figure 14a). The theoretically predicted and experimentally obtained CO_2 uptake is comparable. CO_2 being a quadrupolar molecule have more interaction with oxygen functionalities present on the graphene basal plane and has been correctly predicted in the theoretical investigation (Figure 14b). Observed step in the theoretically predicted isotherm is due to the strong quadrupolar electrostatic interaction between CO_2 molecules beyond a certain density of adsorbed molecules. The quadrupolar interaction between CO_2 molecules further enhances the adsorption.

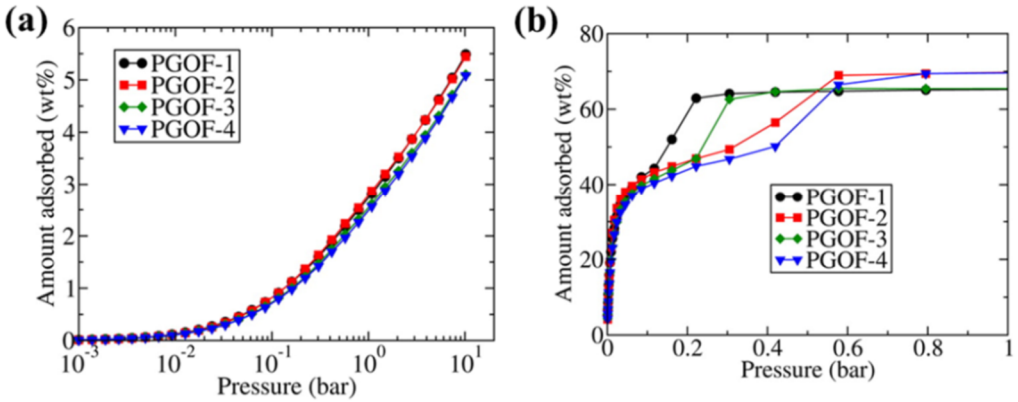

Figure 14. (a) Isotherms of hydrogen adsorption at T = 77 K in the PGOFs modelled in the theoretical study. (b) Isotherms of CO_2 adsorption at T = 195 K in the PGOFs modeled in the theoretical study. Reproduced with permission from ref [13].

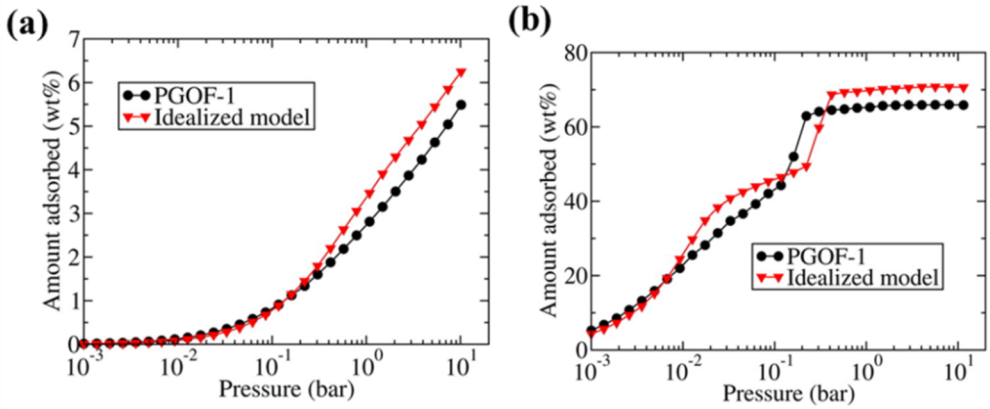

Figure 15. (a) Adsorption isotherm of H_2 at T = 77 K in PGOF-1 (circles) and in the idealized model (triangle). (b) Adsorption isotherm of CO_2 at T = 195 K in PGOF-1 (circles) and in the idealized model (triangle). Reproduced with permission from ref [13].

The theoretical study also considers the ideal flat graphene sheets in the structure frequently modelled in different theoretical investigations and differences between the ideal flat model and realistic corrugated sheets. Due to the corrugation crests and troughs are present which provides more binding energy to gas molecules at lower pressure due to strong adsorbate – adsorbent interaction. The realistic model in comparison to ideal flat sheet structure shows higher gas uptake in the low-pressure regime whereas at higher pressure ideal flat sheet model overestimates the uptake (Figure 15).

Figure 16 shows the snapshot of hydrogen molecule adsorbed in both PGFs and the flat model. The theoretically predicted selectivity of the CO_2/H_2 mixture in PGFs is comparable to MOFs and displays similar pressure dependence (Figure 17). The idealized models underestimate $S(CO_2/H_2)$ by about 15%. Further, theoretical investigations using classical molecular dynamics (MD) simulation of ideal flat model graphene sheets have predicted the high performance of these pillared graphene oxide based membranes for reverse osmosis membranes to achieve efficient water desalination.

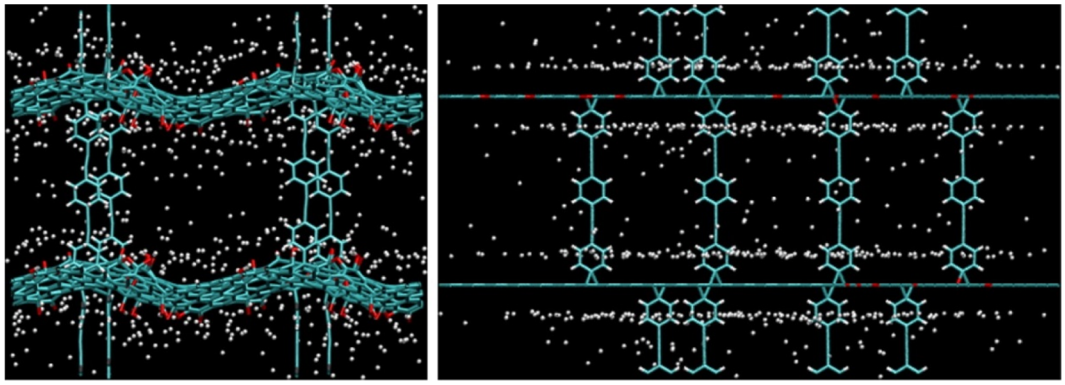

Figure 16. Simulation snapshots showing the typical distribution of hydrogen molecules (represented by white circles) adsorbed in PGOF-1 (left) and the flat model (right), at T = 77 K and P = 10 bar. Reproduced with permission from ref [13].

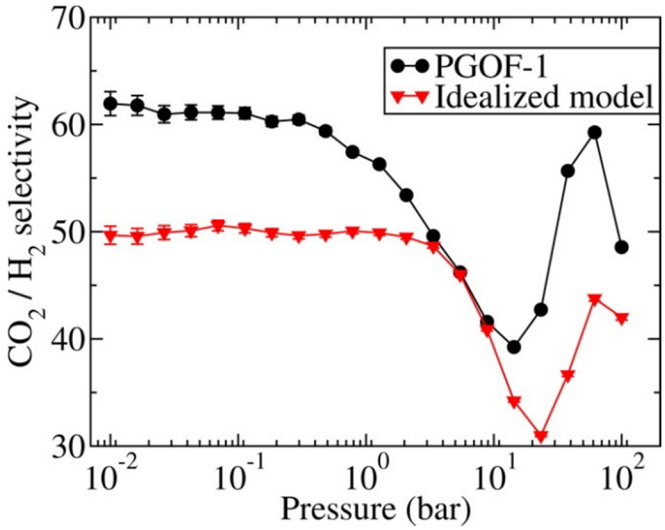

Figure 17. Pressure dependence of the CO_2/H_2 selectivity for an equimolar mixture at T = 298 K for PGOF-1 (circles) and its idealized model (triangles). Reproduced with permission from ref [13].

5.6 Conclusions

In conclusion, robust graphene frameworks were synthesized with organic linkers using the Sonogashira coupling strategy. These frameworks exhibit tunable porosity and surface area and significant storage capacity for CO_2 and H_2. The measured heats of adsorption suggest a moderate interaction between these molecules and the frameworks. The pillared materials described by us are somewhat comparable to the 3D pillared layer MOFs reported by Kitagawa *et al.*,[33] where 2D metal carboxylates are pillared by organic linkers. The entirely new carbon-based porous solids based on pillared graphene frameworks reported here suggest the possibility of designing related materials with desirable attributes. The use of palladium catalyzed C-C coupling reaction for covalent modification of nanocarbon is clearly a worthwhile strategy for further exploration.[34] A theoretical investigation based on present experimental results suggests the gas adsorption and separation performance comparable to metal–organic frameworks (MOFs) with open metal centres. Further, experimental investigations based on the present study have shown the promising application of pillared graphene frameworks in supercapacitors, oxygen reduction reaction (ORR) and CO_2 adsorption.

References

[1] a) A. K. Geim and K. S. Novoselov, *Nat. Mater.* **2007**, *6*, 183; b) K. S. Novoselov, A. K. Geim, S. V. Morozov, D. Jiang, Y. Zhang, S. V. Dubonos, I. V. Grigorieva and A. A. Firsov, *Science* **2004**, *306*, 666; c) C. N. R. Rao, A. K. Sood, K. S. Subrahmanyam and A. Govindaraj, *Angew. Chem. Int. Ed.* **2009**, *48*, 7752.

[2] M. D. Stoller, S. Park, Y. Zhu, J. An and R. S. Ruoff, *Nano Lett.* **2008**, *8*, 3498.

[3] a) A. Ghosh, K. S. Subrahmanyam, K. S. Krishna, S. Datta, A. Govindaraj, S. K. Pati and C. N. R. Rao, *J. Phys. Chem. C* **2008**, *112*, 15704; b) N. Kumar, K. S. Subrahmanyam, P. Chaturbedy, K. Raidongia, A. Govindaraj, K. P. S. S. Hembram, A. K. Mishra, U. V. Waghmare and C. N. R. Rao, *ChemSusChem* **2011**, *4*, 1662.

[4] a) M. Herrera-Alonso, A. A. Abdala, M. J. McAllister, I. A. Aksay and R. K. Prud'homme, *Langmuir* **2007**, *23*, 10644; b) A. Gupta and S. K. Saha, *Nanoscale* **2012**, *4*, 6562; c) K. Zhang, L. Mao, L. L. Zhang, H. S. On Chan, X. S. Zhao and J. Wu, *J. Mater. Chem.* **2011**, *21*, 7302; d) Y. F. Huang and C. W. Lin, *Polymer* **2012**, *53*, 1079; e) L. Chen, Z. Xu, J. Li, Y. Li, M. Shan, C. Wang, Z. Wang, Q. Guo, L. Liu, G. Chen and X. Qian, *J. Mater. Chem.* **2012**, *22*, 13460.

[5] a) G. K. Dimitrakakis, E. Tylianakis and G. E. Froudakis, *Nano Lett.* **2008**, *8*, 3166; b) L. L. Zhang, Z. Xiong and X. S. Zhao, *ACS Nano* **2010**, *4*, 7030; c) F. Du, D. Yu, L. Dai, S. Ganguli, V. Varshney and A. K. Roy, *Chem. Mater.* **2011**, *23*, 4810.

[6] a) J. W. Burress, S. Gadipelli, J. Ford, J. M. Simmons, W. Zhou and T. Yildirim, *Angew. Chem. Int. Ed.* **2010**, *49*, 8902; b) G. Srinivas, J. W. Burress, J. Ford and T. Yildirim, *J. Mater. Chem.* **2011**, *21*, 11323.

[7] G. Garberoglio, N. M. Pugno and S. Taioli, *J. Phys. Chem. C* **2015**, *119*, 1980.

[8] K. Yuan, Y. Xu, J. Uihlein, G. Brunklaus, L. Shi, R. Heiderhoff, M. Que, M. Forster, T. Chassé, T. Pichler, T. Riedl, Y. Chen and U. Scherf, *Adv. Mater.* **2015**, *27*, 6714.

[9] K. Yuan, T. Hu, Y. Xu, R. Graf, G. Brunklaus, M. Forster, Y. Chen and U. Scherf, *ChemElectroChem* **2016**, *3*, 822.

[10] P. Sekar, B. Anothumakkool and S. Kurungot, *ACS Appl. Mater. Interfaces* **2015**, *7*, 7661.

[11] B. Yao, C. Li, J. Ma and G. Shi, *PCCP* **2015**, *17*, 19538.

[12] J. Liu, G. Hu, Y. Yang, H. Zhang, W. Zuo, W. Liu and B. Wang, *Nanoscale* **2016**, *8*, 2787.

[13] a) B. Li, K. Fan, X. Ma, Y. Liu, T. Chen, Z. Cheng, X. Wang, J. Jiang and X. Liu, *J. Colloid Interface Sci.* **2016**, *478*, 36; b) R. Balasubramanian and S. Chowdhury, *J. Mater. Chem. A* **2015**, *3*, 21968; c) T. Tsoufis, F. Katsaros, Z. Sideratou, G. Romanos, O. Ivashenko, P. Rudolf, B. J. Kooi, S. Papageorgiou and M. A. Karakassides, *Chem. Commun.* **2014**, *50*, 10967.

[14] K. Pramoda, U. Gupta, I. Ahmad, R. Kumar and C. N. R. Rao, *J. Mater. Chem. A* **2016**, *4*, 8989.

[15] K. Pramoda, R. Kumar and C. N. R. Rao, *Chem. Asian J.* **2015**, *10*, 2147.

[16] a) I. V. Lightcap and P. V. Kamat, *Acc. Chem. Res.* **2013**, *46*, 2235; b) H. Chang and H. Wu, *Adv. Funct. Mater.* **2013**, *23*, 1984.

[17] a) Y. Zhu, S. Murali, W. Cai, X. Li, J. W. Suk, J. R. Potts and R. S. Ruoff, *Adv. Mater.* **2010**, *22*, 3906; b) Z.-J. Fan, W. Kai, J. Yan, T. Wei, L.-J. Zhi, J. Feng, Y.-m. Ren, L.-P. Song and F. Wei, *ACS Nano* **2011**, *5*, 191; c) C. N. R. Rao, K. S. Subrahmanyam, H. S. S. R. Matte, B. Abdulhakeem, A. Govindaraj, D. Barun, K. Prashant, G. Anupama and J. L. Dattatray, *Sci. Tech. Adv. Mater.* **2010**, *11*, 054502.

[18] a) X. Wan, Y. Huang and Y. Chen, *Acc. Chem. Res.* **2012**, *45*, 598; b) L. Dai, *Acc. Chem. Res.* **2013**, *46*, 31; c) S. Mao, G. Lu and J. Chen, *Nanoscale* **2015**, *7*, 6924.

[19] A. Peigney, C. Laurent, E. Flahaut, R. R. Bacsa and A. Rousset, *Carbon* **2001**, *39*, 507.

[20] C. Lee, X. Wei, J. W. Kysar and J. Hone, *Science* **2008**, *321*, 385.

[21] a) E.-i. Negishi, *J. Organomet. Chem.* **2002**, *653*, 34; b) K. Sonogashira, *J. Organomet. Chem.* **2002**, *653*, 46; c) M. Bakherad, *Appl. Organomet. Chem.* **2013**, *27*, 125.

[22] W. S. Hummers and R. E. Offeman, *J. Am. Chem. Soc.* **1958**, *80*, 1339.
[23] M. Jahan, Q. Bao, J.-X. Yang and K. P. Loh, *J. Am. Chem. Soc.* **2010**, *132*, 14487.
[24] M. M. Dubinin, *Chem. Rev.* **1960**, *60*, 235.
[25] Z. Jin, W. Lu, K. J. O'Neill, P. A. Parilla, L. J. Simpson, C. Kittrell and J. M. Tour, *Chem. Mater.* **2011**, *23*, 923.
[26] S.-T. Zheng, J. J. Bu, T. Wu, C. Chou, P. Feng and X. Bu, *Angew. Chem. Int. Ed.* **2011**, *50*, 8858.
[27] a) E. Neofotistou, C. D. Malliakas and P. N. Trikalitis, *Chem. Eur. J.* **2009**, *15*, 4523; b) R. Banerjee, A. Phan, B. Wang, C. Knobler, H. Furukawa, M. O'Keeffe and O. M. Yaghi, *Science* **2008**, *319*, 939.
[28] a) M. Dincă, A. Dailly, Y. Liu, C. M. Brown, D. A. Neumann and J. R. Long, *J. Am. Chem. Soc.* **2006**, *128*, 16876; b) K. S. Park, Z. Ni, A. P. Côté, J. Y. Choi, R. Huang, F. J. Uribe-Romo, H. K. Chae, M. O'Keeffe and O. M. Yaghi, *Proc. Natl. Acad. Sci. USA* **2006**, *103*, 10186.
[29] a) S. Sircar and D. V. Cao, *Chem. Eng. Technol.* **2002**, *25*, 945; b) M. M. Biswas and T. Cagin, *J. Phys. Chem. B* **2010**, *114*, 13752.
[30] E. Tylianakis, G. K. Dimitrakakis, S. Melchor, J. A. Dobado and G. E. Froudakis, *Chem. Commun.* **2011**, *47*, 2303.
[31] a) W. Liu, Y. H. Zhao, Y. Li, Q. Jiang and E. J. Lavernia, *J. Phys. Chem. C* **2009**, *113*, 2028; b) P. Chen, X. Wu, J. Lin and K. L. Tan, *Science* **1999**, *285*, 91; c) E. Tylianakis, G. M. Psofogiannakis and G. E. Froudakis, *J. Phys. Chem. Lett.* **2010**, *1*, 2459; d) W.-Q. Deng, X. Xu and W. A. Goddard, *Phys. Rev. Lett.* **2004**, *92*, 166103.
[32] a) R. Vaidhyanathan, S. S. Iremonger, G. K. H. Shimizu, P. G. Boyd, S. Alavi and T. K. Woo, *Science* **2010**, *330*, 650; b) B. Chen, N. W. Ockwig, A. R. Millward, D. S. Contreras and O. M. Yaghi, *Angew. Chem. Int. Ed.* **2005**, *44*, 4745; c) A. M. Plonka, D. Banerjee, W. R. Woerner, Z. Zhang, N. Nijem, Y. J. Chabal, J. Li and J. B. Parise, *Angew. Chem. Int. Ed.* **2013**, *52*, 1692.
[33] R. Kitaura, R. Matsuda, Y. Kubota, S. Kitagawa, M. Takata, T. C. Kobayashi and M. Suzuki, *J. Phys. Chem. B* **2005**, *109*, 23378.
[34] X. Zhuang, F. Zhang, D. Wu, N. Forler, H. Liang, M. Wagner, D. Gehrig, M. R. Hansen, F. Laquai and X. Feng, *Angew. Chem. Int. Ed.* **2013**, *52*, 9668.

Chapter 6: BN-graphene composites generated by covalent cross-linking with organic linkers *

Summary

In this chapter, a new synthesis protocol for synthesizing uniform composites of two different layered materials is explained. Covalent cross-linking instead of van der Waals interaction between two different layered materials results in more uniform and homogeneous composites with better control over the functional properties. Composites of hexagonal boron nitride (BN) and carboxylated graphene (G) have been prepared for the first time by covalent cross-linking employing the carbodiimide reaction. $BN_{1-x}G_x$ ($x \approx 0.25$, 0.5 and 0.75) so obtained, has been characterized by a variety of spectroscopic techniques and thermogravimetric analysis. The composites show composition–dependent electrical resistivity, the resistivity decreasing with increase in the graphene content. The composites exhibit microporosity and the $x \approx 0.75$ composite especially exhibits satisfactory performance with high stability as an electrode in supercapacitors. The $x \approx 0.75$ composite is also found to be a good electrocatalyst for the oxygen reduction reaction in fuel cells.

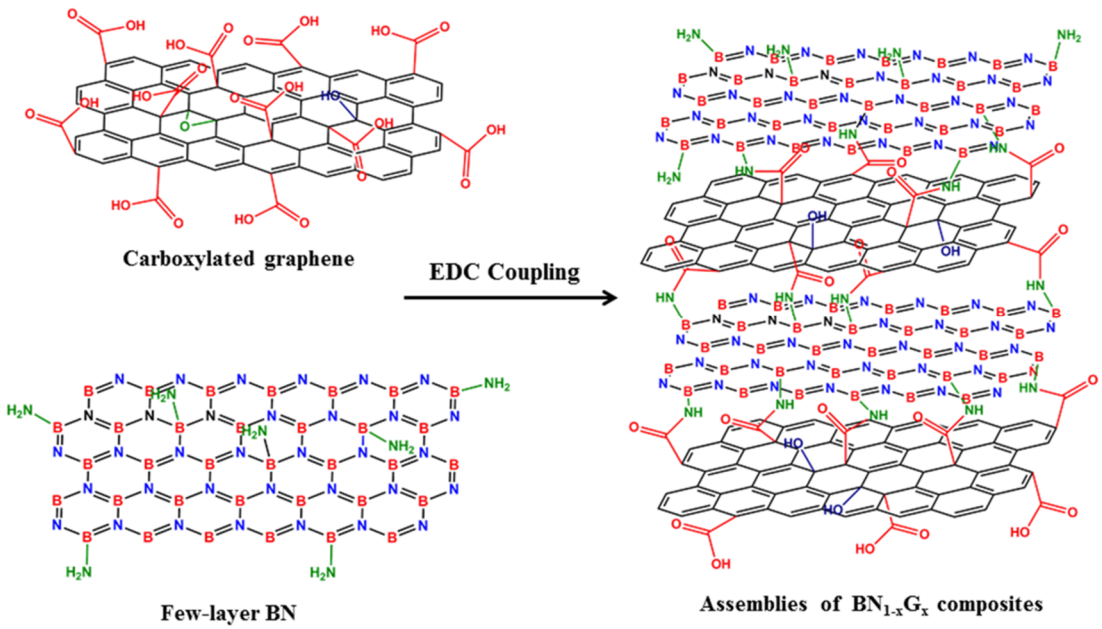

A paper based on these studies has appeared in Adv. Funct. Mater. 2015, 25, 5910.

6.1 Introduction

Hexagonal boron nitride (BN) is a layered insulator while graphene is a layered conductor. Although *h*-BN nanosheets and graphene are isoelectronic with the same layered structure, there are essential differences in the chemistry and properties of BN nanosheets. One B atom and one N atom have the same number of valence electrons as two C atoms. Thus *h*-BN sp^2 hybridized layer of B–N bonds has almost the same structure as graphene. Although BN is isoelectronic with graphene the electronegativity difference (Pauling electronegativity, B = 2 and N = 3) between the B and N atom causes essential differences in chemical bonding and B–N bond is ≈ 22% ionic in character whereas C–C bond is covalent.[1] This is observed in properties and *h*-BN is a large band gap insulator (~5.8 eV) whereas graphene is a conductor. Numerous potential applications of these two nanomaterials have been reported in the recent literature.[2] Composites of BN and graphene are expected to be materials of great interest and there have been efforts to study ternary borocarbonitrides, $B_xC_yN_z$ with varying carbon content.[3] Synthesis of few-layer *h*-BCN has been achieved by solid state chemistry route and chemical vapor deposition (CVD) techniques.[3b,4] These systems consist of hybridized, randomly distributed domains of *h*-BN and C phases with variable compositions. By varying the C content optical, electrical and other functional properties of the borocarbonitrides can be tuned.[3a,4b,5] There has also been an effort to deposit BN sheets over graphene and vice versa.[3a,6] Two different approaches have been employed to prepare such hybrid heterostructures of BN and graphene. Graphene and BN nanosheets were prepared by exfoliation of graphite powder and bulk *h*-BN. Subsequently, graphene and BN were mixed and self-assembled using van der Waals interaction.[7] The second approach involves sequential CVD growth of BN and graphene on a substrate.[6] The present investigation involves a new approach for preparing hybrid composites of BN and graphene with different compositions by covalent cross-linking using organic linkers. Recently this new approach of covalent cross-linking has been utilized to prepare assemblies of single-walled carbon nanotubes as well as graphene.[8] Use of strong covalent bond instead of weak van der Waals interaction has resulted in very robust assemblies with many interesting functional properties. Graphene–BN composites prepared by covalent cross-linking would be expected to possess properties different from those obtained by depositing BN and graphene sheets on each other where van der Waals interaction plays the lead role. Synthesis of $BN_{1-x}G_x$ composites with varying graphene content (x = 0 – 1), their electrical and functional properties are investigated in detail. Since heavily nitrogenated graphene, as well as borocarbonitrides, are reported to show good

characteristics as electrodes in supercapacitors as well as in the ORR,[9] the use of the $BN_{1-x}G_x$ composites in supercapacitors and as catalysts in the oxygen reduction reaction (ORR) in fuel cells is explored. The present study of synthesizing composites of two different materials by linking them through strong covalent bond gives a better control over properties and composition and can be used to design several such composite materials for different applications.

6.2 Scope of the present investigations

Composites often find novel applications much enhanced properties relative to the constituent components.[10] Many times the composites have superior performance in comparison to individual components due to synergistic effects.[10b] This synergistic effect depends on the interaction between individual component and the effects are high when interactions between the individual components are good. One of the main problems in composite synthesis is of heterogeneity and many times the obtained composites are just a physical mixture. If the composites have chemical interaction observed synergistic effects are high.[11] In this chapter a new strategy for the composite synthesis of 2D materials is explained, namely covalent cross-linking. The 2D materials have a very strong in-plane chemical bond but have van der Waals interaction between the individual layers along the perpendicular direction. Recently, there has been significant interest to combine two different layered materials to prepare composite heterostructures with new physical properties.[6-7,12] The approach involves mixing these layered materials in polar solvent and sonication followed by filtration.[7] The van der Waals interactions bring the two different layered materials together. Another approach involves sequential CVD growth of one material over another or physically depositing one over the other.[6b,12a,b] The van der Waals force controls the interactions of such composite heterostructures. The present study focuses on a new strategy of composite synthesis where the individual components of composites BN and graphene are covalently bonded to each other. The formation of a uniform covalent bond between the constituent components results in better homogeneity and control over the physical and chemical properties of the resulting composites. The covalent cross-linking strategy results in better control over the composition and properties of $BN_{1-x}G_x$ composites ($x = 0 - 1$) due to control over the assembly of individual components in the composite. The rate of reaction between two different solid reactants is generally low in comparison to gas and liquid phase reactions.

Rate of a chemical reaction can be given by

$$Rate = PZe^{-Ea/RT} \quad \text{..... (1)}$$

Where,

P = probability factor *e* = 2.718 (base of natural logarithms)

Z = collision frequency *R* = 1.986 (gas constant)

Ea = activation energy *T* = absolute temperature

Probability factor is the fraction of collisions that have proper orientation and collision frequency is the total number of collisions per cc per sec.

Reactions in the gaseous and liquid state are faster in comparison to solid state because of higher probability factor, collision frequency, and lower activation energy. Often stirring, an increase in reaction temperature or use of a catalyst to decrease the activation energy barrier is employed to increase the rate of reaction in the liquid phase. The solid state reactions are generally carried out at a higher temperature to overcome the constraints of a pre-exponential factor and overcome the activation energy barrier in rate equation. Formation of an amide bond between BN and graphene nanosheets is also hindered by these factors. In order to overcome the difficulty of performing a reaction in the liquid phase, we have carried out the reaction using EDC coupling method which decreases the activation energy barrier and catalyzes the amide bond formation between two substrates very efficiently. The carboxylate group on graphene and amine functional groups on the BN basal plane undergoes amide bond formation using EDC coupling reagents. The amide bond formation between the two substrates namely BN and graphene drives the assembly of BN and graphene resulting in the formation of homogeneous composites. The resulting composites are very uniform with control over composition and properties. The $BN_{1-x}G_x$ (x = 0.25, 0.5 and 0.75) composites have been extensively characterized using solid-state NMR, IR, EELS, Raman, and XPS. The properties of these composites can be tuned by varying the composition. Thus, the composites show an increase in resistivity with increasing BN content. The covalent bond between BN and graphene nanosheets results in high synergistic interactions between individual components in the composites. The $BN_{1-x}G_x$ composites show better performance with high stability as an electrode in supercapacitors and electrocatalyst for the oxygen reduction reaction in fuel cells in comparison to the individual component attributed to synergistic interactions. Covalent chemistry of BN nanosheets is

largely unexplored and the present investigation may encourage the development of covalent modification protocols of BN nanosheets and other materials for different applications.

6.3 Experimental section

Reagents and precursors: All the chemicals used in synthesis were of high purity and obtained from commercial sources. *N*,*N*-Dimethylformamide (DMF) was pre-dried before reaction. Amine functionalized few-layer BN (~1–4 layers) was prepared by mixing boric acid and urea in 1:48 molar ratio and heating in high purity ammonia atmosphere at 900 °C for 5h.[13] Graphite oxide (GO) was synthesized using modified Hummers method.[8a] GO was placed in an alumina boat inside a quartz tube and inserted into the heating zone of the furnace at 1050 °C under constant N_2 flow to obtain the exfoliated graphene (EG). Carboxylate functionalized graphene was obtained by microwave irradiation. In a typical batch 200 mg, EG was placed in 125 ml microwave reactor, 8 ml conc. HNO_3, 8 ml conc. H_2SO_4, 64 ml deionized H_2O was added and irradiated with microwave for 10 min at 450 W followed by heating in an oven at 100 °C for 12 h.[14] Obtained product was filtered using 0.45 μm PTFE membrane, washed with copious amount of water to remove excess acid and dried at 100 °C.

Synthesis of $BN_{1-x}G_x$ composites using EDC coupling: Three different composites $BN_{1-x}G_x$ ($x \approx 0.25$, 0.5 and 0.75) were obtained by varying the ratio of BN with respect to carboxylated graphene. In a Schlenck flask 150 mg of BN and carboxylated graphene was mixed in an appropriate ratio, purged with N_2, sealed using septum and 35 ml DMF was added. Uniform dispersion was obtained by sonication. In the uniform dispersion *N*-(3-Dimethylaminopropyl)-*N'*-ethylcarbodiimide hydrochloride (EDC.HCl) 80 mg, 1-Hydroxybenzotriazole (HOBt) 80 mg and *N,N*-Diisopropylethylamine (DIPEA) 1.2 ml was added under constant stirring and allowed for 48 h. A nitrogen atmosphere was maintained during the reaction. Obtained product was filtered using 0.45 μm PTFE membrane, washed with copious amount of DMF and water. The solid product was further washed with methanol in a Soxhlet extractor for 48 h and dried at 100 °C under vacuum. Further, $BN_{1-x}G_x$ samples were annealed at 300 °C in N_2 atmosphere for 6 h and IR spectra were recorded to monitor the loss of amide bond between BN and graphene.

Electrochemical measurements:

(a) Supercapacitor: Supercapacitor measurements were performed on PGSTAT 262 A (Techno Science Instruments) electrochemical workstation in 2 M H_2SO_4 aqueous electrolyte.

Three-electrode assembly was used with a catalyst coated glassy carbon (GC) electrode as the working electrode (WE), large-area Pt foil and standard calomel electrode (SCE) as counter and reference electrodes respectively. The working electrode was fabricated by dispersing 3 mg of sample in 1 mL ethanol-water mixture (1:1) and drop casting 10 µL on glassy carbon electrode followed by 10 µL of 0.05 wt.% Nafion solution as a binder. The electrodes were dried at 60 °C. Cyclic voltammetry (CV) measurements were carried out at different scan rates from 2 to 100 mV/s. Electrochemical impedance spectroscopy (EIS) measurements were studied by applying an AC voltage with 10 mV amplitude in the frequency range from 0.1 Hz to 100 kHz. A galvanostatic charge–discharge (GCD) test was also conducted at different current densities. The specific capacitance (C_{sp}) was calculated using the following formula from CV, $C_{sp} = (i_+ - i_-)/(m \times \text{scan rate})$. Where, i_+ and i_- are the maximum values of current in the positive scan and negative scan respectively and m is the mass of single electrode. Specific capacitance was calculated from galvanostatic charge-discharge curves using the formula, $C_{sp} = (i)(\text{dt})/(m \times dv)$.

(b) Oxygen reduction reaction (ORR): A standard three-electrode cell with Pt plate as the counter electrode was used for the ORR study. For the oxygen reduction reaction, the catalyst was prepared by dispersing the catalyst (5 mg) in 1 mL mixture of ethanol and water in the presence of 0.05 wt% Nafion. From this solution, 4 µL catalyst ink was drop cast on a glassy carbon electrode (GCE) (3 mm diameter). Electrochemical measurements were performed in an O_2-saturated aqueous 0.1 M potassium hydroxide (KOH) solution (standard calomel electrode (SCE) reference electrode). Rotating disc electrode (RDE) measurements were carried out with a system from Beckman instruments, USA by coupling with a galvanostat/potentiostat PGSTAT 262A, Techno Science Instruments, Bangalore. The number of electrons transferred per oxygen molecule from the $BN_{1-x}G_x$ modified electrode can be calculated by using the Koutechy-Levich equation:

$$1/I = 1/i_k + 1/i_d$$

$$1/i = -1/(nFkC_0) - 1/(0.62\, nFD_0^{2/3}\gamma^{-1/6}C_0\omega^{1/2})$$

Here, I denote the measured current densities at the respective potentials, whereas i_k and i_d represent kinetic and diffusion current densities respectively and n gives the overall number of electrons transferred per O_2 molecule. F is the Faraday constant (96485 C mol^{-1}), C_0 the bulk concentration of O_2 (1.2×10^{-6} mol mL^{-1}), k the electron transfer rate constant, D_0 the O_2 diffusion coefficient (1.73×10^{-5} cm^2 s^{-1}) in 0.1 M KOH, γ kinematic viscosity (0.0109 cm^2 s^{-1})

and ω the rotation speed of the electrode. The number of electrons transferred, *n*, is obtained by calculating the slope of i^{-1} *vs* ω^{-1} plot.

The kinetic current density was calculated by the following equation.

$i_k = (i \times i_d)/(i_d - i)$

Where i_k is the kinetic current density, i_d is the measured diffusion limited current density, and *i* is the measured current density.

Instrumentation and characterization: FTIR spectra were recorded on a Bruker FT-IR spectrometer using attenuated-total-reflectance accessories. Raman spectra were recorded at several different spots in backscattering geometry using 514.5 nm Ar^+ laser in HORIBA LabRam HR800 spectrometer. Solid state ^{13}C magic angle spinning (MAS) NMR spectrum was collected in Bruker AVANCE 400 MHz spectrometer. Elemental mapping using energy-dispersive X-ray spectroscopy (EDX) and scanning electron microscope images were obtained using Nova Nano SEM 600, FEI. Transmission Electron Microscope (TEM) images were collected using the FEI Tecnai with an accelerating voltage of 200 kV. Electron energy loss spectra (EELS) were recorded in Titan FEI, TEM with an accelerating voltage of 300 kV. Thermogravimetric analysis (TGA) was performed using Mettler Toledo TGA 850 in an oxygen atmosphere with a heating rate of 3 °C/ min. X-ray photoelectron spectra (XPS) were collected in an Omicron Nanotechnology Spectrometer with Mg Kα as the X-ray source. PXRD pattern was recorded in Bruker diffractometer using Cu K-α radiation. The N_2 sorption isotherm at 77 K was obtained using QUANTACHROME QUADRASORB-*SI* analyzer. The samples were heated at 383 K under vacuum for 12 h prior to the measurement of the isotherm. Electrical resistivity was obtained using four probe method on the composite pellets in physical property measuring system by Quantum design. Four equidistant linear contact points of gold were made over 8 mm composite pellet using RF sputtering. Copper wires were connected to these gold contact points using silver paste.

6.4 Results and discussion

Scheme 1 shows the steps involved in the synthesis of the amide bond cross-linked assemblies of BN and graphene ($BN_{1-x}G_x$, $x \approx 0.25, 0.5, 0.75$). Carboxylate functionalized graphene (G) obtained by microwave irradiation of graphene in an HNO_3/H_2SO_4 mixture,[14] was reacted with amine–functionalized few-layer BN (~ 1 – 4 layers) prepared by heating boric acid and urea in 1:48 molar ratio in an ammonia atmosphere.[13,15] The carbodiimide

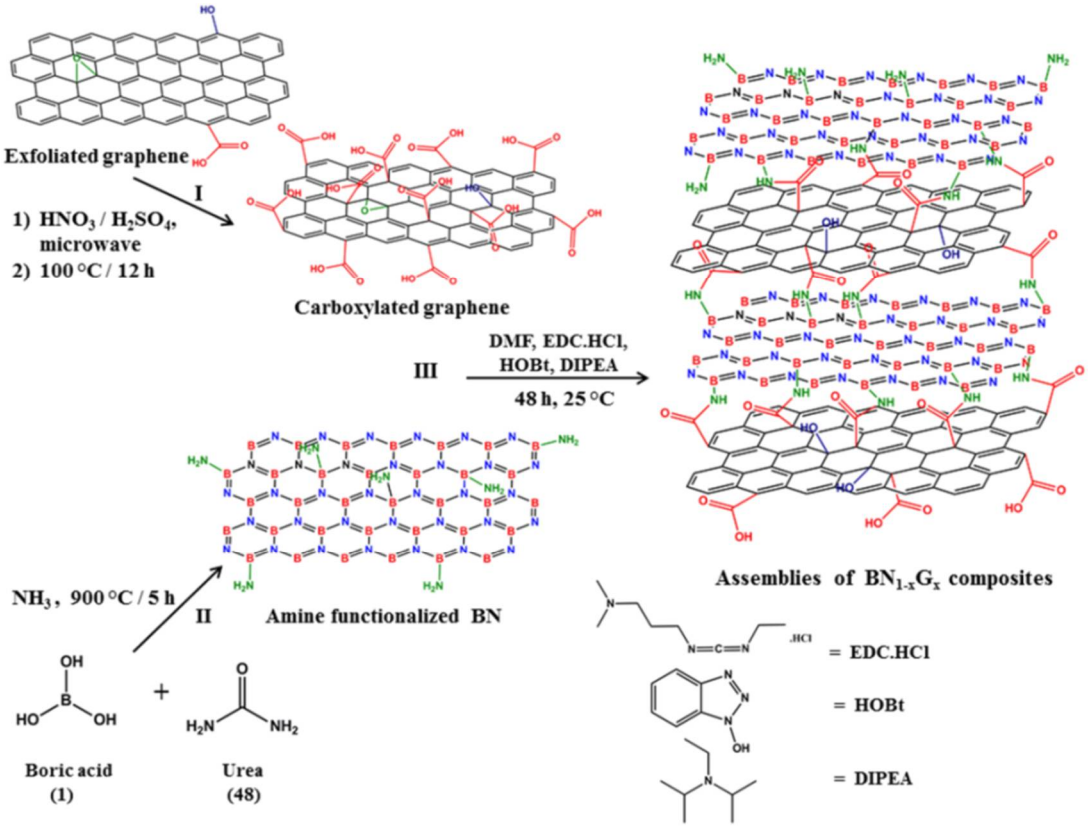

Scheme 1. Schematic representation of the synthesis of covalently cross-linked assemblies of BN and graphene using EDC coupling. **(I)** Synthesis of carboxylated graphene; **(II)** synthesis of amine functionalized few-layer BN; **(III)** Synthesis of assemblies of $BN_{1-x}G_x$ composites by amide bond cross-linking using EDC coupling.

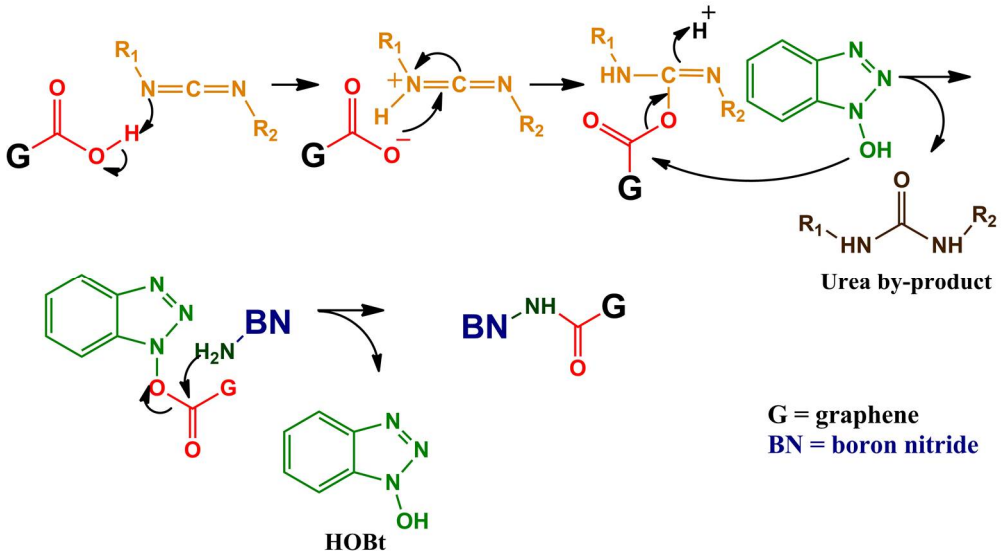

Figure 1. Mechanism of the activation of carboxylate groups on graphene basal plane for amide bond formation with BN using the EDC coupling protocol. The present mechanism shows representative activation of one carboxylate group and amide bond formation with BN. Several such functional groups on graphene and BN basal plane are activated and amide bond formation directs the assembly of BN—graphene composite heterostructure $BN_{1-x}G_x$ where ($x \approx 0.25, 0.5$ and 0.75).

method was used to link BN and G with an amide bond, by using EDC {1-ethyl-3-(3-dimethylaminopropyl)carbodiimide)} as the reagent (see experimental section 6.3 for details).[16] The advantage of EDC coupling over $SOCl_2$ - based activation is that no HCl is liberated and urea obtained as a by-product is a water soluble. Three different compositions of the $BN_{1-x}G_x$ composites ($x \approx 0.25$, 0.5 and 0.75) were obtained by varying the ratio of BN with respect to graphene.

The $BN_{1-x}G_x$ composites were examined using electron microscopy. Figure 2 shows typical electron microscope images of few-layer BN, carboxylated graphene and $BN_{0.5}G_{0.5}$. Transmission electron microscope (TEM) images of few-layer BN and carboxylated graphene show wrinkled transparent sheets. The TEM and scanning electron microscope (SEM) images of the $BN_{1-x}G_x$ composites show layer by layer self-assembly of the component sheet structures (Figure 2). The layer by layer self-assembly of graphene and BN is facilitated by amide bond formation between the amine group on the BN sheets and the carboxylate groups on the graphene sheets. Elemental mapping of the $BN_{1-x}G_x$ using energy-dispersive X-ray spectroscopy (EDAX) shows a uniform distribution of B, N, and C confirming homogeneous nature of the composite (Figure 3).

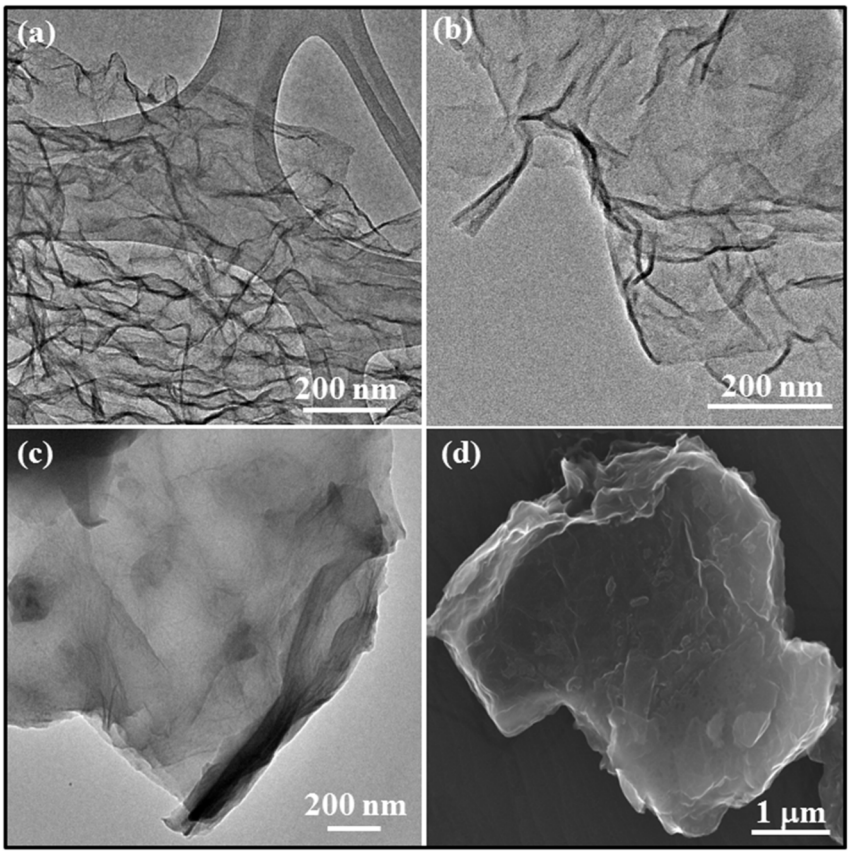

Figure 2. TEM images of (a) few-layer BN, (b) carboxylated graphene, (c) and (d) TEM and SEM images of $BN_{0.5}G_{0.5}$.

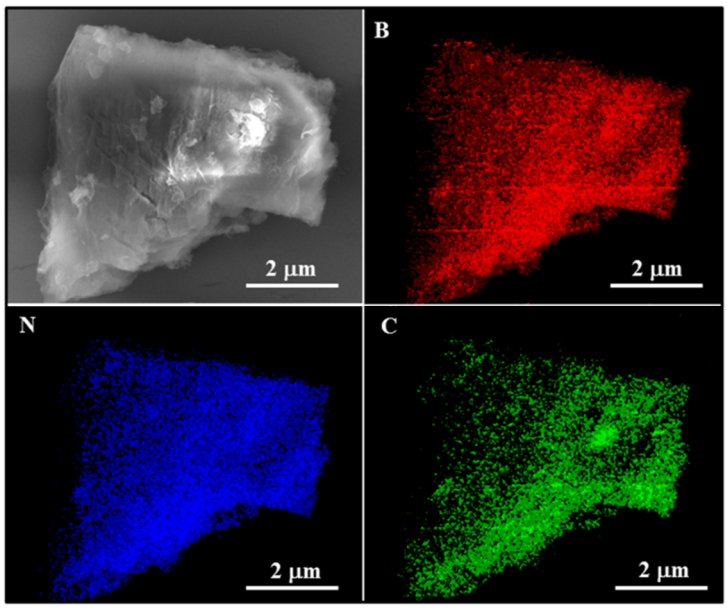

Figure 3. Elemental mapping of $BN_{0.5}G_{0.5}$. B (red), N (blue) and C (green).

The electron energy loss spectrum (EELS) of $BN_{0.5}G_{0.5}$ displayed in figure 4 shows the K-shell ionization edges of B, N, C and O respectively. The K-shell ionization edge at 192.6 eV is due to the transition of B 1s electron to the π^* antibonding orbitals, associated with planar bonding and sp^2 hybridization of boron. The signals in 200 - 216 eV range are due to 1*s* $\rightarrow \sigma^*$ transition of boron in BN. The N EEL spectrum have peak at 402.5 eV assigned to 1*s* $\rightarrow \pi^*$ whereas peaks at 409 and 416 eV are due to 1*s* $\rightarrow \sigma^*$ transitions from BN. [17] The C K-shell ionization edge have bands at 286 and 296 eV corresponding to 1*s* $\rightarrow \pi^*$ and 1*s* $\rightarrow \sigma^*$ transitions of graphene.[17a,18] The O-K shell ionization is also observed at 541 eV due to oxygen-containing functional groups in the composite.[19]

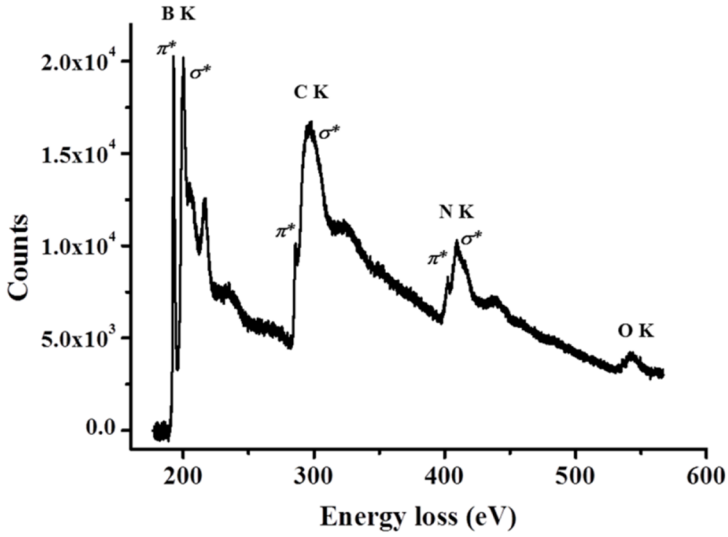

Figure 4. Electron energy loss spectrum (EELS) of the $BN_{0.5}G_{0.5}$ composite.

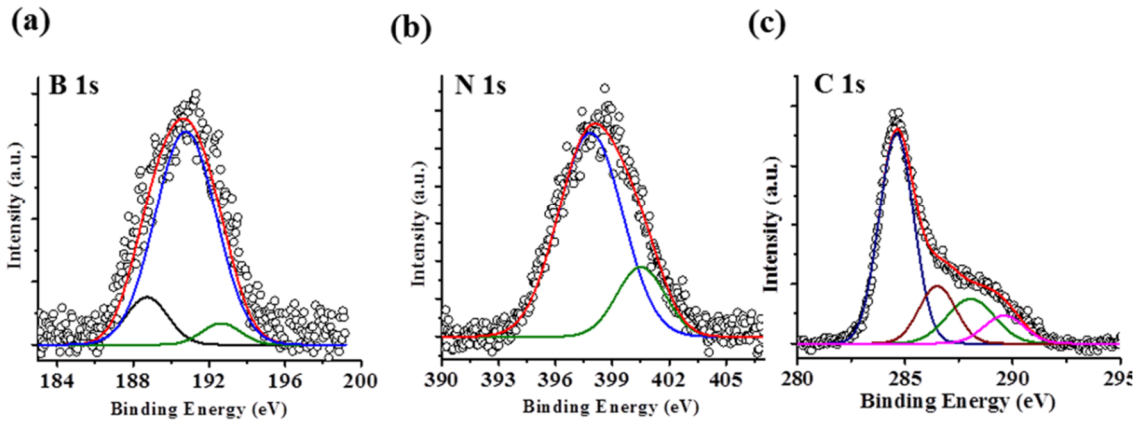

Figure 5. X-ray photoelectron spectrum of $BN_{0.5}G_{0.5}$ composite (a) B 1s, (b) N 1s, (c) C 1s.

Core level X-ray photoelectron spectra (XPS) of $BN_{0.5}G_{0.5}$ are shown in figure 5. The B 1s core level has the main peak at 190.7 eV corresponding to B−N bonding along with two minor contributions at 188.8 eV and 192.7 eV due to the interaction of B with C and O of graphene basal plane.[20] The N 1s core level has signal at 398 eV due to bonding with B. The peak at 400.5 eV is due to N of amide groups on the BN basal plane.[15b,20a] The C 1s core level spectrum shows signals at 284.6 and 288 eV due to graphene (sp^2) and amide carbons.[21] The carboxylate functionalization of graphene involves HNO_3/H_2SO_4 treatment which introduces minor density of epoxide and hydroxyl groups. This is reflected as additional broadness of the C 1s spectrum. The peak at 286.4 eV has contributions from sp^3 C along with the minor concentration of epoxide and hydroxyl groups. Unreacted carboxylate group is reflected as a minor contribution at 289 eV.[21a]

The direct pulse ^{13}C and ^{11}B solid state NMR spectra of $BN_{0.5}G_{0.5}$ were collected at 20 kHz and 14 kHz MAS respectively at a magnetic field of 9.4 T (Figure 6). The ^{13}C NMR spectrum has signals centered at 122 ppm corresponding to the sp^2 aromatic carbon domains present on the carboxylated graphene basal plane. The aromatic signal at 142 ppm can be attributed to C in the vicinity of electronegative O and N atom. Signals in the 165–173 ppm region are assigned to the amide bond carbon along with residual unreacted carboxylate carbon. The broad signal in the 40-70 ppm region is due to the sp^3 C.[4] The broad aromatic C signal is due to the heterogeneity in the chemical environment of carbon in the sample. Thermal exfoliation of graphite oxide is used for the synthesis of graphene followed by oxidative treatment with HNO_3/H_2SO_4 to incorporate carboxylate groups on the basal plane. The synthesis method introduces defects on the graphene basal plane along with the minor density of various other oxygen-containing functional groups such as epoxide and hydroxyl, also reflected in the infrared spectra of $BN_{1-x}G_x$ composites. This heterogeneity in the

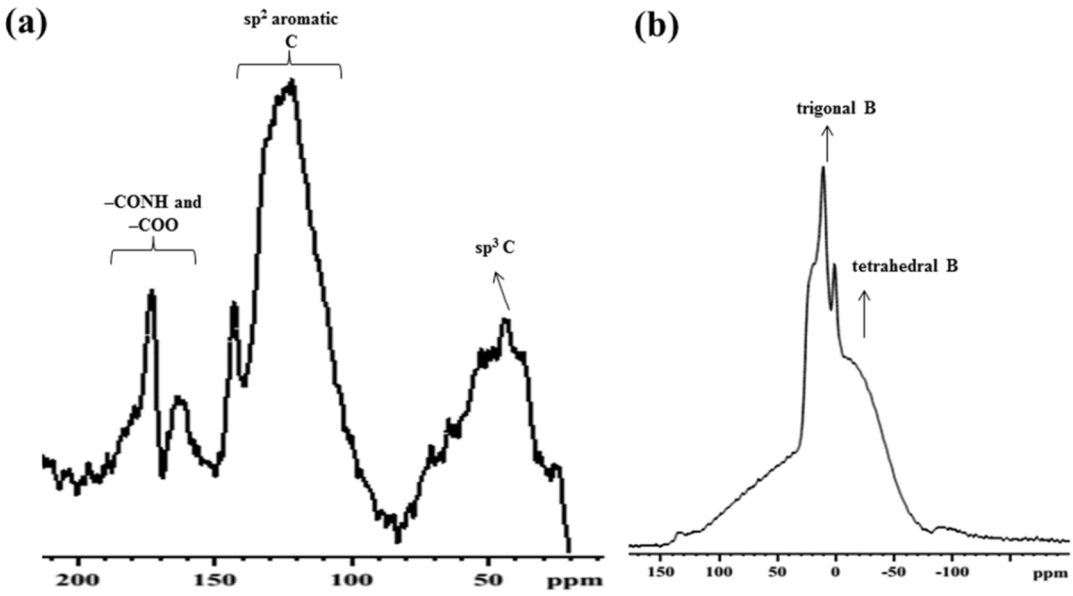

Figure 6. ^{13}C solid state NMR spectrum of the $BN_{0.5}G_{0.5}$ composite at 20 kHz MAS. (b) ^{11}B solid state NMR spectrum of the $BN_{0.5}G_{0.5}$ composite at 14 kHz MAS.

chemical environment of carbon is reflected in the broad NMR spectral line width as the spectrum is collected at 20 kHz which is reasonable to remove various anisotropic effects. The ^{11}B solid state NMR spectrum of $BN_{0.5}G_{0.5}$ has the splitting of the main peak at 10 ppm consistent with the trigonal boron site symmetry of hexagonal boron nitride.[5] The spectral line-width of synthesized few-layer BN using urea route is significantly more than that h-BN reported by Marchetti *et al*.[5] The chemical shift ranges for trigonal boron (90 to -10 ppm) and tetrahedral boron (10 to -130 ppm) are decided by the hybridization (sp^2 versus sp^3) and the resulting higher electron density at the boron atom in the tetrahedral geometry relative to that in the trigonal geometry.[5-6] The amine or amide functional group on BN basal plane will change the site symmetry of B from trigonal to tetrahedral and hence signal is expected at higher field. The ^{11}B NMR signal at the higher field (-30 ppm) can be reasonably attributed to amine or amide functionalized tetrahedral B sites of BN.

Further separation of few-layers and homogeneous mixing of BN and graphene is expected in DMF due to sonication.[7,10d,22] Subsequently, EDC coupling reagents were added which activate the carboxylate groups on graphene basal plane. The activated carboxylate group directs the assembly formation by allowing the amide bond formation with BN. Such covalent cross-linking results in greater homogeneity and better control of the composite ordering. Two or three layers of graphene sandwiched between BN sheets or vice-versa is also possible. Powder X-ray diffraction patterns of $BN_{1-x}G_x$ composites show reflections due to the (002) planes suggesting the turbostatic ordering of BN and graphene.

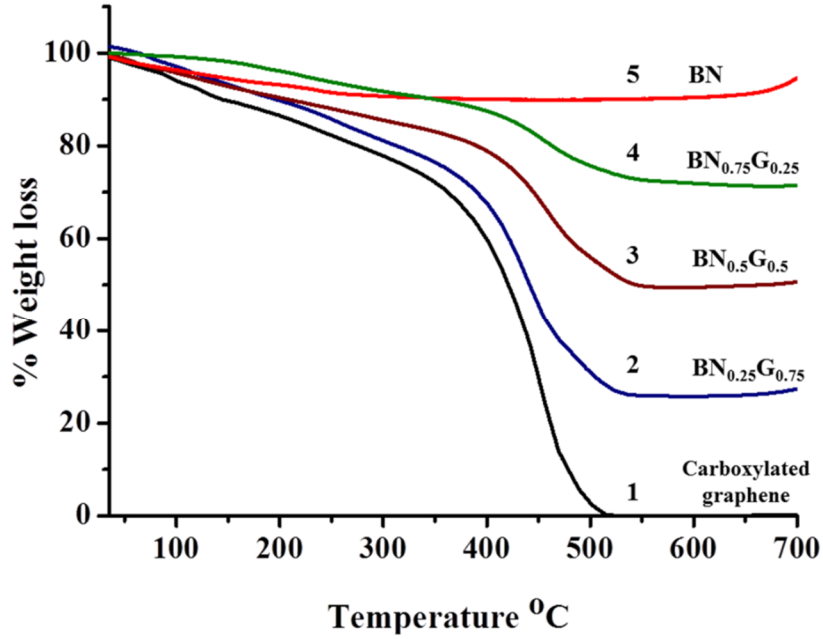

Figure 7. Thermogravimetric analysis of (1) carboxylated graphene, (2) $BN_{0.25}G_{0.75}$, (3) $BN_{0.5}G_{0.5}$, (4) $BN_{0.75}G_{0.25}$ and (5) BN in an oxygen atmosphere.

Thermogravimetric analysis was carried out in an oxygen atmosphere to determine the compositions of the composites (Figure 7). Few-layer BN has high thermal stability with no weight loss in the 500 – 700 °C range. The TGA profile of carboxylated graphene shows complete combustion in the 400 – 500 °C temperature range. The BN content in the composites can be determined from the residual weight in this temperature range. The residual weight for $BN_{0.25}G_{0.75}$, $BN_{0.5}G_{0.5}$, and $BN_{0.75}G_{0.25}$ are 24, 49.5, and 72 % respectively which match with the stated compositions.

The infrared spectrum of few-layer BN shows two strong and broad bands at 800 and 1367 cm^{-1} corresponding to the out-of-plane B−N−B bending mode (A_{2u}) and the in-plane B−N transverse optical mode (E_{1u}) respectively (Figure 8a).[23] Carboxylated graphene has IR bands at 1576, 1723 and 3450 cm^{-1} assigned to the aromatic C═C, C═O, and O–H stretching of carboxylate groups. Weak signal around 1250 cm^{-1} is attributed to the C–O stretching of epoxide and hydroxyl groups on graphene. [24] IR spectra of $BN_{1-x}G_x$ composites have bands at 1653 and 1724 cm^{-1} due to the amide bond between graphene and BN nanosheets and remaining carboxylate group on the graphene basal plane (Figure 8a).[24] As the amount of BN in the composites increases the relative intensity of the 1653 cm^{-1} amide band increases, $BN_{0.75}G_{0.25}$ showing an almost negligible intensity of the 1724 cm^{-1} band. The weak band around 1250 cm^{-1} of the composites is associated with the minor concentration of epoxide and hydroxyls on graphene and disappears on heating at 300 °C. The Raman spectrum of

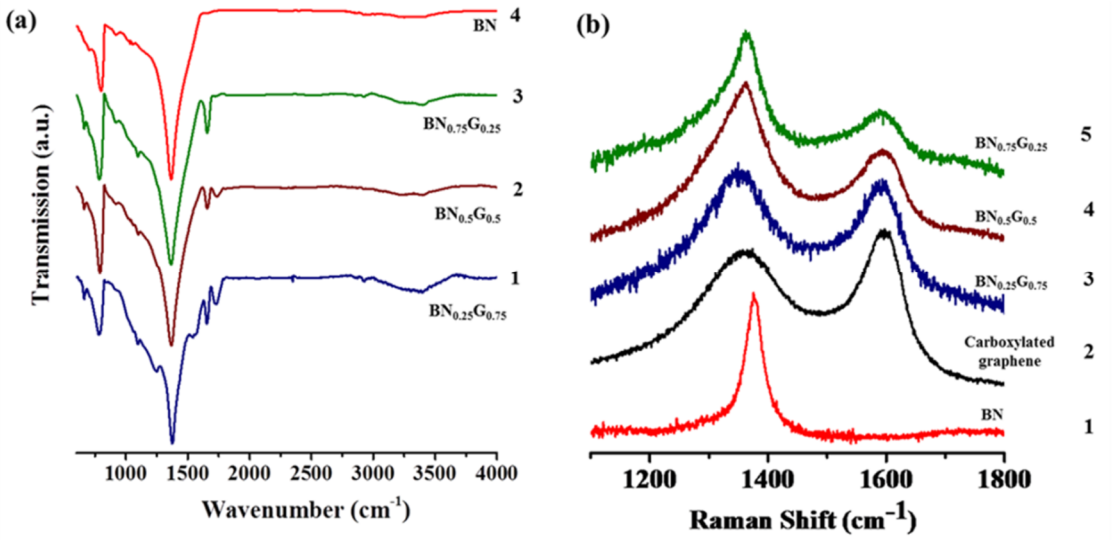

Figure 8. (a) Infrared spectra of (1) $BN_{0.25}G_{0.75}$, $BN_{0.5}G_{0.5}$ (2), $BN_{0.75}G_{0.25}$ and (3) BN. (b) Raman Spectra of (1) BN, (2) carboxylated graphene, (3) $BN_{0.25}G_{0.75}$, (4) $BN_{0.5}G_{0.5}$ and (5) $BN_{0.75}G_{0.25}$.

few-layer BN has a relatively narrow (~ 35 cm^{-1}) band at 1375 cm^{-1} corresponding to the E_{2g} mode of BN (Figure 8b).[25] Carboxylated graphene shows the characteristic *D* and *G* bands at 1359 and 1593 cm^{-1} with line widths of 165 and 75 cm^{-1} respectively.[26] Raman spectra of composites have features of both BN as well as graphene (Figure 8b). As the BN content increases in the $BN_{1-x}G_x$ composites, the spectrum shows dominating BN feature and decrease in the *G*-band intensity.

Surface area and porosity of the $BN_{1-x}G_x$ composites were obtained by N_2 adsorption at 77 K (Figure 9). The Brunauer-Emmet-Teller (BET) surface areas of $BN_{0.25}G_{0.75}$, $BN_{0.5}G_{0.5}$

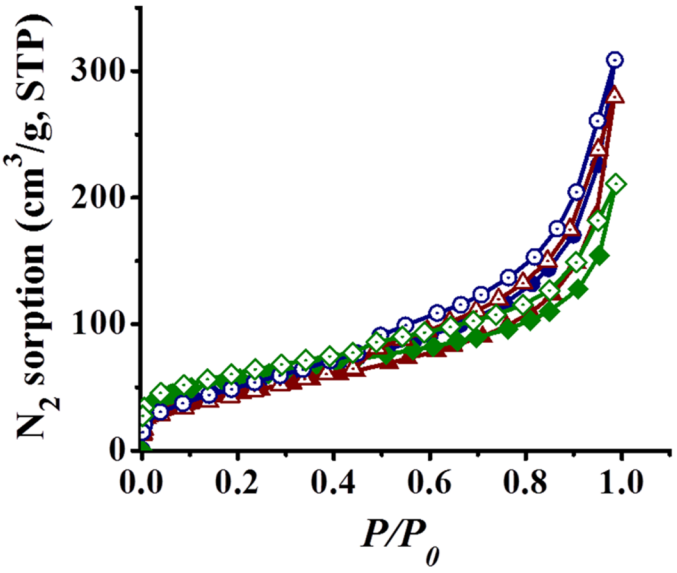

Figure 9. Nitrogen sorption profile of $BN_{0.25}G_{0.75}$ (circles), $BN_{0.5}G_{0.5}$ (triangles) and $BN_{0.75}G_{0.25}$ (diamonds) at 77 K.

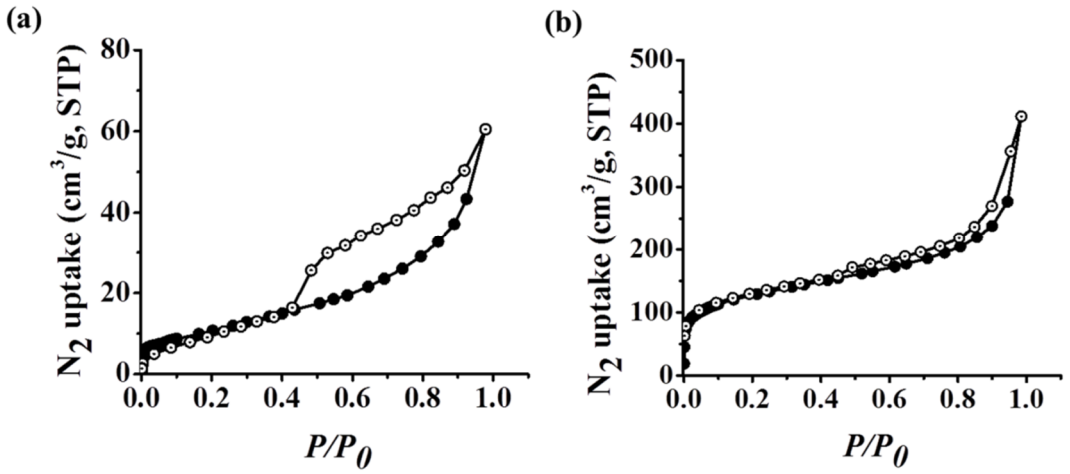

Figure 10. N_2 sorption profile of (a) Carboxylated graphene and (b) few-layer BN at 77 K. BET surface area of carboxylated graphene = 38 m^2/g and few-layer BN = 452 m^2/g respectively.

and $BN_{0.75}G_{0.25}$ are 183, 171 and 197 m^2/g respectively. The sorption profiles show type H4 hysteresis loop associated with narrow slit-like pores, with type-I isotherm character in the low-pressure region indicative of microporosity according to IUPAC classification.[27] Slit-like micropores are created due to cross-linking and stacking of BN and graphene sheets. Carboxylated graphene has a BET surface area of 38 m^2/g with type-IV mesoporous sorption profile due to agglomeration of graphene sheets (Figure 10a). Few–layer BN has type-II sorption profile with BET surface area of 452 m^2/g (Figure 10b).

Electrical resistivity data of the $BN_{1-x}G_x$ composites are shown in Figure 11. The $BN_{1-x}G_x$ composites show typical semiconducting behavior with the resistance decreasing on

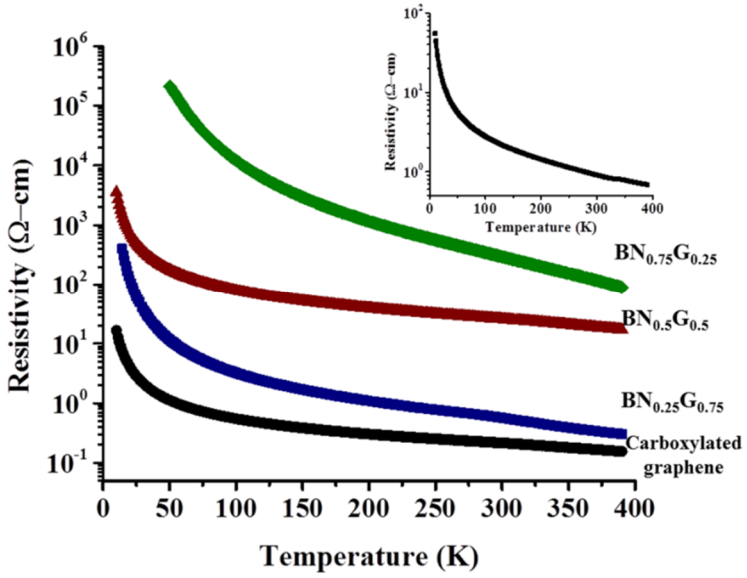

Figure 11. Temperature dependence of resistivity in $BN_{1-x}G_x$ composites (measured using four probe method). **(Inset)** Temperature–dependent resistivity of $BN_{0.5}G_{0.5}$ on annealing at 300 °C in a nitrogen atmosphere.

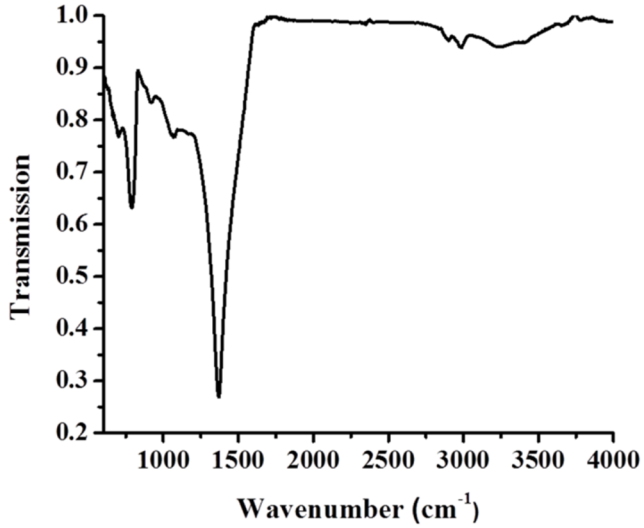

Figure 12. The infrared spectrum of $BN_{0.5}G_{0.5}$ after annealing at 300 °C in N_2 atmosphere showing the loss of amide bond.

increasing the temperature. The resistivity of the composites is least in the case of $BN_{0.25}G_{0.75}$ and increases on increasing the BN content. This is expected since BN is a known large band gap insulator. This interesting variable resistivity suggests the possible use of different $BN_{1-x}G_x$ composites for various potential applications. The resistivity of $BN_{0.5}G_{0.5}$ decreases significantly on annealing at 300 °C (see inset of Figure 11) due to the loss of the amide-linkers (Figure 12).

The presence of a slit-like microporous network in the $BN_{1-x}G_x$ composites prompted to investigate the performance of $BN_{1-x}G_x$ as supercapacitor electrode material. Electrochemical performance of the $BN_{1-x}G_x$ composites was investigated by means of cyclic voltammetry (CV), galvanostatic charge-discharge curves and electrochemical impedance spectroscopy (EIS) in 2 M H_2SO_4 electrolyte. Cyclic voltammograms of carboxylated graphene, $BN_{0.25}G_{0.75}$, $BN_{0.5}G_{0.5}$ and $BN_{0.75}G_{0.25}$ are measured at different scan rates (2 – 100 mV/s) at a voltage window of -0.2 – 0.6 V. The CV curves measured at 40 mV/s are shown in Figure 13a. The CV curves show a rectangular feature even at higher scan rates which indicate that these materials are good charge storage supercapacitor electrodes. A maximum capacitance of 217 F/g at a scan rate of 2 mV/s in the case of $BN_{0.25}G_{0.75}$ was obtained. The specific capacitance values of carboxylated graphene, $BN_{0.5}G_{0.5,}$ and $BN_{0.75}G_{0.25}$ are 89, 180, 92 F/g respectively at 2 mV/s. The galvanostatic charge-discharge curves of the BNG samples were measured in a voltage window of -0.2 – 0.6 V at different current densities. Figure 13b shows the charge-discharge curves of carboxylated graphene and $BN_{1-x}G_x$ composites measured at 1 A/g. The

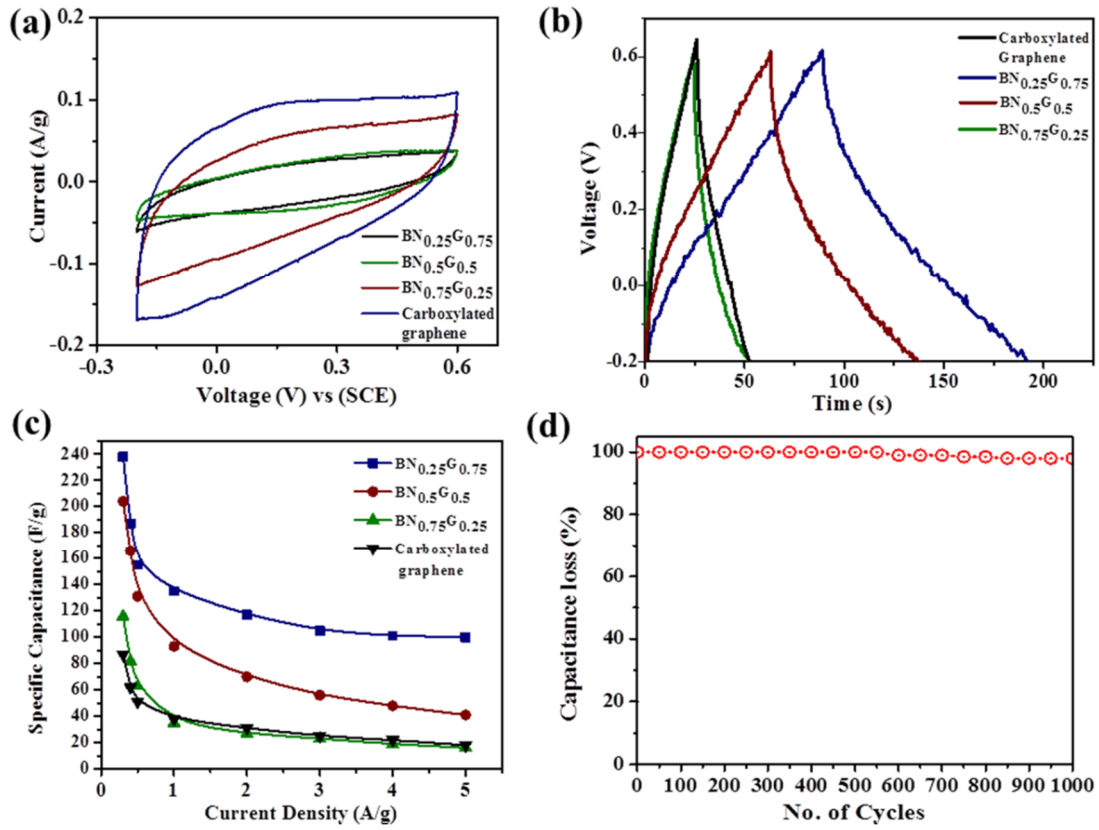

Figure 13. (a) Cyclic voltammograms of carboxylated graphene and $BN_{1-x}G_x$ electrodes at a scan rate of 40 mV/s; (b) Galvanostatic charge-discharge curves for carboxylated graphene and $BN_{1-x}G_x$ electrodes (at 1 A/g); (c) Specific capacitance as a function of discharge current and (d) % capacitance loss *versus* the cycle number of $BN_{0.25}G_{0.75}$ measured at a current density of 1 A/g within an operational window of -0.2-0.6 V. Aqueous 2 M H_2SO_4 solution used as electrolyte.

discharge time of $BN_{0.25}G_{0.75}$ was longer when compared to carboxylated graphene and other two composites. The charge-discharge curves look symmetric for the $BN_{1-x}G_x$ composites resembling those of ideal capacitors. The specific capacitance values decrease with increase in the current density as shown in Figure 13c. The specific capacitance of $BN_{0.25}G_{0.75}$, $BN_{0.5}G_{0.5}$ and $BN_{0.75}G_{0.25}$ is 238, 204 and 116 F/g respectively at 0.3 A/g, while carboxylated graphene alone exhibits a value of 87 F/g. The high specific capacitance of $BN_{1-x}G_x$ is attributed to the enhanced surface area along with the presence of slit-like microporous channels created in the composite due to covalent cross-linking.

The cycling stability for $BN_{0.25}G_{0.75}$ was studied by charge-discharge experiments between -0.2 and 0.6 V at a current density of 1 A g^{-1} for 1000 cycles. $BN_{0.25}G_{0.75}$ showed a loss of only ~ 2 % from the initial specific capacitance with excellent stability and capacitance retention (Figure 13d). BN has exceptionally high chemical and thermal stability, its presence in the conductive graphene matrix provides synergistic interactions with high electrochemical stability. The Nyquist plots in the frequency range 100 kHz – 0.01 Hz are shown Figure 14.

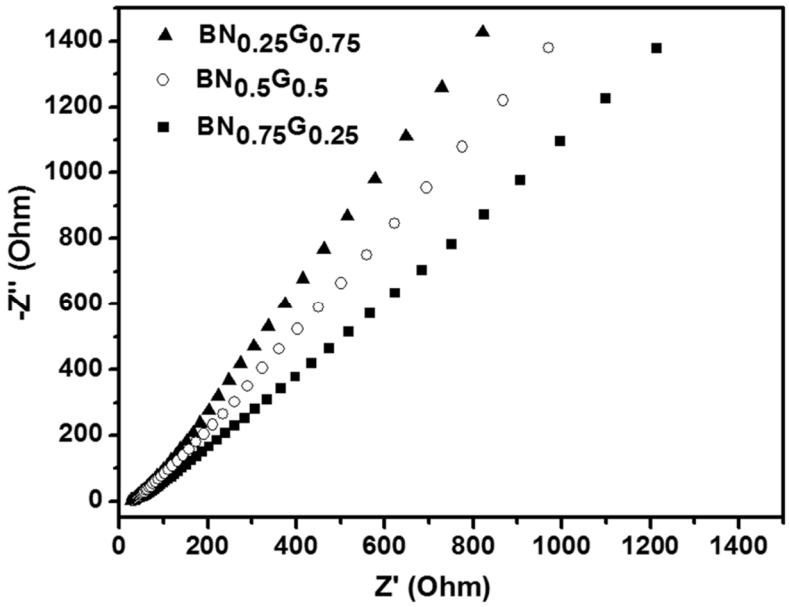

Figure 14. Nyquist plots for $BN_{1-x}G_x$ electrodes.

These plots show the excellent capacitive behavior of the $BN_{1-x}G_x$ composites as indicated by the near vertical line over the lower frequency range. The charge transfer resistance (C_t) in $BN_{0.25}G_{0.75}$, $BN_{0.5}G_{0.5}$ and $BN_{0.75}G_{0.25}$ is small and the equivalent series resistances (ESRs) are 26.7, 29.0 and 45.3 Ω respectively. The specific capacitance increases with increasing graphene content going up to ~ 200 F/g for $BN_{0.25}G_{0.75}$ and $BN_{0.5}G_{0.5}$. It is noteworthy that the resistivity decreases in the same order although the surface area remains nearly constant.

The electrocatalytic activity of carboxylated graphene and $BN_{1-x}G_x$ composites in the oxygen reduction reaction (ORR) was investigated by cyclic voltammetry (CV) at a slow scan rate of 5 mV/s in O_2-saturated and N_2-saturated 0.1 M KOH electrolytes, using a conventional three-electrode system (Figure 15a). The $BN_{1-x}G_x$ composites show cathodic peaks ranging from -0.25 to -0.35 V *vs* SCE in an O_2-saturated electrolyte, indicating a good O_2 reduction property whereas carboxylated graphene does not show a prominent reduction peak. This shows that addition of BN to graphene assists the reduction of oxygen. Linear-sweep voltammetry (LSV) of carboxylated graphene and $BN_{1-x}G_x$ composites at a rotation speed of 1600 rpm is displayed in Figure 15b. The $BN_{1-x}G_x$ composites exhibit higher current density on the addition of graphene to BN representing an enhanced activity for ORR. $BN_{0.25}G_{0.75}$ shows a more positive onset potential than $BN_{0.5}G_{0.5}$, $BN_{0.75}G_{0.25}$ and carboxylated graphene. The Koutecky–Levich plots (i^{-1} *vs* $\omega^{-1/2}$) were obtained from the polarization curves at a potential of -0.6 V *vs* SCE for all the catalysts as shown in Figure 15c. The transferred electron number (n) per O_2 calculated from the slopes of Koutecky–Levich plots ranges from

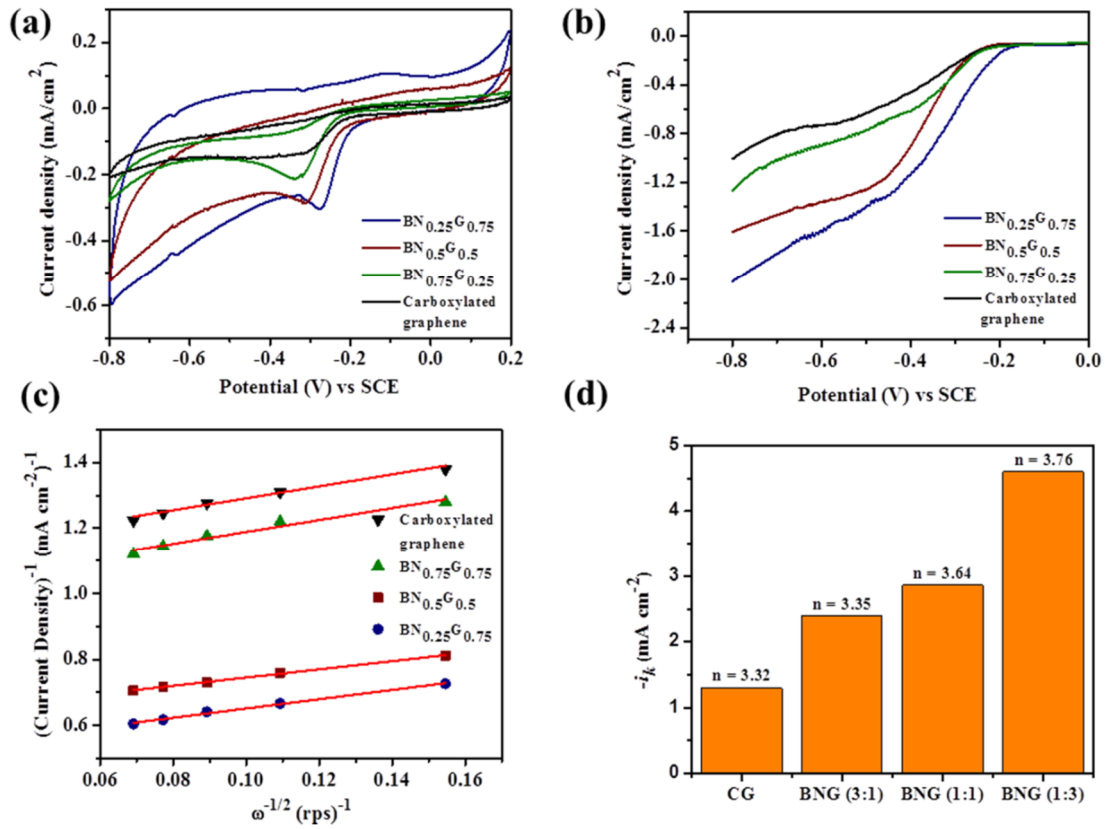

Figure 15. (a) Cyclic voltammetry curves of carboxylated graphene and $BN_{1-x}G_x$ composites in oxygen saturated 0.1 M KOH with a scan rate of 5 mV/s; (b) LSV curves of EG and $BN_{1-x}G_x$ composites in oxygen saturated 0.1 M KOH with a scan rate of 5 mV s^{-1} and a rotation rate of 1600 rpm; (c) Koutecky–Levich plots obtained at -0.6 V *vs* SCE and (d) Variation of kinetic current density (i_k) at -0.4 V *vs* SCE for EG and $BN_{1-x}G_x$ composites. Aqueous 0.1 M potassium hydroxide (KOH) solution used as the electrolyte.

3.3 to 3.8. $BN_{0.25}G_{0.75}$ shows electron transfer of 3.8 per oxygen molecule. The kinetic current density (i_k) values at -0.4 V *vs* SCE of $BN_{0.25}G_{0.75}$ is -4.6 mA/cm^2 which is higher than $BN_{0.5}G_{0.5}$, $BN_{0.75}G_{0.25}$ and carboxylated graphene which showed -2.9, -2.4 and -1.3 mA/cm^2 respectively. The present study demonstrates that addition of a small amount of BN to the graphene matrix enhances the ORR activity significantly.

6 .5 Conclusions

In conclusion, composites of BN and graphene with different compositions were successfully prepared by covalent cross–linking with amide bonds by using EDC coupling. The composites exhibit tunable-resistivity depending on the composition. The composites, especially $BN_{0.25}G_{0.75}$ show microporosity and satisfactory performance with high stability as supercapacitor electrode material. The composite with higher graphene content is also a good catalyst for the oxygen reduction reaction (ORR). Clearly, covalent cross-linking can be employed as a strategy to generate novel composites with useful properties.

References

[1] a) L. Pauling, *The nature of the chemical bond* Cornell University, **1960**; b) D. Golberg, Y. Bando, Y. Huang, T. Terao, M. Mitome, C. Tang and C. Zhi, *ACS Nano* **2010**, *4*, 2979.

[2] a) A. Pakdel, Y. Bando and D. Golberg, *Chem. Soc. Rev.* **2014**, *43*, 934; b) C. N. R. Rao, A. K. Sood, K. S. Subrahmanyam and A. Govindaraj, *Angew. Chem. Int. Ed.* **2009**, *48*, 7752.

[3] a) L. Song, Z. Liu, A. L. M. Reddy, N. T. Narayanan, J. Taha-Tijerina, J. Peng, G. Gao, J. Lou, R. Vajtai and P. M. Ajayan, *Adv. Mater.* **2012**, *24*, 4878; b) N. kumar, K. Moses, K. Pramoda, S. N. Shirodkar, A. K. Mishra, U. V. Waghmare, A. Sundaresan and C. N. R. Rao, *J. Mater. Chem. A* **2013**, *1*, 5806.

[4] a) K. Raidongia, A. Nag, K. P. S. S. Hembram, U. V. Waghmare, R. Datta and C. N. R. Rao, *Chem. Eur. J.* **2010**, *16*, 149; b) L. Ci, L. Song, C. Jin, D. Jariwala, D. Wu, Y. Li, A. Srivastava, Z. F. Wang, K. Storr, L. Balicas, F. Liu and P. M. Ajayan, *Nat Mater* **2010**, *9*, 430; c) A. Pakdel, X. Wang, C. Zhi, Y. Bando, K. Watanabe, T. Sekiguchi, T. Nakayama and D. Golberg, *J. Mater. Chem.* **2012**, *22*, 4818.

[5] K. Moses, S. N. Shirodkar, U. V. Waghmare and C. N. R. Rao, *Mater. Res. Express* **2014**, *1*, 025603.

[6] a) M. P. Levendorf, C.-J. Kim, L. Brown, P. Y. Huang, R. W. Havener, D. A. Muller and J. Park, *Nature* **2012**, *488*, 627; b) K. Zhang, F. L. Yap, K. Li, C. T. Ng, L. J. Li and K. P. Loh, *Adv. Funct. Mater.* **2014**, *24*, 731.

[7] G. Gao, W. Gao, E. Cannuccia, J. Taha-Tijerina, L. Balicas, A. Mathkar, T. N. Narayanan, Z. Liu, B. K. Gupta, J. Peng, Y. Yin, A. Rubio and P. M. Ajayan, *Nano Lett.* **2012**, *12*, 3518.

[8] a) R. Kumar, V. M. Suresh, T. K. Maji and C. N. R. Rao, *Chem. Commun.* **2014**, *50*, 2015; b) R. Kumar and C. N. R. Rao, *J. Mater. Chem. A* **2015**, *3*, 6747.

[9] a) K. Gopalakrishnan, A. Govindaraj and C. N. R. Rao, *J. Mater. Chem. A* **2013**, *1*, 7563; b) K. Gopalakrishnan, K. Moses, A. Govindaraj and C. N. R. Rao, *Solid State Commun.* **2013**, *175–176*, 43.

[10] a) J. W. Kaczmar, K. Pietrzak and W. Włosiński, *J. Mater. Process. Technol.* **2000**, *106*, 58; b) K. E. Prasad, B. Das, U. Maitra, U. Ramamurty and C. N. R. Rao, *Proc. Natl. Acad. Sci. USA* **2009**, *106*, 13186; c) X. Huang, X. Qi, F. Boey and H. Zhang, *Chem. Soc. Rev.* **2012**, *41*, 666; d) C. Zhi, Y. Bando, C. Tang, H. Kuwahara and D. Golberg, *Adv. Mater.* **2009**, *21*, 2889; e) R. Kumar, D. Raut, U. Ramamurty and C. N. R. Rao, *Angew. Chem. Int. Ed.* **2016**, *55*, 7857.

[11] a) K. Pramoda, R. Kumar and C. N. R. Rao, *Chem. Asian J.* **2015**, *10*, 2147; b) Z. Xu and C. Gao, *Macromolecules* **2010**, *43*, 6716.

[12] a) G.-H. Lee, Y.-J. Yu, X. Cui, N. Petrone, C.-H. Lee, M. S. Choi, D.-Y. Lee, C. Lee, W. J. Yoo, K. Watanabe, T. Taniguchi, C. Nuckolls, P. Kim and J. Hone, *ACS Nano* **2013**, *7*, 7931; b) J. Y. Kwak, J. Hwang, B. Calderon, H. Alsalman, N. Munoz, B. Schutter and M. G. Spencer, *Nano Lett.* **2014**, *14*, 4511; c) C.-J. Shih, Q. H. Wang, Y. Son, Z. Jin, D. Blankschtein and M. S. Strano, *ACS Nano* **2014**, *8*, 5790.

[13] A. Nag, K. Raidongia, K. P. S. S. Hembram, R. Datta, U. V. Waghmare and C. N. R. Rao, *ACS Nano* **2010**, *4*, 1539.

[14] K. S. Subrahmanyam, S. R. C. Vivekchand, A. Govindaraj and C. N. R. Rao, *J. Mater. Chem.* **2008**, *18*, 1517.

[15] a) C. Zhi, Y. Bando, C. Tang, S. Honda, K. Sato, H. Kuwahara and D. Golberg, *Angew. Chem. Int. Ed.* **2005**, *44*, 7932; b) T. Sainsbury, T. Ikuno, D. Okawa, D. Pacilé, J. M. J. Fréchet and A. Zettl, *J. Phys. Chem. C* **2007**, *111*, 12992.

[16] a) E. Valeur and M. Bradley, *Chem. Soc. Rev.* **2009**, *38*, 606; b) C. A. G. N. Montalbetti and V. Falque, *Tetrahedron* **2005**, *61*, 10827.

[17] a) H. K. Schmid, *Microsc. Microanal. M.* **1995**, *6*, 99; b) R. Arenal, M. Kociak and N. J. Zaluzec, *Appl. Phys. Lett.* **2007**, *90*, 204105.

[18] a) B. M. Kincaid, A. E. Meixner and P. M. Platzman, *Phys. Rev. Lett.* **1978**, *40*, 1296; b) R. D. Leapman, P. L. Fejes and J. Silcox, *Phys. Rev. B, PRB* **1983**, *28*, 2361.

[19] K. A. Mkhoyan, A. W. Contryman, J. Silcox, D. A. Stewart, G. Eda, C. Mattevi, S. Miller and M. Chhowalla, *Nano Lett.* **2009**, *9*, 1058.

[20] a) X. Gouin, P. Grange, L. Bois, P. L'Haridon and Y. Laurent, *J. Alloys Compd.* **1995**, *224*, 22; b) H. A. Castillo, P. J. Arango, J. M. Vélez, E. Restrepo-Parra, G. Soto and W. D. la Cruz, *Surf. Coat. Technol.* **2010**, *204*, 4051.

[21] a) Z.-J. Fan, W. Kai, J. Yan, T. Wei, L.-J. Zhi, J. Feng, Y.-m. Ren, L.-P. Song and F. Wei, *ACS Nano* **2011**, *5*, 191; b) T. Ramanathan, F. T. Fisher, R. S. Ruoff and L. C. Brinson, *Chem. Mater.* **2005**, *17*, 1290.

[22] V. Nicolosi, M. Chhowalla, M. G. Kanatzidis, M. S. Strano and J. N. Coleman, *Science* **2013**, *340*.

[23] Y. Gu, M. Zheng, Y. Liu and Z. Xu, *J. Am. Ceram. Soc.* **2007**, *90*, 1589.

[24] D. W. Mayo, F. A. Miller and R. W. Hannah in *Course notes on the interpretation of infrared and Raman spectra*, John Wiley & Sons, Inc, **2004**.

[25] a) S. Saha, D. V. S. Muthu, D. Golberg, C. Tang, C. Zhi, Y. Bando and A. K. Sood, *Chem. Phys. Lett.* **2006**, *421*, 86; b) J. Wu, W.-Q. Han, W. Walukiewicz, J. W. Ager, W. Shan, E. E. Haller and A. Zettl, *Nano Lett.* **2004**, *4*, 647.

[26] L. M. Malard, M. A. Pimenta, G. Dresselhaus and M. S. Dresselhaus, *Phys. Rep.* **2009**, *473*, 51.

[27] K. S. W. Sing, D. H. Everett, R. A. W. Haul, L. Moscou, R. A. Pierotti, J. Rouquerol and T. Siemieniewska, *Pure Appl. Chem.* **1984**, *57*, 603.

Chapter 7: Functionality preservation with enhanced mechanical integrity in the nanocomposites of the metal-organic framework, ZIF-8, with BN nanosheets*

Summary

Metal-organic frameworks (MOFs) and boron nitride both possess novel properties, the former associated with microporosity and the latter with good mechanical properties, thermal and chemical stabilities. In this chapter, synthesis of composites of the imidazolate based MOF, ZIF-8, and few-layer BN is investigated, in order to see whether the properties of both these materials can be incorporated in the composites. The composites so prepared between BN nanosheets and ZIF-8 have compositions ZIF-1BN, ZIF-2BN, ZIF-3BN and ~ZIF-4BN. The composites have been characterized by PXRD, TGA, XPS, electron microscopy, IR, Raman and solid-state NMR spectroscopy. The composites possess good surface areas, the actual value decreasing only slightly with the increase in the BN content. The CO_2 uptake remains nearly same in the composites as in the parent ZIF-8. More importantly, the addition of BN markedly improves the mechanical properties of ZIF-8, a feature that is much desired in MOFs. Observation of microporous features along with improved mechanical properties in a MOF is indeed noteworthy. Such manipulation of properties can be profitably exploited in practical applications.

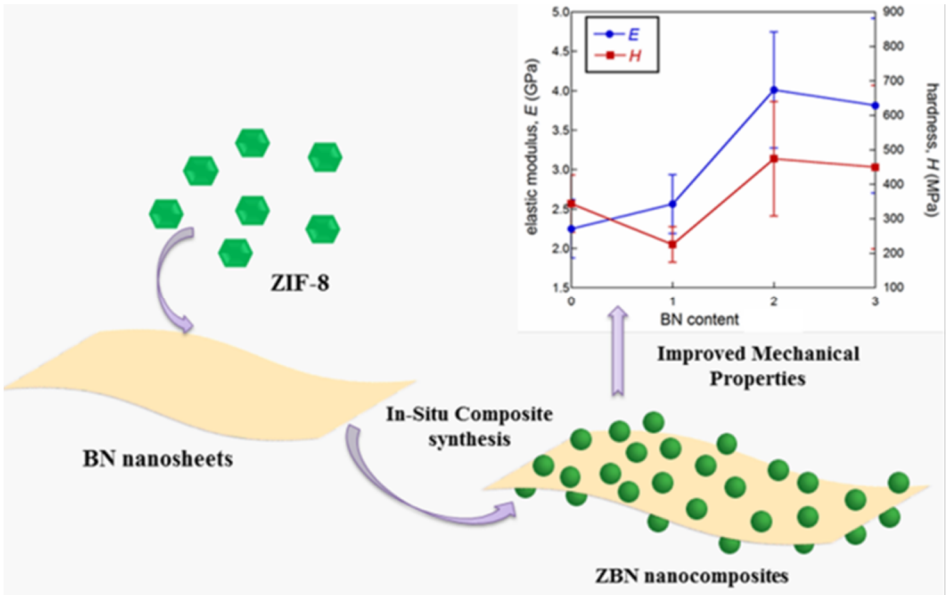

A paper based on these studies has appeared in Mater. Horz. 2014, 1, 513.

7.1 Introduction

Single and few-layer graphene and their analogues exhibit many novel physical, mechanical and adsorption properties.[1] Recently, layered inorganic compounds of which, hexagonal boron nitride (BN) is an important member with high thermal and chemical stabilities as well as good mechanical properties, have attracted considerable attention.[2] Nanosheets of BN-containing few-layers have been prepared by mechanical exfoliation, chemical exfoliation using ultrasonication in a polar solvent and chemical vapor deposition.[2c,3] Although metal-organic frameworks (MOFs) are known as an important class of compounds for potential applications in gas storage and catalysis,[4] a key challenge to overcome is their low mechanical robustness and stability. These materials are generally fragile in nature.[5] MOFs undergo amorphization under pressure.[6] A possible way of overcoming such a drawback would be through compositing MOFs with two-dimensional nanomaterials such as graphene and BN.[2b,7] The advantages of composites of MOFs prepared with nanoparticles has been nicely described by Doherty *et al.,*[8] and multifunctional nanoparticle-MOF core-shell structures with interesting properties such as gas sensing and catalysis are reported by Tang *et al.*[9] Nanocomposites can also exhibit synergistic interactions between the MOF particles and the layered nanosheets, as demonstrated in the case of few-layer graphene and nanodiamond reinforced polymer composites.[10] In the literature, MOF-graphene nanocomposites have been prepared and their adsorption and electrical properties examined.[11] There has been no study of mechanical properties of the composites or effort to improve the mechanical properties of MOFs. For the first time, the possibility of enhancing the mechanical performance of a microporous zeolitic imidazolate framework (ZIF-8) is investigated, which possesses good chemical and thermal stabilities[12], by compositing it with few-layer BN.

7.2 Scope of the present investigations

As mentioned earlier in the thesis, metal–organic frameworks (MOFs) are an important class of crystalline porous materials with potential applications in gas storage, separation, catalysis, and sensing.[13] One of the key challenges for their practical applications is low mechanical robustness and stability as they contain significant structural porosity and are typically fragile in nature.[5,14] The porous open–framework structure, where metal ions are chemically bonded with organic linkers using moderate energy coordinate bonds are vulnerable to framework collapse when subjected to mechanical stress and strain.[13b,15]

Various practical applications involve the formation of densely packed adsorption bed and subjecting to hydrostatic pressure. In fact, the external hydrostatic pressure of several GPa is common in practical situations. Thin films and membranes for sensing, catalytic and gas separation applications involve subjecting the MOFs to shear stress and strain. The amorphous structure loses the porosity and functional properties. One possible way of overcoming this drawback is by making composites of MOFs with a two-dimensional nanomaterial such as BN which has high mechanical strength.[2b,c] Such an effort to improve the mechanical properties of MOFs has not been reported hitherto. For the first time, the possibility of enhancing the mechanical properties of an MOF, in the case of microporous zeolitic imidazolate framework ZIF-8 was investigated. For this purpose, a composite where ZIF-8 is chemically bonded to few-layer BN was prepared. The ZIF-8 nanoparticles grow on 2D–BN nanosheets by chemically bonding with amine functional groups present on BN basal plane and Lewis acidic B sites of BN with 2–methylimidazole linker. Incorporating the properties of both BN and the MOF, especially to improve the mechanical strength of the latter, is indeed novel. The present chapter explores the improvement of mechanical properties in prototypical MOF nanoparticle–BN composites, where the nanoparticle grows on BN nanosheets.

7.3 Experimental section

Reagents and chemicals: All the chemicals used in the synthesis were of high purity, and obtained from commercial sources. High purity (99.999 %) anhydrous ammonia was used for the synthesis of few-layer BN.

BN synthesis: Few-layer boron nitride (BN) nanosheets were prepared by the reported procedure using boric acid and urea in 1:48 molar ratio and heating in an ammonia atmosphere.[2a]

Synthesis of ZIF-8 nanoparticles: ZIF-8 nanocrystals were prepared using a procedure reported by Wiebcke *et al*.[16] In a typical synthesis, 0.751 g (2.5 mmol) $Zn(NO_3)_2.6H_2O$ was dissolved in 50 ml methanol and 1.658 g (20 mmol) of 2-methylimidazole dissolved in 50 ml methanol was added to it slowly under constant stirring. The resulting solution was stirred for 12 hours. The product was centrifuged, washed properly with methanol and dried in 60 °C oven. The yield obtained was ~ 56 % based on zinc.

Synthesis of ZBN composites: Different mole ratios of BN (between 1 to 4) with respect to ZIF-8 were taken in methanol and sonicated for 90 minutes to form a uniform dispersion. Under constant stirring, $Zn(NO_3)_2.6H_2O$ was added and allowed to stir for ~10 min. 2-Methylimidazole dissolved in methanol was then added slowly. The remaining steps were similar to those employed in the synthesis of ZIF-8. The resulting composites with increasing BN content are denoted as ZBN-1, ZBN-2, ZBN-3 and ZBN-4.

Characterization: Powder X-ray diffraction (PXRD) patterns were recorded on Bruker D8 Discover using Cu-Kα radiation. FT-IR spectra were recorded on a Bruker IFS 66v/S spectrophotometer. Raman spectra of the samples were collected at several different locations in backscattering arrangement, using a 632.8 nm He-Ne laser in LabRam HR 800 spectrometer. TEM images were obtained using a JEOL JEM-3010 microscope at an accelerating voltage of 300 kV. Thermogravimetric analysis (TGA) was carried out in an oxygen atmosphere with a Metler Toledo TGA-850 at a heating rate of 3 °C / min. SEM images of samples were obtained from Nova Nano SEM 600, FEI Company. X-ray photoelectron spectra (XPS) were recorded using Omicron Nanotechnology Spectrometer with Mg Kα as the X-ray source. The high-speed MAS ^{11}B solid state NMR spectra were collected at a frequency of 160.47 MHz using Bruker 500 MHz AVANCE III Solid-state FT-NMR Spectrometer at room temperature. ZrO_2 rotor and CPMG pulse sequence were used. Elemental analysis was carried out using Thermo FLASH 2000 elemental analyser.

Gas adsorption: Adsorption isotherms for N_2 and CO_2 (at 77K and 195 K) were carried out using *QUANTACHROME AUTOSORB-1C* analyzer. Approximately 100 – 150 mg samples were activated at 433 K under vacuum for 12 h before the measurement. The amount of gas adsorbed was calculated from pressure difference (P_{cal} - P_e), where P_{cal} is the calculated pressure with no gas adsorption and P_e is the observed equilibrium pressure. All operations were computer-controlled and automatic.

Mechanical property measurements: As it was not possible to measure mechanical properties of powders, they were pelletized using the following procedure. 100 mg of powder was placed in a 12 mm diameter hardened stainless steel die and was heated to 160 °C where it was held for 30 min before loading to 10 kN at a rate of 0.1 mm/s (Zwick/Roell, Z-100). The load was held constant for 15 minutes. Subsequently, the sample was unloaded, cooled to room temperature and then the pellet was extracted from the die. The thickness of the mechanically robust pellets was approximately 0.9 mm. Before mechanical property measurements, PXRD pattern was recorded on all the pellets prepared to examine phase

purity. The diffraction patterns confirmed that hot-pressing procedure adopted did not alter the phases.

Mechanical properties of the nanocomposite pellets were evaluated by employing the nanoindentation technique using the Triboindenter (Hysitron, Minneapolis, USA). In these experiments, the applied load, *P*, and the corresponding depth of the penetration of the indenter, *h*, were collected and evaluated. A Berkovich tip diamond indenter with the tip radius of 100 nm is used for the indentation. In all cases, the peak load, P_{max}, was maintained at 2 mN and the loading and unloading rates were 0.4 mN/s. The hold time at P_{max} was 5 s. A minimum of 30 indentations was performed on each pellet so to obtain statistically significant information. The *P-h* curves are analysed using the Oliver-Pharr method to extract the elastic modulus, *E*, and the hardness, *H*, of the samples.

7.4 Results and discussion

Prototypical ZIF-8 ($Zn(MeIM)_2$, MeIM = 2-methylimidazolate) with the sodalite zeolitic structure, possessing large cavities (~11.6 Å diameter) and interconnected by narrow windows (3.4 Å) was used for studying mechanical and adsorption properties (Scheme 1). Recognizing that physical mixing of ZIF-8 with BN may not impart the necessary mechanical stability to ZIF-8, ZBN nanocomposites where ZIF-8 attaches to BN by chemical bonds was prepared

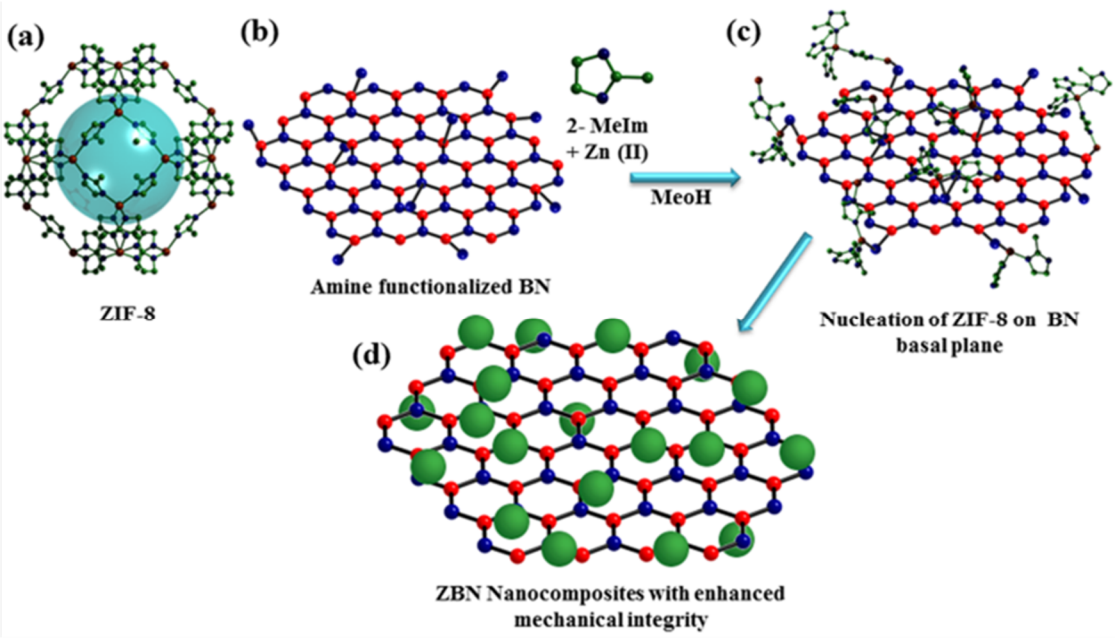

Scheme 1. Schematic representation of *in situ* ZBN synthesis. (a) ZIF-8 framework; (b) amine functionalized few layer BN nanosheet; (c, d) nucleation and formation of ZIF-8 nanocrystals on BN basal plane.

in situ in the colloidal dispersion of few-layer BN. Few-layer BN was prepared by the urea route in an ammonia atmosphere and have a reasonably high surface area. [2a] Formation of the nanocomposite is favoured by amine groups present on the BN basal plane, resulting from the urea route which creates an ammonia atmosphere in the reaction medium.[17] The mole ratio of BN in the composite with respect to ZIF-8 was varied between 1 to 4, and the composites so-obtained with increasing BN content are denoted by ZBN-1, ZBN-2, ZBN-3, and ZBN-4 (see experimental section 7.3 for details).

The phase purity of the ZBN composites was examined by powder X-ray diffraction. The patterns of the ZBN composites are consistent with the cubic space group of ZIF-8 (Figure 1a). ZIF-8 nanocrystals are present on the BN basal plane with the Zn(II) centres having the same coordination environment as ZIF-8. Hence, no significant change in powder X-ray diffraction patterns is observed except for a slight broadening in the patterns and decrease in intensity due to the decrease in particle size. Thermogravimetric analysis of the composites in oxygen atmosphere shows high thermal stability up to ca. 260 °C before decomposition of the framework structure (Figure 1b and Figure 2). ZIF-8 on heating in an oxygen atmosphere decomposes to ZnO leaving 35.4 wt % of ZnO as the residue (experimental weight loss 35 %). Pure BN does not show any weight loss up to high temperatures. The nanocomposites ZBN-1, 2, 3 and 4 show weight losses gives ZnO-BN, ZnO-2BN, ZnO-3BN and ~ ZnO-4BN respectively as product. XRD patterns and other measurements confirm the product residues contain only ZnO and BN (Figure 2).

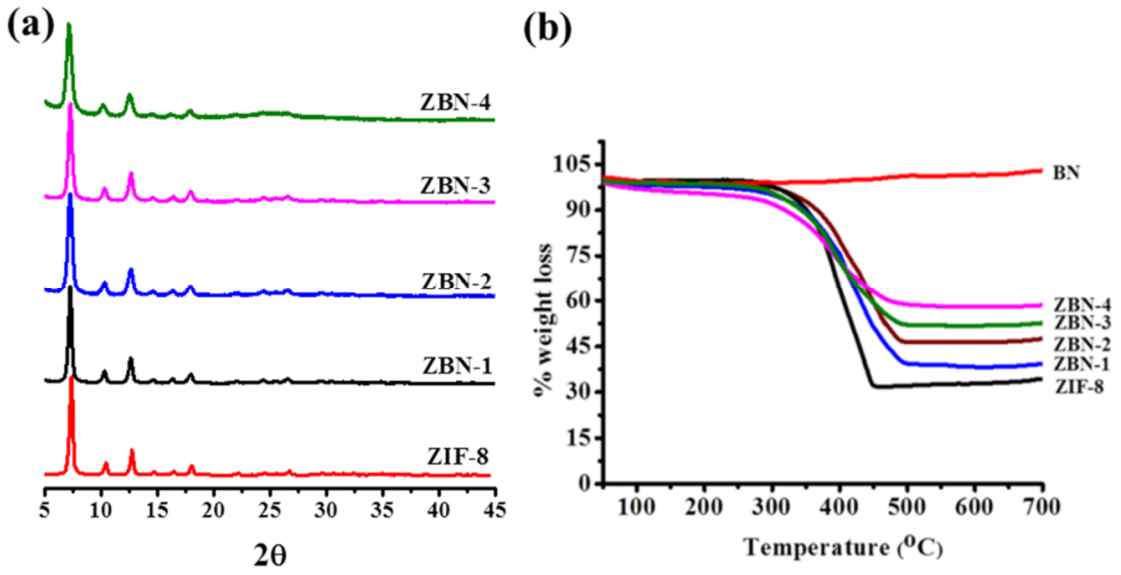

Figure 1. (a) PXRD patterns of ZIF-8 and the ZBN nanocomposites. (b) Thermograviametric profile ZIF-8 (black), ZBN-1 (blue), ZBN-2 (wine), ZBN-3 (olive), ZBN-4 (magenta) and BN (red) nanocomposites in oxygen atmosphere.

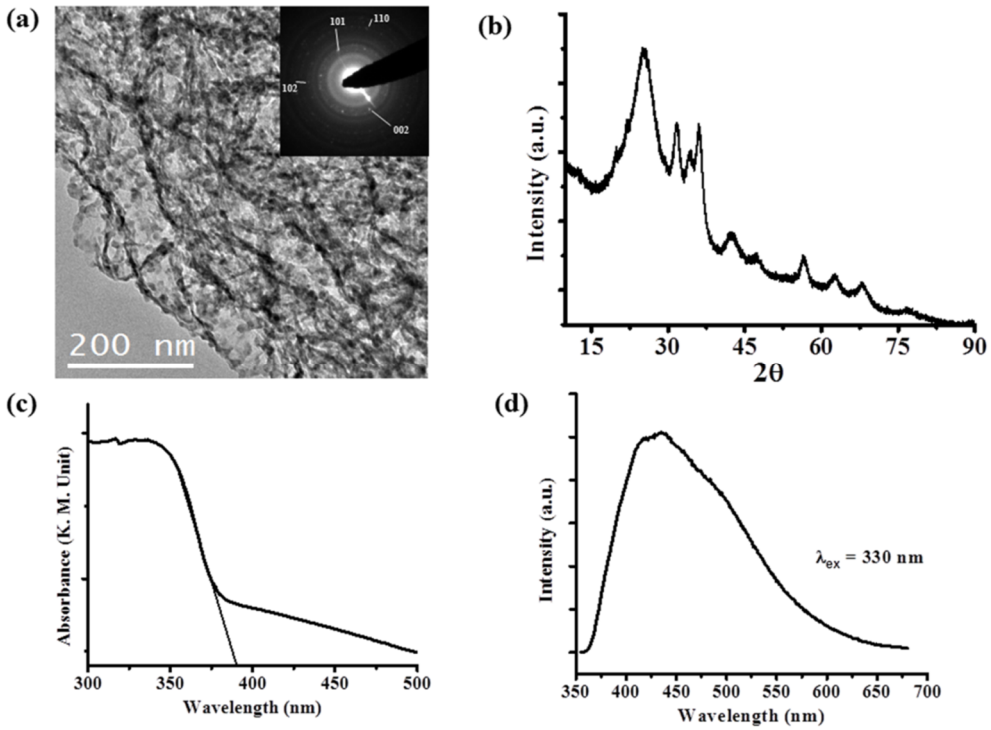

Figure 2. BN@ZnO composite obtained on heating ZBN-2 in an oxygen atmosphere. (a) TEM image; (b) PXRD pattern; (c) UV-visible absorption spectrum and (d) Photoluminescence emission spectrum of obtained BN@ZnO composite.

In Figure 3, a typical X-ray photoelectron spectrum (XPS) in the case of ZBN-2 is displayed, which shows signals due to B (1s) and Zn (2p) with the expected B:Zn ratio of ~ 2. Figure 4 show the infrared (IR) spectra of BN, ZIF-8, and ZBNs. The IR spectrum of BN shows bands at 803 and 1378 cm^{-1} attributed to out-of-plane B–N–B bending mode and the in-plane B–N transverse optical mode respectively, along with the N–H stretching band due to the amine groups.[17a,18]

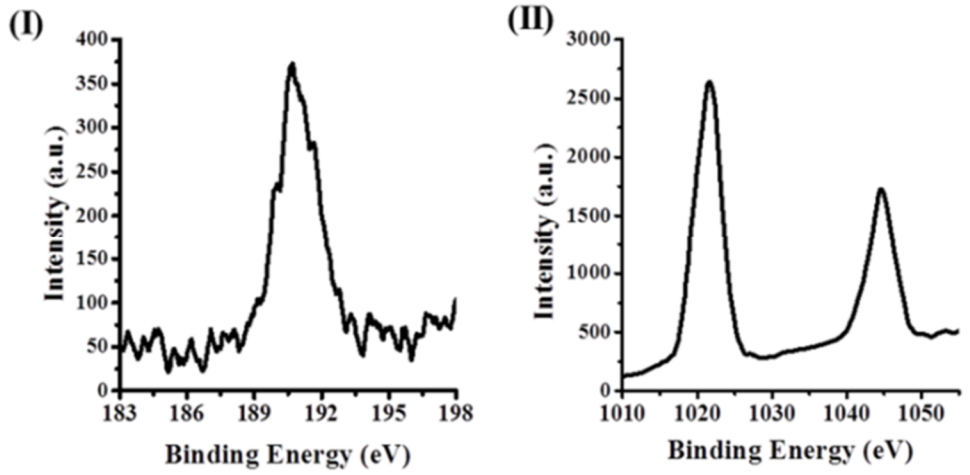

Figure 3. (I) High-resolution B (1s) X-ray photoelectron spectrum (XPS) of ZBN-2; (II) High-resolution Zn (2p) XP spectrum of ZBN-2.

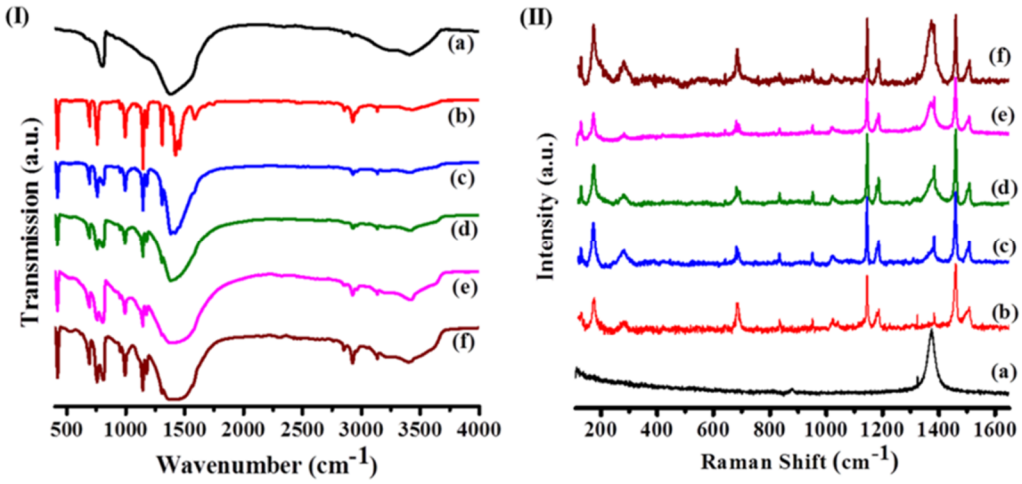

Figure 4. (I) Infrared spectra and (II) Raman Spectra of (a) few-layer BN, (b) ZIF-8, (c) ZBN-1, (d) ZBN-2, (e) ZBN-3 and (f) ZBN-4.

The IR spectrum of ZIF-8 shows a band at 421 cm^{-1} due to Zn–N stretching. The bands at 2854, 2927, 2958 and 3136 cm^{-1} arise from aliphatic and aromatic C-H stretching of 2-methylimidazole (Figure 4). The IR spectra of ZBNs have bands corresponding to ZIF-8 besides those at 807 and near 1377 cm^{-1} due to BN. Raman spectra collected at several different locations of ZBNs show bands at 1373 cm^{-1} corresponding to the E_{2g} tangential mode of BN besides bands due to ZIF-8 (Figure 4(II)).[19] The spectrum of ZIF-8 has bands at 174, 686, 1146 and 1459 cm^{-1} corresponding to Zn–N stretching, imidazole ring puckering, C–N stretching and methyl bending respectively.[20] Bands corresponding to aliphatic and aromatic C–H stretching is observed at 2928, 3114 and 3135 cm^{-1}. The ^{11}B solid state NMR spectra of the BN and ZBN-2 prepared by us were recorded at 11 kHz MAS and

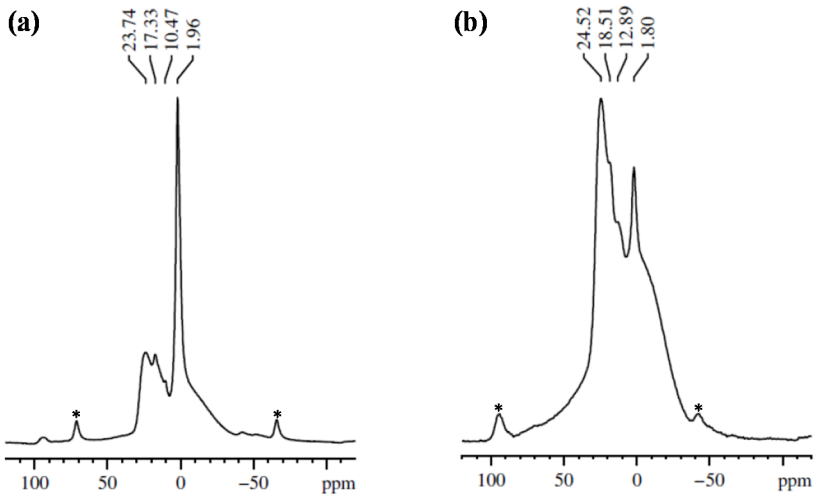

Figure 5. 160.47 MHz ^{11}B NMR spectra of (a) few layer BN and (b) ZBN-2 at 11 kHz MAS. Aestrik represents spinning sidebands.

160.47 MHz frequency (Figure 5). The BN sample shows ^{11}B spectrum different from that of pure hexagonal BN[21] due to the presence of amine groups. Few-layer BN shows a strong signal at 1.96 ppm with much weaker signals in the 11-24 ppm region. The ^{11}B spectrum of ZBN-2 is different with strong signals at 1.8 and 24.5 ppm with weaker features at 18.5 and 12.9 ppm.

The morphology and homogeneity of ZBNs were characterized using transmission electron microscopy (TEM). Typical TEM images of few-layer BN and ZBNs and particle size distributions are displayed in Figures 6 and 7. ZIF-8 nanocrystals have rhombic dodecahedral morphology with most particles having a size in the range of 150 - 220 nm. ZBN-1 has an irregular morphology embedded in the few-layer BN matrix with a particle size in the same

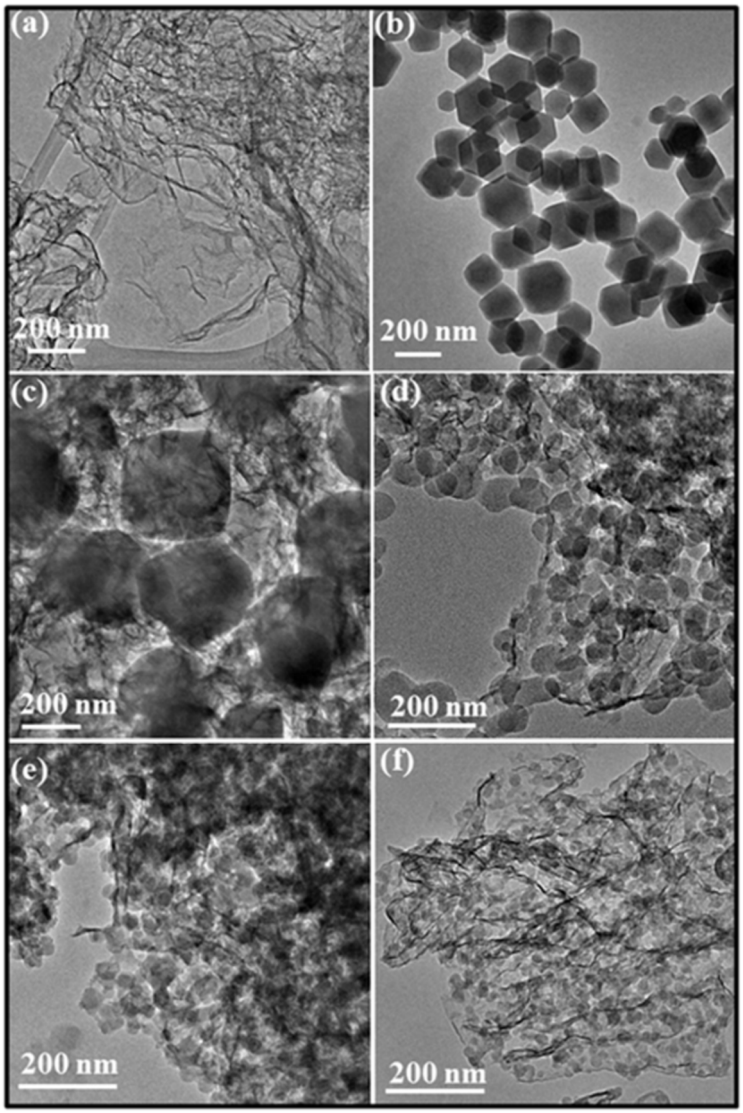

Figure 6. TEM images of (a) few-layer BN, (b) ZIF-8, (c) ZBN-1, (d) ZBN-2, (e) ZBN-3 and (f) ZBN-4.

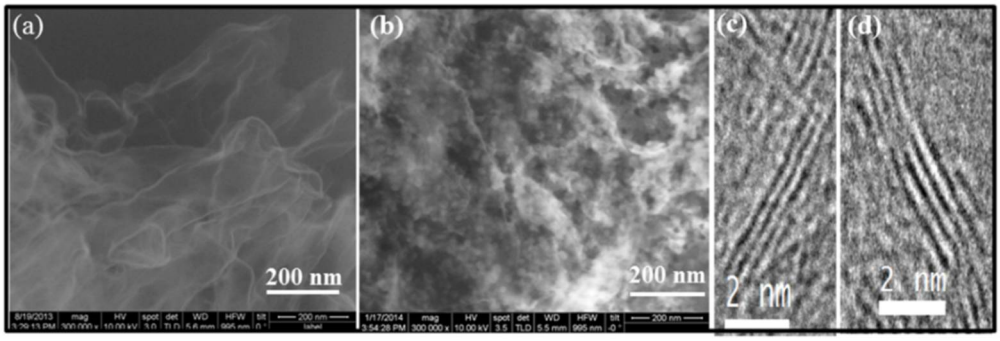

Figure 8. (a) FESEM image of few-layer BN, (b) FESEM image of ZBN-4 and (c, d) HRTEM images of few layer-BN corresponding to the TEM image shown in figure 6.

range as ZIF-8. With increasing BN content in the composite, the particle size decreases and a change from rhombic dodecahedral to spherical morphology occurs. Thus, the image of ZBN-2 shows dense and uniformly decorated spherical ZIF-8 nanocrystals. Most of the particles have a size in the range of 18 - 35 nm for ZBN-2 and ZBN-3. The size of the particles decreases to

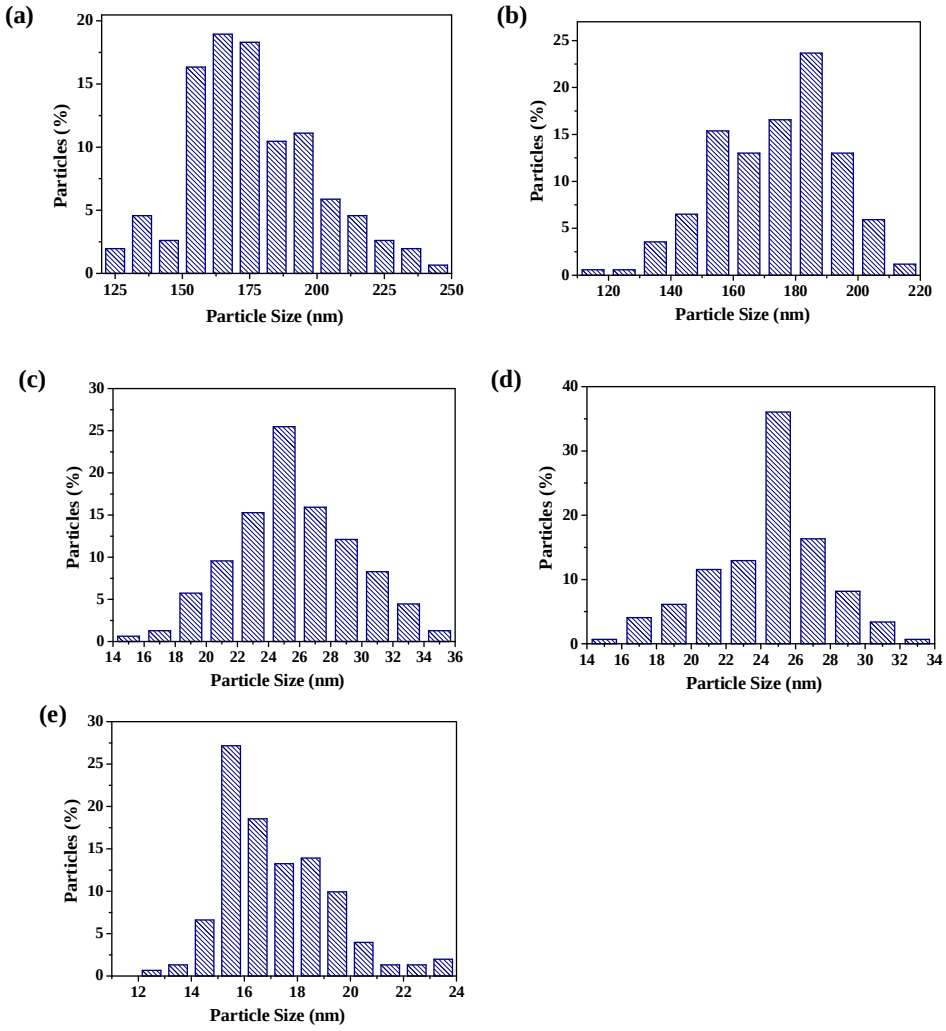

Figure 7. Particle size distribution in (a) ZIF-8, (b) ZBN-1, (c) ZBN-2, (d) ZBN-3 and (e) ZBN-4.

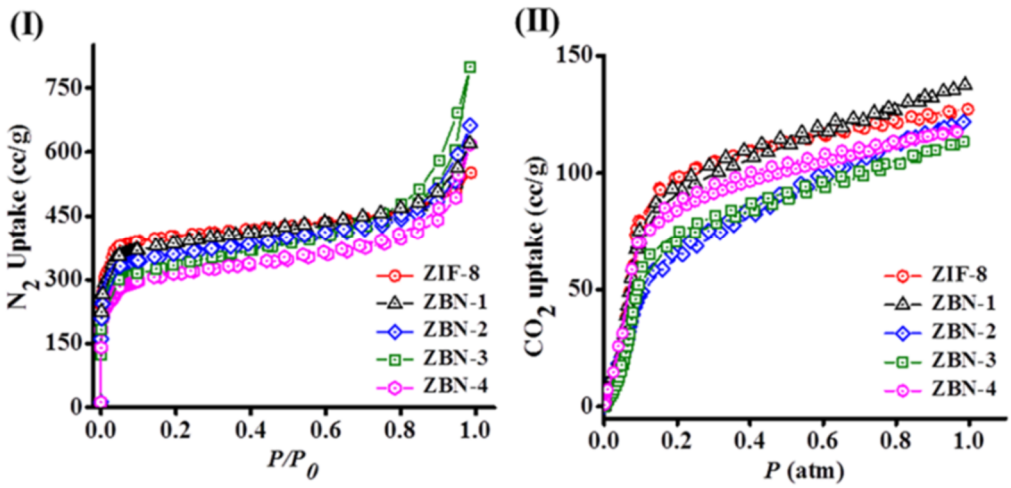

Figure 9. (I) N_2 adsorption profile at 77 K and (II) CO_2 adsorption profile at 195 K of ZIF-8 (red circle), ZBN-1 (black triangle), ZBN-2 (blue diamond), ZBN-3 (green square) and ZBN-4 (magenta circle).

14 – 20 nm in ZBN-4. A similar role of graphene in controlling the particle size and morphology of the composites with a MOF and photoactive zeolite has been reported.[11a,11c,22] The decrease in particle size and change in morphology of ZIF-8 nanocrystals is attributed to the interaction of Zn(II) with the amine functional group present on BN basal plane. It is to be noted that boron in BN being electron deficient can interact with the nitrogen of 2-methylimidazole to stabilize ZIF-8 nanocrystals on the BN basal plane.[23] Scanning electron microscope images confirm the presence of ZIF-8 nanoparticles on BN sheets (Figure 8).

Surface areas of ZIF-8, BN and ZBNs were determined using N_2 adsorption at 77 K (Figure 9(I)). Few-layer BN prepared under the ammonia atmosphere has a surface area of 537 m^2/g calculated using the BET model (Figure 10). The BET surface areas of ZIF-8, ZBN-1, ZBN-2, ZBN-3 and ZBN-4 are 1450, 1379, 1272, 1196 and 1110 m^2/g respectively.

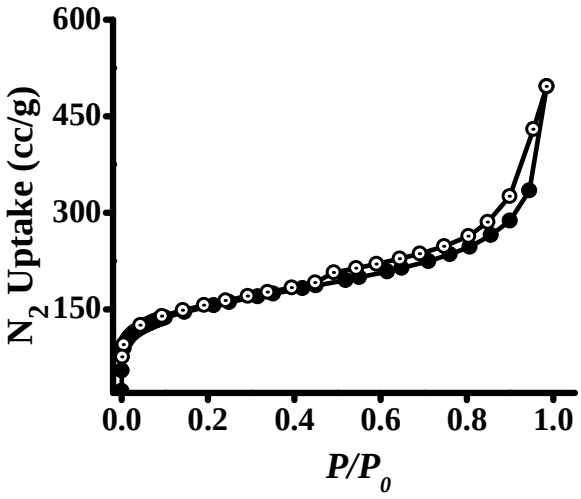

Figure 10. N_2 adsorption profile of few-layer BN at 77 K.

The adsorption profile has microporous type-I adsorption behaviour with small hysteresis in the case of ZBN-3 and ZBN-4. Interestingly, the uptake of CO_2 at 195 K and 1 atm of the ZBN nanocomposites is essentially the same as that of ZIF-8, the actual values of ZBN-1, 2, 3 and 4 being 27, 24 and 23 wt% compared to 25 wt % of ZIF-8 (Figure 9(II)).

Figure 11 shows the variation of the elastic modulus, *E*, and hardness, *H*, with the BN content in the nanocomposite. The error bars correspond to the standard deviations on 30 indents that were made on each pellet (see experimental section 7.3 for details). The measured values *E* and *H* for the pure ZIF-8 are 2.25 GPa and 343 MPa. These values are ~ 25 and 35% lower than the respective *E* and *H* values measured on [20a] faces of single crystals by Tan *et al*.[24] Since, the sintered pellets are polycrystalline, it is to be expected that the measured values are somewhat lower as they are 'volume averaged' properties of different crystals with each oriented randomly. In addition, the sizes of the crystals are much smaller in the present case. The addition of one BN to ZIF-8 as in ZBN-1 enhances *E* marginally (by ~10%) whereas the hardness gets reduced, which is somewhat surprising. However, the nanocomposite with 2 BN units, ZBN-2, shows a remarkable improvement in both the properties, with *E* nearly-double that of the bare ZIF-8 while *H* is ~30% greater. Further increase in the BN content to ZIF-8 does not lead to additional enhancement in *E* and *H* with the mechanical properties of ZBN-3 nanocomposite being somewhat lower than those of the ZBN-2. The mechanical properties of nanocomposite pellets wherein the ZIF-8 and

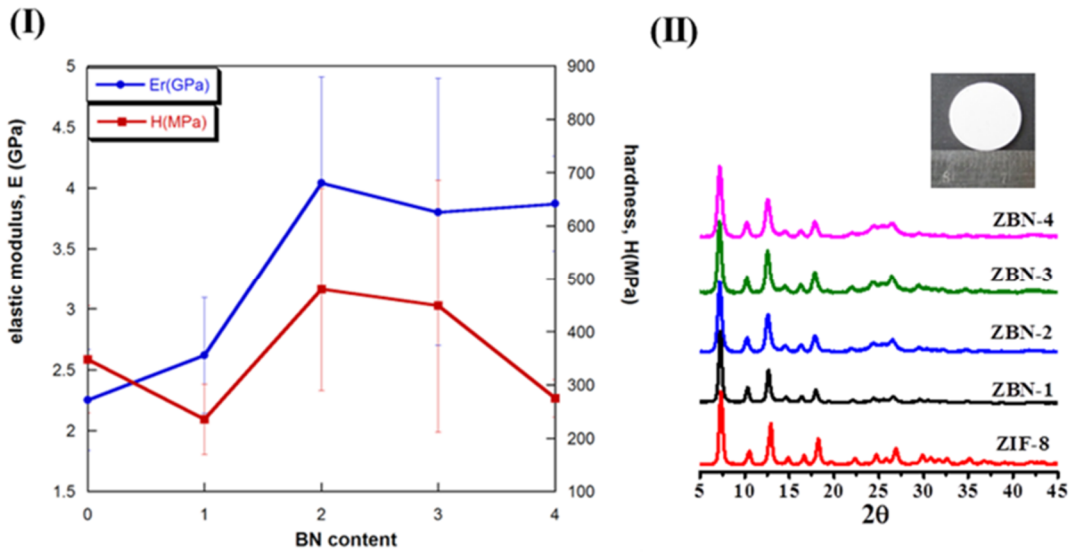

Figure 11. (I) Variations of the elastic modulus, *E*, (blue) and hardness, *H*, (red) with BN content in the ZIF-8-BN nanocomposites, measured by employing the nanoindentation technique. (II) PXRD pattern of pellets used for mechanical property measurement ZIF-8 (red), ZBN-1 (black), ZBN-2 (blue), ZBN-3 (green) and ZBN-4 (magenta). (Inset) The typical image of a pellet used for mechanical property measurement.

BN were physically mixed before pelletizing was also investigated as a control sample. These mixtures showed property enhancements, the scatter in data being significantly more. This observation is on expected lines as significant heterogeneity is inevitable in pellets made by physical mixing of the components. It is noteworthy that the composites did not amorphized after nanoindentation. Enhancement in the elastic modulus is attributed to the synergistic interaction between ZIF-8 nanocrystals and BN sheets. Maximum synergy is observed up to certain BN content with no property enhancement on increasing the BN content. This behaviour is similar to that of polymer matrix composites reinforced with nanocarbons where maximum enhancement is observed up to a certain concentration, with further addition leading to no improvement.[10] If there were to be a matrix, the matrix material will provide for such synergy as both the particles and sheets would interact with each other through the matrix. Since there is no matrix the chemical interaction between ZIF-8 nanocrystals and BN basal plane ensures synergy. The above results confirm that the presence of BN in the ZIF-8-BN composites markedly enhances the mechanical properties of ZIF-8 and bestows the much needed structural integrity. The approach used in the present study - namely the chemical synthesis of nanocomposites can be utilized to engineer framework materials with not only desired functional properties but also mechanical robustness required in practical situations.

7.5 Conclusions

In conclusion, nanocomposites wherein the imidazolate based metal-organic framework (ZIF-8) is chemically bonded with nanosheets of BN are investigated for improvement of mechanical and adsorption properties. It is noteworthy that the nanocomposites retain the microporous characteristics, good surface areas, and CO_2 adsorption, while at the same time possessing improved mechanical properties, afforded by the presence of BN sheets. Such manipulation of properties of MOF composites may have useful applications.

References

[1] a) A. K. Geim and K. S. Novoselov, *Nat. Mater.* **2007**, *6*, 183; b) C. N. R. Rao, A. K. Sood, K. S. Subrahmanyam and A. Govindaraj, *Angew. Chem. Int. Ed.* **2009**, *48*, 7752; c) C. N. R. Rao, H. S. S. Ramakrishna Matte and U. Maitra, *Angew. Chem. Int. Ed.* **2013**, *52*, 13162.

[2] a) A. Nag, K. Raidongia, K. P. S. S. Hembram, R. Datta, U. V. Waghmare and C. N. R. Rao, *ACS Nano* **2010**, *4*, 1539; b) M. S. R. N. Kiran, K. Raidongia, U. Ramamurty and C. N. R. Rao, *Scripta Mater.* **2011**, *64*, 592; c) C. Zhi, Y. Bando, C. Tang, H. Kuwahara and D. Golberg, *Adv. Mater.* **2009**, *21*, 2889.

[3] a) A. Pakdel, Y. Bando and D. Golberg, *Chem. Soc. Rev.* **2014**, *43*, 934; b) K. S. Novoselov, D. Jiang, F. Schedin, T. J. Booth, V. V. Khotkevich, S. V. Morozov and A. K. Geim, *Proc. Natl. Acad. Sci. U.S.A.* **2005**, *102*, 10451.

[4] a) S. Kitagawa, R. Kitaura and S.-i. Noro, *Angew. Chem. Int. Ed.* **2004**, *43*, 2334; b) L. J. Murray, M. Dinca and J. R. Long, *Chem. Soc. Rev.* **2009**, *38*, 1294; c) A. K. Cheetham, C. N. R. Rao and R. K. Feller, *Chem. Commun.* **2006,** 4780; d) D. Bradshaw, J. B. Claridge, E. J. Cussen, T. J. Prior and M. J. Rosseinsky, *Acc. Chem. Res.* **2005**, *38*, 273.

[5] J. C. Tan and A. K. Cheetham, *Chem. Soc. Rev.* **2011**, *40*, 1059.

[6] K. W. Chapman, G. J. Halder and P. J. Chupas, *J. Am. Chem. Soc.* **2009**, *131*, 17546.

[7] D. Barun, K. E. Prasad, U. Ramamurty and C. N. R. Rao, *Nanotechnology* **2009**, *20*, 125705.

[8] C. M. Doherty, D. Buso, A. J. Hill, S. Furukawa, S. Kitagawa and P. Falcaro, *Acc. Chem. Res.* **2013**, *47*, 396.

[9] a) L. He, Y. Liu, J. Liu, Y. Xiong, J. Zheng, Y. Liu and Z. Tang, *Angew. Chem. Int. Ed.* **2013**, *52*, 3741; b) Y. Liu and Z. Tang, *Adv. Mater.* **2013**, *25*, 5819; c) M. Zhao, K. Deng, L. He, Y. Liu, G. Li, H. Zhao and Z. Tang, *J. Am. Chem. Soc.* **2014**, *136*, 1738.

[10] K. E. Prasad, B. Das, U. Maitra, U. Ramamurty and C. N. R. Rao, *Proc. Natl. Acad. Sci. U.S.A.* **2009**, *106*, 13186.

[11] a) M. Jahan, Q. Bao, J.-X. Yang and K. P. Loh, *J. Am. Chem. Soc.* **2010**, *132*, 14487; b) C. Petit and T. J. Bandosz, *Adv. Mater.* **2009**, *21*, 4753; c) R. Kumar, K. Jayaramulu, T. K. Maji and C. N. R. Rao, *Chem. Commun.* **2013**, *49*, 4947.

[12] K. S. Park, Z. Ni, A. P. Côté, J. Y. Choi, R. Huang, F. J. Uribe-Romo, H. K. Chae, M. O'Keeffe and O. M. Yaghi, *Proc. Natl. Acad. Sci. U.S.A.* **2006**, *103*, 10186.

[13] a) H. Furukawa, K. E. Cordova, M. O'Keeffe and O. M. Yaghi, *Science* **2013**, *341*; b) J. L. C. Rowsell and O. M. Yaghi, *Microporous Mesoporous Mater.* **2004**, *73*, 3; c) J. Lee, O. K. Farha, J. Roberts, K. A. Scheidt, S. T. Nguyen and J. T. Hupp, *Chem. Soc. Rev.* **2009**, *38*, 1450; d) S. Ma and H.-C. Zhou, *Chem. Commun.* **2010**, *46*, 44; e) L. E. Kreno, K. Leong, O. K. Farha, M. Allendorf, R. P. Van Duyne and J. T. Hupp, *Chem. Rev.* **2012**, *112*, 1105.

[14] Y. H. Hu and L. Zhang, *Phys. Rev. B, PRB* **2010**, *81*, 174103.

[15] S. L. James, *Chem. Soc. Rev.* **2003**, *32*, 276.

[16] J. Cravillon, S. Münzer, S.-J. Lohmeier, A. Feldhoff, K. Huber and M. Wiebcke, *Chem. Mater.* **2009**, *21*, 1410.

[17] a) C. Zhi, Y. Bando, C. Tang, S. Honda, K. Sato, H. Kuwahara and D. Golberg, *Angew. Chem. Int. Ed.* **2005**, *44*, 7932; b) C. Zhi, Y. Bando, C. Tang and D. Golberg, *J. Am. Chem. Soc.* **2005**, *127*, 17144; c) C. Zhi, Y. Bando, C. Tang and D. Golberg, *J. Phys. Chem. B* **2006**, *110*, 8548; d) T. Ikuno, T. Sainsbury, D. Okawa, J. M. J. Fréchet and A. Zettl, *Solid State Commun.* **2007**, *142*, 643.

[18] Y. Gu, M. Zheng, Y. Liu and Z. Xu, *J. Am. Ceram. Soc.* **2007**, *90*, 1589.

[19] S. Saha, D. V. S. Muthu, D. Golberg, C. Tang, C. Zhi, Y. Bando and A. K. Sood, *Chem. Phys. Lett.* **2006**, *421*, 86.

[20] a) G. Kumari, K. Jayaramulu, T. K. Maji and C. Narayana, *J. Phys. Chem. A* **2013**, *117*, 11006; b) L. M. Markham, L. C. Mayne, B. S. Hudson and M. Z. Zgierski, *J. Phys. Chem.* **1993**, *97*, 10319; c) D. A. Carter and J. E. Pemberton, *J. Raman Spectrosc.* **1997**, *28*, 939.

[21] P. S. Marchetti, D. Kwon, W. R. Schmidt, L. V. Interrante and G. E. Maciel, *Chem. Mater.* **1991**, *3*, 482.

[22] Z. Ren, E. Kim, S. W. Pattinson, K. S. Subrahmanyam, C. N. R. Rao, A. K. Cheetham and D. Eder, *Chem. Sci.* **2012**, *3*, 209.

[23] S. Pal, S. R. C. Vivekchand, A. Govindaraj and C. N. R. Rao, *J. Mater. Chem.* **2007**, *17*, 450.

[24] J.-C. Tan, B. Civalleri, C.-C. Lin, L. Valenzano, R. Galvelis, P.-F. Chen, T. D. Bennett, C. Mellot-Draznieks, C. M. Zicovich-Wilson and A. K. Cheetham, *Phys. Rev. Lett.* **2012**, *108*, 095502.

Chapter 8: Remarkable improvement in the mechanical properties and CO_2 uptake of MOFs brought about by covalent linking to graphene*

Summary

Metal–organic frameworks (MOFs) are exceptional as gas adsorbent but their mechanical properties are poor. In this chapter a successful strategy to improve the mechanical properties along with gas adsorption characteristics is explored, wherein graphene (Gr) is covalently bonded with M/DOBDC (M = Mg^{2+}, Ni^{2+} and Co^{2+}, DOBDC = 2,5-dioxido-1,4-benzene-dicarboxylate) MOFs. The surface area of the graphene–MOF composites increases up to 200 – 300 m^2/g whereas the CO_2 uptake increases by ~ 3 – 5 wt% at 0.15 atm and by 6 – 10 wt% at 1 atm. What is significant is that the composites exhibit improved mechanical properties. In the case of Mg/DOBDC, a three–fold increase in both the elastic modulus and hardness with 5 wt % graphene reinforcement is observed. Improvement in both the mechanical properties and gas adsorption characteristics of porous MOFs on linking them to graphene reported here is a novel observation and suggests a new avenue for the design and synthesis of porous materials.

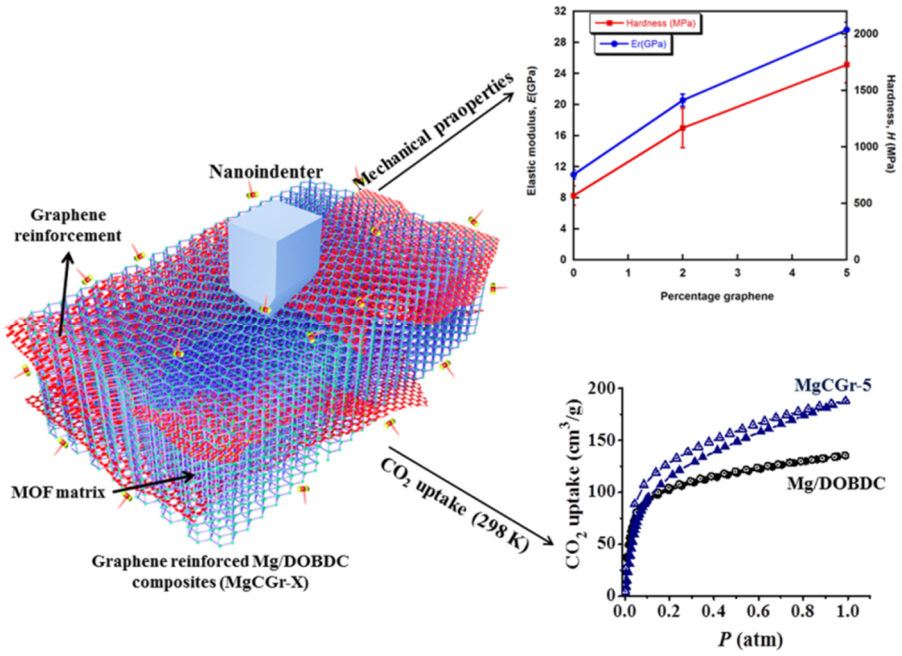

A paper based on these studies has appeared in Angew. Chem. Int. Ed. 2016, 55, 7857.

8.1 Introduction

Metal-organic frameworks (MOFs) which are important materials for gas storage, separation, and catalysis,[1] are expected to decrease the energy penalty of CO_2 capture from flue gas in coal-fired power plants.[2] For CO_2 capture and long-term performance in above-mentioned applications, the material should be chemically and mechanically stable to allow dense packing of the adsorbent bed without loss of the porous network.[2b] For CO_2 separation from post-combustion flue gas, the hydrothermal stability of the MOFs is an important factor.[2b,3] Most of the low–density (density < 1 g/cm^3) porous open frameworks are, not mechanically robust with an elastic modulus, of 3 – 4 GPa and hardness of 200 – 500 MPa.[3-4] Inorganic zeolites have a low surface area in comparison to MOFs but have an elastic modulus of 40 – 100 GPa and a hardness of 2.5 – 10 GPa.[5] It is, therefore, highly desirable to adopt a strategy that would enhance the mechanical properties of MOFs without imposing a penalty on their intrinsic surface area and gas adsorption properties. In view of the excellent mechanical properties of graphene,[6] Selected MOFs covalently linked with graphene were investigated for mechanical properties and CO_2 uptake. It should be noted that there is some evidence for increased hydrothermal stability, enhanced gas adsorption and selectivity for gas separation in MOF–graphene composites.[7] Composites of M/DOBDC or CPO-27-M, (M = Mg^{2+}, Ni^{2+} and Co^{2+} and DOBDC = 2,5-dioxido-1,4-benzene-dicarboxylate) were synthesized, which are known to exhibit the highest uptake of CO_2 at low pressure,[2c,8] covalently linked to Gr, and their surface area, gas storage (for both CO_2 and H_2), and mechanical properties were studied.

The strategy employed, involves benzoic acid functionalization of the graphene basal plane. The carboxylate groups of the benzoic acid functionalized graphene (BFG) bond with metal ions just as the carboxylate groups in DOBDC linker. Although Mg/DOBDC has the highest low–pressure CO_2 uptake reported to date in the literature, the performance deteriorates significantly in the presence of moisture with the recovery of only 16 % of its initial capacity after regeneration. Although Ni/DOBDC and Co/DOBDCs exhibit a smaller CO_2 uptake than Mg/DOBDC but show significant retention (61 – 85 %) of uptake capacity after exposure and regeneration.[9] The results of the present study of the different MOF–graphene composites demonstrate that it is possible to design composites that are highly functional and mechanically robust simultaneously.

8.2 Scope of the present investigations

Metal–organic frameworks (MOFs) which are highly porous and crystalline materials comprise metal ions connected by organic linkers using moderate energy coordinate bonds.[10] This makes MOFs suitable for wide range of potential applications in gas storage, separation, catalysis and molecular sensing.[1c,d,11] The moderate energy coordinate bonds linking metal ion with organic linkers makes it vulnerable to framework collapse under hydrostatic pressure, shear stress and strain and attack on metal ion by moisture or other electron donating adsorbents such as NH_3 and H_2S.[2b,3,12] One of the potential applications of MOFs under consideration is CO_2 capture from flue gas in coal–fired power plants.[2b] All the above-mentioned applications involve subjecting the framework structures to various modes of mechanical stress and strain. External hydrostatic pressures of several GPa being common place in practical situations. Most of the low density (density < 1 g/cm^3) MOFs are not mechanically robust and have a low elastic modulus in the range of $3 - 4$ GPa and hardness $200 - 500$ MPa.[3-4] Inorganic zeolites, although having a significantly lower surface area in comparison to MOFs, have an elastic modulus of $40 - 100$ GPa and hardness of $2.5 - 10$ GPa.[5] The above-mentioned applications of MOFs cannot be realized if the porous framework architecture is perturbed. Thus a strategy which can enhance the mechanical properties of highly porous frameworks without compromising with intrinsic porosity and gas storage properties is required. A successful strategy of significantly enhancing the mechanical properties along with enhanced surface area and gas storage (CO_2 and H_2) properties by covalently linking MOF with graphene is the subject of the present chapter. Composites of M/DOBDC or CPO-27-M, (M = Mg^{2+}, Ni^{2+} and Co^{2+} and DOBDC = 2,5-dioxido-1,4-benzene-dicarboxylate) with different weight % of graphene were synthesized. The elastic modulus and hardness increase significantly up to 170 and 204 % in the case of 5 wt% graphene reinforced Mg/DOBDC composite. The surface area of the composites increases by $200 - 300$ m^2/g whereas the intrinsic microporous feature of MOF is retained in the composite. An enhancement in the CO_2 uptake of $3 - 5$ wt% at $P \approx 0.15$ atm and $6 - 10$ wt % at $P \approx 1$ atm is also observed. The strategy of reinforcing the MOF matrix with few weight % graphene to bestow it with significantly enhanced mechanical properties and gas storage properties is of significant practical importance.

8.3 Experimental section

Benzoic acid functionalization of graphene: Graphite oxide (GO) was synthesized using modified Hummers method.[13] Exfoliated graphene (EG) was obtained by introducing graphite oxide in the heating zone of a furnace maintained at 1050 °C under constant N_2 flow. Basal plane benzoic acid functionalization of graphene was carried out using the procedure reported earlier by Loh *et al*.[14]

MCGr-X (M = Mg^{2+}, Ni^{2+} and Co^{2+}; X = 0, 2, 5 and 10 wt% of graphene): $Mg(NO_3)_2.6H_2O$ (480 mg, 1.87 mmol), and 2, 5-dihydroxyterephthalic acid (H_4DOBDC) (110 mg, 0.5 mmol) was added to a 15:1:1 (v/v/v) mixture of *N,N*-Dimethylformamide (DMF)–ethanol–water (50 ml), allowed to stir for 30 min to obtain a homogeneous dispersion, transferred to 100 ml glass bottle and heated at 125 °C for 24 h.[8a] The product was filtered (0.45 μm, nylon), washed with DMF and methanol (MeOH), transferred to a glass vial and dipped in MeOH for 4 days. MeOH was replaced every 12 h. Obtained yellow solid was used for adsorption and mechanical property measurements. Different weight % of functionalized graphene (based on the total mass of starting solid precursors) was added to the solvent, sonicated for 30 min to obtain a homogeneous dispersion, $Mg(NO_3)_2.6H_2O$ and H_4DOBDC was added followed by stirring and sonication for 30 min each. The remaining steps were same.

NiCGr-X (X = 0, 2, 5 and 10 wt%): $Ni(NO_3)_2.6H_2O$ (600 mg, 2 mmol) and H_4DOBDC (120 mg, 0.53 mmol) was added to 1:1:1 (v/v/v) DMF–ethanol–water (50 ml) and stirred for 30 min to obtain a homogeneous solution. The remaining steps were same for both composites as well as pristine MOF as for MgCGr-X except the temperature used was 100 °C.

CoCGr-X (X = 0, 2, 5 and 10 wt%): $Co(NO_3)_2.6H_2O$ (600 mg, 2 mmol) and H_4DOBDC (120 mg, 0.53 mmol) was added to 1:1:1 (v/v/v) DMF–ethanol–water (50 ml) and stirred for 30 min to obtain a homogeneous solution. The remaining steps were same for both composites as well as pristine MOF as for MgCGr-X except the temperature used was 100 °C.

Mechanical properties: Mechanical properties were measured on pellets of the composites. For MgCGr-X samples, 100 mg powder was placed in 8 mm diameter stainless steel die and heated to 170 °C, where it was held for 30 minutes before loading to 15 kN at a rate of 0.1 mm/s in an electro-mechanical machine (Zwick/Roell, Z-100). The load was held constant

for 15 minutes. Subsequently, the sample was unloaded and cooled to room temperature before extracting the pellet. The thickness of mechanically robust pellets is ~ 0.8 mm. For NiCGr-X, composites the sample was heated to 160 °C and a load of 12 kN was applied. Remaining conditions were same. PXRD patterns confirmed that the pelletization process did not alter the phases (Figures S19 and S20). Mechanical properties of the pellets were evaluated by employing the nanoindentation technique using the Triboindenter (Hysitron, Minneapolis, USA). The applied load, *P*, and the corresponding depth of penetration of the indenter, *h*, were collected and evaluated. A Berkovich tip diamond indenter with the tip radius of 100 nm was used for the indentation. The peak load, P_{max}, was maintained at 2 mN and the loading and unloading rates were 0.4 mN/s. The hold time at P_{max} was 5 s. A minimum of 30 indentations was performed on each pellet so to obtain statistically significant information. The *P-h* curves are analyzed using the Oliver-Pharr method to extract the elastic modulus, *E*, and the hardness, *H*, of the samples.

Characterization: PXRD patterns were recorded on Bruker D8 Discover X-ray diffractometer using Cu K-α radiation. Infrared (IR) spectra were recorded using attenuated–total–reflectance (ATR) accessories from Perkin Elmer. Raman spectra were recorded in backscattering geometry using 514.5 nm Ar^+ laser in HORIBA LabRam HR800 spectrometer. Morphological studies were carried out using Nova Nano SEM 600, FEI Company. TEM images were obtained using FEI Tecnai at an accelerating voltage of 200 kV. Thermogravimetric analysis was performed using Mettler Toledo TGA in a nitrogen atmosphere with a heating rate of 5 °C/ min.

Adsorption measurements: The N_2 (77 K and 298 K), H_2 (77 K) and CO_2 (298 K) adsorption–desorption isotherms were obtained by using QUANTACHROME QUADRASORB-*SI* analyzer. In the sample tube ~100 – 150 mg sample was placed and degassed at 250 °C under vacuum for about 10 h prior to the measurement. Adsorbate was charged into the sample tube and change in pressure was monitored. The degree of adsorption was determined by monitoring the decrease in pressure at equilibrium state. All the operations were computer-controlled and automatic.

8.4 Results and discussion

Scheme 1 shows the steps involved in the synthesis of graphene-reinforced–M/DOBDC composites (see experimental section 8.3 for details). The composites (C) are denoted as MCGr-X where M = Mg^{2+}, Ni^{2+} and Co^{2+} and X corresponds to the weight % of graphene

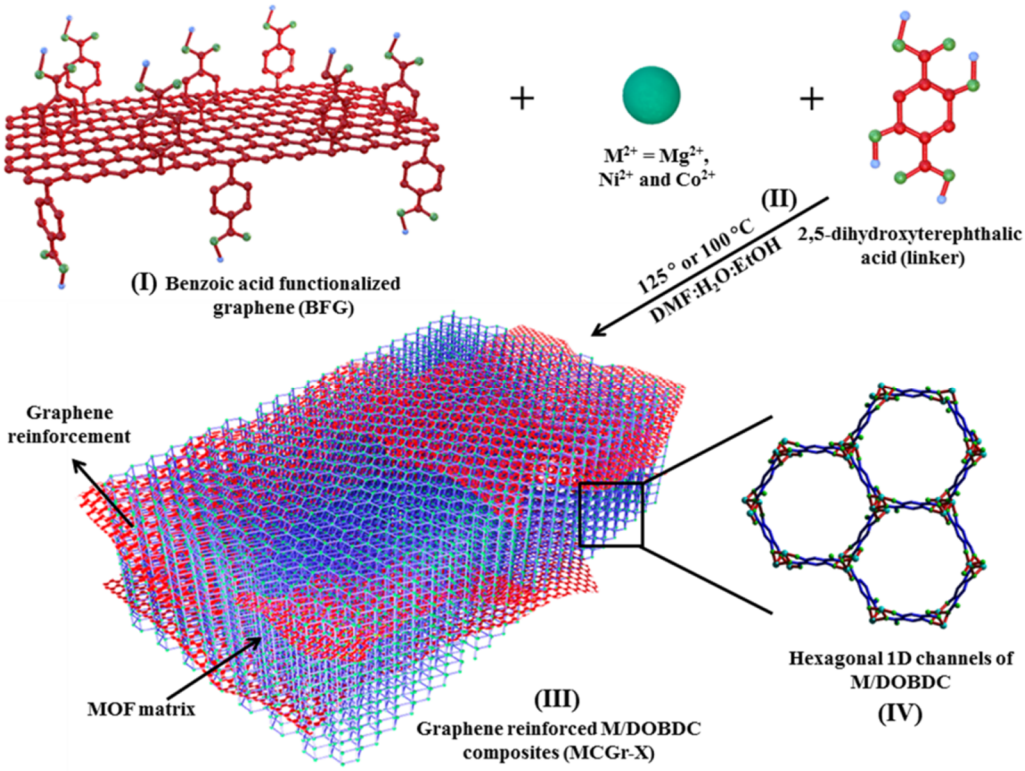

Scheme 1: Schematic representation of the synthesis of covalently linked MCGr-X composites. (I) Benzoic acid functionalized graphene (BFG). (II) *In-situ* growth of M/DOBDC crystals on the graphene basal plane. (III) Graphene reinforced MCGr-X composites (M = Mg^{2+}, Ni^{2+} and Co^{2+}; X = 0, 2, 5 and 10 wt%), where M is the metal ion and Gr-X different weight% of graphene-reinforced in the M/DOBDC matrix. (IV) Hexagonal (~ 1.1 × 1.1 nm^2) 1-D channels of M/DOBDC.

incorporated (X = 2, 5, and 10 wt%). Figure 1 show powder X-ray diffraction (PXRD) patterns of the as–synthesized M/DOBDC and the MCGr-X composites. The PXRD patterns of MCGr-X are consistent with the reported pattern of isostructural M/DOBDC indexed on a trigonal cell.[8a,15] The M^{2+} ions are bridged by the carboxylate and oxy groups of the fully deprotonated 2,5-dihydroxybenzene-1,4-dicarboxylic acid, resulting in cross–linking chains arranged in a hexagonal manner. All the oxygen of the ligand is involved in coordination to the metal ions resulting in hexagonal 1D pore with an average cross-sectional channel dimension of ~ 1.1 × 1.1 nm^2.[8a,15-16] The MOF matrix is uniformly reinforced by the large area 2 D graphene sheets in all random directions. Parent MOF determines the structure, with graphene just reinforcing the MOF matrix, thus same PXRD pattern for MCGr-X is observed as for pristine MOF.

Infrared spectra (IR) of methanol–exchanged MgCGr-X are shown in Figure 1. The spectra of all the MCGr-X show bands at 818, 1122, 1570, and 1637 cm^{-1} corresponding to C–H out of plane bending, C–O stretch, C═C ring stretch and carboxylates attached to the metal center (Figure 1). The sharp band at 1415 cm^{-1} and the broad band around 3330 cm^{-1}

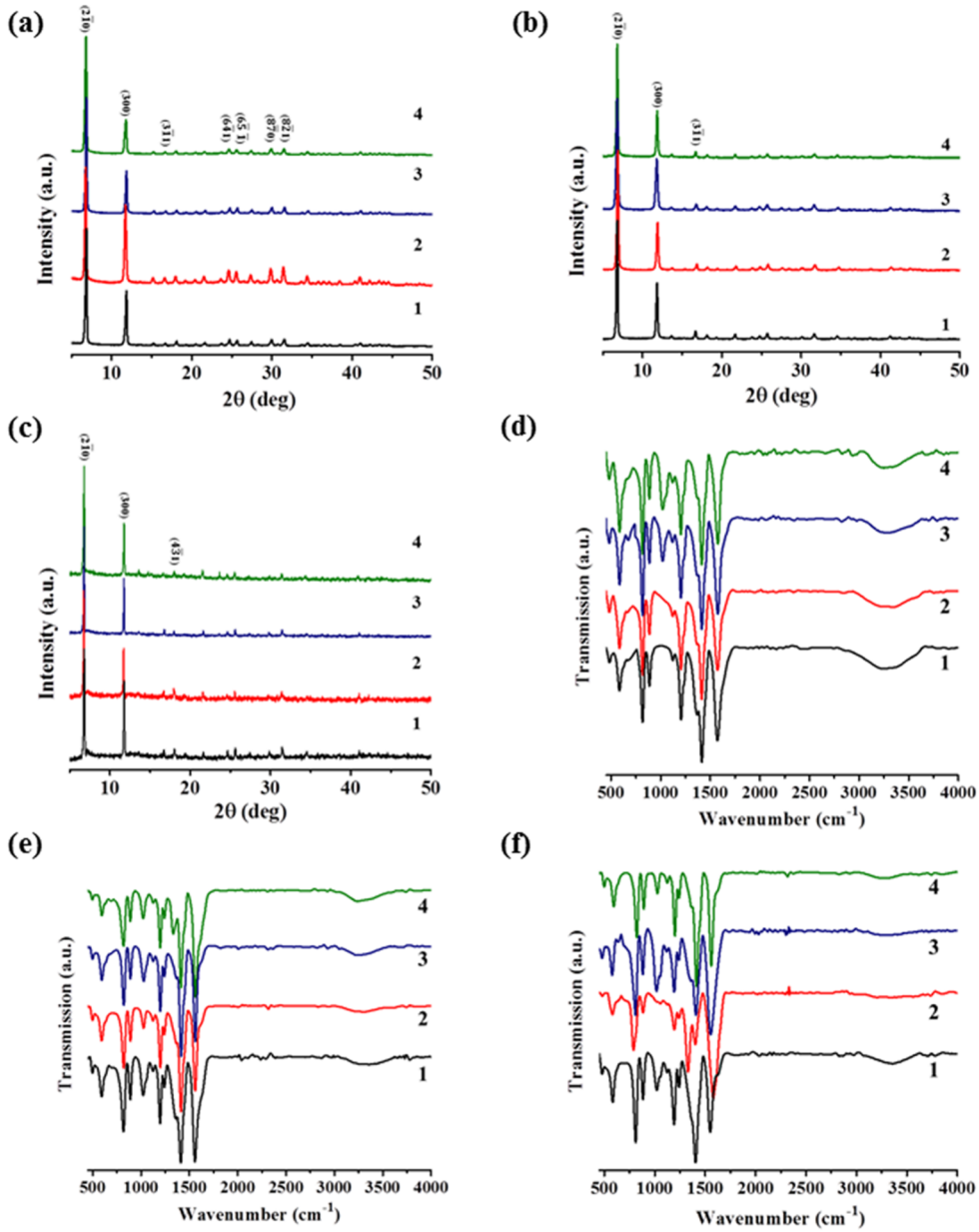

Figure 1: (a) Powder X-ray diffraction (PXRD) patterns of (1) Mg/DOBDC, (2) MgCGr-2, (3) MgCGr-5 and (4) MgCGr-10. Gr-X (X = 2, 5 and 10 wt%) corresponds to different weight% of graphene reinforcement. (b) PXRD patterns of (1) Ni/DOBDC, (2) NiCGr-2, (3) NiCGr-5 and (4) NiCGr-10. (c) PXRD patterns of (1) Co/DOBDC, (2) CoCGr-2, (3) CoCGr-5 and (4) CoCGr-10. (d) Infrared spectra of (1) Mg/DOBDC, (2) MgCGr-2, (3) MgCGr-5 and (4) MgCGr-10. (e) Infrared spectra of (1) Ni/DOBDC, (2) NiCGr-2, (3) NiCGr-5 and (4) NiCGr-10. (f) Infrared spectra of (1) Co/DOBDC, (2) CoCGr-2, (3) CoCGr-5 and (4) CoCGr-10.

are assigned to the C–O–H in-plane bend and hydrogen bonded O–H stretch of methanol trapped inside the 1D channel after the solvent exchange.[17] Raman spectra of the MCGr-X composites show bands of the ligand and M–O stretching band (Figure 2).[17] The broad bands at 1343 and 1585 cm^{-1} merging with the MOF bands in the 1150–1670 cm^{-1} range arise

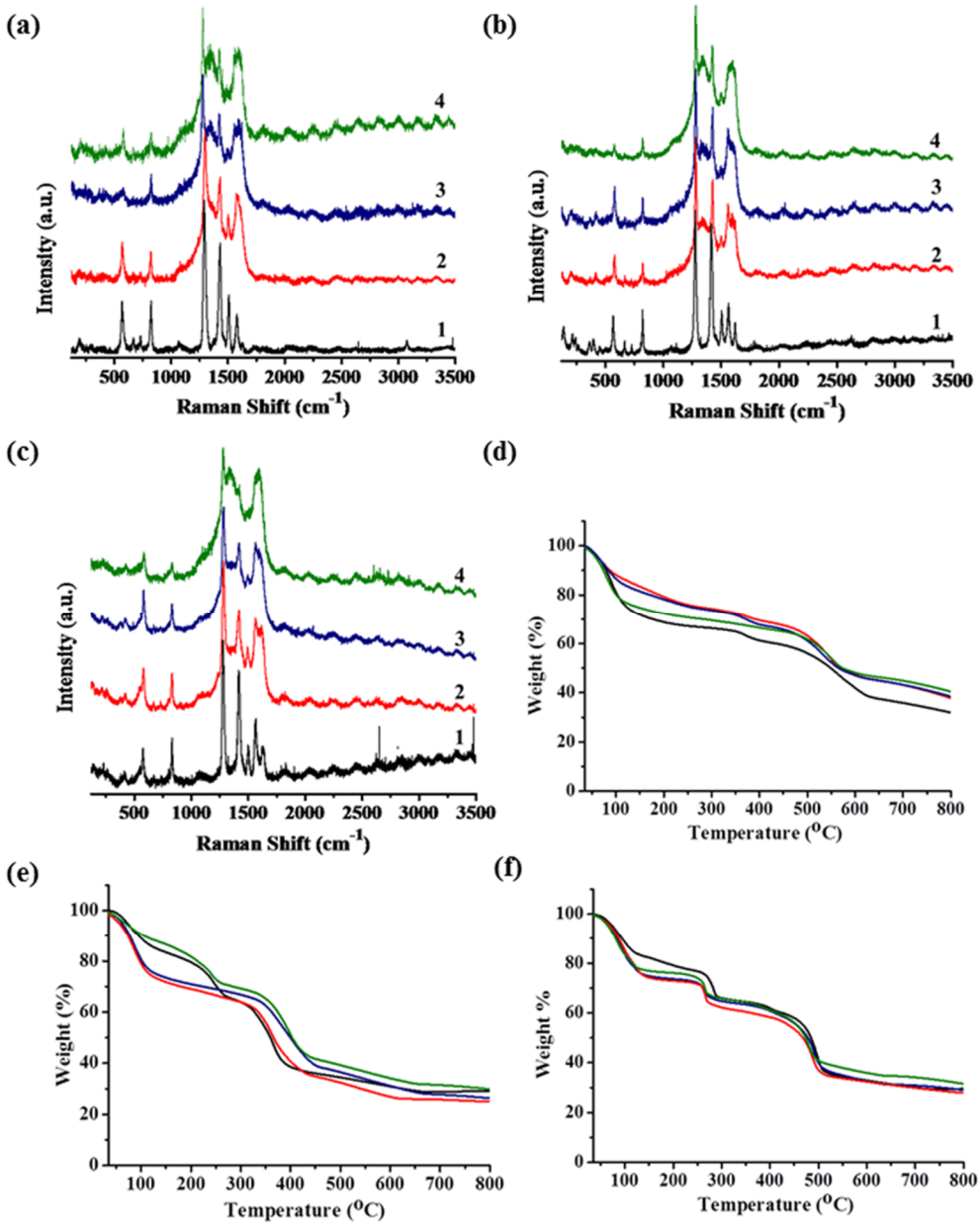

Figure 2: (a) Raman spectra of (1) Mg/DOBDC, (2) MgCGr-2, (3) MgCGr-5 and (4) MgCGr-10. Where, Gr-X (X = 2, 5 and 10 wt%) corresponds to different weight% of graphene reinforced in the Mg/DOBDC matrix. (b) Raman spectra of (1) Ni/DOBDC, (2) NiCGr-2, (3) NiCGr-5 and (4) NiCGr-10. (c) Raman spectra of (1) Co/DOBDC, (2) CoCGr-2, (3) CoCGr-5 and (4) CoCGr-10. (d) Thermogravimetric analysis (TGA) profiles of Mg/DOBDC (black), MgCGr-2 (red), MgCGr-5 (blue) and MgCGr-10 (olive). (e) TGA profiles of Ni/DOBDC (black), NiCGr-2 (red), NiCGr-5 (blue) and NiCGr-10 (olive). (f) TGA profiles of Co/DOBDC (black), CoCGr-2 (red), CoCGr-5 (blue) and CoCGr-10 (olive). TGA was performed in a nitrogen atmosphere.

from the *D* and *G* bands of graphene.[18] The intensities of these bands increase on increasing the graphene content. Raman spectra of the MgCGr-X composites show bands at 1430, 1508, and 1576 cm^{-1} corresponding to the benzene stretching modes (Figure 2a). Bands in the 450 – 300 cm^{-1} region are attributed to M–O (M = Mg^{2+}, Ni^{2+} and Co^{2+}) stretching modes whereas

modes below 250 cm^{-1} are due to phonon vibrations.[17] Raman spectra of NiCGr-X and CoCGr-X (Figures 2b, c) are similar to those of MgCGr-X. Raman spectroscopy confirms the successful reinforcement of MOF crystals with graphene by covalent linking. While collecting the Raman spectra high stability of MgCGr-X composites was observed in comparison with NiCGr-X and CoCGr-X composites for laser-induced damages (514.5 nm, Ar^+ laser). On considering just pristine Mg/DOBDC and Ni/DOBDC mechanical property data and observed higher stability of Mg/DOBDC with respect to Ni/DOBDC to laser-induced damages, it can be concluded that Mg–O bond due to the increased ionic character is more stable in comparison to Ni–O and Co–O bond. MgCGr-X composites are structurally more robust in comparison to NiCGr-X and CoCGr-X composites. Thermogravimetric analysis of the MCGr-X composites in nitrogen shows the same thermal stability as the pristine MOFs (Figure 2).

Figure 3 shows scanning and transmission electron microscopy (SEM and TEM respectively) images of MgCGr-X samples. Pristine Mg/DOBDC comprises irregularly shaped 10 – 20 μm crystals (Figure 3a). With the addition of 2 and 5 wt% graphene, rectangular crystals less than 10 μm are observed (Figures 3b and c). Although a smooth rectangular surface is observed in the case of MgCGr-2 and MgCGr-5, observation of the edges shows sandwiched graphene sheets between the MOF layers (Figure 3). The addition of 10 wt% graphene significantly alters the crystal morphology and 100 – 200 nm diameter MOF nanowires wrapped in a graphene matrix is observed. Figure 4 shows SEM and TEM images of NiCGr-X samples. Pristine Ni/DOBDC has 5 to 10 μm flower shaped agglomerated morphology (Figure 4a). The addition of 2 wt% graphene gives rise to morphology similar to that of pristine Ni/DOBDC with the graphene sheets sandwiched in the MOF matrix (Figure 4b). The addition of 5 and 10 wt% graphene affects the nucleation and growth of Ni/DOBDC crystals significantly and bean shaped 500 nm – 1 μm crystals sandwiched by graphene sheets (Figures 4c and d) is observed. A time–dependent study of crystal growth process shows the evolution of Ni/DOBDC crystals on graphene surface and its effect on the morphology (Figure 7). Co/DOBDC has a mixture of rectangular and irregular 5 – 10 μm crystals (Figure 5) and the addition of graphene leads to rectangular shaped crystals with graphene sandwiched between the layers for CoCGr-X crystals (Figures 5 and 6). Microscopic investigations clearly show uniform reinforcement of MOF matrix by large micron-sized graphene sheets. The change in morphology and crystal size with the addition of graphene to the MOFs arises from coordination modulation. [19]

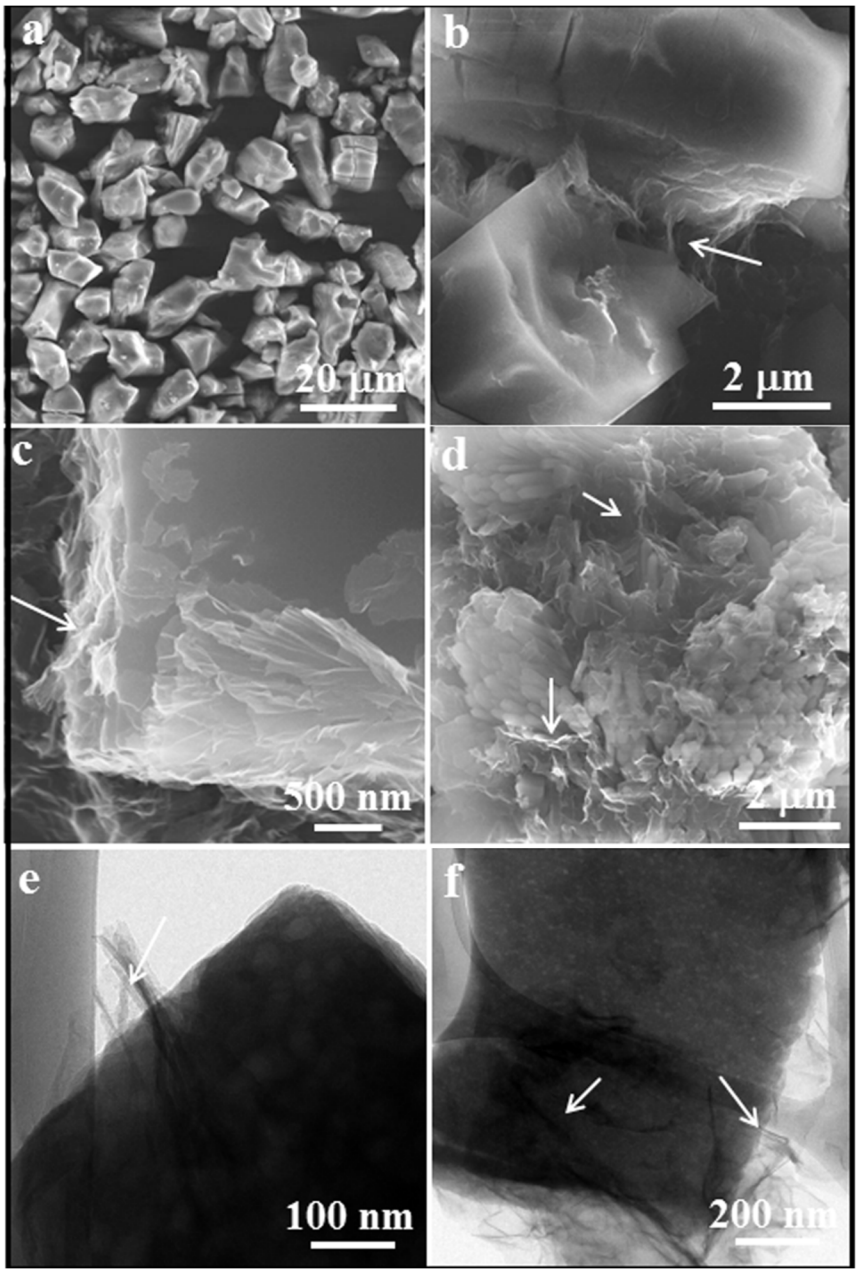

Figure 3: Scanning electron microscopy (SEM) images of (a) Mg/DOBDC, (b) MgCGr-2, (c) MgCGr-5 and (d) MgCGr-10. Transmission electron microscopy (TEM) images of (e) MgCGr-2 and (f) MgCGr-5. Arrows show graphene reinforced in the Mg/DOBDC matrix.

For NiCGr-X composites significant change in the morphology and crystal size was observed with increasing graphene concentration. The NiCGr-5 and NiCGr-10 have completely different morphology in comparison to pristine Ni/DOBDC. Such change in morphology is attributed to the coordination modulation. Benzoic acid functionalized graphene acts as a support for the growth of MOF building blocks. MOF building units grow on the graphene surface by covalently cross-linking with the metal ion which modulates the crystal growth process. Such growth leads to a graphene reinforced MOF composite with

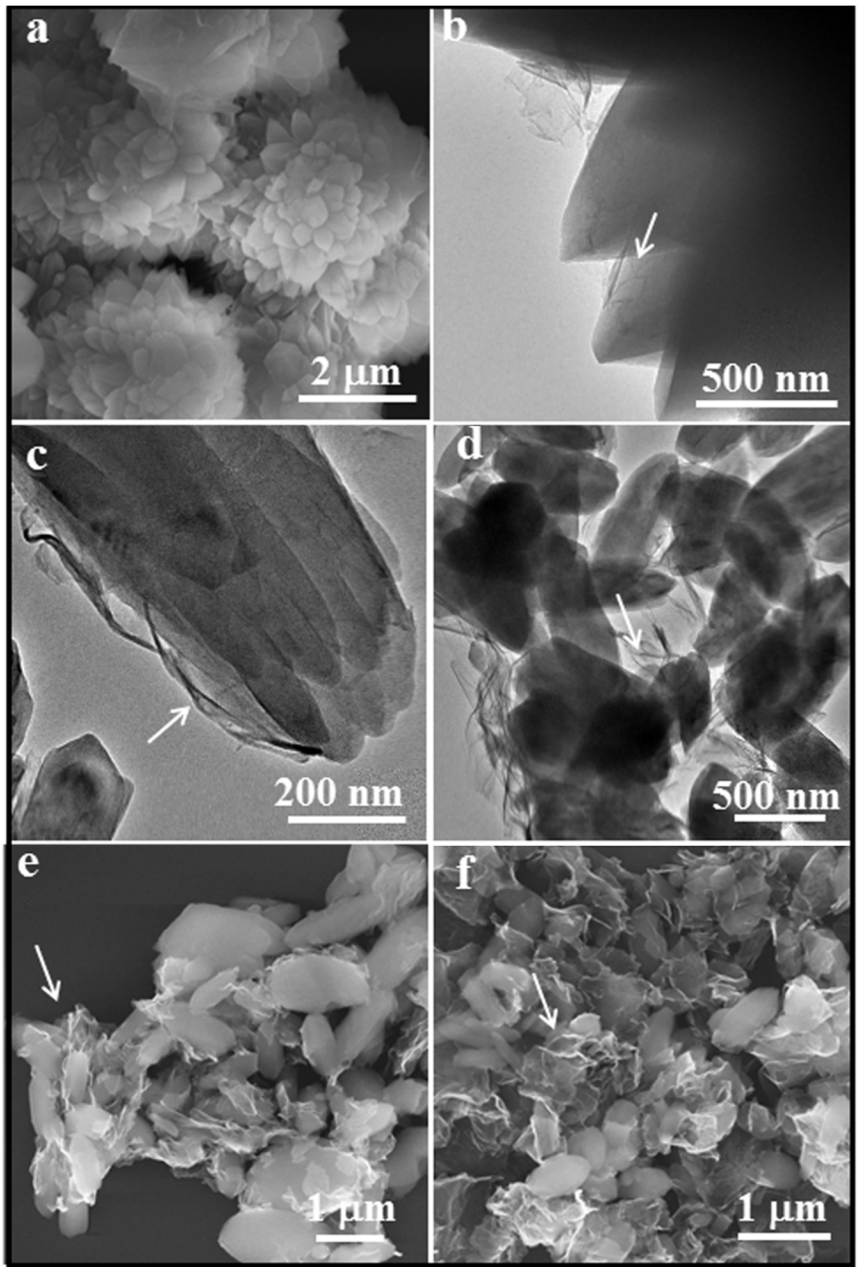

Figure 4: (a) SEM image of Ni/DOBDC; TEM images of (b) NiCGr-2, (c) NiCGr-5 and (d) NiCGr-10. SEM images of (e) NiCGr-5 and (f) NiCGr-10. Arrows show graphene reinforced in the Ni/DOBDC matrix.

significantly enhanced mechanical properties. Initial Ni/DOBDC has 5 – 10 μm flower shaped agglomerated morphology whereas, NiCGr-5 and NiCGr-10 have 500 nm to 1 μm bean shaped crystals with graphene sheets sandwiched between the MOF layers as observed in SEM and TEM images. In order to investigate the crystal growth process intermediate 5 wt% NiCGr-5 composite was selected and a microscopic investigation was carried out at 8 h, 12 h, and 24 h respectively. In a 50 ml Schlenck flask 10 ml reaction mixture was placed and sealed with a rubber septum. The reaction mixture was purged with N_2 for 30 min followed

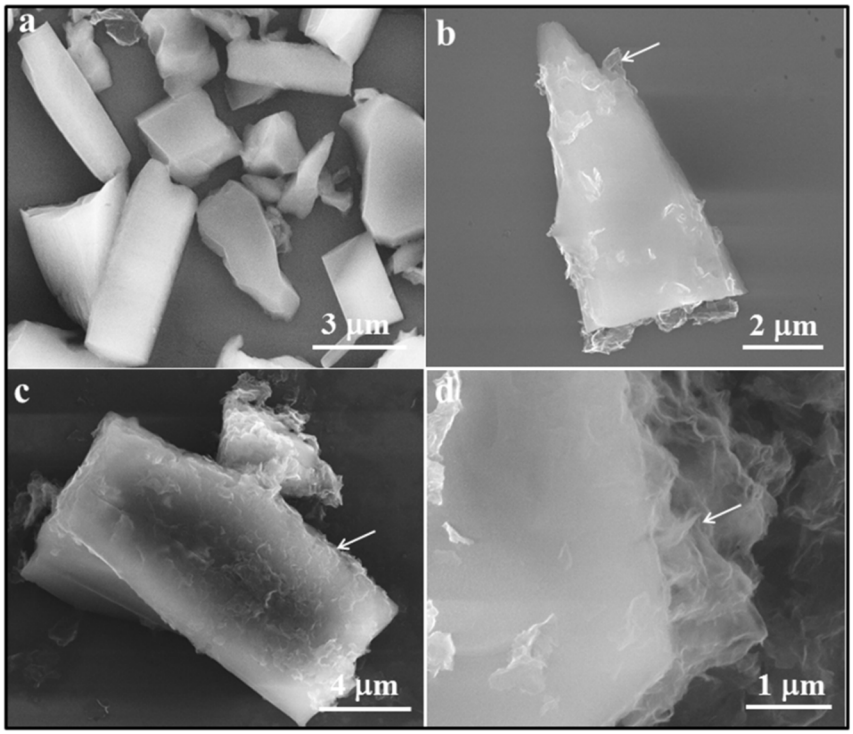

Figure 5: Scanning electron microscope (SEM) images of (a) Co/DOBDC, (b) CoCGr-2, (c) CoCGr-5 and (d) CoCGr-10. Arrows show graphene reinforced in the Co/DOBDC matrix.

by heating at 100 °C in an oil bath. Using a syringe the solid precipitate was collected at different time interval, filtered using 0.45 μm nylon membrane, washed with DMF followed by washing with a copious amount of methanol. A small amount of sample was dispersed in methanol and drop cast on a copper TEM grid. Figure 7 show the TEM images of sample collected at different time interval. Partial nucleation with irregular morphology on graphene basal plane is visible for initial 8 h sample. As graphene sheets are several microns in lateral dimension and MOF crystals have a lateral dimension of 500 nm to 1 μm, on one graphene sheet average 3 to 4 MOF crystals grow. Evolution of bean-shaped morphology with

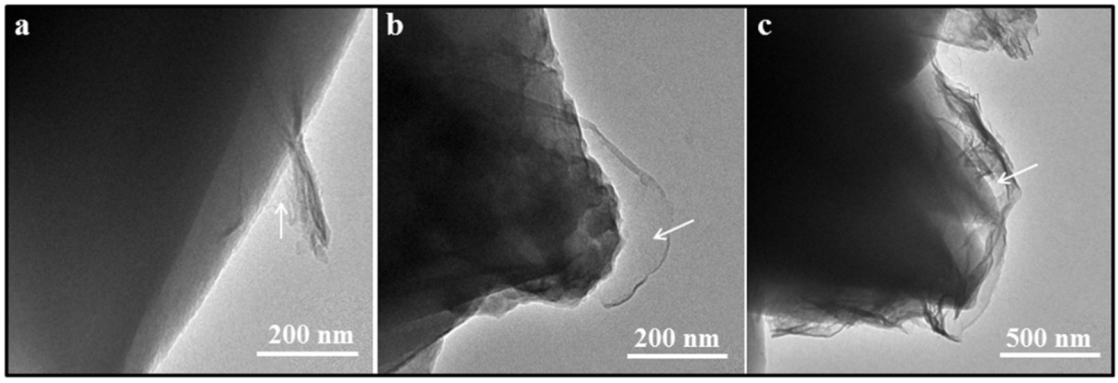

Figure 6: Transmission electron microscope (TEM) images of (a) CoCGr-2, (b) CoCGr-5 and (c) CoCGr-10. Arrows show graphene reinforced in the Co/DOBDC matrix.

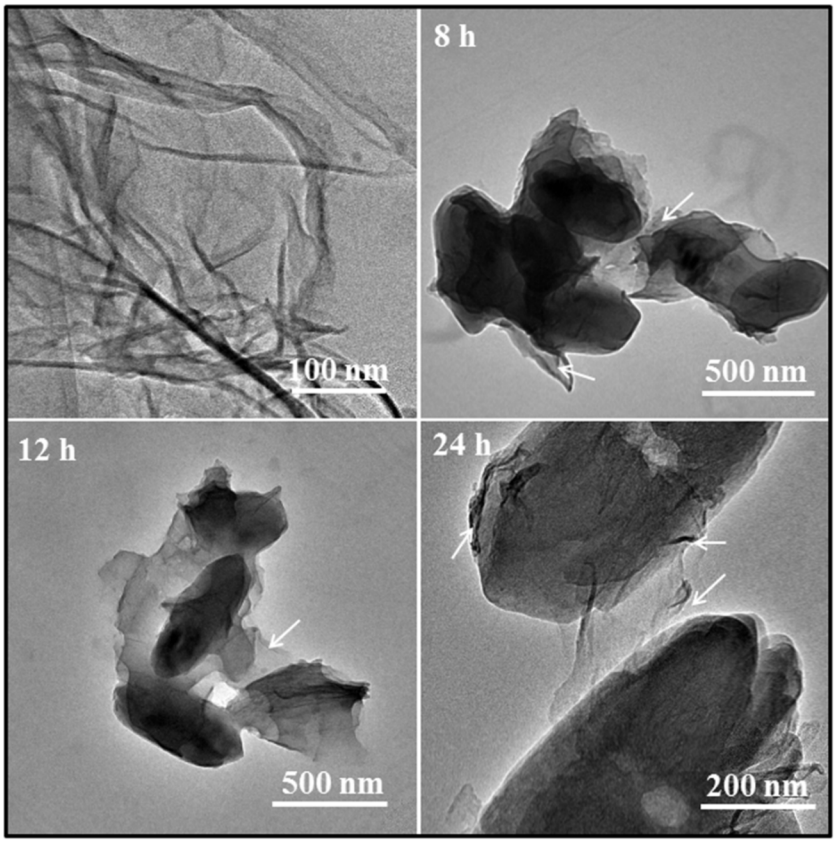

Figure 7: TEM images of the time-dependent study of the nucleation and growth of 5 wt% graphene reinforced Ni/DOBDC composite NiCGr-5. Arrows show graphene reinforced in the Ni/DOBDC matrix.

graphene sheets reinforced between MOF layers is clearly visible for 12 h sample. After 24 h uniformly arranged graphene reinforced MOF crystals were observed. The time-dependent microscopic investigation clearly shows that benzoic acid functionalized graphene significantly alters the nucleation and growth of MOF crystals by coordination modulation. Both the linker 2,5-dihydroxybenzene-1,4-dicarboxylic acid, as well as benzoic acid, functionalized graphene have carboxylate groups which bind with the metal ion. Such effect of modulators with the same functionality as linker controlling the nucleation and growth of MOF crystals and hence resulting morphology is well documented in the literature.[19-20]

Surface areas and porosities of MCGr-X (M = Mg^{2+}, Ni^{2+} and Co^{2+}; X = 2, 5 and 10 wt% graphene) were determined by nitrogen adsorption at 77 K. Figure 8 shows the nitrogen adsorption–desorption and pore size distribution profiles of MCGr-X composites. The results are summarized in Table 1. The Brunauer-Emmet-Teller (BET) surface area of Mg/DOBDC is 1161 m^2/g whereas the surface areas of MgCGr-X samples are in the range of 1282 – 1474 m^2/g (Table 1), the surface area of the sample with 2 wt% graphene being

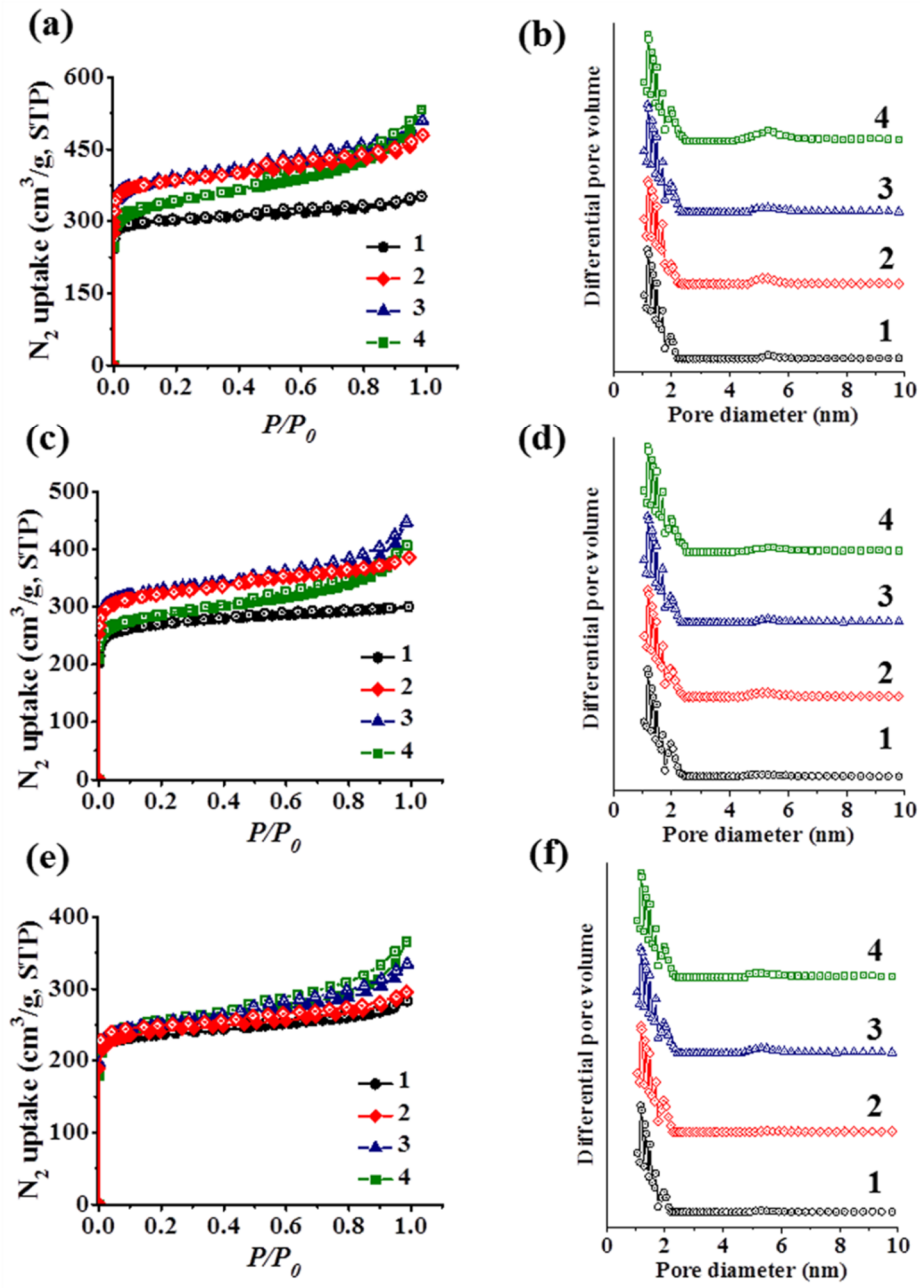

Figure 8: (a, b) Nitrogen adsorption-desorption isotherms at 77 K and corresponding pore size distribution calculated using non-local density functional theory (NLDFT) of (1) Mg/DOBDC, (2) MgCGr-2, (3) MgCGr-5 and (4) MgCGr-10. (c, d) Nitrogen adsorption-desorption isotherms at 77 K and corresponding pore size distribution calculated using (NLDFT) of (1) Ni/DOBDC, (2) NiCGr-2, (3) NiCGr-5 and (4) NiCGr-10. (e, f) Nitrogen adsorption-desorption isotherms at 77 K and corresponding pore size distribution calculated using non-local density functional theory (NLDFT) of (1) Co/DOBDC, (2) CoCGr-2, (3) CoCGr-5 and (4) CoCGr-10.

highest. The pore volume increases from 0.54 cm^3/g for Mg/DOBDC to ~ 0.7 cm^3/g in the MgCGr-X composites (Table 1). A similar increase in surface area and pore volume are observed in NiCGr-X and CoCGr-X as well (Tables 1). The lighter metal Mg in comparison to heavier transition metal counterparts Ni and Co causes a higher surface area in a series of

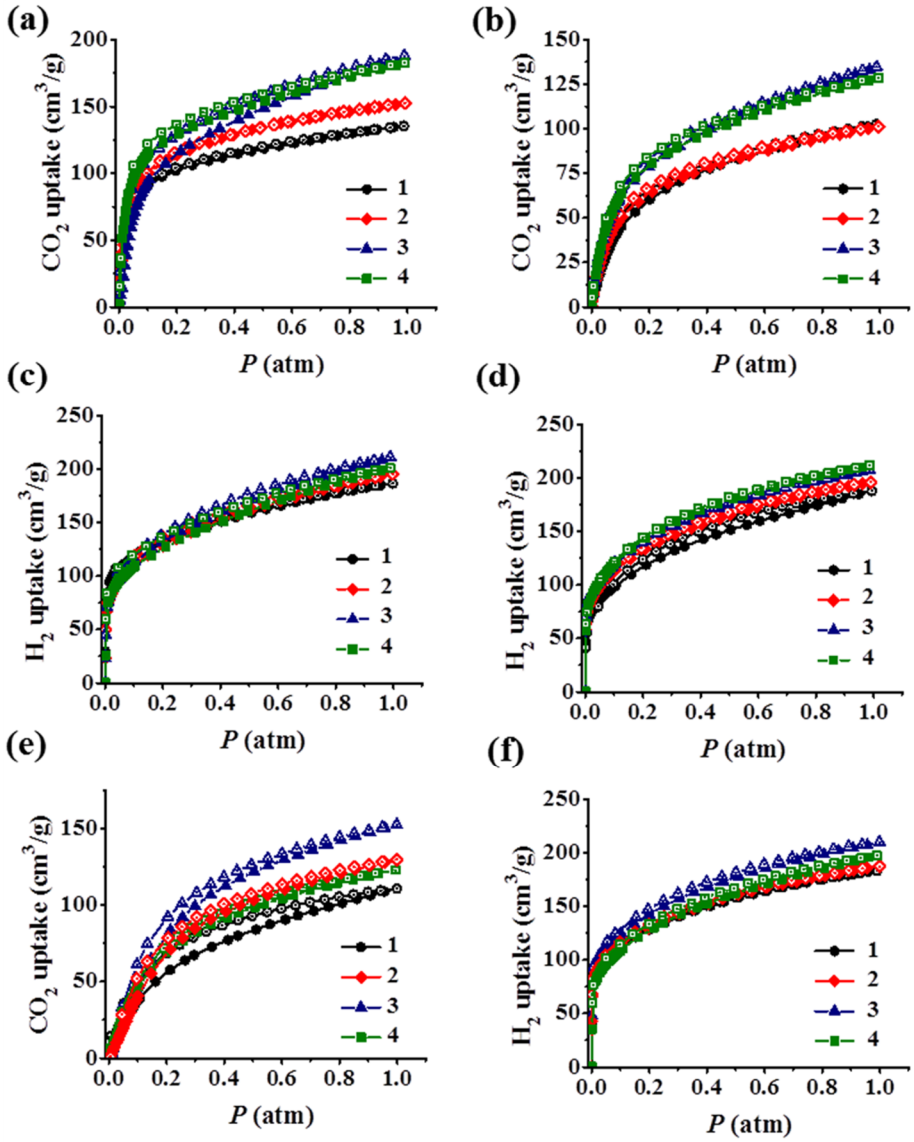

Figure 9: (a) Carbon dioxide adsorption-desorption isotherms of (1) Mg/DOBDC, (2) MgCGr-2, (3) MgCGr-5 and (4) MgCGr-10 at 298 K. (b) Carbon dioxide adsorption-desorption isotherms of (1) Ni/DOBDC, (2) NiCGr-2, (3) NiCGr-5 and (4) NiCGr-10 at 298 K. (c) Hydrogen adsorption-desorption isotherms of (1) Mg/DOBDC (2) MgCGr-2, (3) MgCGr-5 and (4) MgCGr-10 at 77 K. (d) Hydrogen adsorption-desorption isotherms of (1) Ni/DOBDC, (2) NiCGr-2, (3) NiCGr-5 and (4) NiCGr-10 at 77 K. (e) Carbon dioxide adsorption-desorption isotherms of (1) Co/DOBDC, (2) CoCGr-2, (3) CoCGr-5 and (4) CoCGr-10 at 298 K. (f) Hydrogen adsorption-desorption isotherms of (1) Co/DOBDC, (2) CoCGr-2, (3) CoCGr-5 and (4) CoCGr-10 at 77 K.

isostructural materials. Enhancement in the porous properties occurs up to a certain weight % of graphene, subsequent addition of graphene not leading to further enhancement. Pore size distribution of MCGr-X composites was calculated using non-local density functional theory (NLDFT) (Figure 8). The pore sizes of MCGr-X are in 1 – 2 nm microporous range just as in pristine M/DOBDC. Thus, the microporous feature and architectures of the frameworks are retained in the composites on the addition of up to 10 wt% graphene.

Table 1: Summary of the Brunauer-Emmet-Teller (BET) surface areas, pore volume, CO_2 and H_2 uptake, CO_2/N_2 selectivity and mechanical properties of the M/DOBDC and graphene reinforced MCGr-X composites. Gr-X (X = 2, 5 and 10 wt%) corresponds to different weight% of graphene-reinforced in the M/DOBDC (M = Mg^{2+} and Ni^{2+}) matrix.

Sample name	BET surface area (m^2/g); (Pore volume, cm^3/g)	CO_2 uptake at 298 K, P = 0.15 atm (wt%) and (wt% at P = 1 atm)	H_2 uptake at 77 K and 1 atm (wt%)	Initial slope CO_2 / Initial slope N_2 selectivity at 298 K
Mg/DOBDC	1161 (0.54)	19 (26.6)	1.6	123
MgCGr-2	1474 (0.72)	21.4 (30)	1.7	144
MgCGr-5	1465 (0.72)	21 (37)	1.9	233
MgCGr-10	1282 (0.7)	24 (35.7)	1.8	335
Ni/DOBDC	1022 (0.46)	10.4 (20)	1.7	86
NiCGr-2	1235 (0.57)	11.6 (19.8)	1.7	112
NiCGr-5	1257 (0.6)	14 (26)	1.8	154
NiCGr-10	1075 (0.56)	14.3 (25)	1.9	160
Co/DOBDC	910 (0.42)	9.6 (21.8)	1.6	-
CoCGr-2	926 (0.43)	10.8 (25.3)	1.6	-
CoCGr-5	953 (0.47)	12.7 (29.7)	1.9	-
CoCGr-10	948 (0.48)	11.6 (24)	1.8	-

Figure 9 show the CO_2 uptake profiles of MCGr-X (M = Mg^{2+}, Ni^{2+} and Co^{2+}; X = 2, 5 and 10 wt% of graphene) at 298 K. Table 1 summarize the CO_2 uptake data of the composites. Due to the relatively low concentration of CO_2 (15 –16%) in the flue gas, the low-pressure CO_2 uptake at pressure, $P \approx 0.15$ atm is of relevance for post–combustion CO_2 capture.[2b] MCGr-X composites exhibit an enhancement in CO_2 uptake at both $P \approx 0.15$ and 1 atm. Amongst the materials examined, MgCGr-X samples show the best low–pressure CO_2 uptake performance with pristine Mg/DOBDC showing an uptake of 19 wt%. The MgCGr-X samples exhibit a CO_2 uptake of 21 – 24 wt% at 0.15 atm (Table 1). At $P \approx 1$ atm, Mg/DOBDC shows an uptake of ~ 27 wt% whereas the MgCGr-X composites have an uptake of 30 – 37 wt%. The Co and Ni/DOBDC have an initial CO_2 uptake of ~ 10 wt%, whereas the CoCGr-X and NiCGr-X samples show an uptake in the range of ~ 11 – 14 wt% at $P \approx 0.15$ atm (Table 1). At $P \approx 1$ atm, Ni/DOBDC has CO_2 uptake of 20 wt% whereas NiCGr-X samples have CO_2 uptake in the range of 20 – 25 wt% (Table 1). The Co/DOBDC has an uptake of 22 wt% whereas CoCGr-X samples have an uptake of 24 – 29 wt% at $P \approx 1$ atm (Table 1). Thus, the CO_2 uptake data of MCGr-X samples reveal an enhancement of ~ 3 – 5 wt% at $P \approx 0.15$ atm and an enhancement of ~ 6 – 10 wt% at $P \approx 1$ atm (Table 1). The

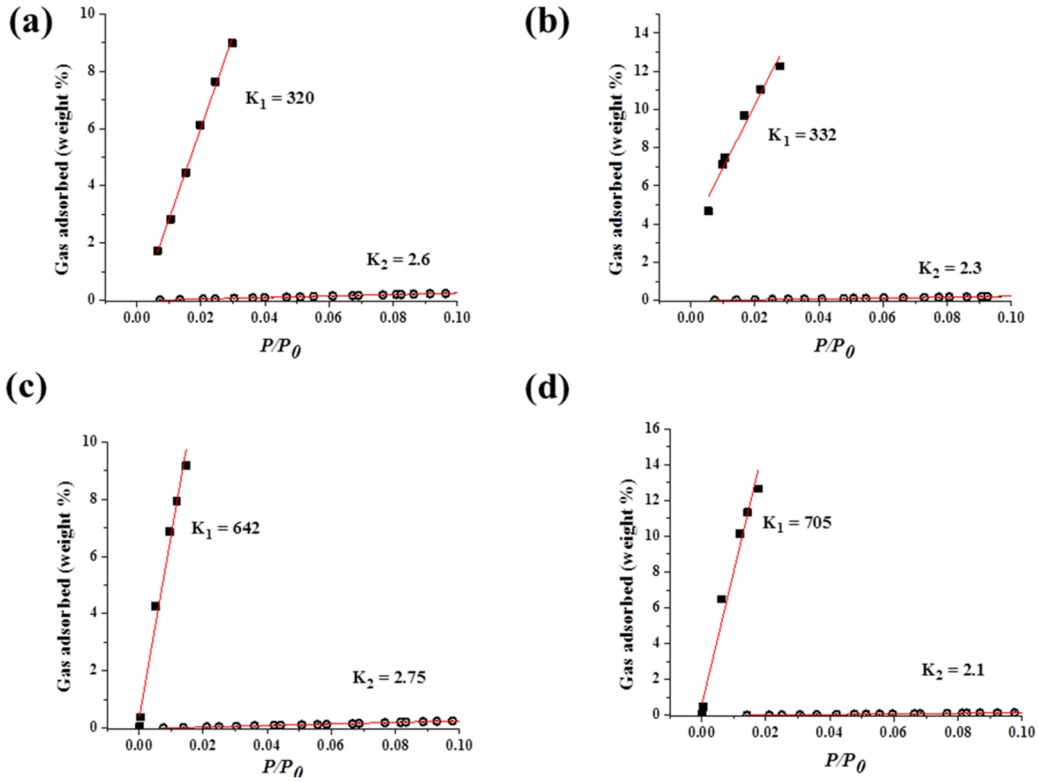

Figure 10: Linearly fitted plots of initial adsorption data points of MgCGr-X (X = 2, 5 and 10 wt%) for selectivity calculation of CO_2 over N_2 by employing the initial slope ratio method. The data points correspond to the adsorption isotherms collected at 298 K. The fitted initial adsorption data points of CO_2 and N_2 and corresponding slopes K_1 and K_2 of (a) Mg/DOBDC, (b) MgCGr-2, (c) MgCGr-5 and (d) MgCGr-10.

significantly higher CO_2 uptake in Mg/DOBDC and composites in comparison to the Ni and Co counterparts is attributed to the increased ionic character of Mg–O bond which provides strong affinity and additional uptake of CO_2 beyond simple weight effects of the lighter metal.

The CO_2/N_2 adsorption selectivity was examined by using the initial slope ratios (Henry's law constant) for single-component adsorption isotherms at 298 K (Table 1).[2a,21] This method is useful and convenient to compare the performances of different porous materials under similar conditions. The adsorption selectivity of Mg/DOBDC and corresponding different weight ratio composites are calculated by taking the ratio of low-pressure region slopes of CO_2 and N_2 adsorption isotherms. CO_2/N_2 selectivity increases markedly on the addition of graphene (Table 1). The selectivity of Mg/DOBDC and MgCGr–2, 5 and 10 wt% composites are 123, 144, 233 and 335 respectively (Table 1 and Figure 10). The CO_2/N_2 selectivity values for Ni/DOBDC and NiCGr– 2, 5 and 10 wt% composites are 86, 112, 154 and 160 respectively (Table 1 and Figure 11). The enhancement of CO_2 uptake and selectivity with the addition of graphene in the MOF matrix suggests a significant role of graphene.

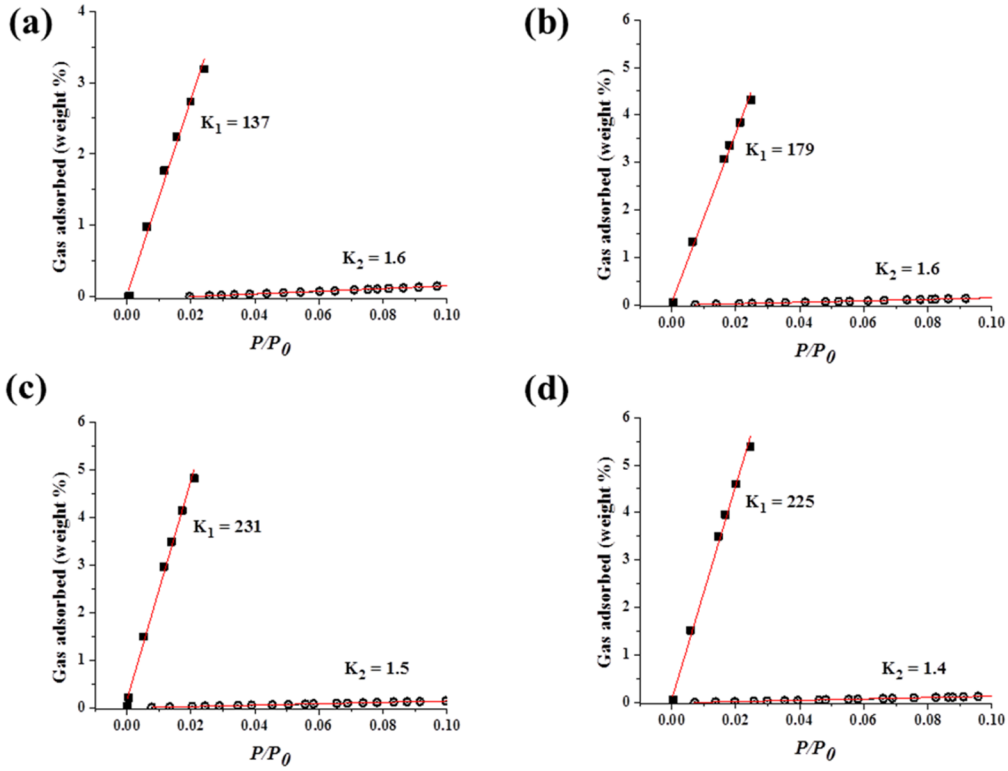

Figure 11. Linearly fitted plots of initial adsorption data points of NiCGr-X (X = 2, 5 and 10 wt%) composites for selectivity calculation of CO_2 over N_2 by employing initial slope ratio method. The data points correspond to the adsorption isotherms collected at 298 K. (a) The fitted initial adsorption data points of CO_2 and N_2 and corresponding slopes K_1 and K_2 of (a) Ni/DOBDC, (b) NiCGr-2, (c) NiCGr-5 and (d) NiCGr-10.

Figure 9 shows the hydrogen uptake profiles of MCGr-X (X = 2, 5 and 10 wt% of graphene) at 77 K. Mg/DOBDC has an H_2 uptake of 1.6 wt% at 1 atm whereas the composites show a marginal increase in the H_2 uptake, in the range of 1.7 – 1.9 wt % (see Table 1). A similar trend in hydrogen uptake is found for NiCGr-X and CoCGr-X samples, with the uptake in the range of 1.6 – 1.9 wt% (Table 1). The marginal increase in the hydrogen uptake of composites is attributed to the enhanced surface area of the composites in comparison with the pristine MOF. From the CO_2 and H_2 uptake measurements, it can be concluded that dispersive forces provided by the π electron cloud of graphene may have an influence on quadrupolar CO_2 with a higher polarizability than H_2.

The mechanical property measurements were carried out on pellets of MCGr–X composites using the nanoindentation technique, and the results are summarized in Figure 12 and Table 1. The elastic modulus, *E*, and hardness, *H*, were extracted from the load-depth of penetration (*P-h*) curves (see figure 13 for representative ones) using the standard Oliver-Pharr method. The *E* and *H* data are plotted as a function of the wt% graphene in the composite. In the case of NiCGr-X samples (Figure 12b), a linear increase in both *E* and *H*

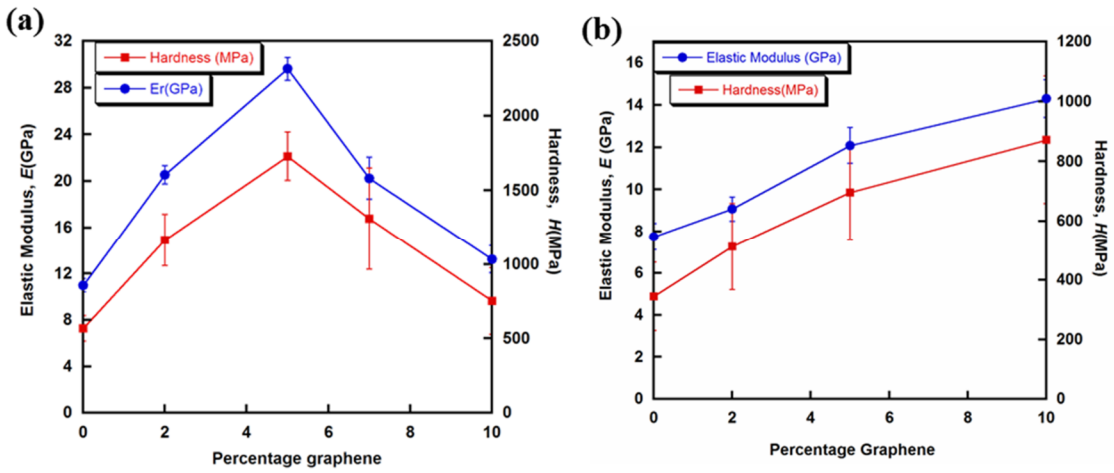

Figure 12: (a) Elastic modulus and hardness of (a) Mg/DOBDC and MgCGr-X and (b) Ni/DOBDC and NiCGr-X (X = different wt% of graphene-reinforced in the M/DOBDC matrix).

are noted, and the enhancements in both the properties are significant. For example, a 5 wt% addition of graphene to Ni/DOBDC enhances its *E* and *H* by 56% and 102% respectively. The observed enhancements are even more significant (at 170 and 204%) in the case of MgCGr-5. While the continued increase of the graphene content to 10 wt% further enhances the Ni/DOBDC mechanical properties, the mechanical performance of Mg/DOBDC with 10 wt% is markedly inferior to those with 2 and 5 wt% graphene. Interestingly, some of the gas absorption characteristics of Mg/DOBDC-graphene composites also exhibit such a reversal when the graphene content is increased to 10 wt% (see for example, Figures 8a).

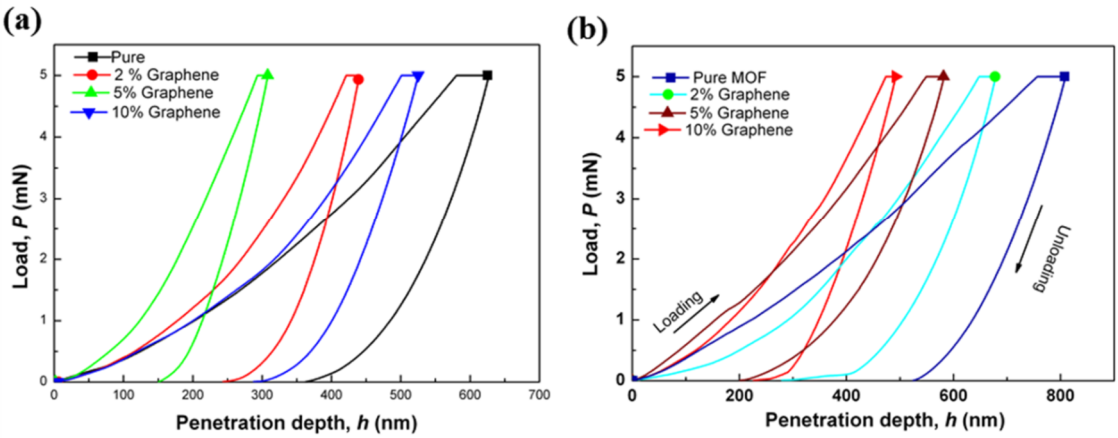

Figure 13. Representative *P-h* curves of graphene reinforced-M/DOBDC composites (M = Mg^{2+} and Ni^{2+}). (a) Load-depth (*P-h*) curve of Mg/DOBDC (black), MgCGr-2 (red), MgCGr-5 (green) and MgCGr-10 (blue). Gr-X (X = 0, 2, 5 and 10 wt%) corresponds to different weight % of graphene. (b) Load-depth (*P-h*) curve of Ni/DOBDC (black), NiCGr-2 (red), NiCGr-5 (green) and NiCGr-10 (blue). Gr-X (X = 0, 2, 5 and 10 wt%) corresponds to different weight % of graphene reinforced in the MOF matrix.

A possible reason for this marked drop in both mechanical and functional properties in MgCGr-10 graphene composites could be the significant change in the crystal morphology and agglomeration of graphene in the MOF matrix at this reinforcement level, as already noted (Figures 2 and 14). The 7 wt% contrast sample confirms the effect of agglomeration in decreasing the mechanical properties. It should be noted that higher concentrations of graphene in the polymer, metal, and ceramic composites are known to degrade mechanical properties due to agglomeration.[22] Higher mechanical properties of Mg/DOBDC system in comparison to the Ni counterpart is attributed to increased ionic character of the Mg–O bond resulting in more robust framework. Nevertheless, the substantial enhancements in the mechanical properties that accrue due to 5 wt% graphene reinforcement demonstrate the utility of such a composite route for imparting mechanical robustness to the MOFs that are otherwise fragile in nature.

Table 2: Mechanical properties of the MCGr-X composites (M = Mg^{2+} and Ni^{2+}; X = different wt% graphene reinforcement).

Sample Name	Graphene reinforcement (wt%)	Elastic Modulus, *E* (GPa) ; (Standard deviation, GPa)	Hardness, *H* (MPa); (Standard deviation, MPa)
Mg/DOBDC	0	11 (0.5)	569 (85)
MgCGr-2	2	20.5 (0.78)	1167 (174)
MgCGr-5	5	29.6 (0.98)	1730 (162)
MgCGr-7	7	20.3 (1.8)	1310 (342)
MgCGr-10	10	13.3 (1)	754 (225)
Ni/DOBDC	0	7.7 (0.6)	345 (115)
NiCGr-2	2	9.1 (0.57)	513 (145)
NiCGr-5	5	12.1 (0.85)	696 (159)
NiCGr-10	10	14.3 (0.9)	872 (213)

A precipitous drop in both *E* and *H* occurs in MgCGr-X hybrids when the graphene content is increased. The reduction in *E* and *H* after an initial increase of up to 5 wt% graphene reinforcement is attributed to the agglomeration of graphene in the MgCGr-X matrix. The mechanical properties significantly depend on the dispersion of graphene in the MOF matrix and resulting morphology. The benzoic acid groups on graphene interact with the MOF matrix by chemical bonding resulting in a uniform dispersion and a strong chemically bonded interface with the matrix. There are three possibilities for increasing the graphene concentration. For low wt% reinforcements, graphene is uniformly chemically bonded and

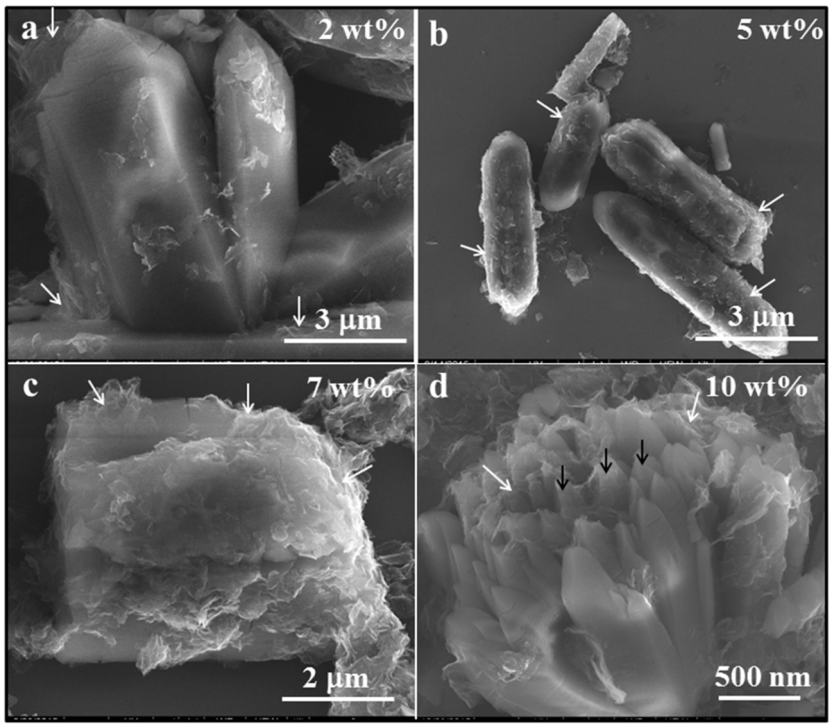

Figure 14: Scanning electron microscope (SEM) images of different weight% graphene reinforced MgCGr-X composites. SEM image of (a) MgCGr-2; (b) MgCGr-5; (c) MgCGr-7 and (d) MgCGr-10. Gr-X (X = 2, 5 and 7 wt%) corresponds to different wt% graphene reinforced in the Mg/DOBDC matrix. White arrows show graphene reinforced in the Mg/DOBDC matrix whereas black arrows show the MOF nanorods.

distributed in the matrix, causing an increase in mechanical properties. After the optimum concentration random agglomeration in the matrix occurs but reinforcement is still homogeneous and no increase or onset of reduction in the mechanical properties is observed. Further increase in the concentration leads to significant agglomeration and reinforcement causing change in morphology due to excess graphene. This condition results in significant decrease in mechanical properties. For MgCGr-2 and MgCGr-5 composites, rectangular crystals with graphene uniformly reinforced in the MOF matrix are observed (Figures 2 and 14). SEM images show an increase in agglomeration of graphene in the MgCGr-7 matrix whereas along with increased agglomeration change in morphology and ~ 200 nm MOF nanorods blended with graphene is observed for MgCGr-10. Thus, a reduction in mechanical properties after the initial increase for higher weight% reinforcement in MgCGr-X is observed. These results confirm that the maximum in the mechanical properties of MgCGr-X hybrids occur around 5 wt% graphene reinforcement, with a reduction in properties at higher graphene content. A similar decrease in mechanical properties for higher weight% reinforcement of graphene and other fillers has been observed in the polymer, metal and ceramic composites due to agglomeration.[22] In the case of NiCGr-X composites, graphene

is uniformly dispersed in the matrix even up to 10 wt% reinforcement as observed in microscopic investigations (Figure 3) and hence no decrease in the mechanical properties are observed. Interestingly, surface area and porosity also decrease for higher weight% graphene reinforcement due to agglomeration and pore blockage.

The microscopic and Raman studies showing homogeneous and intimate mixing of graphene with the MOF matrix by covalent linking and its exceptionally high mechanical properties prompted to investigate the mechanical properties of composites. Graphene with its 2-D geometry, very high surface area and exceptionally high mechanical properties along with benzoic acid groups on the surface provides an interface for the nucleation and growth of MOF. Graphene reinforced MOF composites are expected to have significantly enhanced mechanical properties due to the effective load transfer to graphene sheets.[22b,22d,23] The mechanical properties of such composites will depend on how homogeneously graphene is incorporated in the MOF matrix, interface chemistry between graphene and MOF and nanoscale morphology. By engineering these three parameters, even low weight % reinforcement with graphene will result in significantly enhanced mechanical properties. Although there is no study of mechanical properties of graphene–MOF or graphene–molecular solids composites, these parameters have been shown to play a key role in the enhancement of mechanical properties of graphene-reinforced polymer, ceramic and metal composites.[23-24] The benzoic acid functionalized graphene enhances the dispersion of graphene in reacting solvent and hence dispersion in the MOF matrix, as nucleation and growth of MOF occur in these well-dispersed graphene sheets. The interface between MOF and graphene is a layer of strong chemical bonds between benzoic acid groups and a metal ion. Such role of chemically bonded interface with divalent (Mg^{2+}, Ca^{2+}) ions in enhancing the mechanical properties of graphene oxide papers has been observed.[25] The role of chemically bonded interface in enhancing the mechanical properties of polymer composites is well investigated.[1c,d,10-11,26] The mechanical properties depend on the homogeneity and interfacial interaction of the graphene with the MOF matrix and resulting microstructure. Uniform chemically bonded MOF-graphene structure results in effective load transfer to high mechanical strength graphene sheets, as it can sustain up to 25% in-plane tensile elastic strain.[6] Further, the chemically bonded 2D graphene-MOF interface will provide a barrier for dislocation motion and crack propagation resulting in a significant strengthening of the framework.[22d,24e,27] Such uniformly reinforced metal matrix has been previously observed to significantly enhance the mechanical properties of metal-graphene composites.[24e] The role of the microstructure is clearly observed in mechanical properties where the elastic modulus and

hardness increase linearly with increasing homogeneous dispersion of graphene in the MOF matrix. The above results show that homogeneous dispersion of graphene in the MOF matrix, interface between the MOF and graphene, morphology and hence resulting microstructure are key for enhancing the mechanical properties of MOFs. The detailed microscopic investigation of microstructure and corresponding mechanical properties shows that there is a clear structure-property relationship of the composite. Better the homogeneity and interaction between 2D graphene and MOF matrix higher are the mechanical properties. Low-density porous MOFs (density < 1 g/cm^3) are compliant structures with elastic modulus $E \approx 3 - 4$ GPa and hardness $H \approx 200$ – 500 MPa.[3-4,4d] By comparing the present results even pristine Mg/DOBDC and Ni/DOBDC have a reasonably high elastic modulus of 11 and 7.7 GPa respectively, whereas hardness is in the range of porous frameworks. One of the strategies used to enhance the elastic modulus and hardness is to use rigid organic linkers where covalent bond gives higher mechanical properties in comparison to M–O–M coordination bonded building blocks.[3-4] Graphene with in-plane sp^2 bonded carbon atoms has a similar role of enhancing the mechanical strength by reinforcing the MOF structure with a rigid building block. The commercially used inorganic zeolites Silicalite-1 has $E \approx 40$ GPa, $H \approx 2.5$ GPa and ZSM-5 has $E \approx 57$ GPa and $H \approx 7$ GPa.[5a,b] On comparing the mechanical properties of MgCGr-2, and MgCGr-5 with $E \approx 20$ and 29 GPa and $H \approx 1.1$ and 1.6 GPa, although less than inorganic zeolites is a significant improvement. Further, improvement of mechanical properties is expected by carefully selecting the MOF structure and functional groups on graphene in future investigations. Considering the low cost of graphite and ease of synthesizing graphene in bulk amount by utilizing chemical route of graphene oxide along with the ease of grafting various functional groups on the graphene basal plane, it can be a useful strategy to reinforce MOF matrix with few weight% graphene and bestow it with enhanced mechanical, gas adsorption and other properties. The present detailed investigation of M/DOBDC (M = Mg^{2+}, Ni^{2+} and Co^{2+}, DOBDC = 2,5-dioxido-1,4-benzene-dicarboxylate) family of graphene composites shows a successful strategy of enhancing both mechanical as well as adsorption properties along with retained intrinsic microporous feature of the parent MOFs.

8.5 Conclusions

In summary, composites of M/DOBDC (M = Mg^{2+}, Ni^{2+} and Co^{2+}; DOBDC = 2,5-dioxido-1,4-benzene-dicarboxylate) covalently linked with different proportions of graphene were synthesized, to examine if such composites exhibit an enhancement in mechanical as well as

functional properties. The experimental results show that these composites possess significantly higher surface area, enhanced gas (both CO_2 and H_2) adsorption capability, and substantially improved elastic modulus and hardness. It appears that 5 wt% graphene reinforcement is optimal for the improvement of gas adsorption as well as mechanical properties. The results reported in this chapter are significant and indicate a means to enhance the mechanical strength of MOFs without affecting their gas adsorption characteristics.

References

[1] a) A. K. Cheetham, C. N. R. Rao and R. K. Feller, *Chem. Commun.* **2006**, 4780; b) J.-R. Li, R. J. Kuppler and H.-C. Zhou, *Chem. Soc. Rev.* **2009**, *38*, 1477; c) J. Lee, O. K. Farha, J. Roberts, K. A. Scheidt, S. T. Nguyen and J. T. Hupp, *Chem. Soc. Rev.* **2009**, *38*, 1450; d) H. Furukawa, K. E. Cordova, M. O'Keeffe and O. M. Yaghi, *Science* **2013**, *341*.

[2] a) S. Keskin, T. M. van Heest and D. S. Sholl, *ChemSusChem* **2010**, *3*, 879; b) K. Sumida, D. L. Rogow, J. A. Mason, T. M. McDonald, E. D. Bloch, Z. R. Herm, T.-H. Bae and J. R. Long, *Chem. Rev.* **2012**, *112*, 724; c) A. Ö. Yazaydın, R. Q. Snurr, T.-H. Park, K. Koh, J. Liu, M. D. LeVan, A. I. Benin, P. Jakubczak, M. Lanuza, D. B. Galloway, J. J. Low and R. R. Willis, *J. Am. Chem. Soc.* **2009**, *131*, 18198.

[3] J. C. Tan and A. K. Cheetham, *Chem. Soc. Rev.* **2011**, *40*, 1059.

[4] a) J. C. Tan, T. D. Bennett and A. K. Cheetham, *Proc. Natl. Acad. Sci. USA* **2010**, *107*, 9938; b) D. F. Bahr, J. A. Reid, W. M. Mook, C. A. Bauer, R. Stumpf, A. J. Skulan, N. R. Moody, B. A. Simmons, M. M. Shindel and M. D. Allendorf, *Phys. Rev. B, PRB* **2007**, *76*, 184106; c) T. D. Bennett, J.-C. Tan, S. A. Moggach, R. Galvelis, C. Mellot-Draznieks, B. A. Reisner, A. Thirumurugan, D. R. Allan and A. K. Cheetham, *Chem. Eur. J.* **2010**, *16*, 10684; d) Y. H. Hu and L. Zhang, *Phys. Rev. B, PRB* **2010**, *81*, 174103.

[5] a) M. C. Johnson, J. Wang, Z. Li, C. M. Lew and Y. Yan, *Mater. Sci. Eng. A* **2007**, *456*, 58; b) L. Brabec, P. Bohac, M. Stranyanek, R. Ctvrtlik and M. Kocirik, *Microporous Mesoporous Mater.* **2006**, *94*, 226; c) Z. A. D. Lethbridge, R. I. Walton, A. Bosak and M. Krisch, *Chem. Phys. Lett.* **2009**, *471*, 286.

[6] C. Lee, X. Wei, J. W. Kysar and J. Hone, *Science* **2008**, *321*, 385.

[7] a) D.-D. Zu, L. Lu, X.-Q. Liu, D.-Y. Zhang and L.-B. Sun, *J. Phys. Chem. C* **2014**, *118*, 19910; b) R. Kumar, K. Jayaramulu, T. K. Maji and C. N. R. Rao, *Chem. Commun.* **2013**, *49*, 4947; c) A. Huang, Q. Liu, N. Wang, Y. Zhu and J. Caro, *J. Am. Chem. Soc.* **2014**, *136*, 14686; d) Y. Hu, J. Wei, Y. Liang, H. Zhang, X. Zhang, W. Shen and H. Wang, *Angew. Chem. Int. Ed.* **2016**, *55*, 2048.

[8] a) S. R. Caskey, A. G. Wong-Foy and A. J. Matzger, *J. Am. Chem. Soc.* **2008**, *130*, 10870; b) P. D. C. Dietzel, V. Besikiotis and R. Blom, *J. Mater. Chem.* **2009**, *19*, 7362.

[9] a) A. C. Kizzie, A. G. Wong-Foy and A. J. Matzger, *Langmuir* **2011**, *27*, 6368; b) J. Liu, A. I. Benin, A. M. B. Furtado, P. Jakubczak, R. R. Willis and M. D. LeVan, *Langmuir* **2011**, *27*, 11451.

[10] a) J. L. C. Rowsell and O. M. Yaghi, *Microporous Mesoporous Mater.* **2004**, *73*, 3; b) M. O'Keeffe, *Chem. Soc. Rev.* **2009**, *38*, 1215.

[11] O. M. Yaghi and Q. Li, *MRS Bull.* **2009**, *34*, 682.

[12] a) K. W. Chapman, G. J. Halder and P. J. Chupas, *J. Am. Chem. Soc.* **2009**, *131*, 17546; b) T. D. Bennett and A. K. Cheetham, *Acc. Chem. Res.* **2014**, *47*, 1555; c) Y. H. Hu and L. Zhang, *Phys. Rev. B, PRB* **2010**, *81*, 174103.

[13] W. S. Hummers and R. E. Offeman, *J. Am. Chem. Soc.* **1958**, *80*, 1339.

[14] M. Jahan, Q. Bao, J.-X. Yang and K. P. Loh, *J. Am. Chem. Soc.* **2010**, *132*, 14487.

[15] a) P. D. C. Dietzel, Y. Morita, R. Blom and H. Fjellvåg, *Angew. Chem. Int. Ed.* **2005**, *44*, 6354; b) P. D. C. Dietzel, B. Panella, M. Hirscher, R. Blom and H. Fjellvag, *Chem. Commun.* **2006**, 959.

[16] N. L. Rosi, J. Kim, M. Eddaoudi, B. Chen, M. O'Keeffe and O. M. Yaghi, *J. Am. Chem. Soc.* **2005**, *127*, 1504.

[17] a) D. W. Mayo, F. A. Miller and R. W. Hannah in *Course notes on the interpretation of infrared and Raman spectra,* John Wiley & Sons, Inc, **2004**; b) K. Nakamoto, *Infrared and Raman spectra of inorganic and coordination compounds*, John Wiley & Sons, Inc, New Jersey **2009**.

[18] a) L. M. Malard, M. A. Pimenta, G. Dresselhaus and M. S. Dresselhaus, *Phys. Rep.* **2009**, *473*, 51; b) M. A. Pimenta, G. Dresselhaus, M. S. Dresselhaus, L. G. Cancado, A. Jorio and R. Saito, *PCCP* **2007**, *9*, 1276.

[19] a) T. Tsuruoka, S. Furukawa, Y. Takashima, K. Yoshida, S. Isoda and S. Kitagawa, *Angew. Chem. Int. Ed.* **2009**, *48*, 4739; b) D. Li, H. Wang, X. Zhang, H. Sun, X. Dai, Y. Yang, L. Ran, X. Li, X. Ma and D. Gao, *Cryst. Growth Des.* **2014**, *14*, 5856; c) F. Wang, H. Guo, Y. Chai, Y. Li and C. Liu, *Microporous Mesoporous Mater.* **2013**, *173*, 181.

[20] A. Umemura, S. Diring, S. Furukawa, H. Uehara, T. Tsuruoka and S. Kitagawa, *J. Am. Chem. Soc.* **2011**, *133*, 15506.

[21] a) W. Lu, W. M. Verdegaal, J. Yu, P. B. Balbuena, H.-K. Jeong and H.-C. Zhou, *Energy Environ. Sci.* **2013**, *6*, 3559; b) J. Zhang, Z.-A. Qiao, S. M. Mahurin, X. Jiang, S.-H. Chai, H. Lu, K. Nelson and S. Dai, *Angew. Chem. Int. Ed.* **2015**, *54*, 4582; c) A. L. Myers, *Fundamental of Adsorption* Engineering Foundation, New York **1986**.

[22] a) K. E. Prasad, B. Das, U. Maitra, U. Ramamurty and C. N. R. Rao, *Proc. Natl. Acad. Sci. USA* **2009**, *106*, 13186; b) C. N. R. Rao, A. K. Cheetham and A. Thirumurugan, *J. Phys.: Condens. Matter* **2008**, *20*, 083202; c) J. Liu, Y. Yang, H. Hassanin, N. Jumbu, S. Deng, Q. Zuo and K. Jiang, *ACS Appl. Mater. Interfaces* **2016**, *8*, 2607; d) J. Liu, H. Yan and K. Jiang, *Ceram. Int.* **2013**, *39*, 6215.

[23] L.-Y. Chen, H. Konishi, A. Fehrenbacher, C. Ma, J.-Q. Xu, H. Choi, H.-F. Xu, F. E. Pfefferkorn and X.-C. Li, *Scripta Mater.* **2012**, *67*, 29.

[24] a) RamanathanT, A. A. Abdala, StankovichS, D. A. Dikin, M. Herrera Alonso, R. D. Piner, D. H. Adamson, H. C. Schniepp, ChenX, R. S. Ruoff, S. T. Nguyen, I. A. Aksay, R. K. Prud'Homme and L. C. Brinson, *Nat. Nano* **2008**, *3*, 327; b) J. R. Potts, D. R. Dreyer, C. W. Bielawski and R. S. Ruoff, *Polymer* **2011**, *52*, 5; c) T. Kuilla, S. Bhadra, D. Yao, N. H. Kim, S. Bose and J. H. Lee, *Prog. Polym. Sci.* **2010**, *35*, 1350; d) J. Wang, Z. Li, G. Fan, H. Pan, Z. Chen and D. Zhang, *Scripta Mater.* **2012**, *66*, 594; e) Y. Kim, J. Lee, M. S. Yeom, J. W. Shin, H. Kim, Y. Cui, J. W. Kysar, J. Hone, Y. Jung, S. Jeon and S. M. Han, *Nat. Commun* **2013**, *4*.

[25] S. Park, K.-S. Lee, G. Bozoklu, W. Cai, S. T. Nguyen and R. S. Ruoff, *ACS Nano* **2008**, *2*, 572.

[26] a) H. Furukawa, N. Ko, Y. B. Go, N. Aratani, S. B. Choi, E. Choi, A. Ö. Yazaydin, R. Q. Snurr, M. O'Keeffe, J. Kim and O. M. Yaghi, *Science* **2010**, *329*, 424; b) S. L. James, *Chem. Soc. Rev.* **2003**, *32*, 276.

[27] a) J. Wang, R. G. Hoagland, J. P. Hirth and A. Misra, *Acta Mater.* **2008**, *56*, 5685; b) J. S. Carpenter, A. Misra and P. M. Anderson, *Acta Mater.* **2012**, *60*, 2625.

Chapter 9: Assemblies of single-walled carbon nanotubes generated by covalent cross-linking with organic linkers *

Summary

In this chapter synthesis, characterization and gas adsorption properties of covalently cross-linked single-walled carbon nanotube (SWNTs) assemblies is discussed. The covalently cross-linked single-walled carbon nanotube assemblies (ASWNT-1 and ASWNT-2) were synthesized using the Sonogashira coupling reaction. Two different linkers, 1,4-diethynylbenzene and 4,4′-diethynylbiphenyl, have been used to covalently cross-link iodobenzene functionalized SWNTs, resulting in the formation of three-dimensional assemblies, ASWNT-1 and ASWNT-2. These assemblies exhibit high surface areas of 742 and 788 m^2/g respectively, while pristine SWNTs have a surface area of 400 m^2/g. The CO_2 and H_2 uptake capacity are also increased in the ASWNTs. The application of efficient Pd(0) catalysed coupling reactions in the covalent chemistry of carbon nanotube is explored. The Pd(0) catalysed C–C coupling reactions can be further utilized to design several other functional nanocarbon materials for different applications.

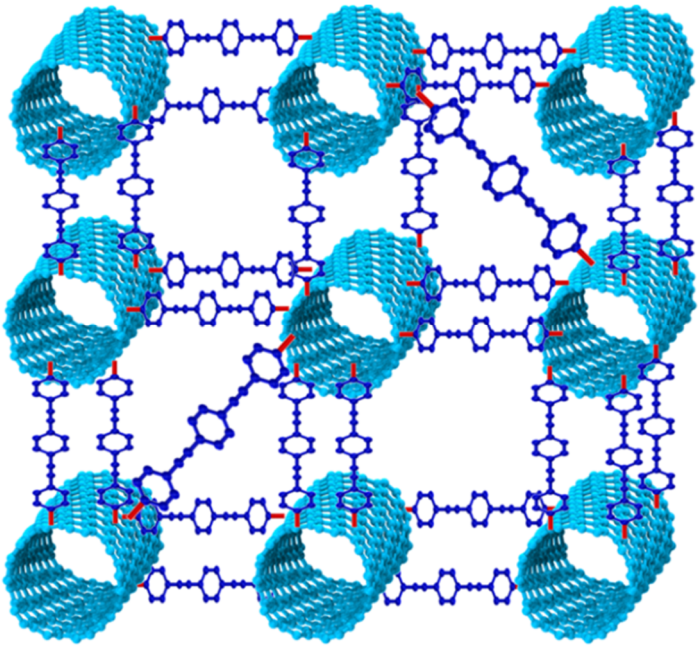

A paper based on these studies has appeared in J. Mater. Chem. A, 2015, 3, 6747.

9.1 Introduction

Carbon nanotubes have emerged as an important class of new materials with many unique properties.[1] In particular, single-walled carbon nanotubes (SWNTs) exhibit interesting electronic, mechanical, thermal and gas adsorption properties. SWNTs exhibit surface areas going up to 400 m^2/g. They have been functionalized and attached to a variety of organic and biological species. For example covalent functionalization of SWNTs with cross-linked polymeric micelles has been carried out.[2] Supramolecular assemblies of nucleoside functionalized nanotubes have been explored,[3] as well as films of covalent-cross linked polymer-SWNT composites.[4] Carbon nanotube arrays for hydrogen adsorption have been examined theoretically.[5] SWNT fibers have been engineered as scaffolds for hydrogen storage.[6] SWNTs have been linked with each other by employing the cycloaddition reaction,[7] but there are only a few such examples of chemical manipulation of SWNTs for specific purposes.

Assemblies of SWNTs generated by cross-linking them are expected to exhibit interesting morphological features as well as new properties.[8] SWNTs forms bundles due to van der Waals interaction and most of the external surface area gets excluded. Covalent cross-linking with uniform length linkers is expected to increase the surface area. Covalent linking of SWNTs by rigid organic pillars employing the Sonogashira C–C coupling reaction with 1,4-diethynylbenzene and 4,4′-diethynylbiphenyl as the linkers (see Scheme1) has been carried out.[9] Although application of Pd(0) catalysed C–C coupling reactions are well explored in synthetic organic chemistry, there are only two reports of its application in carbon nanotube chemistry.[10] Molecularly-bridged single-walled carbon nanotubes have been prepared using Sonogashira coupling and their electrical properties investigated.[10b] Suzuki coupling for the surface functionalization and dispersion of SWNTs in different organic solvents have been studied.[10a] In this context, the use of palladium catalysed C–C coupling reactions for the covalent modifications of carbon nanotubes is a worthwhile strategy for further exploration. The resulting assemblies are characterized by a variety of techniques including electron microscopy, IR and Raman spectroscopy, X-ray photoelectron spectroscopy and solid state NMR spectroscopy. The surface areas and gas adsorption characteristics of the SWNT assemblies is also examined. The obtained assemblies are superhydrophobic with high surface area and good CO_2 and hydrogen uptake. The ASWNTs also have high thermal and chemical stabilities which make it promising for gas storage, separation, and catalytic applications

The present investigation have resulted in the synthesis of similar such assemblies for different applications. The assemblies of SWNTs covalently cross-linked by benzene have been used to synthesize SWNT cryogels by freeze drying. These assemblies show good performance and stability over long cycles in supercapacitor device.[11] The individual multi–walled carbon nanotube has a tensile strength in the range of 11 to 63 GPa whereas the Young's modulus varies between 270 to 950 GPa.[12] Although carbon nanotubes have very high mechanical properties along the axial direction, the carbon nanotubes bundles have weak van der Waals interaction along the radial direction. The weak π-π interaction provides new slip planes and overall mechanical properties of carbon nanotube bundles are significantly less than the individual nanotubes. By cross-linking individual carbon nanotube with covalent bond Zhu *et al.* have shown six times improvement in the tensile strength of covalently cross-linked assemblies in comparison to control counterpart of multi–walled carbon nanotube (MWNT) bundle.[13] Covalent cross-linking is clearly a worthwhile strategy for the design of functional materials.

9.2 Scope of the present investigations

Single-walled carbon nanotubes (SWNTs) are important class 1-D nanomaterials with interesting physical and chemical properties.[1b,14] These properties make them suitable for a wide range of applications in electronics, energy storage devices and as a gas adsorbent.[14a,15] In particular, the electronic properties are most significant characteristics of SWNTs. The SWNTs can be either metallic or semiconducting depending on diameter and chirality, while the local carbon–carbon bonding remains constant.[14a,b] Raman spectroscopy is an important characterization technique that probes electronic properties as well as the characteristic radial breathing modes.[16] By covalently linking carbon nanotubes with uniform length linkers significant changes in the Raman spectrum, in particular the radial breathing modes are expected. There are theoretical investigations reported in the literature of such assemblies as potential hydrogen storage materials.[17] As produced SWNTs using arc discharge and chemical vapour deposition methods are highly agglomerated and bundled due to van der Waals interactions (~ 40 K_BT nm^{-1}) which blocks the adsorption accessible space and have low surface area.[18] These theoretical investigations suggest that by forming a uniform assembly of SWNTs using uniform length linkers significantly higher surface area and hydrogen uptake is expected. The present experimental investigation is the realization of such theoretically predicted SWNT assemblies. Significant improvement in surface area and hydrogen uptake was observed in the synthesized assemblies of single–walled carbon

nanotube (ASWNTs). The ASWNTs show high thermal stability with good CO_2 uptake under ambient condition. Further a decrease in radial breathing mode intensity due to damping of vibration in the radial direction on covalently linking individual SWNTs was observed. The formations of uniformly cross-linked SWNTs assemblies were further confirmed by direct visualization of a cross-linked porous network of SWNTs in transmission electron microscope (TEM).

The present study also investigates the application of efficient Pd(0) catalysed C–C coupling reaction in the carbon nanotube chemistry for the design of different functional materials. Sidewall halogenation, Birch reduction, carbene [2+1] cycloaddition, radical addition, aryl diazonium salt and carboxylate functionalization using HNO_3/H_2SO_4 mixture followed by amide bond formation with various amines are some of the approaches used for covalent modification of carbon nanotube and Pd(0) catalysed coupling reactions are largely unexplored.[19]

9.3 Experimental section

Chemicals: Chemicals used for synthesis were of high purity and obtained from commercial sources. Solvents were pre-dried before synthesis.

Synthesis of 1,4-diethynylbenzene (linker 1): The reaction was performed under nitrogen. In the mixture of 1,4-diiodobenzene (2g, 6 mmol), $Pd(PPh_3)_4$ (100 mg), CuI (50 mg) and toluene (30 ml) at 80 °C trimethylsilylacetylene (2ml, 14 mmol) dissolved in 10 ml triethylamine was added dropwise and allowed to stir for 1 h. The product was diluted with ethyl acetate, passed through a celite bed, washed with 1% $NaHCO_3$ aqueous solution, dried over anhydrous sodium sulphate, evaporated in a rotary evaporator and purified by column chromatography (silica, hexane) to give 1,4-bis[(trimethylsilyl)ethynyl]benzene as an intermediate. (1.34 g, 82 %). The deprotection was carried out by stirring intermediate (1.25 g, 1equivalent) with K_2CO_3 (5g, ~ 8 equivalents) in 35 ml methanol for 5 h. Excess methanol was evaporated in a rotary evaporator, diluted with ethyl acetate, washed with water and dried over anhydrous sodium sulphate. The organic layer was dried in a rotary evaporator to give 1,4-diethynylbenzene as the final product. (562 mg, 96%) 1H NMR ($CDCl_3$, 400 MHz): δ (ppm) 7.44 (s, 4 H; Ar*H*), 3.16 (s, 2H; C≡CH).

Synthesis of 4,4′-diethynylbiphenyl (linker 2): 4,4′-Diethynylbiphenyl was prepared using the same procedure used for 1,4-diethynylbenzene. 4,4′-diiodobiphenyl (6 mmol) remaining

reagents and condition same. (930 mg, 76.7 %) 1H NMR ($CDCl_3$, 400 MHz): δ (ppm) 7.55–7.56 (m, 8 H; Ar*H*), 3.14 (s, 2H; C≡CH).

Iodobenzene functionalization of SWNT (SWNT-IBz): Purified CoMoCat SWNTs (60 mg) were dispersed in 60 ml 1 wt% sodium dodecylbenzene sulfonate (NaDDBS) using sonication. In 50 ml water 4-iodoaniline (770 mg, 3 mmol) was dissolved by adding the minimum amount of conc. HCl dropwise. Diazonium salt of 4-Iodoaniline was prepared by adding $NaNO_2$ (350 mg, 5 mmol) and 2.5 ml 20% HCl (6.4 M) and stirring for 45 min in an ice bath. Uniform SWNT dispersion was added to the *in situ* prepared diazonium salt and allowed to stir at ice bath temperature for 2 h followed by stirring at room temperature for next 4 h. Obtained product was filtered (0.45 μm, nylon) and washed with water, (1:1) water-ethanol solution, ethanol, and tetrahydrofuran to remove the surfactant properly. The final product was dried at 70 °C under vacuum.

Synthesis of covalently cross-linked three-dimensional assemblies of SWNTs: In a Schlenk flask SWNT-IBz (20 mg) was purged with nitrogen and sealed with a septum. *N*,*N*-Dimethylformamide (DMF) (4ml) and triethylamine 4 ml was added and sonicated for 3 h. In the uniform dispersion, $Pd(PPh_3)_4$ (15 mg) and CuI (7 mg) was added under constant stirring and temperature was raised to 80 °C. In a separate vial 1,4-diethynylbenzene (100 mg) dissolved in 2 ml, DMF was added dropwise to the reaction mixture, the subsequent temperature was raised to 140 °C and allowed to stir for 24 h. A nitrogen atmosphere was maintained during the reaction. Precipitates were collected by filtration and washed properly with DMF and hexane. Further purification was carried out using Soxhlet extraction technique with methanol and hexane for 24 h each. Yield: 74 %. Elemental analysis (%) found: C 86.4, H 3.8. The product is designated ASWNT-1. The same procedure was used for obtaining ASWNT-2 except 4,4′-diethynylbiphenyl was used as the linker. Yield: 71%. Elemental analysis (%): C 85.7, H 4.2.

Characterization: Raman spectra were collected at several different spots in backscattering geometry using HORIBA LabRam HR800. FTIR spectra were recorded using attenuated-total-reflectance accessories in a Bruker FT-IR spectrometer. Solid state ^{13}C magic angle spinning (MAS) NMR spectrum was collected on a Bruker 400 MHz spectrometer. Morphological studies were carried out using Nova Nano SEM 600, FEI Company. Transmission Electron Microscopy (TEM) analysis was performed using the FEI Tecnai with an accelerating voltage of 200 kV. Thermogravimetric analysis (TGA) was done using Mettler

Toledo TGA 850 instrument in a nitrogen atmosphere in the temperature range of 30 – 700 °C with a heating rate of 3 °C/ min. XP spectra were recorded in an Omicron Nanotechnology Spectrometer with Mg Kα as the X-ray source. PXRD pattern was recorded in PANanlytical Empyrean using Cu K-α radiation. Elemental analysis was performed using Thermo Scientific Flash 2000 Elemental Analyzer.

The adsorption isotherms of N_2 (77 K), H_2 (77 K), CO_2 (195 K, and 293 K) up to 1 atm were obtained by using QUANTACHROME QUADRASORB-*SI* analyzer. The sample was heated at 433 K under vacuum for about 12 h prior to the measurement of isotherms. The adsorbate was charged into the sample tube and change in pressure was monitored. The degree of adsorption was determined by monitoring the decrease in pressure at the equilibrium state. All operations involved in sorption experiment were computer controlled and automatic.

Pore size distribution was calculated by non-local density functional theory (NLDFT) using ASiQwin 3 software provided by Quantachrome instruments for the characterization of porous materials. Density Functional Theory (DFT) gives a more realistic sorption and phase behaviour of fluids in narrow pores on a molecular level and is considered a reliable method for pore size analysis. The non-local density functional theory (NLDFT) correctly explains the local fluid structure near curved solid walls. The adsorption isotherms in model pores are obtained by using the intermolecular potentials of the fluid-fluid and solid-fluid interactions. The relation between isotherms determined by NLDFT and the experimental isotherm on a porous solid is given by generalized adsorption isotherm (GAI) equation:

$$N\left(\frac{P}{P_0}\right) = \int_{w_{min}}^{w_{max}} N\left(\frac{P}{P_0}, w\right) f(w)\, dw \quad \text{... ... ... (1)}$$

Where

$N(P/P_0)$ = experimental adsorption isotherm

w = pore width

$N(P/P_0,w)$ = isotherm on a single pore of width w

$f(w)$ = pore size distribution function

In GAI equation it is assumed that the total isotherm consists of a number of individual "single pore" isotherms multiplied by their relative distribution, $f(W)$, over a range of pore sizes. The set of $N(P/P_0,w)$ isotherms for a given system (adsorbate/adsorbent) is obtained by

density functional theory and is available as kernel files with the software (Quantachrome). The pore size distribution is obtained by solving the GAI equation numerically via a fast non-negative least square algorithm.

9.4 Results and discussion

Scheme 1 shows the steps involved in the synthesis of covalently cross-linked single–walled carbon nanotube assemblies (ASWNT-1 and ASWNT-2). In order to synthesize single-walled carbon nanotube (SWNTs) assemblies, purified CoMoCat nanotube was used as the starting material. The SWNTs were functionalized with iodobenzene using the diazonium salt of 4-iodoaniline. The formation of the iodobenzene derivative of SWNT (SWNT-IBz) was confirmed by X-ray photoelectron spectroscopy (XPS) shown in figure 3a. XPS of SWNT-IBz shows signals at 620.4 and 631.8 eV due to I ($3d_{5/2}$) and I ($3d_{3/2}$) respectively.[20] The Raman spectrum of the

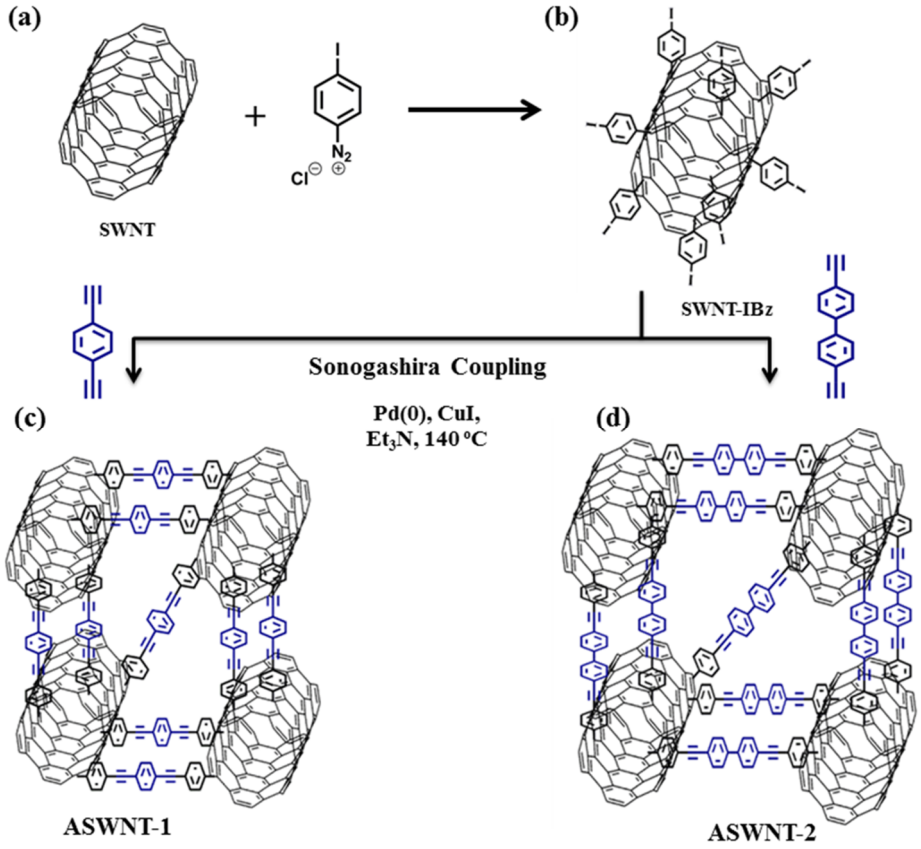

Scheme 1. Schematic representation of three-dimensional assemblies of SWNTs synthesis (ASWNT-1 and ASWNT-2) using Sonogashira coupling reaction. **(a)** Reaction of pristine SWNTs with 4-iodobenzenediazonium chloride; **(b)** Iodobenzene functionalized SWNT (SWNT-IBz); **(c)** ASWNT-1 and **(d)** ASWNT-2.

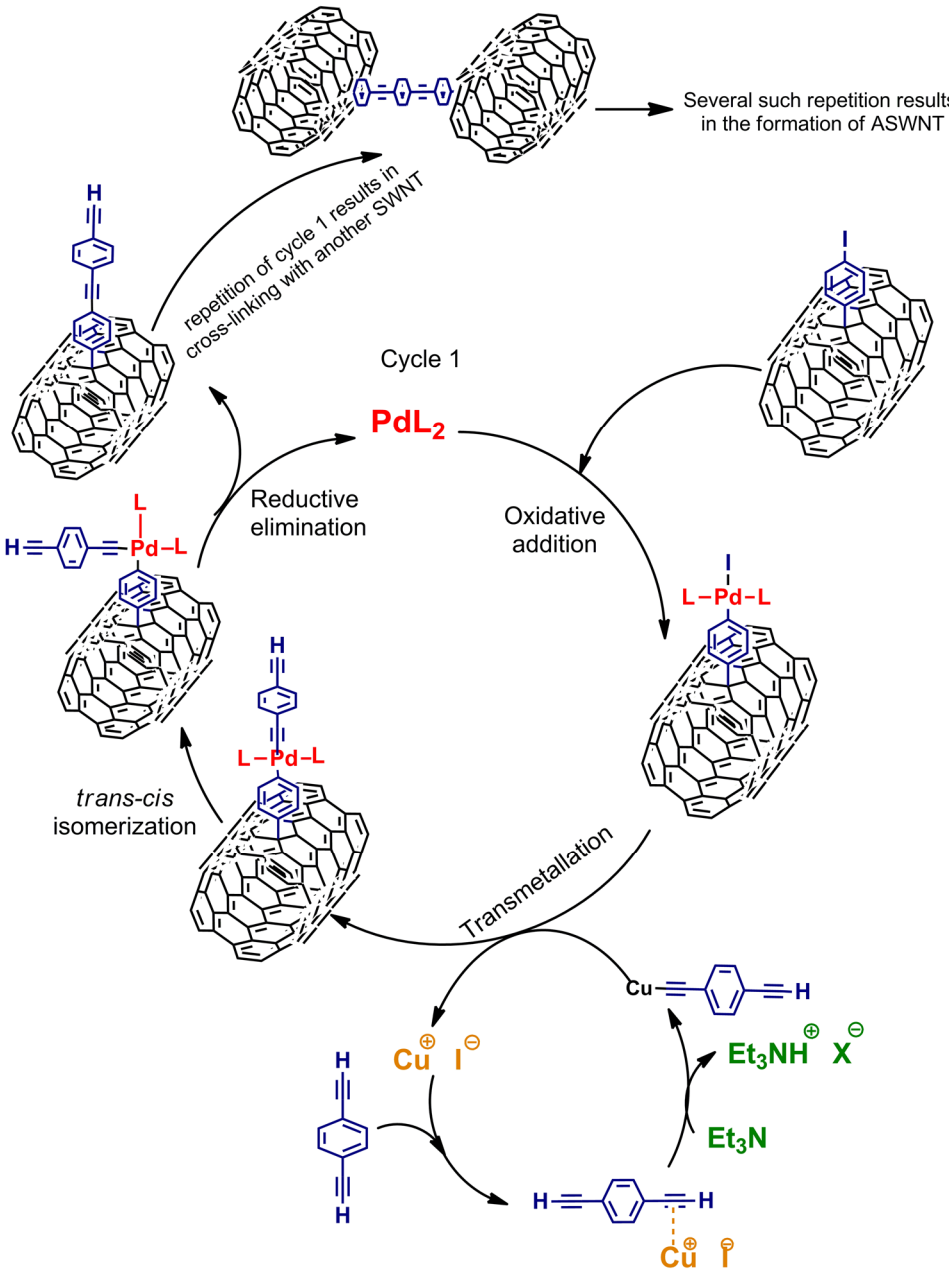

Figure 1. Reaction mechanism of the Sonogashira coupling in iodobenzene functionalized SWNT. Cycle 1 shows the C–C bond formation with 1,4-diethynylbenzene in iodobenzene functionalized SWNT. Subsequent cycle 1 with another SWNT results in the cross-linking of another SWNT. Several catalytic cycles result in PGF formation. Present mechanism shows only one such cycle.

iodobenzene functionalized SWNTs shows an increase in the D-band intensity with respect to pristine SWNTs due to the formation of sp^3 centres (Figure 2).[21] SWNT-IBz was reacted with the required quantity of 1,4-diethynylbenzene or 4,4′-diethynylbiphenyl linker in *N,N*-dimethylformamide following the Sonogashira coupling procedure to obtain the SWNT assemblies, ASWNT-1 and ASWNT-2 respectively (see experimental section 9.3 for details). In this procedure, Pd(0)

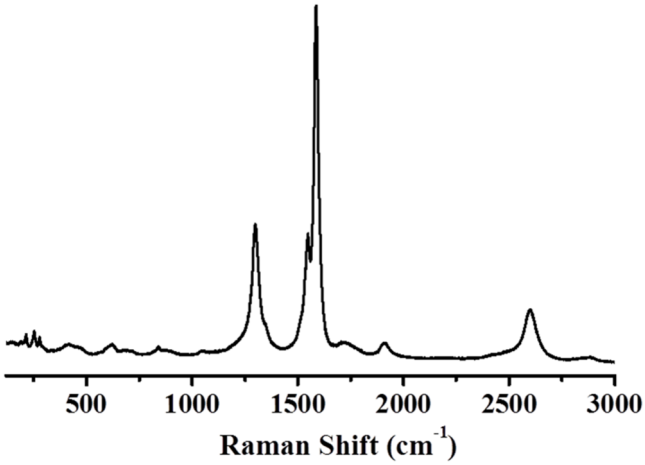

Figure 2. Raman spectrum of iodobenzene functionalized SWNT.

undergoes oxidative addition with the iodobenzene present on the SWNTs and forms a Pd(II) intermediate. This intermediate undergoes transmetallation with copper acetylide and reductive elimination to form C–C bonds, giving rise to the SWNT network assembly (see scheme 1 and figure 1 for reaction mechanism).[9b]

Figure 3b shows typical Raman spectrum of pristine SWNTs along with that of the ASWNT-1 and ASWNT-2 assemblies recorded with a 632.84 nm He-Ne laser. The radial breathing modes were observed in the spectra of ASWNT-1 and ASWNT-2 indicating that this important characteristic of SWNTs is retained in the SWNT assemblies after cross-linking. Other important characteristic bands *D*, *G* and *G'* of

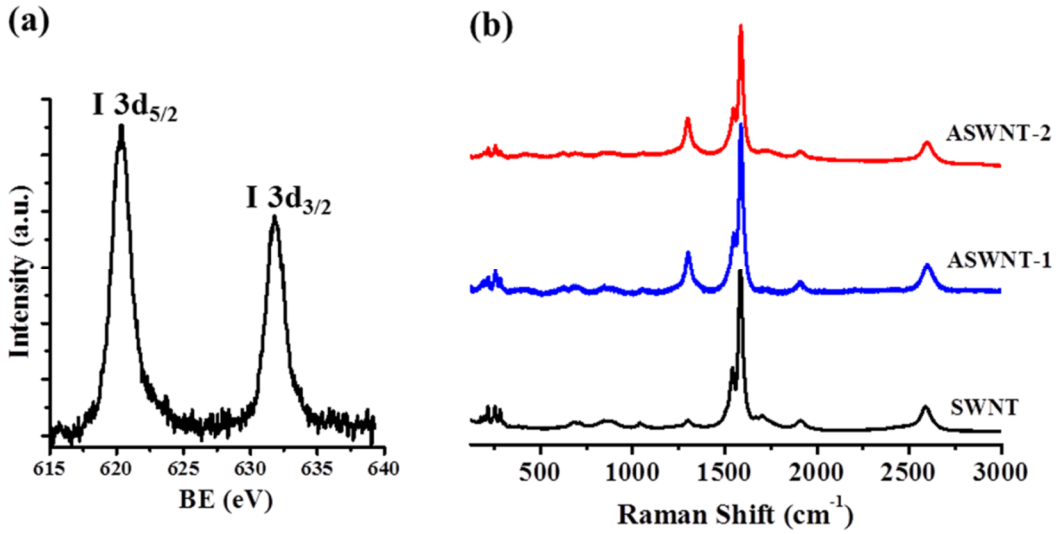

Figure 3. (a) Iodine (3d) X-ray photoelectron spectrum (XPS) of iodobenzene functionalized SWNT (SWNT-IBz); (b) Raman spectra of SWNT (black), ASWNT-1 (blue) and ASWNT-2 (red).

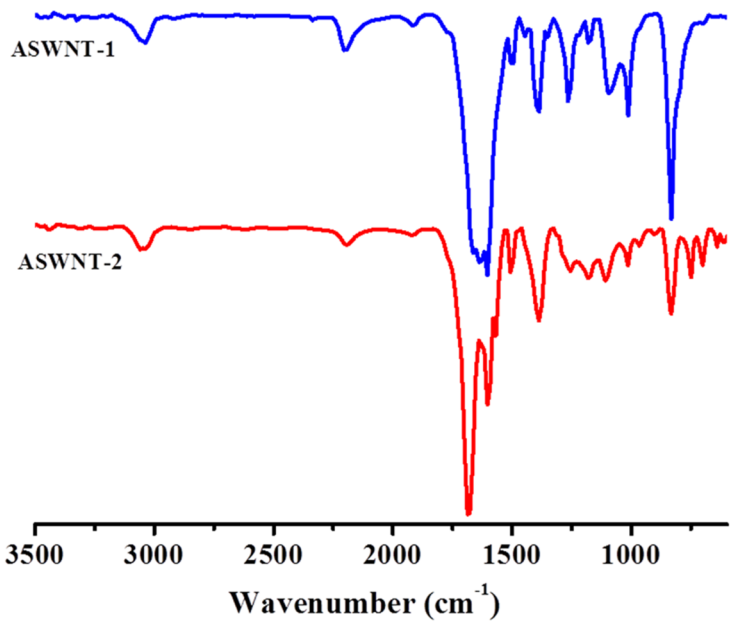

Figure 4. ATR-FTIR spectra of ASWNT-1 (blue) and ASWNT-2 (red).

SWNT are retained in the cross-linked assemblies. The number of sp^3 centres on ASWNT basal plane is same as SWNT-IBz and hence similar D-band intensity is observed.

The attenuated-total-reflectance infrared spectrum (ATR-FTIR) of ASWNT-1 shows bands at 3058 and 3033 cm^{-1} due to the aromatic C–H stretching vibrations (Figure 4). The band at 2197 cm^{-1} is attributed to the C≡C stretching mode while bands at 1600, 1505, and 1438 cm^{-1} are due to the C=C stretching vibrational modes of the benzene ring.[22] The IR spectrum of ASWNT-2 is similar to that of ASWNT-1 and shows vibrational modes in the C–H, C≡C, and C=C regions (Figure 4). Powder X-ray

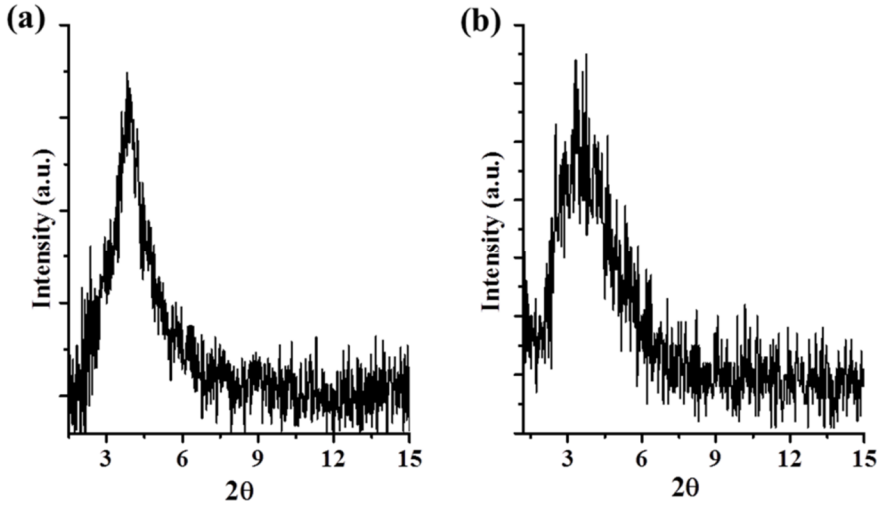

Figure 5. Powder X-ray diffraction pattern of (a) ASWNT-1 and (b) ASWNT-2.

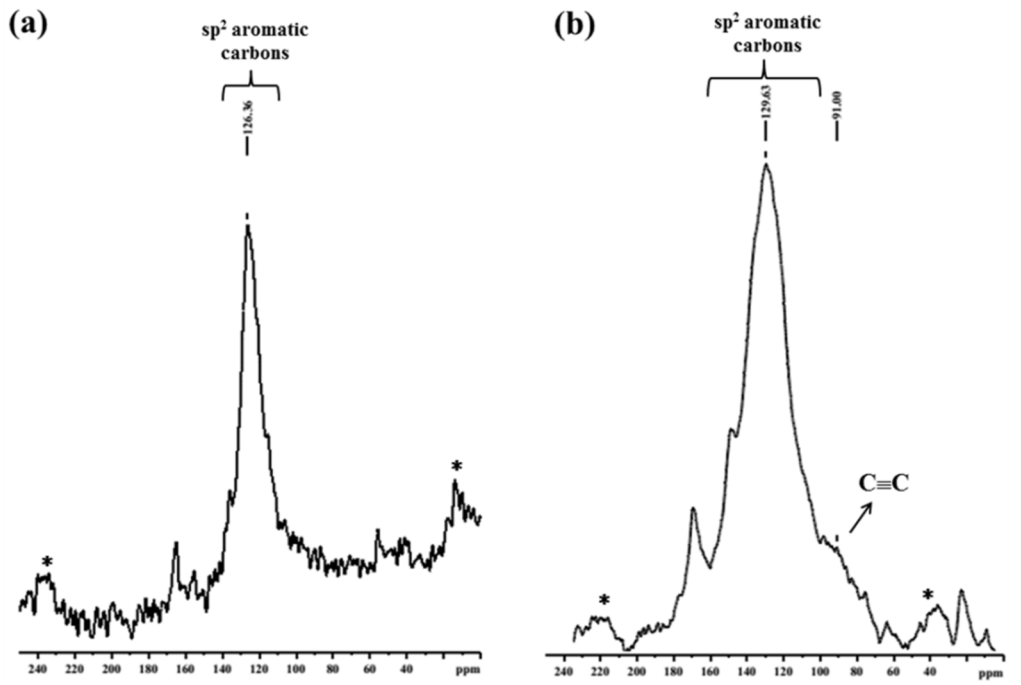

Figure 6. Direct pulse ^{13}C solid state NMR spectra of (a) SWNT and (b) ASWNT-1 at 11 kHz MAS. Asterisks represent spinning side bands.

diffraction patterns of ASWNT-1 and ASWNT-2 show broad reflections at 2θ values ~ 4° corresponding to a separation of ~ 2.2 nm between SWNTs (Figure 5). This separation closely matches the linker length used to covalently cross-link the SWNTs. FTIR spectra and PXRD patterns confirm the cross-linking of carbon nanotubes by 1,4-diethynylbenzene and 4,4′-diethynylbiphenyl linkers and the formation of three–dimensional assemblies.

Direct pulse ^{13}C solid state NMR spectra of SWNTs and ASWNT-1 were collected at 11 kHz MAS (Figure 6). The NMR spectrum of ASWNT-1 shows peaks at 90 ppm and 120-150 ppm region corresponding to C≡C and aromatic carbons respectively. The NMR spectrum of pristine SWNT has a narrow signal centred at 126 ppm corresponding to aromatic carbons.[23] The broad NMR signal of ASWNT-1 in the aromatic region is attributed to the cross-linking of SWNTs by the aromatic linkers increasing the heterogeneity of aromatic C in different chemical environments.

The C 1s and I 3d X-ray photoelectron spectra of SWNT-IBz, ASWNT-1 and ASWNT-2 are shown in figure 7. Sonogashira reaction mechanism involves the oxidative addition of Pd(0) to C−I bond of iodobenzene and formation of Pd(II) intermediate. The intermediate undergoes elimination of I during transmetallation with copper acetylide followed by reductive elimination to form C−C bond (see figure 1 for

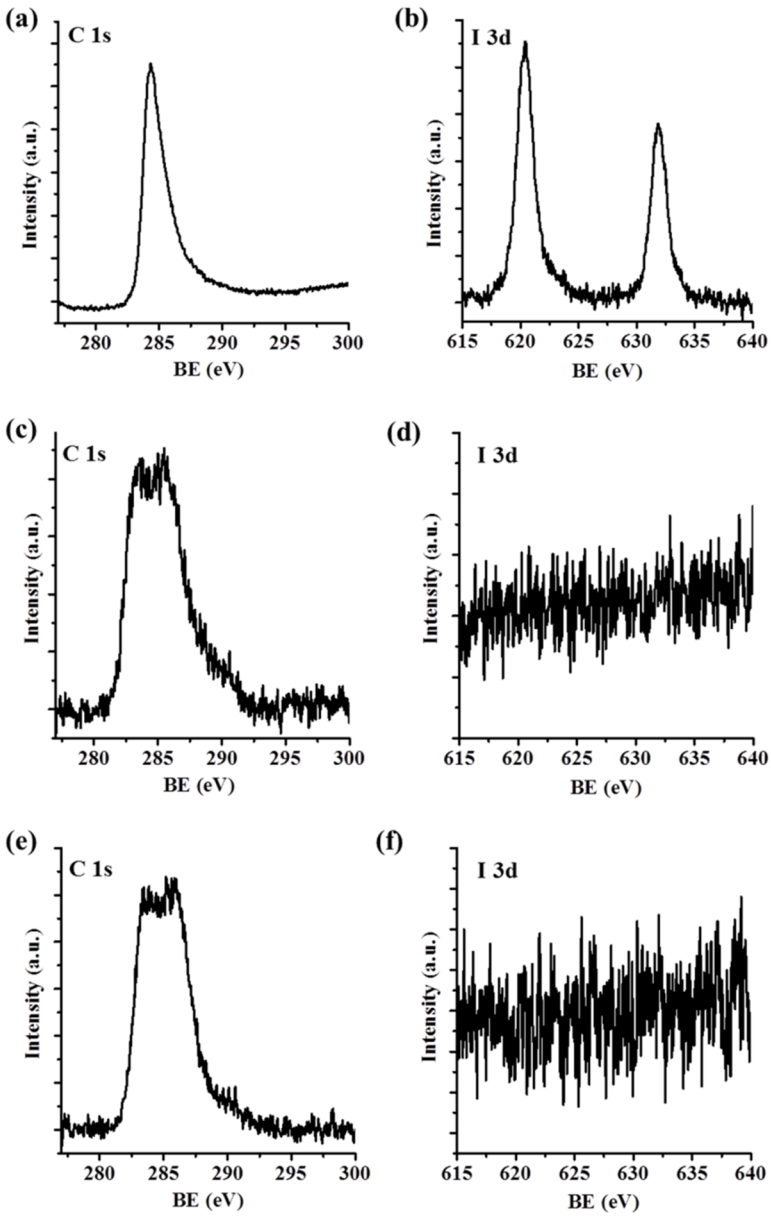

Figure 7. High resolution C 1s and I 3d X-ray photoelectron spectrum of (a, b) Iodobenzene functionalized SWNT (SWNT-IBz); (c, d) ASWNT-1 and (e, f) ASWNT-2.

reaction mechanism).[9b] Monitoring the I 3d signal gives an insight into the effectiveness of reaction. No significant intensity of the I 3d signal in ASWNT-1 and ASWNT-2 in comparison with SWNT-IBz confirms efficient cross coupling and C−C bond formation.

Field emission scanning electron microscope (FESEM) images of ASWNT-1 and ASWNT-2 (Figure 8) show the formation of densely cross-linked porous three-dimensional assemblies of carbon nanotubes. Transmission electron microscope (TEM) images of pristine SWNTs show bundles as expected (Figure 8c). TEM images of ASWNT-1 and ASWNT-2 show a similar porous assembly of cross-linked carbon

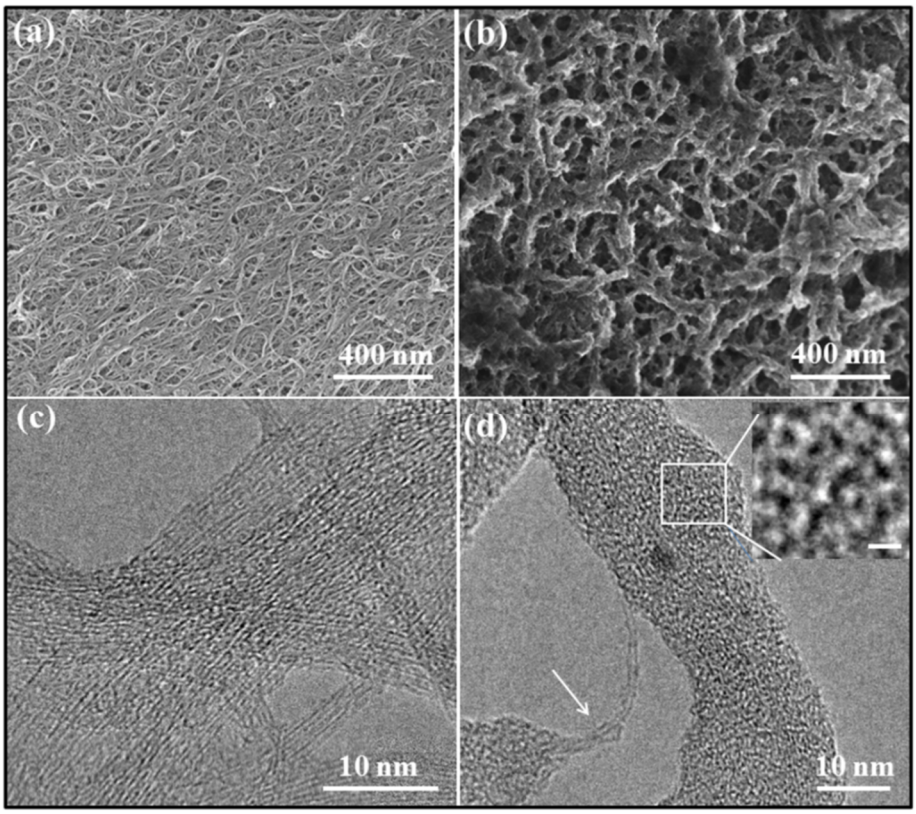

Figure 8. FESEM image of **(a)** SWNTs and **(b)** ASWNT-1. TEM image of **(c)** SWNTs and (d) ASWNT-1. **(Inset)** Formation of 1 – 2 nm pores due to covalent cross-linking with linkers (scale bar 2 nm).

nanotubes (Figure 8d). The magnified TEM image of the cross-linked nanotube bundle shows the formation of 1 – 2 nm pores (see the inset of figure 8d). Thermal stability of ASWNT-1 and 2 was examined by thermogravimetric analysis. ASWNTs show high thermal stability with no weight loss up to 350 °C. Further heating causes a

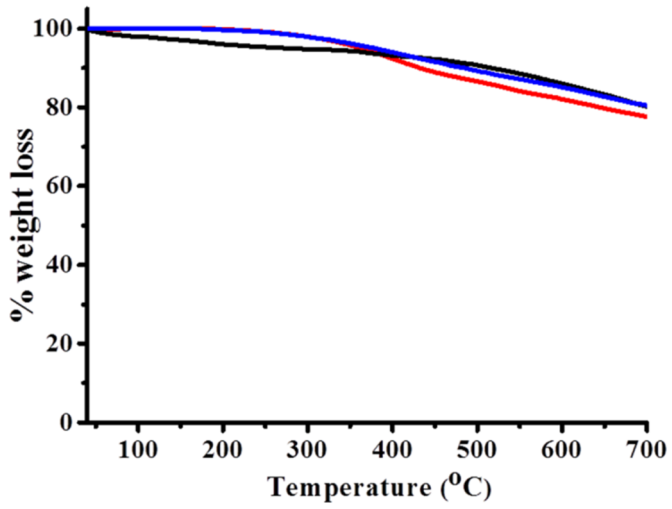

Figure 9. TGA profile of (a) SWNT (black), (b) ASWNT-1 (blue) and ASWNT-2 (red) in N_2 atmosphere (flow rate 40 ml/min) with a heating rate of 3 °C/min.

steady weight loss of ~ 20 % up to 700 °C (Figure 9). The high thermal stability is attributed to extensive cross-linking and chelation of SWNTs by organic linkers which prevent the collapse of the scaffold.

The porosity of ASWNTs was investigated by nitrogen sorption at 77 K (Figure 10). The N_2 sorption isotherms of ASWNT-1 and ASWNT-2 have characteristics of both type-I and type-II profiles following the IUPAC classification.[24] The type-I profile of sorption isotherm can be attributed to adsorption in micropores whereas the type-II feature is due to adsorption in macropores of three-dimensional assembly as seen in the TEM and FESEM images.[24] The Brunauer-Emmet-Teller (BET) surface areas of ASWNT-1 and ASWNT-2 are 742 and 788 m^2/g respectively. Pristine SWNTs have a BET surface area of 400 m^2/g (Figure 11). The pore size distribution in ASWNT-1 and ASWNT-2 was calculated using non-local density functional theory (NLDFT).[25] ASWNT-1 has pores of 1 nm with other pores in the 1.9 – 2.6 nm region whereas ASWNT-2 shows two maxima at 1 and 1.4 nm in addition to pores in the 1.9 – 2.6 nm region (Figure 10b). The pore size distribution of ASWNTs in 1-3 nm range depends on three parameters, diameter of SWNTs, the length of the linker used to covalently cross-link individual SWNTs and density of the linker on SWNTs used to cross-link. The pore volumes in SWNT, ASWNT-1 and ASWNT-2 are 0.54, 0.76 and 1.1 cm^3/g respectively. The increase in pore diameter, pore volume and surface area of ASWNT-2 relative to ASWNT-1 is attributed to the increase in the linker length from 1,4-diethynylbenzene to 4,4′-diethynylbiphenyl as the other two parameters are same.

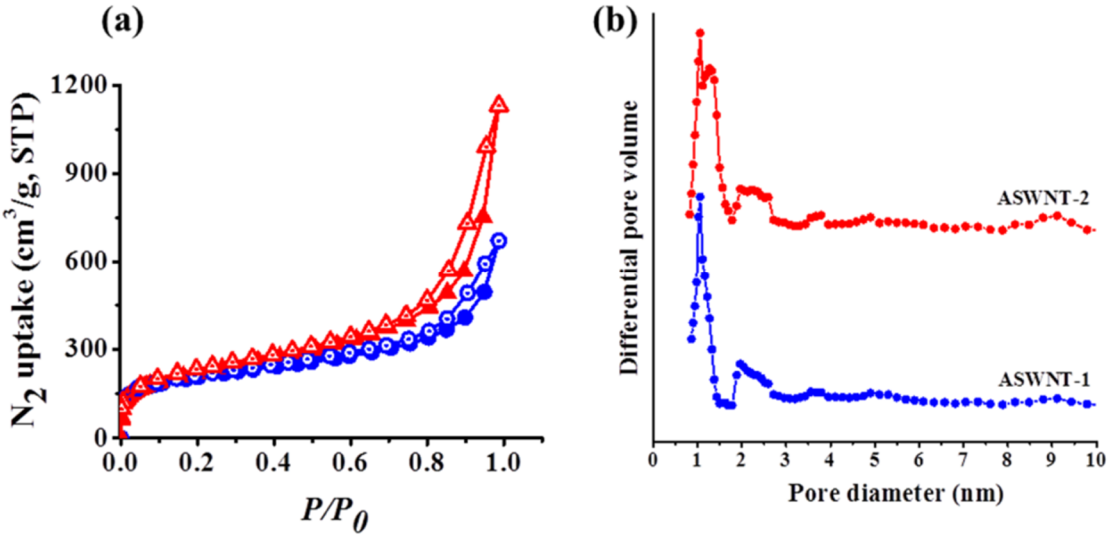

Figure 10. (a) Nitrogen sorption profile of ASWNT-1 (blue) and ASWNT-2 (red) at 77 K. (b) Pore size distribution of ASWNT-1 (blue) and ASWNT-2 (red) calculated using NLDFT.

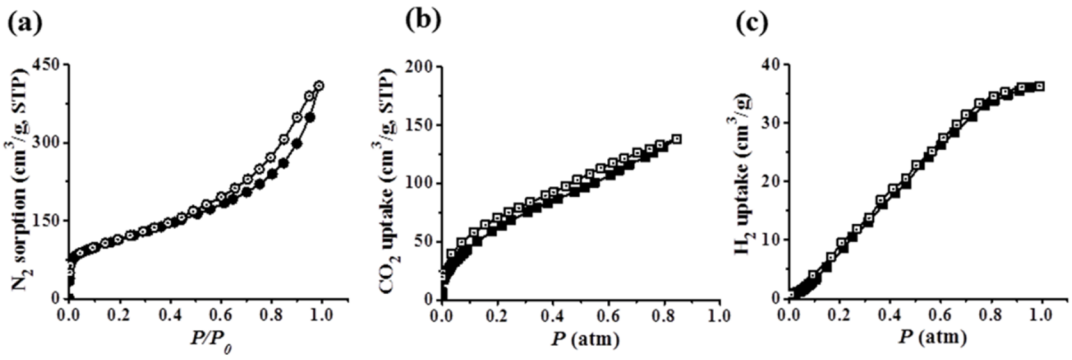

Figure 11. Sorption profiles of pristine SWNTs **(a)** N_2 at 77 K; **(b)** CO_2 195 K and **(c)** H_2 at 77 K.

Thus, by using different length linkers surface area and other porous properties can be tuned. The increase in surface area and porous properties of ASWNTs relative to pristine SWNTs is due to the extra adsorption space in the interstices. Most of the external surface area of the pristine SWNTs is unavailable for adsorption due to bundling arising from van der Waals interactions, with the distance between individual nanotubes of ~ 0.32 nm. Adsorption in the interstices constitutes only a small fraction of the gas adsorbed.

ASWNTs were investigated for storage of CO_2 and H_2. ASWNT-1 and ASWNT-2 exhibit a CO_2 uptake of 45 and 52 wt % respectively at 195 K and ~ 0.85 atm respectively (Figure 12a). The CO_2 uptake of ASWNT-1 and ASWNT-2 at 293 K and

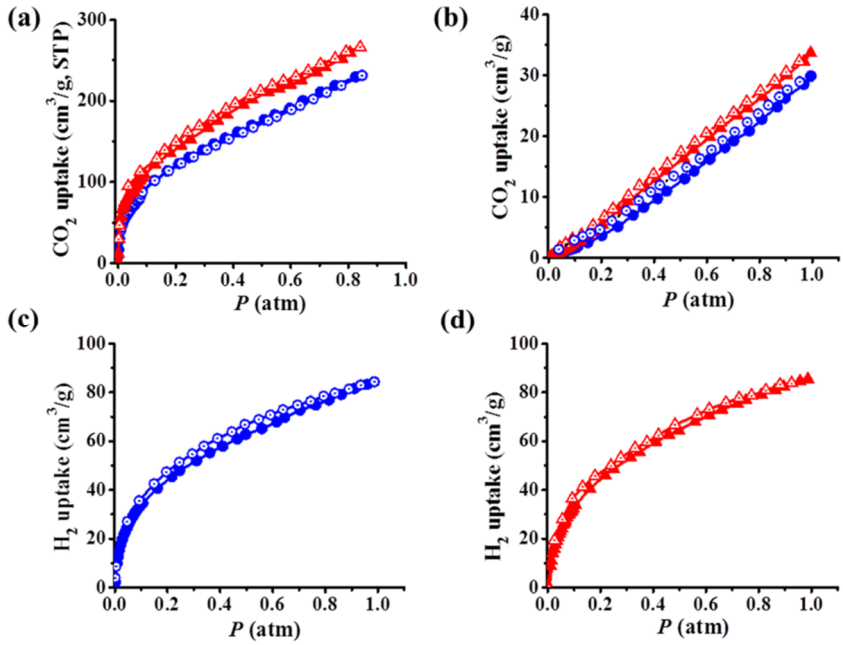

Figure 12. (a) CO_2 sorption profile of ASWNT-1 (blue) and ASWNT-2 (red) at 195 K; **(b)** CO_2 sorption profile of ASWNT-1 (blue) and ASWNT-2 (red) at 293 K. Hydrogen sorption profile of **(C)** ASWNT-1 and **(d)** ASWNT-2 at 77 K.

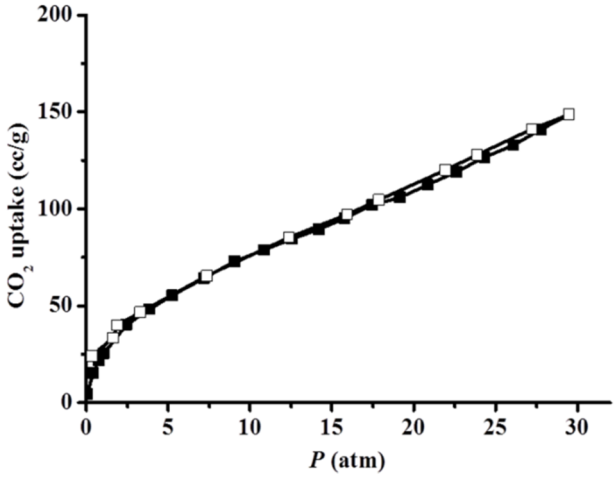

Figure 13. High-pressure CO_2 sorption profile of ASWNT-1 at 273 K.

1 atm is 6 and 6.7 wt% respectively (Figure 12b). High-pressure CO_2 uptake of ASWNT-1 is 29 wt% at 273 K and 30 atm (Figure 13). The CO_2 uptake of SWNTs was 27 wt% at 195 K and ~ 0.85 atm (Figure 11). The CO_2 uptake of ASWNTs is comparable to some of the metal organic frameworks which consist of open metal sites.[26] The CO_2 uptake of ASWNTs is considered to be due to the interaction of the CO_2 molecules and the π cloud of aromatic linkers and the SWNT surface.[27] Although the CO_2 uptake capacity of ASWNTs is reasonable, the hydrophobic nature along with uniform pore size distribution and high chemical and thermal stability of the assembly can be an advantage over existing material.[28] The hydrogen uptake of ASWNT-1 and ASWNT-2 is ~ 0.75 wt% at 77 K and 1 atm (Figure 12c, d). Hydrogen uptake by SWNTs under the same conditions was 0.32 wt% (Figure 11). Theoretical studies on the related structure as potential hydrogen storage material are limited after considering above experimental results.[17]

9.5 Theoretical studies of single–walled carbon nanotube assemblies

Prior to the experimental studies reported here, a significant amount of theoretical studies have been carried out to explore the possibility of SWNT assemblies for hydrogen storage (Figure 14).[17] These theoretical investigations were mainly based upon removing van der Waals interaction between the individual nanotubes in a bundle by cross-linking with uniform length organic linkers or hypothetical uniformly arranged a porous network of carbon nanotubes (Figure 14). New adsorption sites are created in the interstices and these theoretical investigations calculate the interaction energy of hydrogen molecules in these interstices.

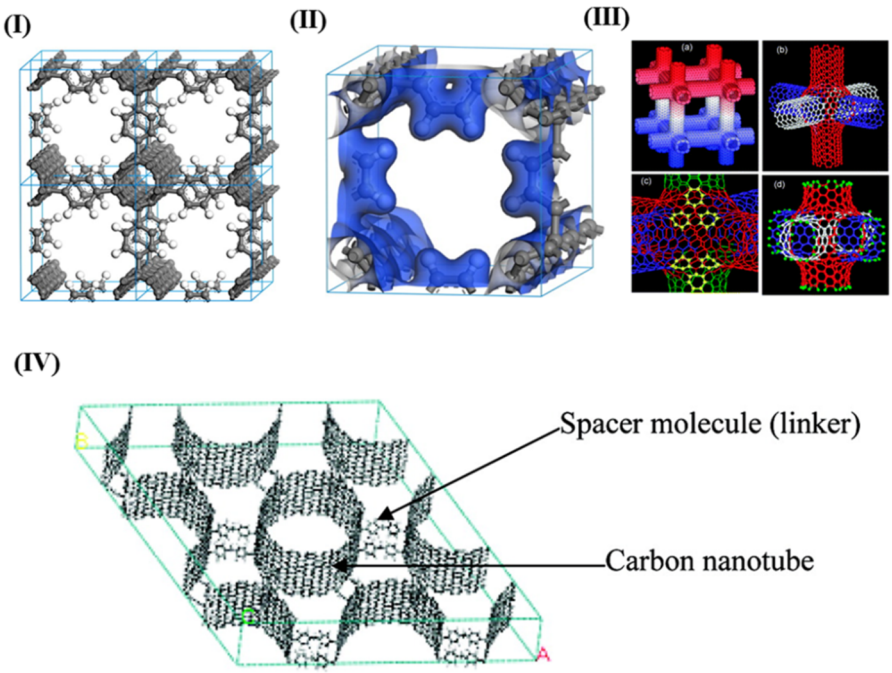

Figure 14. (I) Optimized nanoframework structure consisting of (5,0) SWCNTs constrained by phenyl spacers. (II) The electronic charge density of a framework consisting of (5,0) SWNTs constrained by phenyl spacers. (I) and (II) reproduced with permission from ref [14b]. The value of isosurface corresponds to 0.2 e/ Å^3. (III) Porous nanotube network. Reproduced with permission from ref [14d]. (IV) Carbon nanotube scaffold. Reproduced with permission from ref [14c].

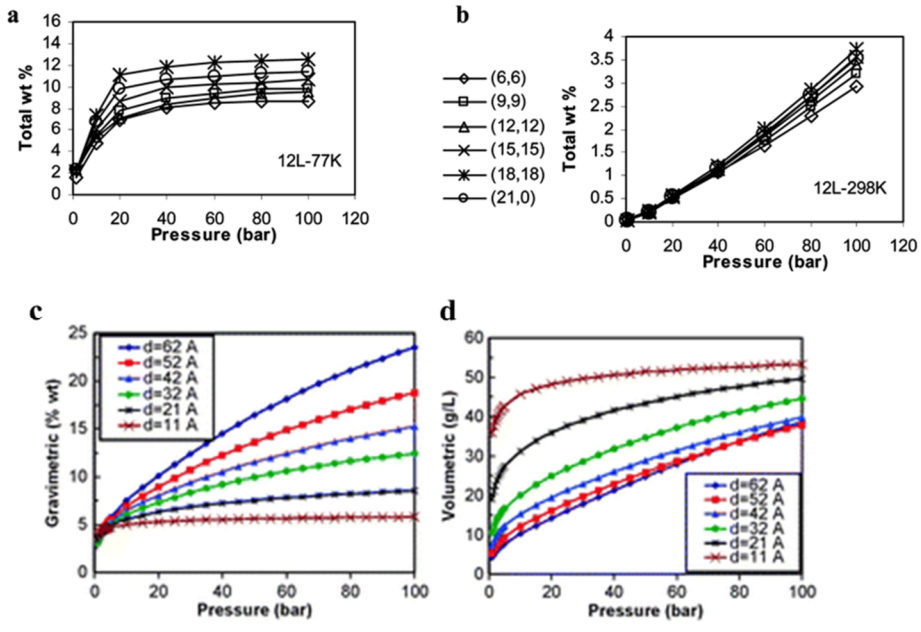

Figure 15. (a, b) Total hydrogen sorption capacity variation with pressure at two different temperatures for structure IV in figure 14. Reproduced with permission from ref [14c]. (c, d) Gravimetric and volumetric hydrogen uptake for the new proposed carbon nanostructures III in figure 14 at 77 K and for a variety of intertube distances *d*. Reproduced with permission from ref [14d].

The theoretical investigations predicted more than 6 wt% (the 2010 United states department of energy target of 6 wt%) hydrogen uptake at cryogenic temperatures (77 K) and high pressure in the range of 60 – 100 bar (Figure 15). Considering the H_2 storage at room temperature the low interaction energy of less than 1 kcal mol^{-1} with C-based material predicted a lower uptake.[17d] In order to improve the hydrogen uptake at room temperature, Li-doping strategy is predicted with an enhancement in adsorption energy of up to 3 kcal mol^{-1} (Figure 16). Although these theoretical studies were promising van der Waals force is the main interaction between a hydrogen molecule and carbon nanotube surface. The present experimental study shows an experimental uptake of ~ 0.75 wt% (at 77 K and 1 atm) with a maximum expected improvement of up to 1.1 or 1.2 wt% on optimizing the linker density. The scope of hydrogen storage at room temperature in such structure is limited.

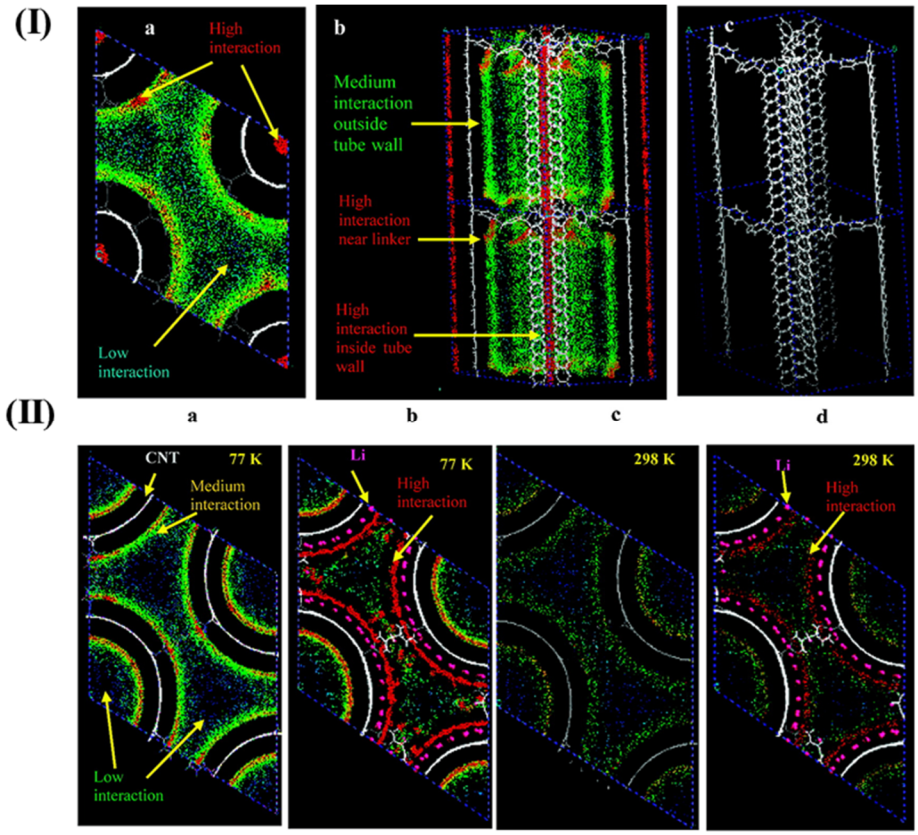

Figure 16. (I) Distribution of hydrogen molecules in the (6, 6) 12 L at 1 atm, 77 K: (a) top view, (b) side view and (c) bare scaffold. (II) Mass density plot for (18, 18), 12 L at 77 and 298 K, 1 atm, with and without Li. 12 L corresponds to interlinked distances of 29.5 Å. Reproduced with permission from ref [14c].

9.6 Conclusions

In conclusion, covalently cross-linked single-walled carbon nanotube assemblies were synthesized using different length organic linkers by employing the Sonogashira coupling reaction. The three-dimensional assemblies exhibit an increase in surface area with respect to pristine SWNTs. The surface area and porosity of the assemblies depend on the length of the linker. The characteristic radial breathing modes of the single-walled carbon nanotubes are retained on covalently cross-linking with organic linkers and assembly formation. Although efficient Pd(0) catalysed C–C coupling reactions have been explored in synthetic organic chemistry, the present study explores its application for the covalent modification of carbon nanotubes. The SWNT assemblies could find useful applications.

References:

[1] a) S. Iijima and T. Ichihashi, *Nature* **1993**, *363*, 603; b) H. Dai, *Acc. Chem. Res.* **2002**, *35*, 1035; c) P. M. Ajayan, *Chem. Rev.* **1999**, *99*, 1787; d) C. N. R. Rao and A. Govindaraj in *Nanotubes and Nanowires*, Royal Society of Chemistry London, **2011**.

[2] Y. Li, D. Yang, A. Adronov, Y. Gao, X. Luo and H. Li, *Macromolecules* **2012**, *45*, 4698.

[3] A. Micoli, A. Turco, E. Araujo-Palomo, A. Encinas, M. Quintana and M. Prato, *Chem. Eur. J.* **2014**, *20*, 5397.

[4] S. Qin, D. Qin, W. T. Ford, Y. Zhang and N. A. Kotov, *Chem. Mater.* **2005**, *17*, 2131.

[5] Q. Wang and J. K. Johnson, *J. Phys. Chem. B* **1999**, *103*, 4809.

[6] A. D. Leonard, J. L. Hudson, H. Fan, R. Booker, L. J. Simpson, K. J. O'Neill, P. A. Parilla, M. J. Heben, M. Pasquali, C. Kittrell and J. M. Tour, *J. Am. Chem. Soc.* **2008**, *131*, 723.

[7] M. Holzinger, J. Steinmetz, D. Samaille, M. Glerup, M. Paillet, P. Bernier, L. Ley and R. Graupner, *Carbon* **2004**, *42*, 941.

[8] a) M. B. Jakubinek, B. Ashrafi, J. Guan, M. B. Johnson, M. A. White and B. Simard, *RSC Adv.* **2014**, *4*, 57564; b) I.-W. P. Chen, R. Liang, H. Zhao, B. Wang and C. Zhang, *Nanotechnology* **2011**, *22*, 485708; c) J. Qu, Z. Zhao, X. Wang and J. Qiu, *J. Mater. Chem.* **2011**, *21*, 5967; d) I. Jurewicz, A. A. K. King, P. Worajittiphon, P. Asanithi, E. W. Brunner, R. P. Sear, T. J. C. Hosea, J. L. Keddie and A. B. Dalton, *Macromol. Rapid Commun.* **2010**, *31*, 609; e) C. Song, T. Kwon, J.-H. Han, M. Shandell and M. S. Strano, *Nano Lett.* **2009**, *9*, 4279.

[9] a) K. Sonogashira, Y. Tohda and N. Hagihara, *Tetrahedron Lett.* **1975**, *16*, 4467; b) K. Sonogashira, *J. Organomet. Chem.* **2002**, *653*, 46.

[10] a) F. Cheng and A. Adronov, *Chem. Mater.* **2006**, *18*, 5389; b) A. S. Jombert, M. K. Bayazit, C. R. Herron, K. S. Coleman and D. A. Zeze, *Sci. Adv. Mater.* **2013**, *5*, 1967.

[11] M. De Marco, F. Markoulidis, R. Menzel, S. M. Bawaked, M. Mokhtar, S. A. Al-Thabaiti, S. N. Basahel and M. S. P. Shaffer, *J. Mater. Chem. A* **2016**, *4*, 5385.

[12] M.-F. Yu, O. Lourie, M. J. Dyer, K. Moloni, T. F. Kelly and R. S. Ruoff, *Science* **2000**, *287*, 637.

[13] Q. Yu, N. Alvarez, P. Miller, R. Malik, M. Haase, M. Schulz, V. Shanov and X. Zhu, *Materials* **2016**, *9*, 68.

[14] a) M. Ouyang, J.-L. Huang and C. M. Lieber, *Acc. Chem. Res.* **2002**, *35*, 1018; b) C. T. White and J. W. Mintmire, *J. Phys. Chem. B* **2005**, *109*, 52; c) H. Kataura, Y. Kumazawa, Y. Maniwa, I. Umezu, S. Suzuki, Y. Ohtsuka and Y. Achiba, *Synth. Met.* **1999**, *103*, 2555; d) R. S. Ruoff and D. C. Lorents, *Carbon* **1995**, *33*, 925; e) Z. Jijun, B. Alper, H. Jie and L. Jian Ping, *Nanotechnology* **2002**, *13*, 195.

[15] a) Y.-P. Sun, K. Fu, Y. Lin and W. Huang, *Acc. Chem. Res.* **2002**, *35*, 1096; b) J. N. Coleman, U. Khan, W. J. Blau and Y. K. Gun'ko, *Carbon* **2006**, *44*, 1624; c) G. Che, B. B. Lakshmi, E. R. Fisher and C. R. Martin, *Nature* **1998**, *393*, 346; d) A. Fujiwara, K. Ishii, H. Suematsu, H. Kataura, Y. Maniwa, S. Suzuki and Y. Achiba, *Chem. Phys. Lett.* **2001**, *336*, 205; e) F. L. Darkrim, P. Malbrunot and G. P. Tartaglia, *Int. J. Hydrogen Energy* **2002**, *27*, 193.

[16] a) R. Saito, C. Fantini and J. Jiang in *Excitonic States and Resonance Raman Spectroscopy of Single-Wall Carbon Nanotubes*, Eds.: A. Jorio, G. Dresselhaus and M. S. Dresselhaus), Springer Berlin Heidelberg, Berlin, Heidelberg, **2008**, pp. 251; b) A. Jorio, R. Saito, G. Dresselhaus and M. S. Dresselhaus, *Phil. Trans. R. Soc. A* **2004**, *362*, 2311.

[17] a) G. E. Froudakis, *Mater. Today* **2011**, *14*, 324; b) P. F. Weck, E. Kim, N. Balakrishnan, H. Cheng and B. I. Yakobson, *Chem. Phys. Lett.* **2007**, *439*, 354; c) M. M. Biswas and T. Cagin, *J. Phys. Chem. B* **2010**, *114*, 13752; d) E. Tylianakis, G. K. Dimitrakakis, S. Melchor, J. A. Dobado and G. E. Froudakis, *Chem. Commun.* **2011**, *47*, 2303.

[18] L. A. Girifalco, M. Hodak and R. S. Lee, *Phys. Rev. B, PRB* **2000**, *62*, 13104.

[19] a) D. Tasis, N. Tagmatarchis, A. Bianco and M. Prato, *Chem. Rev.* **2006**, *106*, 1105; b) S. Niyogi, M. A. Hamon, H. Hu, B. Zhao, P. Bhowmik, R. Sen, M. E. Itkis and R. C. Haddon, *Acc. Chem. Res.* **2002**, *35*, 1105; c) J. L. Bahr and J. M. Tour, *J. Mater. Chem.* **2002**, *12*, 1952; d) S. Banerjee, T. Hemraj-Benny and S. S. Wong, *Adv. Mater.* **2005**, *17*, 17.

[20] a) D. Sloan, Y. M. Sun, H. Ihm and J. M. White, *J. Phys. Chem. B* **1998**, *102*, 6825; b) H. Cabibil, H. Ihm and J. M. White, *Surf. Sci.* **2000**, *447*, 91.

[21] C. A. Dyke and J. M. Tour, *Nano Lett.* **2003**, *3*, 1215.

[22] D. W. Mayo, F. A. Miller and R. W. Hannah in *Course Notes on the Interpretation of Infrared and Raman Spectra*, John Wiley & Sons, Inc., **2003**.

[23] a) H. Peng, L. B. Alemany, J. L. Margrave and V. N. Khabashesku, *J. Am. Chem. Soc.* **2003**, *125*, 15174; b) C. Goze Bac, P. Bernier, S. Latil, V. Jourdain, A. Rubio, S. H. Jhang, S. W. Lee, Y. W. Park, M. Holzinger and A. Hirsch, *Curr. Appl. Phys.* **2001**, *1*, 149.

[24] K. S. W. Sing, D. H. Everett, R. A. W. Haul, L. Moscou, R. A. Pierotti, J. Rouquerol and T. Siemieniewska, *Pure Appl. Chem.* **1984**, *57*, 603.

[25] a) P. I. Ravikovitch, A. Vishnyakov, R. Russo and A. V. Neimark, *Langmuir* **2000**, *16*, 2311; b) J. Landers, G. Y. Gor and A. V. Neimark, *Colloids Surf., A* **2013**, *437*, 3.

[26] a) N. Ko, J. Hong, S. Sung, K. E. Cordova, H. J. Park, J. K. Yang and J. Kim, *Dalton Trans.* **2015**; b) S.-S. Chen, P. Wang, S. Takamizawa, T.-a. Okamura, M. Chen and W.-Y. Sun, *Dalton Trans.* **2014**, *43*, 6012; c) Z. Lin, R. Zou, W. Xia, L. Chen, X. Wang, F. Liao, Y. Wang, J. Lin and A. K. Burrell, *J. Mater. Chem.* **2012**, *22*, 21076; d) Y. Yan, M. Suyetin, E. Bichoutskaia, A. J. Blake, D. R. Allan, S. A. Barnett and M. Schroder, *Chem. Sci.* **2013**, *4*, 1731; e) S.-H. Lo, C.-H. Chien, Y.-L. Lai, C.-C. Yang, J. J. Lee, D. S. Raja and C.-H. Lin, *J. Mater. Chem. A* **2013**, *1*, 324.

[27] A. M. Plonka, D. Banerjee, W. R. Woerner, Z. Zhang, N. Nijem, Y. J. Chabal, J. Li and J. B. Parise, *Angew. Chem. Int. Ed.* **2013**, *52*, 1692.

[28] K. Sumida, D. L. Rogow, J. A. Mason, T. M. McDonald, E. D. Bloch, Z. R. Herm, T.-H. Bae and J. R. Long, *Chem. Rev.* **2011**, *112*, 724.

Chapter 10: Conclusions of the thesis and future directions

The investigations carried out in the thesis contributes to the area of porous solids, materials with optical properties, development of covalent chemistry of 2D materials and its application in the synthesis of composites and complex multifunctional assemblies. The major part of thesis contributes in the area of porous solids. The area of porous solids, major advances, and developments till now have been briefly reviewed in chapter 1 along with some of the challenges and requirements in practical situations. Metal-organic frameworks (MOFs) are an important class of ultrahigh surface area porous solids and there has been significant progress in last 15 years with more than 50, 000 known structures in Cambridge structural database (CSD). Ultrahigh surface area, highly ordered crystalline microporous architecture, control over the design strategy and functionality of framework structure are some of the advantages of MOFs over other porous materials. However due to the presence of moderate energy coordinate bonds building the framework structure; MOFs suffer from low framework stability.[1] They have low mechanical properties and framework structure collapse under hydrostatic pressure. The framework collapse leads to the loss of porous architecture and resulting functional properties. The thesis tries to address this aspect by making composite with 2D materials such as BN and graphene which have very high mechanical properties. On uniformly reinforcing the MOF matrix with graphene significant improvement in the mechanical properties was observed along with an improvement in porosity and gas adsorption/separation properties. The improvement in mechanical properties by reinforcing the MOF matrix with few wt% of 2D materials without compromising the functional properties is an important step towards the practical application of these classes of highly porous materials. The low mechanical properties of MOFs are a major challenge before considering any practical application of these porous solids. The external hydrostatic pressure of several GPa is commonplace in various industrial gas adsorption/separation and catalytic processes and the porous adsorption bed has to withstand several such cycles. The initial result of the role of graphene and BN in enhancing the mechanical properties without compromising intrinsic functional properties will stimulate several such studies and further improvement in the mechanical properties is expected. The present strategy of reinforcing the MOF matrix with few wt% of different functionalized 2D materials is very promising and will overcome the bottleneck of low mechanical properties of MOFs.

The surface of layered materials such as graphene and BN can be grafted with various functional groups which can coordinate with the metal ions and help in the nucleation and growth of MOF units. MOF nanoparticles can be grown on functionalized graphene or BN basal plane. MOF nanoparticles chemically bonded with graphene or BN basal plane has been observed to have significantly different adsorption properties in comparison to the individual components constituting the composite. The enhancement in gas adsorption/separation property is due to the synergistic interaction between the constituent components and chemical bond between the components further improves this interaction. For example, ZIF-8 nanoparticles can be uniformly grown on graphene oxide basal plane by adding Zn(II) ions and 2-methylimidazole linker. The composites show significantly enhanced CO_2 uptake in comparison to pristine ZIF-8 although the surface area is lower. This is due to the formation uniformly blended MOF nanoparticles and graphene oxide. The various oxygen-containing functional groups such as epoxides, hydroxyls, and carboxylates along with microporosity and high surface area contributed by the MOF nanoparticles results in such observation. The investigations outlined in the thesis have resulted in several such analogues MOF-nanocarbon composites (ZIF-8@graphene oxide, ZIF-8@carbon nanotube, and ZIF-8@carbon quantum dot) and have been used for gas and chromatographic separation,[2] increased CO_2 and organic molecule uptake,[3] electrocatalysis in oxygen reduction reaction,[4] photocatalysis, in lithium–ion battery,[5] proton exchange membranes,[6] drug delivery and fluorescence imaging,[7] and as catalysts in cycloaddition reactions.[8] The diverse applications of prototypical ZIF-8@nanocarbon based composites show the importance of combining two materials in the composite form. Synergistic interaction between the two components MOF and graphene plays a key role in determining such properties and applications. Such composite route is promising for enhancing the functional properties of MOFs.

Layered MOFs are other interesting architectures and graphene basal plane with various oxygen-containing functional groups can be used as a template for the growth of these layered MOFs. The growth of 2D-MOFs on 2D-graphene or other layered materials such as BN, MoS_2, $MoSe_2$ is expected to result in hybrid composites with new properties. Chapter 3 tries to address this idea by making two prototypical composites with different functionalized graphene basal plane. Very thin layered assemblies of graphene and MOF were obtained by chemical exfoliation. The colloidal dispersion of these layered architectures can be used for the synthesis of Langmuir-Blodgett films and coatings for various applications. The present investigation has inspired similar analogues studies for various applications. Ultrathin graphene-MOF composites and composites with other 2D-materials such as BN, MoS_2,

$MoSe_2$, WS_2, are promising for gas separation membranes, catalysis and in fuel cell applications.

Rare earth (Eu^{3+}, Tb^{3+}, Pr^{3+}, Gd^{3+}) based luminescent MOFs have sharp emission and interesting magnetic properties. The organic linker in the MOF architecture by antenna effect enhances the quantum yield of rare earth emission. By incorporating graphene in the MOF matrix of a rare earth based MOF, quenching of lanthanide emission has been studied. The mechanism of fluorescence quenching was investigated. The fundamental studies carried out in predicting the role of graphene in quenching the lanthanide emission will be of significant practical importance.

Carbon based porous materials have the advantage of high stability under various harsh chemical environments. High surface area porous carbons are used as support for various catalysts. In addition porous carbon materials and different modified forms are extensively used in energy storage devices such as supercapacitor and batteries and in fuel cells. Although quite economical very high surface area carbon-based porous materials are commercially available, they suffer from highly irregular and random pore sizes. Single or few-layer graphene and single-walled carbon nanotubes (SWNTs) have theoretically predicted very high surface area when all the adsorption sites can be accessible. However due to the presence of Van der Walls interactions they are highly agglomerated and have surface areas of ~ 50 – 300 m^2/G. In addition, they have random pore size distributions. Utilization of 2-D layered graphene or 1-D SWNTs for the synthesis of the uniform porous hierarchical structure with well-defined pore size distributions and high surface area is promising. The thesis tries to address this aspect by using graphene and SWNTs as the building block. Individual graphene and SWNTs were cross-linked with uniform length (~ 2 nm) organic linkers. To synthesize such porous hierarchical structures idea of covalent cross-linking has been used. Covalent bond results in highly robust hierarchical porous architecture. Graphene and SWNTs with sp^2 hybridized carbon basal plane can be functionalized with aryl halides using the free radical mechanism with diazonium salts of different aryl halides. Aryl halides are a standard substrate for Pd(0) catalyzed C–C cross-coupling reactions. Individual graphene and SWNTs were cross-linked using Pd(0) catalyzed C–C cross-coupling reactions with different length organic linkers to make a uniform porous architecture. The obtained pillared graphene frameworks (PGFs) and assemblies of single-walled carbon nanotube (ASWNT) have a uniform pore size and significantly enhanced surface area. Present experimental investigations have resulted in theoretical studies of pillared graphene hierarchical structures for gas adsorption/separations applications. Theoretical studies predict the gas adsorption properties reasonably well with

our experimental reports with a prediction of high performance in gas separation applications which needs to be experimentally investigated. In addition to the aim of synthesis of highly robust and porous carbon-based porous solids, the present synthesis strategies also help in the development of covalent chemistry of nanocarbon. The Pd(0) catalyzed C–C cross-coupling reactions are widely investigated in synthetic organic chemistry the present investigation expands it to nanocarbon chemistry.

The strategy of covalent cross-linking has been used in the design of heterostructures of two different layered materials such as BN and graphene. Layer-by-layer assemblies of BN and graphene have been synthesized by cross-coupling carboxylated graphene with amine functionalized BN using amide bond. The bulk synthesis of such composites is highly promising because the composition of individual component can be controlled in the composite. As both the individual components have significantly different properties, the properties of composites are tuned by varying the composition. These composites are highly promising in supercapacitors and as an electrocatalyst in fuel cell applications. The strategy of covalent cross-linking results in maximum synergy with enhanced or new properties expected in the composites.

In addition to contributing in the area of porous solids, new synthesis strategies for covalent modification of different nanomaterials have been successfully addressed. Surface area is just one of the important parameter and high mechanical strength, stability under harsh chemical environments; recyclability and cost of the material are other important parameters for widespread practical applications. The thesis has tried to address some of these issues as there has been significant progress in last 15 years in the synthesis of many ultrahigh surface area porous solids. Considering the widespread applications of porous materials in various gas/adsorption separation processes many interesting developments are expected in coming years.

References

[1] a) R. Kumar, D. Raut, U. Ramamurty and C. N. R. Rao, *Angew. Chem. Int. Ed.* **2016**, *55*, 7857; b) J. C. Tan and A. K. Cheetham, *Chem. Soc. Rev.* **2011**, *40*, 1059.

[2] a) A. Huang, Q. Liu, N. Wang, Y. Zhu and J. Caro, *J. Am. Chem. Soc.* **2014**, *136*, 14686; b) Y. Hu, J. Wei, Y. Liang, H. Zhang, X. Zhang, W. Shen and H. Wang, *Angew. Chem. Int. Ed.* **2016**, *55*, 2048; c) X. Yang, C. Li, M. Qi and L. Qu, *J. Chromatogr. A* **2016**, *1460*, 173.

[3] a) B. Chen, Y. Zhu and Y. Xia, *RSC Adv.* **2015**, *5*, 30464; b) Y. Yang, L. Ge, V. Rudolph and Z. Zhu, *Dalton Trans.* **2014**, *43*, 7028; c) Y. Zhou, L. Zhou, X. Zhang and Y. Chen, *Microporous Mesoporous Mater.* **2016**, *225*, 488; d) D. Kim, D. W. Kim, W. G. Hong and A. Coskun, *J. Mater. Chem. A* **2016**, *4*, 7710.

[4] H.-x. Zhong, J. Wang, Y.-w. Zhang, W.-l. Xu, W. Xing, D. Xu, Y.-f. Zhang and X.-b. Zhang, *Angew. Chem. Int. Ed.* **2014**, *53*, 14235.

[5] X. Cao, B. Zheng, X. Rui, W. Shi, Q. Yan and H. Zhang, *Angew. Chem.* **2014**, *126*, 1428.

[6] L. Yang, B. Tang and P. Wu, *J. Mater.Chem. A* **2015**, *3*, 15838.

[7] L. He, T. Wang, J. An, X. Li, L. Zhang, L. Li, G. Li, X. Wu, Z. Su and C. Wang, *CrystEngComm* **2014**, *16*, 3259.

[8] Y. Wei, Z. Hao, F. Zhang and H. Li, *J. Mater. Chem. A* **2015**, *3*, 14779.